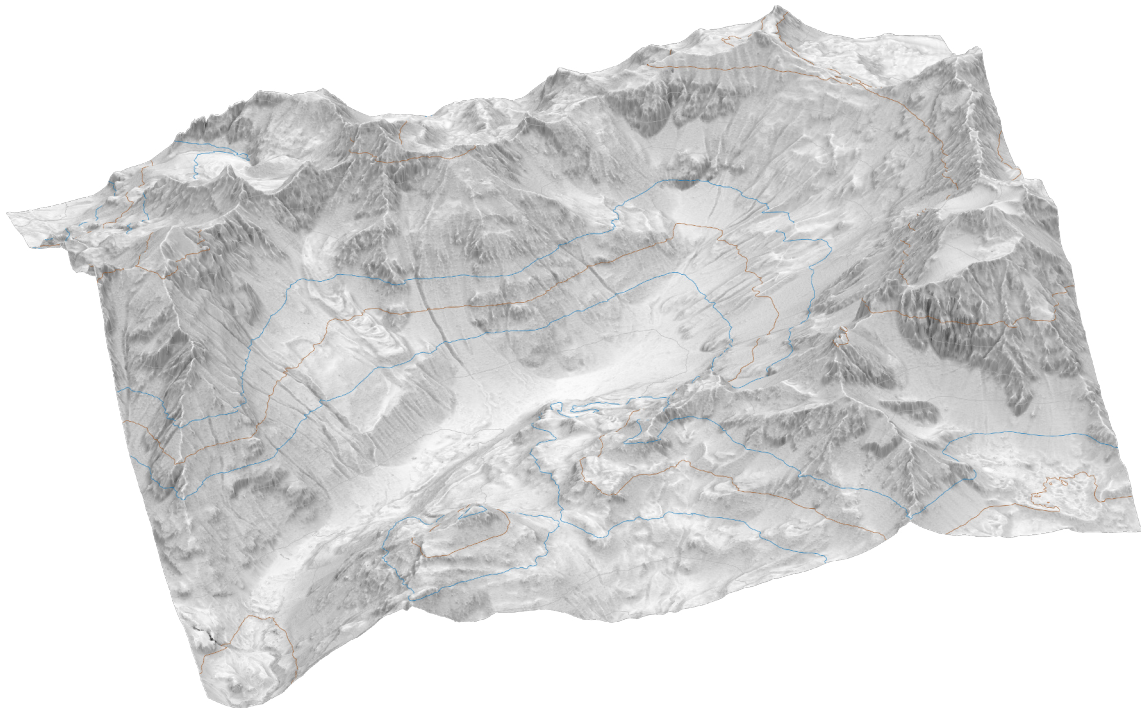


Master's ThesisDepartment of Earth Sciences
Geological Institute
ETH ZürichDominik AMSCHWAND
13-928-395Active, inactive, relict:
Tracking the evolution of the Bleis Marscha rockglacier
(Val d'Err, Grisons) with cosmogenic nuclide dating and
finite-element modellingSupervisor:
PD Dr. Susan IVY-OCHS
Laboratory of Ion Beam Physics, ETH ZürichCo-Supervisors:
PD Dr. Marcel FREHNER
Geological Institute, ETH Zürich

and

Olivia KRONIG
Laboratory of Ion Beam Physics, ETH Zürich

Zürich, 14 September 2018



Synthetic oblique sky-view factor visualisation of Val d'Err, view towards SE. Contour lines equidistance is 100 m. The 2400 and 2600 m contour lines (blue) mark the lower boundary of discontinuous and continuous permafrost, respectively (rule of thumb).

Abstract

We attempt to reconstruct the formation of the *Bleis Marscha* rockglacier in the *Val d'Err*, Grisons (Switzerland) with terrestrial cosmogenic surface exposure dating, aerial image correlation and numerical modelling. The *Bleis Marscha* rockglacier is a 1200 m long, multi-unit talus rockglacier with an active upper part that overrides a lower part. Lichen-covered boulders, vegetated, stabilized slopes, and signs of settling suggest that the parts below ~2500 m a.s.l. are relict. Internal front scarps separate the rockglacier into different units, each with its own activity phase. Morphological evidence suggests that the rockglacier began forming in the earliest Holocene.

Surface exposure dating with cosmogenic ^{10}Be and ^{36}Cl places a temporal framework (ka scale) on rockglacier movement periods. On the presently active part, the exposure ages correlate well with distance from the source and can be addressed as minimal travel times. The oldest age above the internal main scarp suggests that the late Holocene activity period initiated not after 2.8 ± 0.2 ka. The exposure ages on the relict part below have a larger scatter in the order of centuries, suggesting that disturbances (intermittent boulder instabilities, self-shielding caused by boulder rotation) affecting the nuclide inventories are more important during inactivation and collapse. This apparent rejuvenation explains both the tendentially “too-young” ages and the large spread. The oldest age, interpreted as (rough) inactivity age, suggests that first generation of the *Bleis Marscha* rockglacier initiated in the late Younger Dryas and ceased its activity around 9.0 ± 0.6 ka.

Feature-tracking analysis of bi-temporal (2003-2012) orthophotos constrains the present horizontal surface velocity field. An illumination-invariant method for correlating orthophoto-derived orientation images yielded reliable displacements on the rugged rockglacier surface. The image correlation results support the subdivision of the *Bleis Marscha* rockglacier in an active upper part, characterised by moderate to high surface velocities controlled by the topography on a 100-m scale, and a relict, collapsing lower part, characterised by an irregular surface velocity field strongly coupled to the small-scale topography (“effet camembert”). The degree of correlation between morphology and surface creep field indicates the dynamic state of the rockglacier.

Present-day dynamics are numerically modelled using a two-dimensional finite-element approach to gain insights into the mechanical and material properties. The influence of the mechanical layering (boulder mantle, rockglacier core and low-viscosity basal shear layer) on stress distribution and deformation is explored. In an inverse problem constrained with the surface velocity data, the viscosity structure of the rockglacier is inferred. Surface velocities of up to 30 cm a^{-1} on the apparently relict part could only be numerically reproduced assuming a considerable fraction of ice and/or water that weakens the material. The subsurface ice either has been preserved throughout the Holocene or has reformed more recently. Although the model assumes a Newtonian, incompressible rheology, the typical strain localisation towards the basal shear zone resulting from non-linear deformation mechanisms could be emulated (reproduced “by appearance”) with the prescribed viscosity layering.

Nous ampruagn da modelar las fasas da furmaziun digl glatscher da schalada permanenta *Bleis Marscha* an la *Val d'Err* (Grischun) antras dataziuns dalla surfatscha cun nuclids cosmogens, correlaziuns da fotografias or da l'aria e modelaziun da finite-element. Indizis morfologics e la momentana (2003-2012) sveltezza orizzontala dalla surfatscha laschan supponer ena sotdivisiun digl 1200 m lung, poymorf talus-glatscher da schalada permanenta an ena part soura activa tgi avanzescha e vò sur la part sot relict. Tottas dus parts eran durant different taimps activ: La part sot (sot ca. 2500 m s.m.) pi vigla ò sa furmo cunter la fegn digl pi Giuven Dryas ed è neida climaticamaintg inactiva aint igl giuven Olocen. Dalla vigliadetna d'exposiziun da ^{10}Be e ^{36}Cl resultescha ena vigliadetna da 4.8 ± 0.3 anfignen 9.0 ± 0.6 k onns. Las vigliadetnas tendenzial “mengia giuvnas” e la gronda dimensiun (regiuvinaziun apparenta) è da declarar antras l'instabilitad temporara e la protecziun da sasez digls blocs controllos antras igl collaps digl relief scunflo (“effect camembert”). La vigliadetna maximala vign interpretada scu vigliadetna d'inactivitad. La part soura pi giuvna è neida furmada durant igl pigiuramaint climatic digl tardiv Olocen. Igl glatscher da schalada permantenta creschent existeva igl madem mument scu igl glatscher da foppa *Bleis Marscha* tgi avanzava e sa tirava anavos periodicamaintg. La vigliadetna d'exposiziun correlescha cun la distanza tar la zona da rieisch digl glatscher da schalada permantenta e sò uscheia neir interpretada scu (minimal) taimp da viadi dalla blocca. La pi viglia dataziun dalla surfatscha da 2.8 ± 0.2 k onns sur la scarpa digl front datescha la (pi tard') antschatta dalla sagonda fasa d'activitad. Cun ena reologia newtonica ed ena

stratificaziun da viscosità determinada sò igl model linear numeric emular (reproduzier la cumparaziun) mecanissem da deformaziun cumplitgias, betg-linears an igl orizont da forbesch. Igl resultad sugereschan bier glatsch ed/ni avà an la part relicta d'igl glatscher da schalada permanenta, chegl tgi deblescha igl masditg da gera-glatsch e declera la sveltezza dalla surfatscha dad anfigen 35 cm/onn. [*Translato dad Anina Janett-Sonder*]

Wir versuchen die Bildungsphasen des *Bleis Marscha* Blockgletschers im *Val d'Err* (Graubünden) mittels Oberflächendatierung mit kosmogenen Nukliden, Luftbildkorrelation und Finite-Element-Modellierung nachzuzeichnen. Morphologische Hinweise und das derzeitige (2003-2012) horizontale Oberflächengeschwindigkeitsfeld legen eine Unterteilung des 1200 m langen, polymorphen Talusblockgletschers in einen aktiv vorrückenden oberen Teil nahe, der einen relikten unteren Teil überfährt. Beide Teile waren zu verschiedenen Zeiten aktiv: Der untere, ältere Teil (unterhalb ca. 2500 m ü. M.) bildete sich gegen Ende der Jüngeren Dryas und wurde im frühen Holozän klimatisch inaktiv. Die ^{10}Be und ^{36}Cl Expositionsalter geben ein Alter von 4.8 ± 0.3 bis 9.0 ± 0.6 ka. Die tendenziell 'zu jungen' Alter und ihre grosse Bandbreite (scheinbare Verjüngung) wird auf zeitweise Instabilität und Selbstabschirmung der beprobten Blöcke während des Kollapses des wulstigen Oberflächenreliefs zurückgeführt ('effet camembert'). Das Maximalalter wird als (ungefähres) Inaktivierungsalter angesprochen. Der obere, jüngere Teil bildete sich im Verlauf der klimatischen Verschlechterungen im späten Holozän. Der stetig wachsende Blockgletscher bestand gleichzeitig zum periodisch vorstossenden und zurückziehenden *Bleis Marscha* Kargletscher. Die Expositionsalter korrelieren mit der Distanz zur Wurzelzone des Blockgletschers und können daher als (minimale) Reisezeit der Blöcke interpretiert werden. Das älteste Oberflächenalter von 2.8 ± 0.2 ka oberhalb der Stirnböschung datiert den (spätesten) Beginn der zweiten Aktivitätsphase. Mit einer Newtonschen Rheologie und einer festgelegten Viskositätsschichtung kann das lineare numerische Modell kompliziertere, nicht-lineare Deformationsmechanismen in Scherhorizonten emulieren (von der Erscheinung her nachbilden). Oberflächengeschwindigkeiten von bis zu 35 cm a^{-1} im obersten Teil der relikten unteren Blockgletscherhälfte können nur durch Spannungsübertragung der vorstossenden aktiven Zunge unmittelbar darüber und durch einen hohen Anteil an Eis und/oder Wasser im relikten Blockgletscherteil erklärt werden, welcher das Schutt-Eis-Gemisch schwächt.

Abbreviations and notation

AMS	accelerometer mass spectrometry
DEM	digital elevation model <i>or</i> discrete-element modelling
ELA	equilibrium line altitude (\sim firnline)
FEM	finite-element modelling
LGM	Last Glacial Maximum
LIA	Little Ice Age
MAAT	mean annual air temperature
MAGST	mean annual ground surface temperature
MAP	mean annual precipitation
MIS	Marine isotope stage
MPA	mountain permafrost altitude
NCC	normalized cross correlation (of aerial images)
OC	orientation correlation (correlation of orientation images)
SHD	Schmidt-hammer exposure age dating
SVF	sky-view factor
TCND	terrestrial cosmogenic nuclide dating
YD	Younger Dryas

Notation.

Symbol	Unit	Description
Permafrost, rockglacier and climate-related parameters		
T	$^{\circ}\text{C}$	ground or air temperature
T_a	$^{\circ}\text{C}$	mean annual air temperature (MAAT)
T_s	$^{\circ}\text{C}$	annual mean temperature at the ground surface (MAGST)
T_{ps}	$^{\circ}\text{C}$	annual mean permafrost surface temperature
\bar{v}	m a^{-1}	vertically averaged down-slope velocity
v_s	m a^{-1}	surface down-slope velocity
v_b	m a^{-1}	basal down-slope velocity
\dot{x}	m a^{-1}	rockglacier advance rate (down-slope)
t	s, a	time
t_c	s, a	response time
t_{tf}	s, a	thaw time
H, \bar{H}	m	(averaged) rockglacier thickness
H_p	m	permafrost thickness
H_0	m	steady-state permafrost thickness
h_t	1	fraction of talus height to rockglacier front height
$\alpha, \bar{\alpha}$	$^{\circ}$	(100 m-averaged) surface slope
Thermal and mechanical material parameters		
k	$\text{W m}^{-1} \text{K}^{-1}$	thermal conductivity
k_p	$\text{W m}^{-1} \text{K}^{-1}$	thermal conductivity of frozen ground
κ	$\text{m}^2 \text{a}^{-1}$	volumetric thermal diffusivity
L	J m^{-3}	volumetric latent heat of fusion
ρ	kg m^{-3}	density
μ, μ_{eff}	Pa s	(effective) viscosity
R	1	viscosity contrast
K	Pa	bulk modulus (elastic modulus)
G	Pa	shear modulus (elastic modulus)
Image correlation parameters		
x, y	m	(ground) coordinates (horizontal)
I_0, I_1		image
\mathbf{C}, C_{ij}	1	normalized-cross correlation coefficient matrix (NCC matrix)
γ	1	NCC coefficient
C_{max}	1	maximum correlation coefficient
C_{noise}	1	noise level estimate
SNR	1	signal-to-noise ratio
w_t	px	template width
w_s	px	search window width
Δh_{max}	px	maximum trackable displacement
\mathbf{v}_s	m s^{-1}	horizontal surface velocity field with components v_x, v_y
$ \mathbf{v}_s \equiv v_s$	$\text{m s}^{-1}, \text{m a}^{-1}$	magnitude of horizontal surface velocity, speed
$\dot{\epsilon}_s$	$\text{s}^{-1}, \text{a}^{-1}$	horizontal surface strain-rate tensor
$\dot{\epsilon}_{II}$	$\text{s}^{-1}, \text{a}^{-1}$	second invariant of the strain-rate tensor
$\dot{\epsilon}_i$	$\text{s}^{-1}, \text{a}^{-1}$	principal strain rate (eigenvalue)
θ_p	rad	principal angle
$\mathbf{\Omega}$	$\text{s}^{-1}, \text{a}^{-1}$	surface vorticity tensor
ζ	$\text{s}^{-1}, \text{a}^{-1}$	vertical component of the vorticity vector
W_k	1	kinematic vorticity number

Notation (continued)		
Symbol	Unit	Description
Numerical modelling parameters		
x, y	m	coordinates (horizontal)
z	m	coordinate (vertical, depth)
\mathbf{v}	m s^{-1}	velocity field with components v_x, v_y
$\boldsymbol{\sigma}$	Pa	stress tensor
$\boldsymbol{\sigma}'$	Pa	deviatoric stress tensor
σ_{II}	Pa	second invariant of the stress tensor
τ, τ_b	Pa	(basal) shear stress
$\dot{\boldsymbol{\epsilon}}$	$\text{s}^{-1}, \text{a}^{-1}$	strain-rate tensor
$\dot{\epsilon}_{\text{II}}$	$\text{s}^{-1}, \text{a}^{-1}$	second invariant of the strain-rate tensor
p	$\text{N m}^{-2} \equiv \text{Pa}$	pressure
A	$\text{a}^{-1} \text{Pa}^{-n}$	rate factor in GLEN's flow law
n	1	"flow law exponent" in GLEN's flow law
f	1	shape factor
Surface exposure dating parameters		
t	a	time
t_{exp}	a	exposure age
t_{trv}	a	travel time estimate
C	at g^{-1}	<i>in-situ</i> cosmogenic nuclide concentration
P_0	$\text{at g}^{-1} \text{a}^{-1}$	local cosmogenic nuclide production rate
λ	a^{-1}	decay constant
$t_{1/2}$	a	half-life
ρ	g cm^{-3}	density of the irradiated rock
ε	cm a^{-1}	erosion rate
Λ	g cm^{-2}	attenuation length
C_{inh}	at g^{-1}	inherited nuclide concentration
Constants		
g	m s^{-2}	gravitational acceleration
q	W m^{-2}	geothermal heat flow
Mathematical notation		
$\nabla(\cdot)$		Nabla operator
$\mathcal{F}(\cdot)$		Fourier transformation
\mathbf{I}, δ_{ij}		Kronecker delta
e		EULER's number
i		complex imaginary unit

Contents

1	Introduction	1
1.1	Motivation	1
1.2	Aim and research questions	2
1.3	Thesis outline	3
1.4	Terminology and general definitions	4
2	State of research	7
2.1	Alpine Lateglacial and Holocene climate history	7
2.2	Rockglaciers	8
2.2.1	Concepts, definitions and classifications	8
2.2.2	Thermal conditions	9
2.2.3	Form and surface morphology	10
2.2.4	Stratigraphy, composition and internal structure	11
2.2.5	Thermo-mechanical properties and advance mechanisms	11
2.2.6	(Palaeo-)climatic significance and surface speed variations	15
2.3	Rockglacier dating techniques	16
2.4	Kinematic studies	17
2.5	Numerical modelling of rockglaciers	19
3	Study site	24
3.1	Geology of Val d’Err	24
3.2	Geomorphology and climate	27
4	Methods	33
4.1	Field work	33
4.1.1	Field observations	33
4.1.2	Sampling procedure	33
4.2	Geomorphological analysis and mapping	34
4.3	Surface exposure dating	36
4.3.1	Principles of cosmogenic nuclide exposure dating	36
4.3.2	Practical aspects of ^{10}Be and ^{36}Cl	37
4.3.3	Laboratory procedure	38
4.4	Aerial image cross correlation	40
4.4.1	Principle of NCC, Algorithm	40
4.4.2	Pre- and postprocessing, filtering	43
4.4.3	Uncertainty estimate: Significance level for displacements	44
4.4.4	Flowpaths	45
4.4.5	Principal strain rates	45
4.4.6	Kinematic vorticity: hint at deformation mechanism	46
4.4.7	Slope–velocity relation	47
4.5	Numerical modelling	48
4.5.1	Physics and rheology	48
4.5.2	Forward problem: Numerical implementation of FEM algorithm	51

4.5.3	Rockglacier parameterisation	51
4.5.4	Inverse Problem: Towards plausible subsurface structures	54
5	Results	56
5.1	Field work and DEM analysis: Geomorphology	56
5.1.1	Val d'Err	56
5.1.2	<i>Bleis Marscha</i> rockglacier	57
5.1.3	Digital elevation model analysis	70
5.2	Exposure dates	72
5.3	Orthophoto matching	75
5.3.1	Algorithm configuration	75
5.3.2	Image Correlation results	80
5.4	Numerical modelling	89
6	Discussion	98
6.1	Limitations	98
6.2	Synthesis	102
6.3	Outlook	117
7	Conclusion	119
8	Acknowledgements	122
9	References	123
Appendix		133
A1	Rock book	133
A2	Conference submissions	142

List of Figures

1.1	Estimation of possible future ice evolution in the European Alps [Haeberli et al., 2017]	2
1.2	Methods in time and space	4
1.3	Permafrost terminology and definitions	5
1.4	Terminology of debris-ice systems in cold mountain areas [Haeberli, 1996] . .	6
2.1	Climate evolution in the last 13 ka [Ivy-Ochs et al., 2009]	9
2.2	Borehole temperature measurements on Murtèl-Corvatsch rockglacier (2000–2010) [Springman et al., 2012]	10
2.3	Horizontal downslope borehole deformation measurements [Springman et al., 2012]	12
2.4	Schematic rockglacier evolution [Haeberli et al., 1998]	13
2.5	Possible instability mechanisms in rock glaciers [Springman et al., 2012] . .	14
2.6	Height of frontal boulder apron [Haeberli, 1985]	14
2.7	MAAT-precipitation diagram [Humlum, 1998]	15
2.8	Role of ice-debris flux [Whalley, 2009]	15
2.9	Photogrammetrical measurements on the <i>Gianda Grisca</i> rockglacier for the period 1971–1998 [Frauenfelder et al., 2005]	19
2.10	Relationships between the viscosity parameter B of the rheological model and the component fractions in the rockglacier core [Monnier and Kinnard, 2016]	21
2.11	Schematic model of rockglacier stiffness profile [Arenson et al., 2002]	21
2.12	Computed viscosity profile for Murtèl rockglacier [Kannan and Rajagopal, 2013]	21
2.13	Coordinate system for the parallel-sided slab model	22
3.1	Relief map 1:25 000 of <i>Val d’Err</i>	25
3.2	Geological map of <i>Val d’Err</i> [Cornelius, 1932]	26
3.3	Dufour map of <i>Val d’Err</i>	30
3.4	Siegfried map of <i>Val d’Err</i>	30
3.5	Modelled permafrost distribution in <i>Val d’Err</i> according to the potential permafrost distribution map (PPDM) [Gruber et al., 2006]	31
3.6	Modelled permafrost distribution in <i>Val d’Err</i> according to the Alpine permafrost index map (APIM) [Boeckli et al., 2012]	31
3.7	Modelled palaeo-permafrost distribution in the upper <i>Val d’Err</i> [Frauenfelder et al., 2001]	32
3.8	Schmidt-hammer rebound value and weathering rind thickness on the <i>Bleis Marscha</i> rockglacier [Frauenfelder et al., 2005]	32
3.9	Tentative Schmidhammer R value calibration curve for the <i>Julier-Albula</i> region [Böhlert et al., 2011]	32
4.1	DEM processing flow chart	34
4.2	Sky-view factor calculation [Zakšek et al., 2011]	35

4.3	^{10}Be production rate profile [von Blanckenburg, 2005]	38
4.4	^{36}Cl production mechanisms [Alfimov and Ivy-Ochs, 2009]	38
4.5	Lab procedures for the extraction of ^{10}Be and ^{36}Cl	39
4.6	Image correlation: process flow chart	41
4.7	Schematic representation of the cross-correlation	42
4.8	Construction of an orientation image	44
4.9	Inverse problem structure	49
4.10	Forward problem structure	49
4.11	Stencil and integration points	52
4.12	Rockglacier parameterisation (boundary conditions, mesh, initialisation of material parameters)	54
5.2	Glacial landforms at <i>Parsettens</i>	57
5.3	Periglacial landforms at <i>Castalegns</i>	58
5.4	Radiolarite rockfall deposits	59
5.5	Front of unit IV	59
5.6	Longitudinal ridges on lower rockglacier units	59
5.7	Morphological sketch map	60
5.8	Panorama 1: Overview of the rockglacier	61
5.9	Panorama 2: Cirque and uppermost units	62
5.10	Panorama 3: Rock fall deposits	63
5.11	Panorama 4: Middle part of the rockglacier, front of unit IV	64
5.12	Panorama 5: View onto the lower part of the rockglacier	65
5.13	Panorama 6: View on debris flow deposits and lateral terrace	66
5.14	Panorama 7: Front of relict unit II	67
5.15	Panorama 8: Lateral view of the rockglacier front	68
5.16	Panorama 9: Frontal view of the relict lowermost rockglacier front	69
5.17	Topography and small-scale topography along the longitudinal transect	70
5.18	Fourier amplitude spectrum of the small-scale topography	71
5.19	Exposure ages map	73
5.20	Exposure ages result for the <i>Bleis Marscha</i> rockglacier	74
5.21	Exposure ages result for the upper rockglacier part	74
5.22	Example illustration of NCC	77
5.23	Example illustration of OC	77
5.24	Relationship between template size and image correlation results	77
5.25	Cross-correlation coefficient surfaces: Role of template size	78
5.26	Cross-correlation coefficient surfaces: NCC vs. OC	78
5.27	Relationship between search window size and image correlation results for a 7×7 px template	79
5.28	Relationship between search window size and image correlation results for a 41×41 px template	79
5.29	Horizontal surface velocity in the reference area	80
5.30	Histogram of reference area velocities	80
5.31	Horizontal surface velocity of the <i>Bleis Marscha</i> rockglacier	81
5.32	Horizontal effective strain rates, $\dot{\epsilon}_{\text{II}}$	84
5.33	Horizontal principal strain rate axis	84
5.34	Horizontal kinematic vorticity number	85
5.35	Down-flow stream lines from the 2680 m contour line	86
5.36	Up-flow stream lines from the TCN sampling points	86
5.37	Histogram of rockglacier area velocities	87

5.38	Slope and horizontal surface velocity along the profile	87
5.39	Slope–velocity relation for the rockglacier	88
5.40	FEM 1: “Reference model” with simplest configuration.	91
5.41	FEM 2a: Influence of boulder mantle (no basal shear layer).	92
5.42	FEM 2b: Influence of basal shear layer (no boulder mantle).	93
5.43	FEM 3a: Test of geomorphologically-motivated model.	94
5.44	FEM 3b: “Best-fit parameterisation”.	95
5.45	FEM 4a: Influence of rapidly advancing lobe.	96
5.46	Modelled horizontal displacements in “virtual boreholes”	97
6.1	Longitudinal section showing the TCN exposure ages, relief, small-scale relief, slope and velocity	104
6.2	Travel time–exposure age plot	105
6.3	Schematic relation between cirque bottom and snow line and its consequences in glacier/rockglacier formation [Zasadni, 2007]	109
6.4	Debris/moraine and talus rockglaciers [Ballantyne, 2018]	110
6.5	Modelled permafrost distribution in <i>Val d’Err</i> according to the permafrost and ground ice map (PGIM) [Kenner et al., 2017]	112
6.6	Time chart: Glacier variations and climate evolution since the Younger Dryas	114
6.7	Illustrated sequence of events	115
6.8	Data synthesis in map view	116
6.9	Boulder rotation	117

List of Tables

1.1	Overview of methods	4
3.1	Characteristics of main lithologies	27
4.1	Characteristics of used nuclides for surface exposure dating	37
4.2	SWISSIMAGE coverage of the <i>Val d'Err</i>	40
4.3	Interpretation of kinematic vorticity number W_k	47
4.4	Rockglacier interfaces and boundaries	53
5.1	^{10}Be sample information	72
5.2	^{10}Be and ^{36}Cl exposure ages	73
5.3	IMCOR configuration	78


1 Introduction

Permafrost conditions occur in extensive areas in cold mountain regions on Earth. The ground remains at or below the freezing point of water throughout the year and can contain considerable amounts of subsurface ice. In the Alps, the permafrost area exceeds the glacier-covered area [Boeckli et al., 2012]. Despite its common occurrence, Alpine permafrost is difficult to observe or measure and has escaped the attention of systematic research until the early 1970s [Haeberli, 2000; Haeberli et al., 2010; Vitek and Giardino, 1987b,a]. Rockglaciers as “streams of perennially frozen debris” are characterized by their thermal state and kinetics, and are the most prominent Alpine permafrost landform.

Rock glaciers have fascinated scientists since the early twentieth century, even before the phenomenon of mountain permafrost was recognized. Examples of early works on rockglaciers are Domaradzki [1951]; Chaix [1943] and the seminal paper by Wahrhaftig and Cox [1959]. The unfortunate, misleading term “rock glacier”, coined by Cross and Howe [1905] or Capps [1910], is a legacy of that time: Neither does a rockglacier necessarily contain large amounts of sedimentary glacier ice, nor does it simply contain rocks [Haeberli, 2000]. Among other reasons, the terminological confusion is leading to an on-going scientific debate on the exact definition of the term “rock glacier” [Berthling, 2011].

“The accumulations [...] impress one with a sense of motion, looking as if they had flowed as do viscous masses” [Cross and Howe, 1905]. The ground ice cements the loose debris and allows for large-scale stress transmission and steady creep over long time intervals. This accounts for the peculiarly viscous appearance of the rockglaciers. This specific mechanical behaviour is tied to the formation and preservation of ground ice over the life time of a rockglacier (up to millennia) and thus to perennially negative ground temperatures — *rockglaciers are indicators of present and past permafrost conditions* [Barsch, 1996; Haeberli, 2000]. They are of high interest for permafrost researchers, periglacial geomorphologists and palaeoclimatologists.

1.1 Motivation

Main points	
<p>Permafrost as a thermally defined state is not directly visible, but rockglaciers as the most prominent expression of creeping mountain permafrost are. Rockglaciers thus serve as a proxy for the state of permafrost in a warming climate, requiring knowledge on how rockglaciers react to changing climatic conditions. “The past is the key to the future” — exposure-dating of individual rockglacier lobes allows to place a temporal framework on a ka-scale on rockglacier movement periods and to link these to the Holocene palaeoclimate.</p> <p>This thesis presents the first case study where an <i>active</i> rockglacier is exposure-dated with cosmogenic nuclides. It will provide insights on how the exposure ages are to be interpreted as well as on the evolution of the studied rockglacier.</p>	

In a warming climate, subsurface ice melts 10 to 100 times less rapidly than surface ice [Haeberli et al., 2017, and references therein]. Forward projection of today’s volume

estimates of surface ice (from observed glacier inventories) and subsurface ice (from modelled permafrost distribution) indicate that roughly in the second half of 20th century, the periglacial realm will be more important than the glacial one (Fig. 1.1). New hazard chains will emerge in this changed landscape that is in disequilibrium: For example, retreating glaciers leave behind oversteepened moraines that are readily mobilisable, and rockfalls on degrading permafrost slopes might trigger flood waves in lakes that fill the overdeepened bedrock depressions. Destabilizing rockglaciers in a critical topographic setting, where the debris of the oversteepened front is transported away by debris flows, are hazardous themselves.

At the same time, the behaviour and dynamics of creeping permafrost is still poorly understood, and the level of understanding is far behind the one we have of (ice) glaciers. We need to improve the understanding of rockglaciers and their response to external (climate) forcing in terms of temperature, humidity, and debris supply (“transfer function”). In a first step, appreciating the “importance of rockglaciers as highly sensitive indicators of past temperature evolution” [Frauenfelder and Kääb, 2000], the “transfer function” of rockglaciers is investigated. In a second step, the response of Alpine permafrost to climate change is anticipated. One concrete aim is to integrate permafrost creep rates (rock glacier kinematics) as a new associated parameter to the “Essential Climate Variable (ECV) Permafrost” within the Global Climate Observing System (GCOS) initiative [Delaloye et al., 2018].

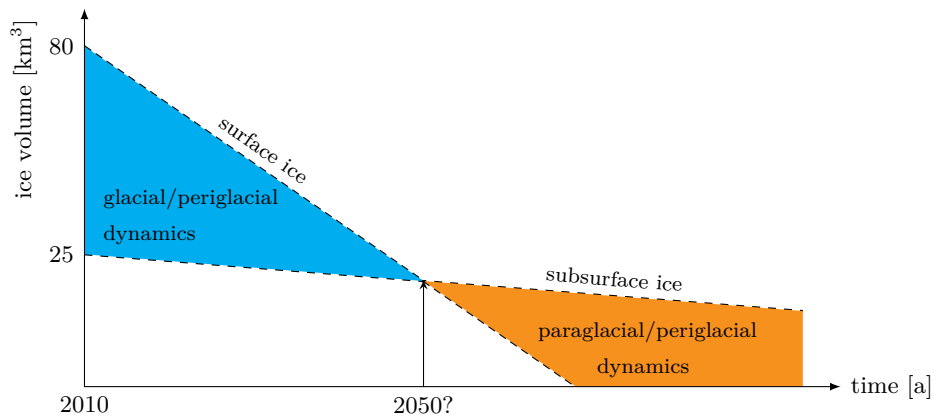


Figure 1.1: Schematic estimation of possible future ice evolution in the European Alps. Redrawn after Haeberli et al. [2017].

1.2 Aim and research questions


This thesis contributes to deciphering the palaeoclimatic significance of rockglaciers in a high-mountain environment. First, we examine the applicability of terrestrial cosmogenic nuclide dating of rockglaciers by exposure dating the *Bleis Marscha* rockglacier. This technique has hitherto never been used on presently moving rockglaciers, we therefore focus on the active lobes. The conclusions drawn will apply generally. Second, we use the absolute age pattern of the *Bleis Marscha* rockglacier complemented by other investigations to infer the local Holocene climate history.

This thesis addresses the following research questions with data of the *Bleis Marscha* rockglacier:

- Applying the method of surface exposure dating with cosmogenic nuclides on the active *Bleis Marscha* rockglacier: Does it yield a consistent exposure age pattern? How are these long-term kinematic information related to the present short-term kinematics obtained by image correlation of orthophotos? How are the surface exposure ages to be interpreted, and what is the relationship to the age of different lobes or the entire landform?
- Reconstructing the development of the *Bleis Marscha* rockglacier: Are the different creep lobes as suggested by the complex morphology, each with its own activity phase, identifiable in the present surface kinematics? What do exposure ages tell on the activity phase of each lobe?
- Reproducing and understanding its present deformation with finite-element numerical experiments: Which plausible subsurface structure and mechanical properties reproduces the observed short-term surface velocity pattern?
- Placing the evolution of the rockglacier in the Holocene climate history: Integrating all information, how did the *Bleis Marscha* rockglacier evolve since its formation? What are the implications for the Holocene permafrost and climate evolution in the Val d'Err?

Constraining the timing of formation and reconstructing the advancement and thrusting of each unit allows to sketch the development of the *Bleis Marscha* rockglacier throughout the Holocene.

1.3 Thesis outline

Main points	
The <i>Bleis Marscha</i> rockglacier is investigated with four methods covering a wide time scale (Fig. 1.2, Table 1.1): aerial image correlation, morphological observations, exposure dating and numerical modelling.	

The *Bleis Marscha* rockglacier is investigated with four methods that cover a wide time scale (Fig. 1.2, Table 1.1):

- We decipher the surface expression of past and present deformation with morphological observations in the field and analysis of aerial photos (MORPH);
- We place rockglacier movement periods in a ka-scale temporal framework by means of surface exposure dating with cosmogenic nuclides (TCN);
- We constrain the present horizontal surface velocity field with feature-tracking on bi-temporal aerial images (IMCOR);
- We investigate the mechanical properties and internal structure with numerical finite-element modelling (FEM).

In the following Section Terminology and general definitions, some introductory remarks on permafrost and periglacial landforms are made. The current state of knowledge on Lateglacial to Holocene climate History in the Alps and on rockglaciers is summarised in Chapter 2 State of research.

The geographical, geological, geomorphological and climatic setting of the study area, the *Val d'Err*, is sketched in Chapter 3 Study site. Chapters 4 Methods and 5 Results treat the procedures and outcomes for each thread separately. Chapter 6 Discussion first

Table 1.1: Overview of methods: coverage in time and space

Method	Exposure dating	Morphological observations	Image correlation	Numerical modelling
Abbreviation	TCN	MORPH	IMCOR	FEM
Parameter	exposition age	surface strain history	horizontal surface velocity field	internal structure
Time	long-term (millennial), .2-9 ka	decades–centuries	short term, present (2003–2012)	present
Space	surface	surface	surface	depth 0–30 m

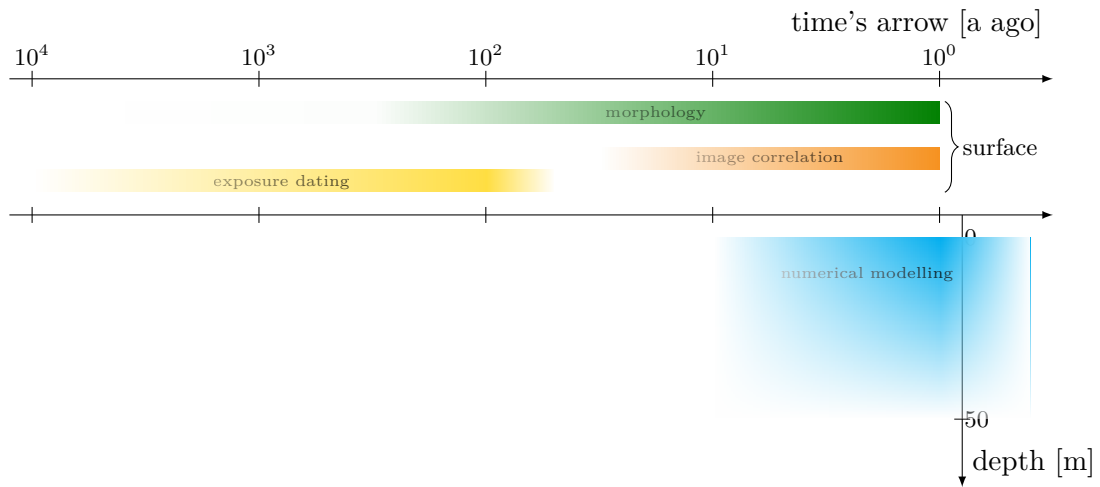


Figure 1.2: Methods in time and space

examines the limitations of each method. In Section 6.2 Synthesis are the threads woven together: The exposure ages are interpreted in light of the past climate evolution, geomorphological observations, present short-term kinematics and inferred subsurface structure. We attempt to sketch the Holocene history of the *Bleis Marscha* rockglacier. Finally, in Chapter 7 Conclusion the implications of our findings for future exposure dating of rockglaciers are highlighted.

The grey-shaded box with the coffee cup sign ☕ collects the main points of each section.

1.4 Terminology and general definitions

Permafrost is defined solely by the ground thermal state as “ground that remains at or below 0°C for at least 2 consecutive years” [Burn, 2013]. Ground ice or perennially frozen ground is not required according to this definition (though most often present on Earth), and pore water can be liquid at temperatures below 0°C. The temperature-related definition is expanded by a description of state (Fig. 1.3).

Ice-rich permafrost forms a perennially frozen layer in between a seasonally thawed active layer at the surface and and permanently unfrozen ground at depth (Fig. 1.3). Permafrost is to a first order controlled by the climatic conditions (air temperature and winter snowfall). The steady-state permafrost thickness H_0 of a homogeneous material is governed by the mean annual temperature at the permafrost table, T_{ps} (°C), the geother-

mal heat flux q (W m^{-2}) and the thermal conductivity of the frozen ground k_p ($\text{W m}^{-1} \text{K}^{-1}$) [Burn, 2013]:

$$H_0 \approx -T_{ps} \frac{k_p}{q}. \quad (1.1)$$

Typical thickness are a few meters in the Alps to a few hundred meters in unglaciated arctic regions.

The aggradation (or degradation) of permafrost from the permafrost base downwards (upwards) are governed by T_{ps} , the thermal conductivity k of frozen (thawed) ground, the volumetric latent heat of fusion of unfrozen ground L (J m^{-3}) and the time since initiation of freezing, t (a) [Burn, 2013]:

$$H_p \approx \sqrt{2k_p T_{ps} t / L}. \quad (1.2)$$

The heat budget is dominated by the latent heat from the ice–water phase change, not by sensible heat from cooling of the ground. This is the reason for the zero-curtain effect. Geothermal heat flow and freezing point depression at the permafrost base are not considered. An important implication of this model is that changes in the depth of the permafrost base scale with \sqrt{t} : Even thin ice-rich permafrost ($H_p \sim 10$ m) takes centuries to degrade [Burn, 2013].

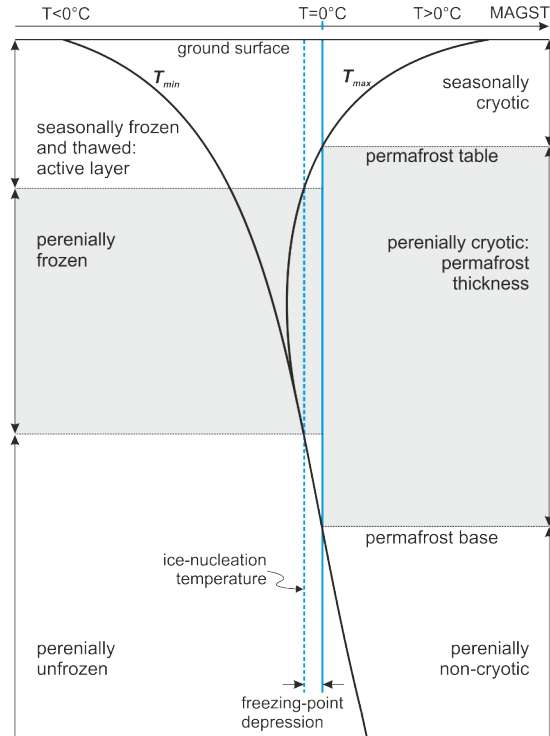


Figure 1.3: Permafrost terminology and definitions with respect to temperature regime. MAGST mean annual ground surface temperature. Redrawn after Associate Committee on Geotechnical Research (ACGR) [1988].

Permafrost is defined by ground thermal conditions with $T \leq 0^\circ\text{C}$, irrespective of material and presence of ground ice/water. Accounting for the freezing-point depression due to dissolved salts in the water, the temperature-related definition is expanded by a description of state: frozen/thawed and cryotic/non-cryotic.

The *cryosphere* “refers to those parts of the Earth’s surface where water is dominantly frozen”, and can be subdivided in the glacial and periglacial domain [Harris and Murton, 2005]. Both is a cold-climate environment: The amount of precipitation makes the difference. The term *glacial* describes environments that are shaped by processes related to flowing ice and meltwater. Glacial landscapes occur in cold-humid areas.

The term *periglacial* is defined as “range of conditions, processes and landforms associated with cold, non-glacial environments” [Ballantyne, 2018]. Periglacial environment

Cryosphere

glacial

periglacial

are characterized by (i) ground freezing and thawing, and/or (ii) the presence of either seasonally or perennally frozen ground (permafrost) [French, 2017]. Terminologically, the permafrost zone is a subset of the periglacial zone. Periglacial landscapes occur in cold-dry areas.

Rockglacier debate

The controversy on the definition of the term “rock glacier” is rooted in the discussion regarding glacial and periglacial systems. While the glacial system is characterized by the body of ice itself as well as all glacier-related processes (“definition by material”), the periglacial system is characterized by the climatic environment (“definition by thermal state”, regardless of material). First, this leaves some overlap (e.g. cold-based glacier: traditionally considered a glacial phenomenon, but is conformable to periglacial definition). Second and more specific to rockglaciers, confusion arises from the fact that similarly looking landforms might develop by different processes [Whalley, 2009], and from the fact that there are interactions between glaciers and permafrost [Harris and Murton, 2005]. The debate on the nature of rockglaciers – glacial or periglacial (or both) – is not a purely semantical issue: Palaeoclimatic reconstructions are only meaningful if rockglaciers are considered as permafrost features created by *zonal* processes. Berthling [2011] advocates a rockglacier definition by genesis, not by appearance (morphology).

Terminology of debris-ice accumulations

The rockglacier debate affects the terminology of debris-ice accumulations in mountainous areas (sketched in Fig. 1.4), namely the usage of the terms “protalus rampart” and “protalus lobe” [Hedding, 2011; Whalley and Azizi, 2003; Scapozza, 2015]. In this thesis, the following convention is adopted: “Protalus rampart” denotes a permafrost-related landform, i.e. an early-stage, “embryonic” rockglacier [Barsch, 1996]. “Pronival rampart” denotes a nivo-gravitational landform [Hedding, 2016].

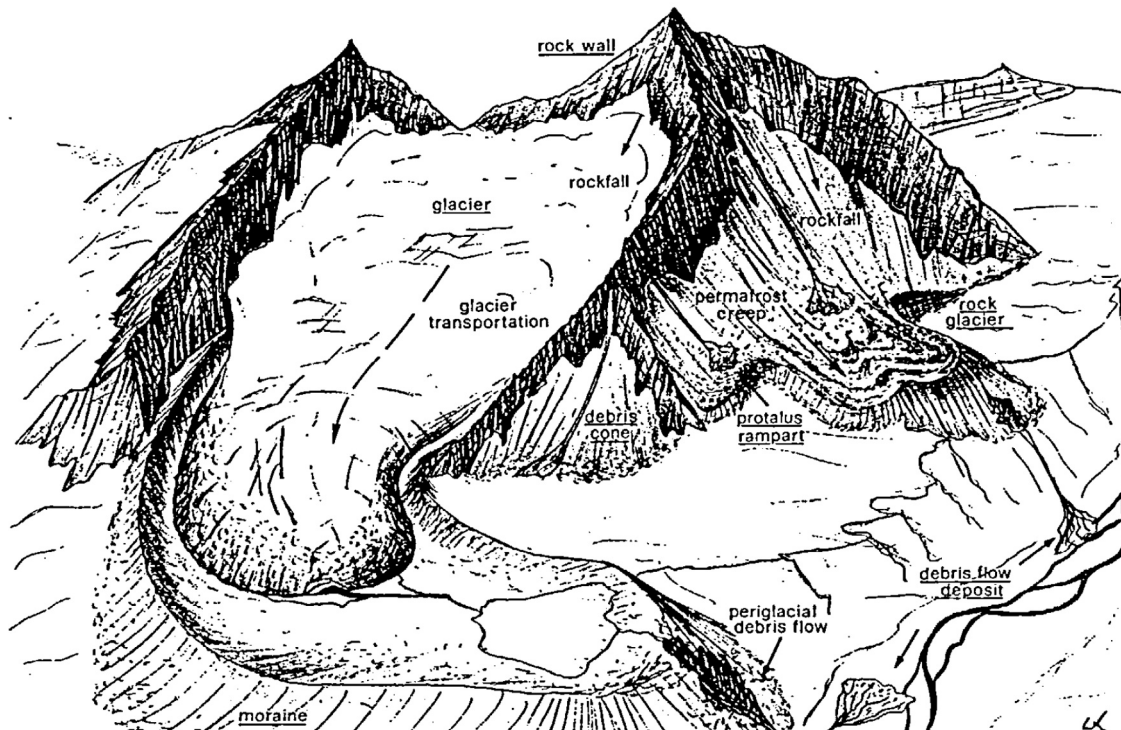


Figure 1.4: Terminology of debris-ice accumulations in cold mountain areas [Haeberli, 1996]. Idealized assemblage of landscape elements (underlined terms) and processes related to debris/ice transport.

2 State of research

2.1 Alpine Lateglacial and Holocene climate history

The late Cenozoic era is characterized by a long-term cooling trend towards an icehouse Earth with ice-sheet covered poles [Zachos et al., 2001]. The glaciation of the European Alps began in the earliest Pleistocene roughly 2.6 Ma ago, marking the beginning of the Quaternary period. The intense glaciations on a 100 ka glacial-interglacial cycle are restricted to the last 800 ka to 1 Ma [Ehlers and Gibbard, 2007; Lisiecki and Raymo, 2005]. Today, we live in an intermittent warm period, the Holocene interglacial, within the current Quaternary ice age. Anthropogenic impact on the climate system has attained a scale that could possibly push it back towards a greenhouse Earth state [Steffen et al., 2018].

Cenozoic era
Quaternary period
Pleistocene and Holocene
epochs

The Alpine glaciation of the latest glacial period (in the Alps traditionally called *Würm* glaciation, superseded by the modern Marine Isotope Stage (MIS) 2 [Lisiecki and Raymo, 2005; Clark et al., 2009]) reached their maximum extent during the *Last Glacial Maximum* (LGM) roughly 18-21 ka ago. Large ice domes in the central Alps [Bini et al., 2009], mostly located south of the present-day water divide, fed glaciers that “reached out onto the forelands on both sides of the main Alpine chains, forming piedmont lobes in the north and filling the Italian amphitheatres to the south” [Ivy-Ochs, 2015]. During the subsequent *Alpine Lateglacial*, the system of ice domes and piedmont glaciers first collapsed to a dendritic glacier system and then finally to isolated valley and cirque glaciers. The deglaciation with rapid ice retreat was repeatedly interrupted by a series of successively smaller ice re-advance periods (stadials) in response to high-frequency climate oscillations in the order of $\sim 10^2$ a (Gschnitz and Egesen stadial [Reitner et al., 2016]).

Pleistocene:
Last glacial maximum
(LGM) 30–19 ka
Alpine Lateglacial
19–11.7 ka

Towards the end of the Pleistocene, after the Bølling/Allerød interstadial, the last pronounced, Alpine-wide ice re-advance before the Holocene was the *Egesen stadial* in response to the Younger Dryas (YD) cold phase that lasted from 12.7 to 11.7 ka [Ivy-Ochs et al., 2009]. The climate instability during the YD is recorded by two (sometimes three) groups of moraines, termed Egesen I (maximum extent attained in early-YD) to Egesen III (Fig. 2.1). ^{10}Be moraine stabilisation ages from the Julier pass (outer moraines) and Schönferwall sites suggest that Egesen I glaciers began to retreat at 12.2 ± 1.0 ka [Ivy-Ochs et al., 2009]. Towards the end of the Younger Dryas, it remained cold (with a MAAT of at least 3.5 to 5 K lower than today), but climatic shifts towards drier conditions “starved” the glaciers [Ivy-Ochs et al., 2009]. Final downwasting of Egesen glaciers was around 11 ka. Prolonged period of cool and dry conditions with climate reversals continued throughout the later part of the Younger Dryas and extended for hundreds of years into the Holocene/early Preboreal [Ivy-Ochs et al., 2008; Ivy-Ochs, 2015]. This is documented by glacier advances and rockglacier activity (inactivity age of 10.4 ± 0.4 ka of a rockglacier at Julier pass [Ivy-Ochs et al., 2006; Ivy-Ochs, 2015]). During the “rockglacier-friendly” (cold, dry) time window in the latest Lateglacial and earliest Holocene, large, polymorphic rockglaciers nourished by the abundant glacial deposits formed [Ivy-Ochs et al., 2006; Ivy-Ochs, 2015, and references therein]. Their relict fronts lie at an altitude as far down as 1700–1900 m a.s.l [Ivy-Ochs et al., 2009]. In summary, rapid glacier retreat

Younger Dryas
Earliest Holocene
12.9–10.0 ka

in cold, dry conditions for a prolonged time scale (ka) as well as high debris availability were favourable conditions for the formation of large, polymorphic rockglaciers during the latest Lateglacial [Kellerer-Pirklbauer et al., 2012; Ivy-Ochs, 2015].

With the onset of the Holocene warming around 10.5 ka, the climate became generally warmer and drier, and the lower permafrost limit shifted upwards. The latest Lateglacial/earliest Holocene transition presents the major termination for the formation and evolution of present relict rock glaciers [Kellerer-Pirklbauer et al., 2012]. “Glacier-hostile” conditions lasted from 8.8 ka until 3.7 ka [Badino et al., 2018] and were only interrupted by infrequent, short cold phases (“climatic reversals”) to which only small glaciers responded. Throughout the early to middle Holocene, the glaciers never exceeded their later 1850 LIA extent, the timberline was ~200 m higher than today, presently ice-covered areas were forested, and varve sedimentation in Lake Silvaplana indicating a glacierised catchment ceased (Fig. 2.1) [Ivy-Ochs et al., 2009]. Badino et al. [2018] note based on pollen analysis that July temperatures between 8.4 and 4 ka were 3.1°C higher than today.

The *late Holocene* was a period of progressive cooling, and glacier advance periods became longer and more frequent, culminating in the *Little Ice Age* (LIA) between the 14th century AD and ~1850 [Ivy-Ochs et al., 2009]. The timberline dropped, and varve deposition in Lake Silvaplana resumed (Fig. 2.1). The LIA glacier limits reached and mapped in 1850 are representative of maximum glacier extent of the last 10.5 ka.

2.2 Rockglaciers

Recent review papers are Haeberli et al. [2006]; Harris et al. [2009]; Springman et al. [2012]; Janke et al. [2013]; Kääb [2013], monographs on rockglaciers are Giardino et al. [1987]; Barsch [1996].

2.2.1 Concepts, definitions and classifications

An *active rockglacier* – creeping mountain permafrost – is a permafrost body defined by its thermal state and characterized by its kinematics [Kääb et al., 2007]. Following Barsch [1996, p. 4], *active rockglaciers* are defined in terms of process, material and form as “lobate or tongue-shaped bodies of perennially frozen unconsolidated material supersaturated with interstitial ice and ice lenses that move downslope or downvalley by creep as a consequence of the deformation of ice contained in them and which are, thus, features of cohesive flow” [see also Barsch, 1992; Berthling, 2011]. Active rockglaciers creep downslope with typical velocities in the order of 0.1 to 1 m a⁻¹. *Inactive rockglaciers* still contain frozen material and have a well-developed form, but presently do not show any surficial movement, either because some ice has melted (climatic inactivity), or the rockglacier has lost contact to the debris source and has thinned out to the point that the shear stresses have fallen below a critical threshold (dynamic inactivity). Active and inactive rockglaciers, which are difficult to differentiate on aerial photographs, are sometimes referred to as *intact*. *Relict (fossil) rockglaciers* are formerly active rockglacier in which the ice has melted completely, forming collapse structures. Transitional forms between these stages exist [Kääb, 2013].

Barsch [1996] puts rockglaciers into the *periglacial realm*, and the difference to glaciers is made clear by the spelling as one word [Barsch, 1992]. A debris-covered glacier, in contrast, belongs to the glacial realm. However, this distinction refers to the creep process, not to the origin of the creeping material [Berthling, 2011]: According to the type of debris incorporated and the position in a landscape, two main types of rockglaciers are

Holocene > 11.7 ka:
Early Holocene transition
period
Mid-Holocene warm
period 10.0–3.3 ka

Late Holocene
(Meghalayan)
3.3 ka–1850 A.D.

Active rockglacier

Climatic and dynamic
inactivity

Talus and debris
rockglaciers

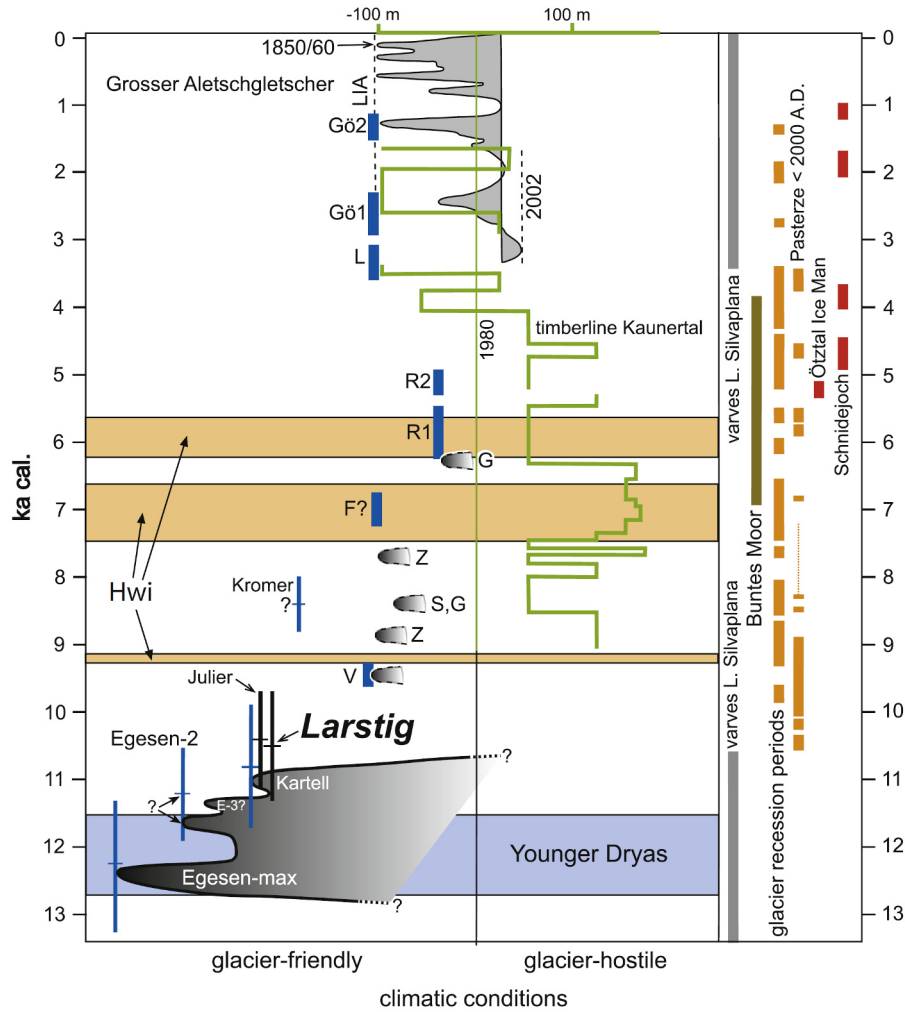


Figure 2.1: Synopsis of glacier variations and general climate evolution during the Younger Dryas and the Holocene, Ivy-Ochs et al. [2009] and references therein. **Left:** Interpreted time–distance glacier extent for Egesen and early Holocene glaciers. Variations in timberline in Kaunertal. **Right:** Varves present in Silvaplanaersee sediment (Engadin), as indicator of active glaciers in the catchment area.

distinguished [Barsch, 1992]: (i) *talus rockglacier* forming below talus slopes and transporting frost-shattered rock fragments, and (ii) *debris rockglacier* developing out of (glacial) morainic debris (till).

2.2.2 Thermal conditions

The thermal state is a defining characteristic of rockglaciers – they owe their existence to the perennially frozen mixture of debris and ice [Haeberli et al., 2006; Kääb, 2013]. An active rockglacier is thermally layered in a seasonally thawed active layer and the perennially frozen permafrost body *s. str.* (~rockglacier core). The (stratigraphically defined) boulder mantle, roughly (but not necessarily) coinciding with the *active layer*, favours ground cooling via Balch ventilation in the openwork structure [Delaloye and Lambiel, 2005; Scherler et al., 2014; Luethi et al., 2016; Wicky and Hauck, 2017; Pruessner et al., 2018], in addition to the insulating effect of the debris itself. Besides heat transfer by air advection, water flow and the timing of snow cover affects heat exchange within

the permafrost body and the atmosphere. Ground temperature conditions are influenced by the surface climate conditions, but also by air circulation in the boulder mantle and intra-permafrost water flow.

As an example that is believed to be typical for active rockglaciers that are located at the lower elevation boundary of permafrost [Arenson et al., 2010], temperature recordings from thermistor cables in borehole 2/2000 on Murtèl-Corvatsch over 10 years are shown in Fig. 2.2. The temperature is near 0°C during summer, kept temperate by percolating meltwater, and seasonally cools from above during winter by conduction and cold air convection. Constant groundwater flow at the base of the permafrost body maintains a sub-permafrost talik, degrading the permafrost from below. The rockglacier ice is ground ice from different sources: buried ice and snow patches from the souree area, but also ice from refreezing rain, meltwater or groundwater.

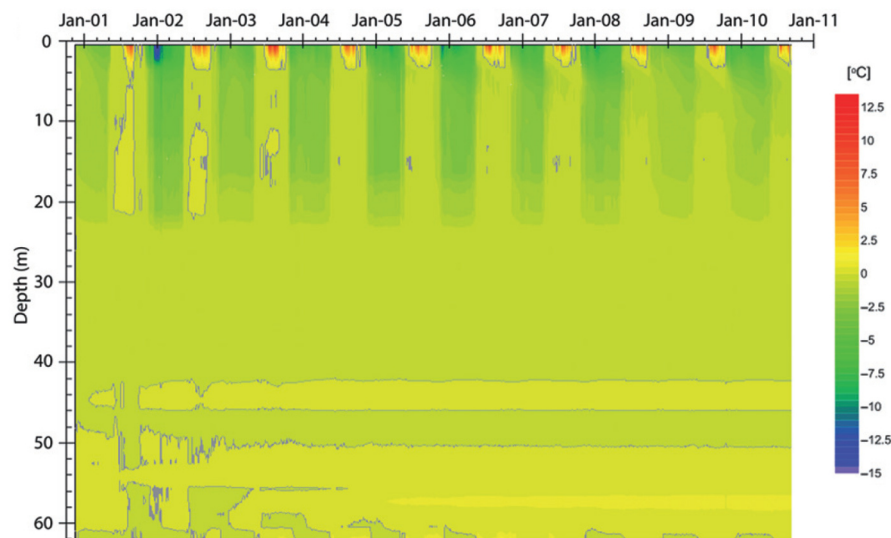


Figure 2.2: Temperature–depth plot measured in borehole 2/2000, Murtèl-Corvatsch rockglacier from December 2000 until September 2010. [Springman et al., 2012; Arenson et al., 2010].

2.2.3 Form and surface morphology

Rockglaciers are meso-scale landforms with lengths in the order of 10^2 to 10^3 m, widths of 10^2 m, and thickness of 10 m. According to their shape and length-to-width ratio, wide *lobate* rockglaciers are distinguished from long *tongue-shaped* (lingulate) ones. The overall form reflects both internal processes (creep over time) and external forcing (topography, mass supply) [Kääb, 2013].

Many rockglacier display a peculiar furrow-and-ridge microrelief akin to a pahoehoe lava stream [Janke et al., 2013]. The mode of formation of the transverse, crescent-shaped ridges across the creep direction and the longitudinal, along-creep ridges is not resolved yet [Kääb, 2013]. Hypotheses are (i) active, dynamic origin via compressive folding or thrusting, (ii) external factors such as variable ice or debris supply, or (iii) passive origin via differential melt (thermokarst) or frost heave. The high thermal inertia and the slow creep preserve the appearance over centuries to millennia. The front and margins of active (i.e. presently advancing) rockglaciers are steep, at the angle of repose, not vegetated and marked by a clear, sharp break in slope at its top. These are clear signs of movement, because otherwise the front would degrade to a more rounded, diffusional

shape [Wahrhaftig and Cox, 1959]. In contrast, the transition to the talus at the rooting zone is gradual and difficult to pin down in the field [Janke and Frauenfelder, 2007]. Relict rockglaciers show typical signs of collapse and subsidence, a subdued microrelief with prominent lateral outer ridges, and are vegetated or forested.

2.2.4 Stratigraphy, composition and internal structure

The internal composition of rockglacier is a heterogeneous mixture of debris and ice. The direct observations at the few drilled boreholes should be generalised with caution [Kääb, 2013]. A robust finding is the **three-tiered stratigraphy** of bouldery rockglaciers [Haeberli et al., 2006; Janke et al., 2013; Kääb, 2013]: The ice-free surface layer of most rockglaciers consists of a matrix-free, clast-supported framework of large, angular boulders (“bouldery rockglacier” according to Ikeda and Matsuoka [2006]). The *boulder mantle* has a thickness of a few meters and is roughly coincident with the thermally defined active layer. The frozen *rockglacier core* beneath has a thickness of several decametres and may be very heterogeneous in terms of volumetric ground ice content (few % to massive ice lenses of different origins) and clast size (sand/silt to pebbles). The fact that the core is generally finer grained than the boulder mantle, as observed at over-steepened front scarps, is explained by fall sorting in the talus and “kinematic sieving” [Haeberli et al., 2006]. The core rests on a third layer of coarse, frozen debris that are believed to have fallen over the rock glacier front and were overridden by the advancing rockglacier (cf. Fig. 2.4) [Humlum, 2000; Kääb, 2013].

2.2.5 Thermo-mechanical properties and advance mechanisms

Rockglaciers “creep down-slope by plastic (irreversible) deformation of the interstitial ice from gravity-induced shear stresses” (Barsch [1996], quoted after Chuang and Greeley [2000]). Ice-supersaturation and stress transmission are fundamental features of rockglaciers, and the morphology and coherent surface velocity field are expressions thereof.

Due to lateral and basal friction, the velocity increases towards the central flowline and the surface. In the few boreholes, the horizontal deformation was concentrated in horizontal shear layers, accounting for up to 60% of the surface displacement (Fig. 2.3). The deformation above the basal shear layer has a parabolic profile similar to glaciers. The creep behaviour depends strongly on temperature, liquid water content and composition of the deforming layers, and is not understood in detail [Haeberli et al., 2006].

Conceptually, rockglacier formation is envisioned as follows (Fig. 2.4, Haeberli et al. [1998, 2003]; Kääb [2013]): The initial conditions is a talus in permafrost area. Debris is deposited on the inclined base of a rock face, either directly via rock fall and back-weathering of the steep **headwall**, or indirectly via glacial transport or avalanches. This *syngenetic debris/ice accumulation* under permafrost conditions leads to piling up of a frozen rock/ice mixture on the **talus slope**. ① Frost heave and shear dilatancy [Nickling and Bennett, 1984] leads to ice over-saturation of the finer material in initially deposited in the upper part of the talus (vertical grains-size sorting). ② When a critical ice fraction in the ice-bearing debris is exceeded, the resistance to deformation changes abruptly from predominantly frictional to predominantly viscous, and a new mechanical behaviour emerges [Arenson et al., 2003, 2006; Springman et al., 2012; Moore, 2014]. The material begins to creep down-slope under its own weight with the highest creep speed at the surface, first forming a bulge (protalus rampart), which develops into a **rockglacier** ③. Coarse blocks that continue to fall onto the scree slope form the boulder mantle of the

Schematic rockglacier evolution

Emergence of viscous deformation

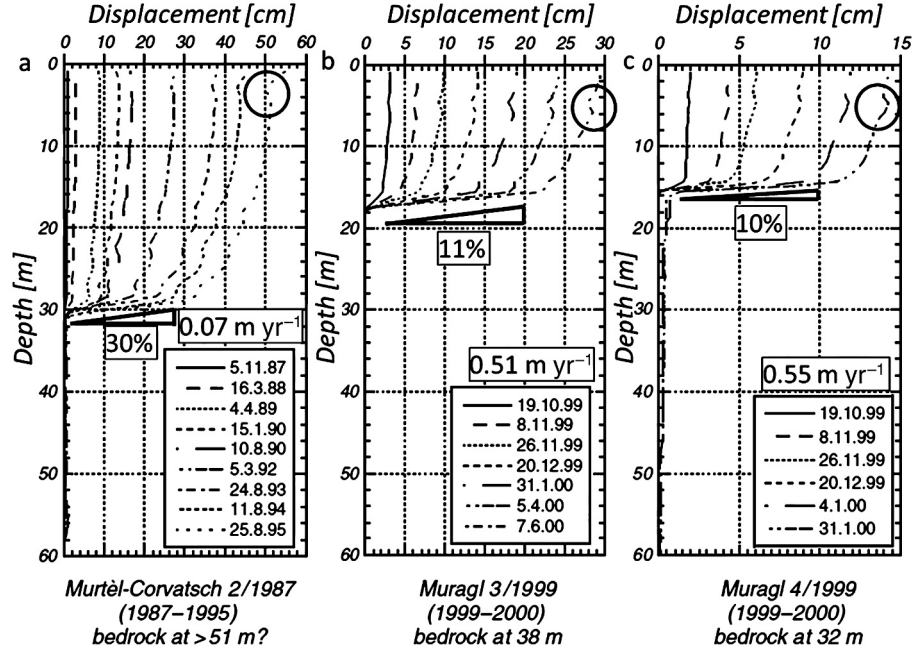


Figure 2.3: Horizontal downslope borehole deformation from inclinometers in the Murtèl-Corvatsch and Muragl rock glaciers after Hoelzle et al. [1998]; Arenson et al. [2002], including annotations of surface deformation rate and average strain in the shear zone. [Springman et al., 2012].

rockglacier and are carried towards its front with surface speed v_s . At the oversteepened front, the debris falls down (Fig. 2.5). The typical boulder apron formed by grain-size sorting is subsequently incorporated and overridden by the advancing permafrost body [Kääb and Reichmuth, 2005]. It may form the stiff, ice-poor and immobile substratum beneath the basal shear horizon. The amount of debris transported is substantial, and rockglaciers play an important role in the coarse-debris cascading system in periglacial environment Gärtner-Roer [2012]; Müller et al. [2016].

This ‘caterpillar’ or ‘conveyor belt’ fashion of advancing, where the rockglacier overrides its own debris, has important implications for its age structure and the interpretation of the exposure ages. This model predicts that (i) the ages along the surface increase along the flow path towards the front, but decrease in the stiff substratum. The age distribution with depth “likely contains sharp time inversions” [Haeberli, 1985; Haeberli et al., 2003; Barsch, 1996]. (ii) Surface ages are minimum ages [Haeberli et al., 2003; Frauenfelder et al., 2005; Scapozza et al., 2014; Winkler and Lambiel, 2018].

Already Chaix [1943]; Domaradzki [1951] and Wahrhaftig and Cox [1959] observed that the surface moves faster than the landform itself. From simplified mass conservation considerations, it follows that the rockglacier advances with the mean velocity \bar{v} (for a constant rockglacier width) [Haeberli, 1996; Kääb, 2005; Frauenfelder et al., 2008]

$$\frac{Q}{H} := \bar{v} = \frac{1}{H} \int_0^H v_x(z') dz', \quad (2.1)$$

where $v_x(z')$ is the slope-parallel velocity component and H the rockglacier thickness (perpendicular to its base). However, since the (excess) ground ice is carried towards the collapsing front where it loses the insulating debris cover, it can melt, and the principle

Role in coarse-debris
transport chain

Theoretical concept of
rockglacier advance

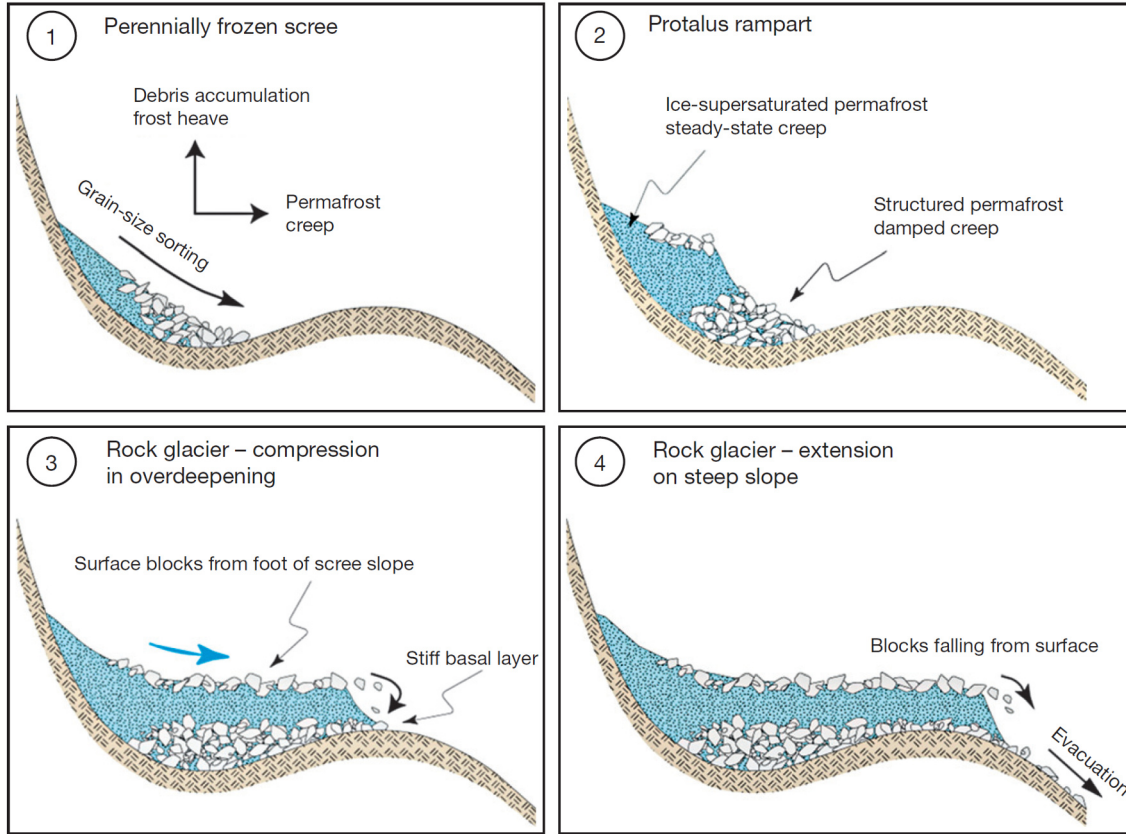


Figure 2.4: Schematic rockglacier evolution: talus, protalus rampart, rockglacier [Kääb, 2013; Haeberli et al., 1998]. (Cf. Fig. 4 in Olyphant [1983]).

of mass conservation is the more severely violated at the rockglacier front the higher the volumetric ice content is [Kääb and Reichmuth, 2005]. Other mass transfers (air, debris) are neglected. Therefore, the mean velocity \bar{v} is an upper limit for the rockglacier advance rate \dot{x} . We note the following inequality between the slope-parallel surface velocity v_s , the mean velocity \bar{v} and the advance rate \dot{x} :

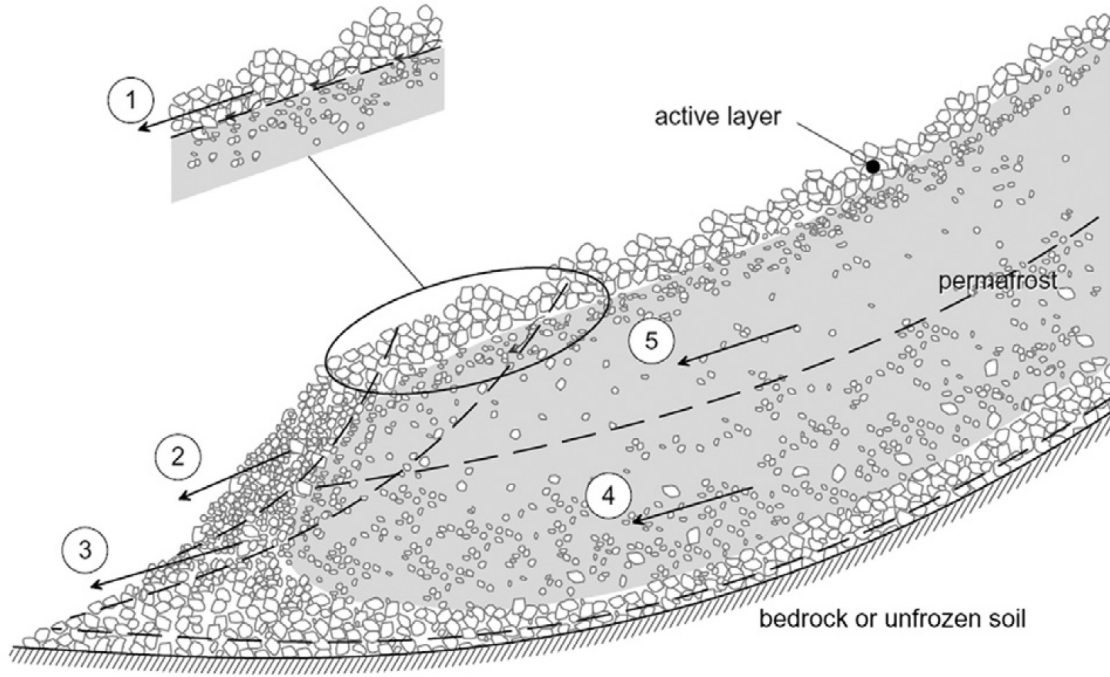
$$v_s \geq \bar{v} \geq \dot{x}. \quad (2.2)$$

Already early observers such as Chaix [1943, Fig. 2] or Wahrhaftig and Cox [1959, Fig. 8] noticed that the position of the top of the talus apron at the front of a presently advancing rockglacier is indicative of the vertical velocity profile: For a convex velocity profile, the height of the talus apron is not more than half of the overall front height, and the lower, the more strain is concentrated towards the base (Fig. 2.6).

Several studies report a wide range of ratios between surface speed above the front and advance rate (cf. Kääb [2005, p. 161 and references therein]). He measured the following ratios: $\dot{x}/v_s \approx 0.15$ to 0.5 (mean of ~ 0.3), and $\dot{x}/\bar{v} \approx 0.45$ to 0.88 (mean of ~ 0.7). It reflects the wide range of compositions (e.g. ice content) and creep mechanisms (vertical velocity profile) observed in rockglaciers [Kääb and Reichmuth, 2005].

To conclude: The advance rate is considerably smaller than the surface speed because of the decrease of horizontal speed with depth, melt-out of ice at the front and in specific circumstances the loss of debris [Harris et al., 2009]. The oldest surface is expected right above the frontal slope, but this surface might be considerably younger than the landform

Implications of advance rate for exposure dating



- | | |
|------------------------|-------------------------------|
| 1) surface instability | 4) failure at permafrost base |
| 2) front instability | 5) failure in shear zone |
| 3) toe instability | |

Figure 2.5: Possible instability mechanisms in rock glaciers. [Springman et al., 2012].

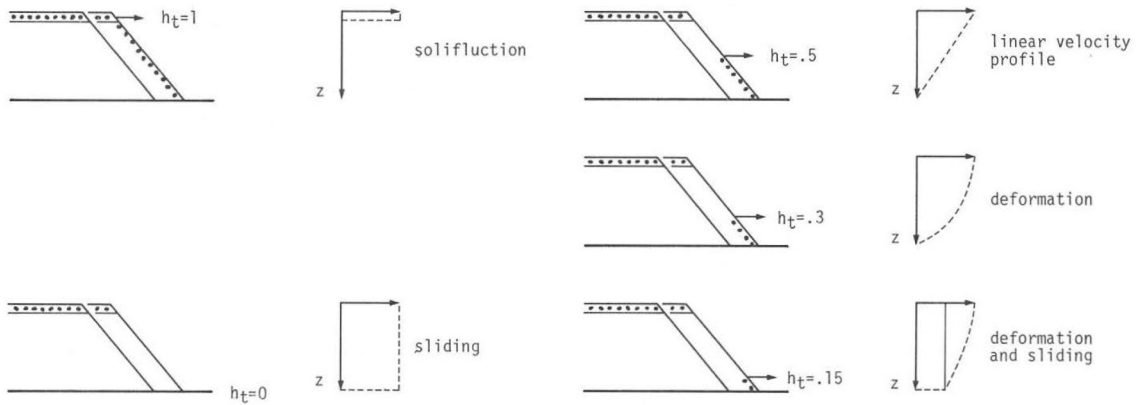


Figure 2.6: Relative height of the frontal boulder apron as a function of the vertical profile of horizontal velocity, after Haeberli [1985, Fig. 59], cf. Wahrhaftig and Cox [1959]. The two end-members (left row) are “solifluction-like” surface creep of the boulder mantle and basal sliding. The latter describes the hypothetical situation of an entire permafrost body sliding *en bloc* over a thin shear zone; no vertical mass redistribution at the front would then be necessary, no talus apron would form, and $v_s = \bar{v} \geq \dot{x}$. An intermediate behaviour (right row) is observed (Fig. 2.3). (Cf. Johnson Jr. and Nickling [1979]; Barsch [1996]; Kääb and Reichmuth [2005]).

itself.

2.2.6 (Palaeo-)climatic significance and surface speed variations

The present-day morphology of a single rockglacier as well as the distribution and activity status of rockglaciers in a region is an expression of past and present environmental conditions [Barsch, 1996; Frauenfelder and Kääb, 2000].

According to Haeberli [1985], active rockglaciers are restricted to altitudes (i) above the lower permafrost limit (MAAT < −2°C, otherwise the permafrost is not conserved, cf. Fig. 2.7), (ii) below the equilibrium line of glaciers (otherwise the snow/ice supply is too high compared to the debris supply and glaciers form, cf. Fig. 2.8 and Humlum [1998]), and (iii) on slopes with slope angle greater ~5° (minimum basal shear stress to permit creep given the observed rockglacier thicknesses (e.g. 50 kPa, [Frauenfelder et al., 2008])¹ but smaller than the angle of repose of unconsolidated debris (otherwise the debris cannot accumulate on the talus, or e.g. rockfalls with a completely different dynamics occur). The first two points imply annual precipitation less than 2500 mm, otherwise the potentially rockglacier-friendly periglacial-cryogenic belt is occupied by glaciers. In summary, continental, comparatively dry mountains with cool summers and cold winters have a greater elevation difference between timberline and firnline [Barsch, 1996, Fig. 5.22] and are favourable environments for the development and the existence of rockglaciers [Humlum, 1998; Barsch, 1996; Etzelmüller and Frauenfelder, 2009]. This rough first-order picture is supported by the abundance of rockglaciers in dry regions and the scarcity of rockglaciers in maritime mountain ranges.

However, these elevation-related “large-scale climatological boundary conditions” [Haeberli, 1985] are modulated by local topographic, geological and microclimatic factors: Aspect and topographic shading controlling solar irradiation, and lithology and joint density of the headwall that determines block size and frequency-magnitude of debris-supplying rock falls. For example, few rockglacier are found in areas of weathering-prone lithologies (shales, schists) that mainly produce finer or platy debris [Evin, 1987; Matsuoka and Ikeda, 2001; Haeberli et al., 2006]. Kellerer-Pirklbauer et al. [2012] hypothesize that deglaciation in the south-exposed slopes proceeded faster than in nearby radiation-sheltered north-facing slopes, so that now relict rock glacier fronts at identical elevation but different slope aspects might be of different age.

Climatic significance

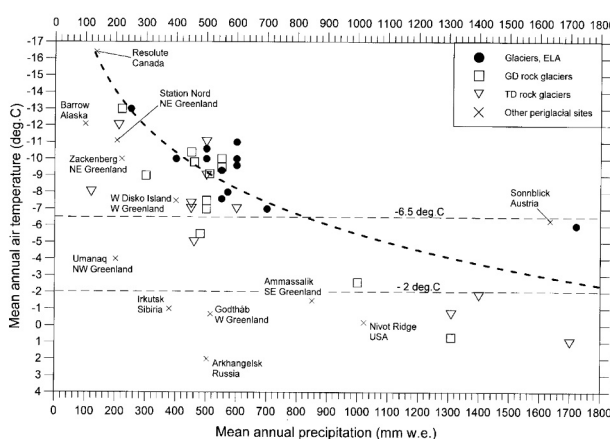
MAAT -2 to -6°C
AP 500—1500 mmelevation range between
lower permafrost limit and
firn line

Figure 2.7: MAAT–precipitation diagram Humlum [1998], after Barsch [1996]; Haeberli [1985].

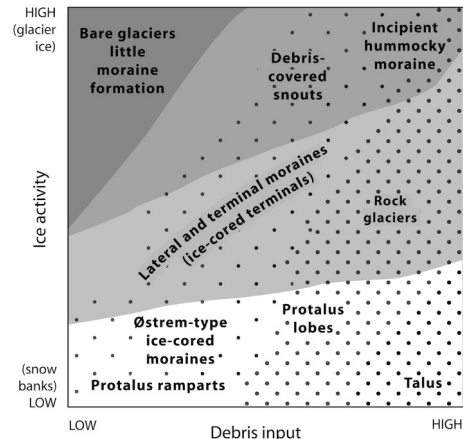


Figure 2.8: Ice-debris flux and topographic forms [Whalley, 2009].

¹ $\bar{\alpha} \cdot \bar{H} \approx \text{const.}$

Climatic sensitivity

Many rockglaciers in the European Alps show remarkably synchronous annual to decennial surface creep rate variations and an overall acceleration following a (summer) air temperature trend [Roer et al., 2005; Delaloye et al., 2010; Kellerer-Pirklbauer and Kaufmann, 2012]. Such a short response time is surprising considering the surface insulation and cooling by the boulder mantle and the thermal inertia of the ice core. “These dampening effects are probably outweighed by the particularly large deformation sensitivity of ice-rock mixtures close to the melting point, with water being a potential coupling agent” [Sorg et al., 2015]. Millennial to seasonal time scales of surface deformation magnitude variations are summarized in Kääb et al. [2007]. Monitoring surface creep rates of rockglaciers, a parameter that is efficiently captured with remote sensing techniques for entire rockglacier inventories, provides insights into sediment transfer rates and impact of climate change on mountain permafrost. A new IPA Action Group intends to promote rockglacier surface kinematics as a new associated parameter to the Essential Climate Variable (ECV) Permafrost within the Global Climate Observing System (GCOS) initiative [Delaloye et al., 2018].

Palaeo-climatic
significance:
permafrost distribution
indicator

Rockglaciers as a permafrost phenomenon indicates continuous or discontinuous mountain permafrost on a regional scale [Harris et al., 2009; Kääb, 2013]. The lower boundary of regional rockglacier distribution is often treated as a proxy for the lower boundary of (palaeo)permafrost distribution (e.g. Frauenfelder et al. [2001]), although rockglaciers may come to a halt earlier (topographic constraints, dynamic inactivity, insufficient time) or advance beyond (Balch circulation in boulder mantle).

2.3 Rockglacier dating techniques

Motivation for age dating

Rockglaciers are long-term (millennial) periglacial archives of past and present climatically determined ground thermal conditions, frost weathering intensity and rockfall activity. In order to decipher this information, they need to be dated Haeberli et al. [2003].

Techniques:
weathering rind thickness
Schmidt-hammer R value
lichenometry
pollen analysis
radiocarbon dating
luminescence dating
cosmogenic nuclide dating

Several relative and absolute age-determination methods have been applied on rockglaciers [Haeberli et al., 2003; Frauenfelder et al., 2005]: Schmidhammer rebound values [Winkler, 2009], weathering rind thickness [Laustela et al., 2003], lichenometry [Haeberli et al., 1979], pollen or floristic composition analysis [Haeberli et al., 1999] can provide insights into the relative age succession of different parts. However, they need to be calibrated either with time scales derived from photogrammetrically obtained, extrapolated present-day velocity field [e.g. Scapozza et al., 2014], correlated with other methods (e.g. weathering rind thickness and the Schmidt-hammer rebound value in Laustela et al. [2003]), or compared to literature values (e.g. empirical lichen growth curve). Radiocarbon dating of plant macrofossils [Krainer et al., 2015, 2017], moss [Haeberli et al., 1999] or wood stems [Scapozza et al., 2010] gives an indirect minimum age of the landform. Direct dating is possible with luminescence techniques (inner sand-rich layer, e.g. Fuchs et al. [2013]) and cosmogenic nuclides (surface of boulders using ^{10}Be , ^{36}Cl , e.g. Barrows et al. [2004]; Ivy-Ochs et al. [2009]; Ballantyne et al. [2009]; Hippolyte et al. [2009]; Cossart et al. [2010]; Hippolyte et al. [2012]; Dede et al. [2017] and Palacios et al. [2017]). The cosmogenic nuclide method is commonly applied on glacial moraines, and is summarized in Ivy-Ochs and Kober [2008].

From surface age to
landform age

A common issue to all dating methods is the a-priori unknown relationship between the dated process and the landform age. As emphasized above, surface ages are minimum ages because of the “caterpillar-like” advance mechanism of rockglaciers and the melt-out

of ice at the front [Kääb and Reichmuth, 2005]. The “missing time” can be estimated by comparing with other dating techniques, geomorphological constraints, or palaeoclimatic considerations. For example, Winkler and Lambiel [2018] report that the exposure age of the Irishman Stream rockglacier front is only slightly younger than confining early-Holocene moraine ridges, implying that the rockglacier initiation age is close to the oldest (lowermost) rockglacier surface age. This is in stark contrast to results by Kääb [2005, Table 9-2, p. 169] who found ratios of advance rate to surface speed of 15–50% (cf. [Kääb and Reichmuth, 2005]).

2.4 Kinematic studies

Kinematics is defined as the quantification of movement (in terms of velocity, acceleration, strain rate) in both horizontal and vertical direction. Changes in the surface elevation z^s are due to (i) the advection of the surface relief and (ii) vertical changes due to vertical movement and mass transfer (Eq. 2.3a). It is derived from the principle of mass conservation and therefore independent of the dynamical situation [Cuffey and Paterson, 2010]. The kinematic boundary conditions along a longitudinal profile at the surface reduces the relief advection term to the along-flow term (in x direction) is Eq. 2.3a with the simplification of Eq. 2.3b [Kääb and Weber, 2004].

Kinematic boundary condition

$$\frac{\partial z^s}{\partial t} + \mathbf{v}^s \cdot \nabla z^s - v_z^s - \dot{b} = 0, \quad (2.3a)$$

$$\mathbf{v}^s \cdot \nabla z^s \equiv v_x^s \frac{\partial z^s}{\partial x} + v_y^s \frac{\partial z^s}{\partial y} \approx v_x^s \frac{\partial z^s}{\partial x}, \quad (2.3b)$$

with surface elevation z^s [m], change in surface elevation with time $\partial z^s / \partial t$ [m a^{-1}], longitudinal horizontal surface velocity v_x^s [m a^{-1}], surface slope component in flow direction $\partial z^s / \partial x$ [m/m], vertical velocity at the surface v_z^s [m a^{-1}], and the mass balance at the surface \dot{b} [m a^{-1}].

The surface kinematics of rockglaciers is today routinely measured because it is the most easily accessible parameter that characterizes their dynamics and deformation patterns. The surface deformation integrates the overall vertical profile of deformation (creeping, shearing, but also aggradation or ice melting), and its changes in time and space are indicative of processes and material parameters that govern the creep (e.g. temperature, water content) [Delaloye et al., 2010; Bodin et al., 2018].

Motivation and purpose

Recent acceleration:
→ Climatic sensitivity

There are three main approaches in measuring the surface kinematics and deformation: photogrammetric, geodetic and interferometric methods. Data acquisition is carried out either in-situ with terrestrial measurements, or remotely with air-borne or space-borne sensors. For this thesis, the digital photogrammetric method is discussed where horizontal displacements between two (optical) ortho-images are determined through offset tracking.

Main measurement techniques:
Geodesy
Photogrammetry
radar interferometry

Matching of orthorectified (geometrically corrected), georeferenced (spatial reference information allocated) and co-registered (spatially aligned) bi/multi-temporal terrestrial, aerial or satellite images can be thought of as looking to the changing object from a fixed camera multiple times with small (or absent) spatial baseline and dominant temporal baseline (time between two consecutive image acquisitions). In fact, the spatial baseline of such pre-processed images is considered noise that must be minimized.

Debella-Gilo and Kääb [2011] explain *image matching* as “a group of techniques of finding corresponding features or image patches in two or more images taken of the same scene from different viewing positions, at different times and/or using different sensors”. Two

groups of matching methods are prevalent in the literature: area-based methods (also known as direct methods) and feature-based methods [Fitch et al., 2002]. Area-based methods match measurable image quantities such as brightness. Feature-based methods match features extracted from the images such as corners, lines, junctions, or gradient orientation (e.g. orientation correlation). Among the developed algorithms, area-based (template-based) approaches with the normalized cross-correlation (NCC) as its similarity measure is widely used due to its reliability and simplicity [Debella-Gilo and Kääb, 2012], despite some drawbacks: NCC is sensitive to noise; sensitive to significant scale, rotation or shearing differences between the images to be correlated; reliable measurements must exceed the mean image (co-)registration error; and the precision is (in principle) limited to one pixel [Debella-Gilo and Kääb, 2011].

Although the normalized cross-correlation accounts for brightness and contrast in the image sequences [Debella-Gilo and Kääb, 2011], the NCC matrix is easily dominated by large digital numbers and is prone to mismatches when only one image shows large grey-value differences (e.g. snow patches) [Heid and Kääb, 2012]. A powerful alternative tool to NCC is *orientation correlation* (OC) developed by Fitch et al. [2002] and later applied by e.g. Haug et al. [2010]; Heid and Kääb [2012]. It is a feature-based method of translatory image matching that matches the orientation of the image intensity gradients. Unlike the (direct) NCC method that only works in the spatial domain, the OC computations can be very efficiently performed in the frequency domain with fast Fourier transform (FFT). Furthermore, OC is less sensitive to image information which is constrained to few frequencies [Haug et al., 2010].

As an example serves the *Gianda Grischia* rockglacier originating in a westward facing cirque of Piz Julier/Piz Güglia (Fig. 2.9) [Frauenfelder et al., 2005]. It is a over one kilometre long, spatulate, W-exposed polymorphic rockglacier *sensu* Frauenfelder and Kääb [2000] with active and inactive parts. The *Gianda Grischia* rockglacier shares many similarities with the *Bleis Marscha* rockglacier in terms of location (and thus local climate), morphology, size, lithology, and presumably deglaciation history. The short-term surface velocity of *Gianda Grischia* (Fig. 2.9) indicates typical velocities of 40 to 50 cm a^{-1} , reaching highest the velocities of 80 cm a^{-1} in the the steep slope between the root zone and the frontal parts, several hundred meters away from the talus. Speeds of the inactive part are below 16 cm a^{-1} . Significance level is 5 cm a^{-1} .

Minimum surface ages can be estimated from the surface velocity field [Haeberli et al., 2003]. It is the time (age) t_{trv} integrated for particle paths p along flow trajectory constructed from the present-day surface flow field \mathbf{v}_s , implying a steady-flow condition over the travel time.

This travel time is the closer to the true rockglacier age (i) the less the measured surface flow field has changed over time, and (ii) the more basal sliding has contributed to the rockglacier advance rate [Haeberli, 1985]. An example of surface age estimation from streamline interpolation is shown in Fig. 2.9 for the *Gianda Grischia* rockglacier [Frauenfelder et al., 2005]. The steady-flow condition assumption “seems to be justified by the fact that the curvature of the isochrones is similar to the curvature of the ogive-like transverse ridges” [Haeberli et al., 2003], at least for some parts of the rockglacier. The data suggest a formation period on a millennial scale, which is in agreement to typical creep and rockglacier advance rates and common to all creeping permafrost bodies with spatial dimensions of 10^2 to 10^3 m . The strength of the streamline age method is that it reveals the

Orientation correlation

Age estimate from stream
line interpolation

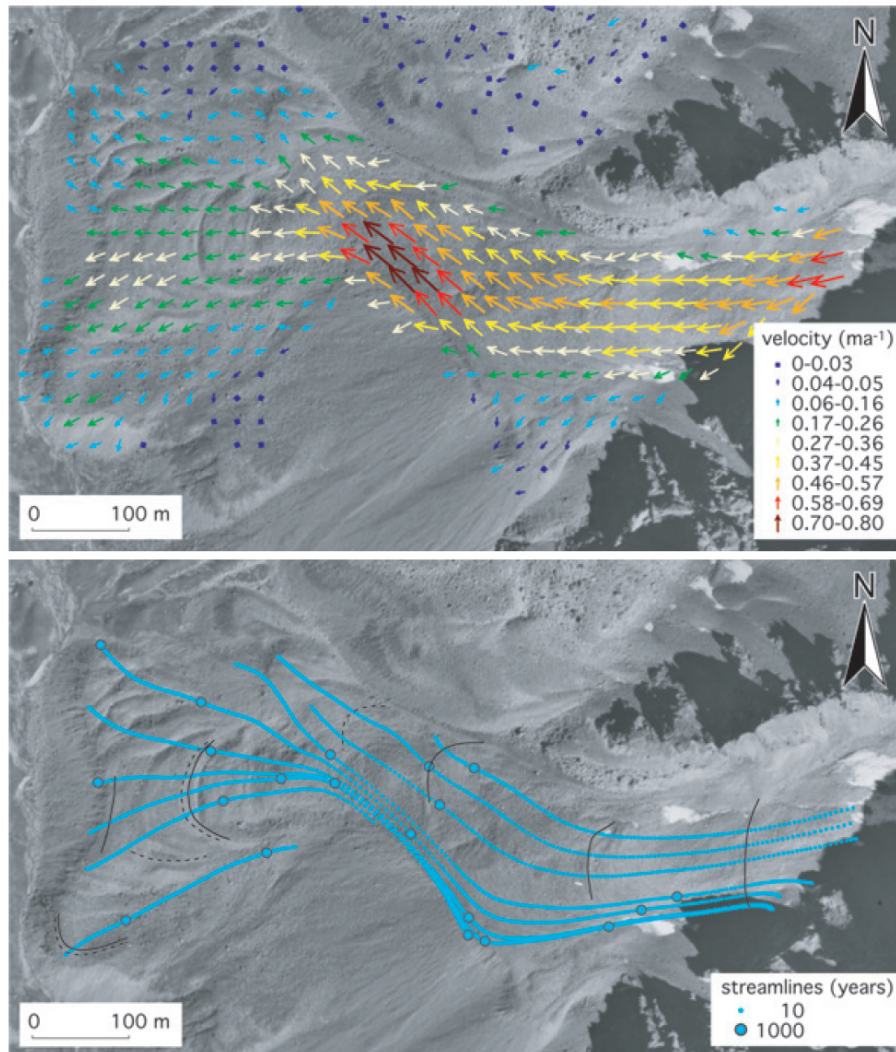


Figure 2.9: Photogrammetrical measurements of the *Gianda Grischia* rockglacier [Frauenfelder et al., 2005]. **Top:** horizontal average annual surface velocities between 1971 and 1998; **Bottom:** interpolated streamlines.

surface age pattern, enabling the interpolation of point-wise ages obtained independently as well as the interpretation of the formation time of individual lobes [Haeberli et al., 2003].

2.5 Numerical modelling of rockglaciers

While numerical modelling of permafrost distribution [e.g. Frauenfelder et al., 2008; Boeckli et al., 2012] or energy balance is common in the permafrost research community, the dynamics and creep behaviour of a rockglacier is difficult to grasp with a model [Haeberli et al., 2006]: Information on the complex three-dimensional structure and heterogeneous internal composition of rockglaciers is difficult to obtain, the influence of debris content, temperature and water flow on the rheology is still incompletely understood, and the incompressibility assumption is not strictly valid [Arenson et al., 2002].

The problem is tackled with various approaches: (i) dynamic (time-dependent) models simulating the rough geometry [Müller et al., 2016] or regional distribution of rockglaciers

Modelling studies

[Frauenfelder et al., 2008]. The dynamics are simplified using the shallow-ice approximation and the models are one-dimensional. The debris/ice mixture is considered a non-linear viscous material, and the constitutive relationship is borrowed from glaciology (*Glen’s flow law*). The behaviour of an individual rockglacier can be modelled with (ii) *discrete element modelling* (DEM) based on the interaction of discrete particles. E.g., the model by Jansen and Hergarten [2006] captures the stick-slip motion associated with strain localisation at discrete shear horizons and occurrence of melt water. However, to fully model the four-phase interaction between solids, water, ice with constitutive models at a particulate level, computer capacity must increase by another order of magnitude [Haeberli et al., 2006]. Another approach is (iii) *finite element modelling* (FEM) relying on the continuum approximation [e.g. Olyphant, 1983; Wagner, 1992; Azizi and Whalley, 1995; Leysinger Vieli and Gudmundsson, 2003; Whalley and Azizi, 2003; Frehner et al., 2015].

Constitutive relationship
of debris-ice mixtures

The susceptibility for steady-state (secondary) creep of debris-ice mixtures depends on debris-ice proportions (specifically the degree of “ice supersaturation”, i.e. ice volume exceeding the pore volume), temperature, water content, fabric and particle size [Ikeda et al., 2008; Moore, 2014]. Shear strength can be conceptually decomposed in friction and cohesion [Coulomb, 1776; Arenson et al., 2002]. The proportions of debris (friction) and ice (cohesion) determines their contribution to shear resistance and the dominating mechanical behaviour.

At temperature below the freezing point, the material weakens with increasing temperatures, increasing ice supersaturation and decreasing interlocking/friction of the solid particles [Arenson and Springman, 2005b,a; Nickling and Bennett, 1984; Springman et al., 2012; Moore, 2014]. Close to the melting point, however, debris exerts the opposite effect, as confirmed by laboratory experiments [Moore, 2014] and field observations [Monnier and Kinnard, 2016]: Interstitial water at debris-ice interfaces and in the ice crystal lattice effectively weakens the material Arenson et al. [2002]; Arenson and Springman [2005a]; Ikeda et al. [2008] (Fig. 2.10). These findings link seasonal velocity variations of Alpine (temperate) rockglacier to snowmelt [Wirz et al., 2016], and the observed interannual acceleration trend to atmospheric and subsequent ground warming. Numerical models aimed at reproducing short-term velocity variations need to account for liquid water, although their pathways in the permafrost body are not well known [Jansen and Hergarten, 2006; Cicoira et al., 2018].

Values for the material parameters are difficult to measure *in-situ* and laboratory experiments cannot be up-scaled in a straightforward manner [Haeberli et al., 2006]. A useful approach is fitting averaged (in time and space) effective creep parameters to a deformation time series [Wagner, 1992; Ikeda et al., 2008; Kannan and Rajagopal, 2013; Monnier and Kinnard, 2016], although it inevitably fails to represent the small-scale deformation field and material heterogeneities [Haeberli et al., 2006].

From observations to
mechanical abstractions

Horizontal deformation measurements suggest a pronounced mechanical layering of the permafrost body. The different equivalent shear stiffnesses (expressed as shear moduli G in Fig. 2.11) are highest in the boulder mantle and the substratum below the basal shear horizon, below which “there is virtually no deformation” [Haeberli et al., 2006]. For the well-studied Murtèl rockglacier, Kannan and Rajagopal [2013] fitted a viscosity increase of ~ 2 orders of magnitude at the base of the shear layer. This layer is most susceptible for creep in the permafrost body and most of the deformation is concentrated within a few meters (Fig. 2.12).

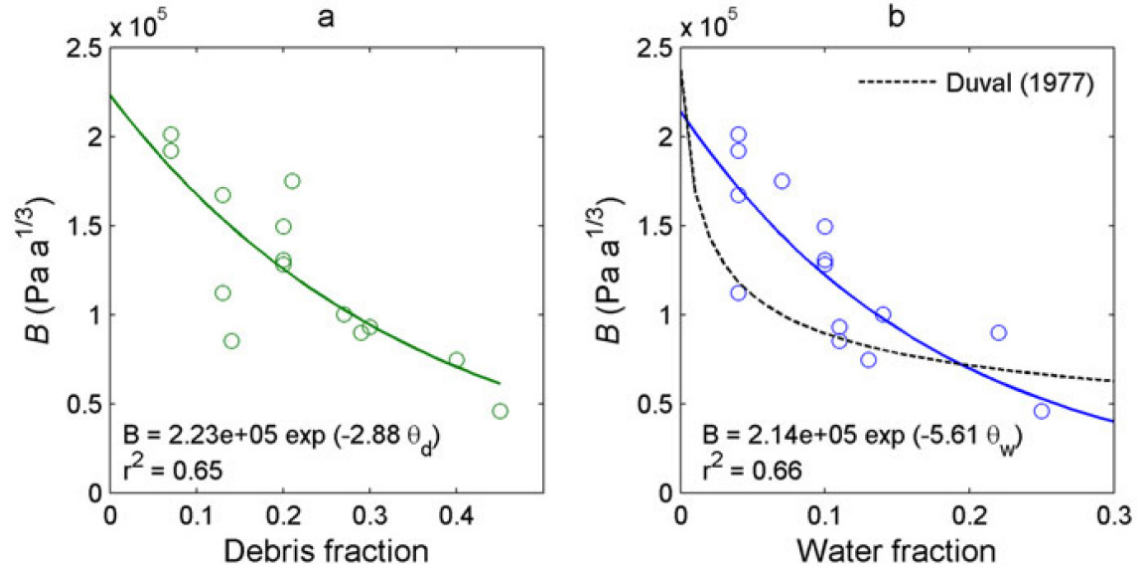


Figure 2.10: Relationships between the viscosity parameter B and the component fractions of debris and unfrozen water for a temperate rockglacier, i.e. temperatures in the core are close to the melting point [Monnier and Kinnard, 2016]. The effective viscosity parameter $B \sim A^{-1/n}$ decreases with increasing debris fraction. High correlation between debris and water content show that the debris fraction is intimately linked with the unfrozen water fraction of a temperate ice-rock mixture. The liquid water film around the solid particle effectively weakens the material.

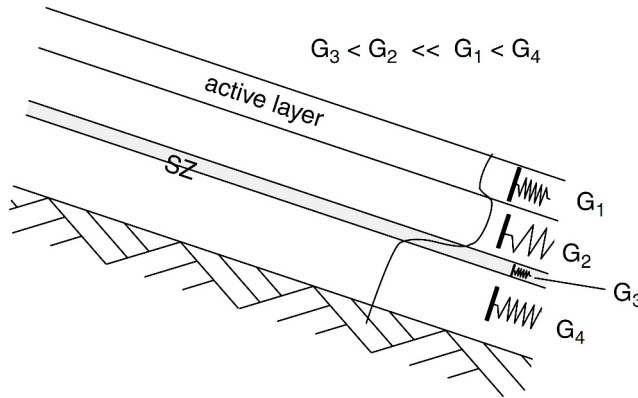


Figure 2.11: Schematic model of rockglacier stiffness profile [Arenson et al., 2002]. G_1 – G_4 are shear moduli. “SZ” stands for “shear zone” that separates the dynamic upper layers from the immobile frozen ones.

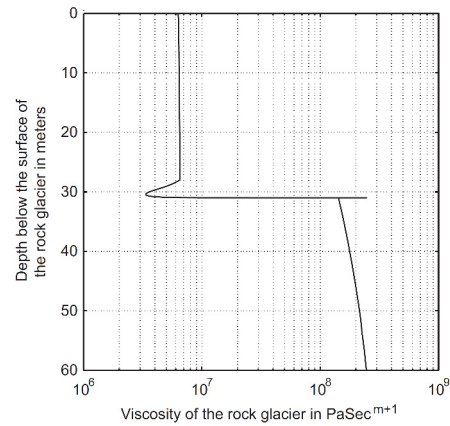


Figure 2.12: Depth-dependent viscosity of the Murtel rockglacier [Kannan and Rajagopal, 2013].

In its simplest form, the internal deformation of the permafrost body (without basal shear deformation or sliding) is considered a *laminar flow* of viscously deforming homogeneous material (ice). According to the parallel-sided slab model, the material deforms by simple shear and the only non-zero stress component is the shear stress component τ_{xz}^n . Assuming incompressibility, the stress and strain rate are collinear, i.e. the shear stress τ_{xz} leads to the strain rate $\dot{\epsilon}_{xz}$. The flow lines are parallel to the surface, the velocity component perpendicular to the base is zero and the only variations are variations with depth z . The relation between the shear strain rate $\dot{\epsilon}_{xz}$ and the shear stress τ_{xz}^n is assumed

A simple but useful model

GLEN's flow law

to be of the form [Glen, 1952]

$$\dot{\epsilon}_{xz} := \frac{1}{2} \frac{dv}{dz} = A \tau_{xz}^n. \quad (2.4)$$

This is commonly called GLEN’s flow “law”, actually an empirical relationship. The driving shear stress at depth $(H - z)$ is the product of the weight of the overburden material, the sine of the surface slope averaged over 5 to 10 times the thickness of the creeping permafrost body and a shape factor that accounts for lateral drag (friction at the valley flanks, $f = 1$ for a parallel-sided slab):

$$\tau_{xz}(z) = f \rho g (\bar{H} - z) \sin \bar{\alpha}. \quad (2.5)$$

This model neglects along-creep deviatoric stress transmission, i.e. the longitudinal stress gradients are assumed to be zero [Haeberli, 1985]. The driving stress and consequently the flow is governed by the average *surface* slope $\bar{\alpha}$, and not by the basal slope [Nye, 1952a,b]. The creep is roughly down the steepest surface descent, and can overcome bedrock depressions.

The vertical velocity profile is obtained by the integration of Eqs. 2.4 and 2.5 with respect to z and with the boundary condition $v(z = 0) = v_b$:

$$v(z) - v_b = \frac{2A}{n+1} (f \rho g \sin \bar{\alpha})^n \left[\bar{H}^{n+1} - (\bar{H} - z)^{n+1} \right] \quad (2.6)$$

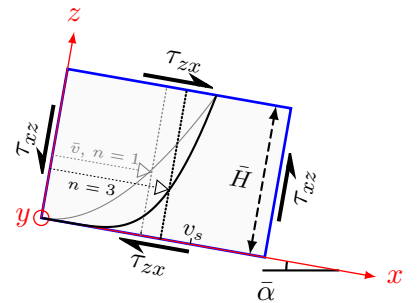
Two important observations are: (i) the velocity decreases from surface to base, and (ii) the larger n , the stronger the deformation is concentrated towards the base (Fig. 2.13).

The three-dimensional generalisation of Eq. 2.4 is the NYE-GLEN Isotropic Law [Nye, 1957], the most commonly used creep relation for glacier ice (in index and vector notation)

$$\dot{\epsilon}_{ij} = A \sigma_{\text{II}}^{n-1} \sigma'_{ij} \quad \Leftrightarrow \quad \dot{\boldsymbol{\epsilon}} = A \sigma_{\text{II}}^{n-1} \boldsymbol{\sigma}', \quad (2.7)$$

The strain-rate tensor $\dot{\epsilon}_{ij}$ and the deviatoric stress tensor σ'_{ij} are related via the rate factor A , the effective stress σ_{II} and the exponent $n \sim 3$. It is a typical example of a power-law fluid, of which the NEWTONIAN fluid (discussed below) is a special case.

Figure 2.13: Coordinate system for the parallel-sided slab model with driving shear stress, τ . Conservation of angular momentum requires $\tau_{xz} = \tau_{zx}$. Isotropic normal stresses which do not cause any deformation due to the incompressibility assumption are not drawn. Normalized theoretical velocity profiles (Eq. 2.6) for exponents $n = 1$ (thin grey line) and $n = 3$ (bold black line), zero basal velocity. The mean speed \bar{v} (Eq. 2.1) as a fraction of the surface speed is shown as vertical dotted lines, and the fractional height above the bed at which $v = \bar{v}$ (Eq. ??) as horizontal dotted lines. With increasingly non-linear rheology, the mean speed approaches the surface speed, and the depth of mean speed approaches the bed. Pure sliding is the end member for $n \rightarrow \infty$.




For non-NEWTONIAN fluids, the apparent viscosity μ [Pa s] depends (among other factors) on the stress or the shear rate (Eq. 2.8). This is a so-called *power-law fluid*: For $n > 1$, the apparent viscosity decreases with increasing stress or strain rate. Ice is a

strain-rate softening material:

$$\mu_{eff} := \frac{\tau}{2\dot{\epsilon}_{xz}} = \begin{cases} \frac{1}{2}[A\tau_{xz}^{n-1}]^{-1} & \text{stress-dependent formulation} \\ \frac{1}{2}\left[A^{\frac{1}{n}}\left|\frac{dv}{dz}\right|^{\frac{n-1}{n}}\right]^{-1} & \text{strain-rate dependent formulation.} \end{cases} \quad (2.8)$$

For a NEWTONIAN fluid with $n = 1$, the dependency on stress or strain rate vanishes and the apparent viscosity becomes a material constant, specifically called NEWTONIAN viscosity. It is important to note that the (apparent) viscosity is sensitive to temperature, ice crystal size, amount of liquid water in the lattice and material impurities.

3 Study site

Main points	
<p>The <i>Bleis Marscha</i> rockglacier is located in the Err-Julier area, Grisons (SE Switzerland). The dry-cold climate is favourable for rockglaciers. The lithologies are suitable for exposure dating.</p>	

Rockglacier selection criteria

A rockglacier suitable for this study is required to meet the following conditions: (i) the rockglacier must show signs of present activity, (ii) consists of quartz-bearing rocks (necessary condition for ¹⁰Be dating), (iii) has a simple outline, making its internal structure inferable from surface features within an acceptable margin of uncertainty, (iv) is accessible for field work, and (v) is covered by at least two aerial photos. 239 rockglaciers in the crystalline areas of the Julier–Upper Engadine, Gotthard and Saas–Turtmanntal regions were assessed. In the *Err-Julier* area in Grisons, SE Switzerland, many rockglaciers have developed in the continental, dry-cold climate that are located less than a one-hour walk away from a road. Several authors have already exposure dated the local granite [e.g. Ivy-Ochs et al., 1996, 2007, 2008; Böhlert et al., 2011].

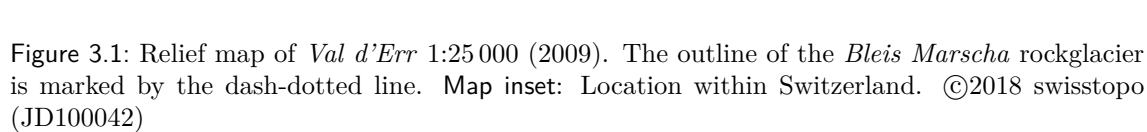
Geology & Geomorphology of Val d’Err

The studied rockglacier lies on the eastern slope of the upper part of *Val d’Err* (“snow valley” [Studer, 1896, p. 192]), a side valley of the Surses (Oberhalbstein) in Grisons (Fig. 3.1). The *Ragn d’Err*, the stream draining the Upper Val d’Err towards the NNW, is a tributary of the river *Gelgia* (Julia). It is a high valley with the valley floor at altitudes above 2000 m a.s.l and surrounding peaks reaching over 3000 m a.s.l. The geological standard work on the *Val d’Err* is still Cornelius [1935, 1950, 1951], even though aspects on tectonics and permafrost need to be re-assessed in the light of recent research findings [P. Nievergelt, pers. comm.]. Geomorphological mapping was carried out by O. Schlosser in 1990, but is not published [Frauenfelder et al., 2001].

3.1 Geology of Val d’Err

Stratigraphy & tectonics

The NNW-SSE oriented valley lies in a tectonically complex zone between the Upper Penninic Platta nappe overlain by the Lower Austroalpine Err nappe [Manatschal and Nievergelt, 1997; Pfiffner, 2014]. The main thrust crops out at the Flanks of Castellins, Piz d’Err and Piz Salteras, but runs mostly hidden beneath the Quaternary deposits across the valley (Fig. 3.2). It separates remnants of oceanic lithosphere (ophiolites, serpentinites) and post-rift sediments deposited on the southern margin of the Jurassic Piemont-Liguria ocean from post-Variscan granitoids and Permo-Triassic to Lower Cretaceous sediments of the Apulian continental margin. The Err detachment, a Jurassic low-angle detachment fault developed during rifting and opening of the Piemont-Liguria ocean, was partly re-activated in Late Cretaceous to Tertiary times during the subsequent convergence of the Tethys and nappe stacking during Alpine orogenesis. Still, it is a “unique witness” of a continental break-up at a passive margin [Masini et al., 2012; Masini and Manatschal,



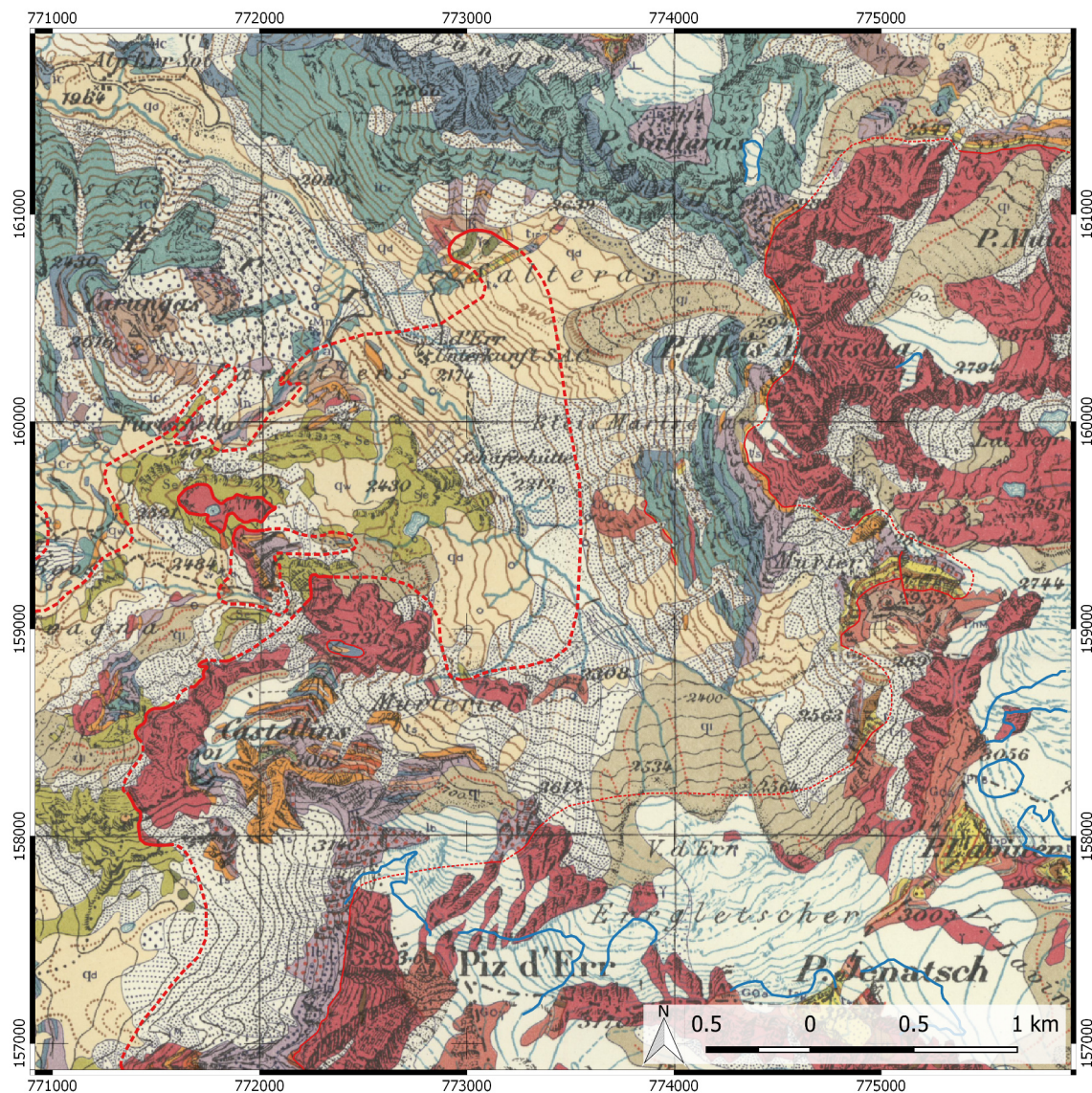
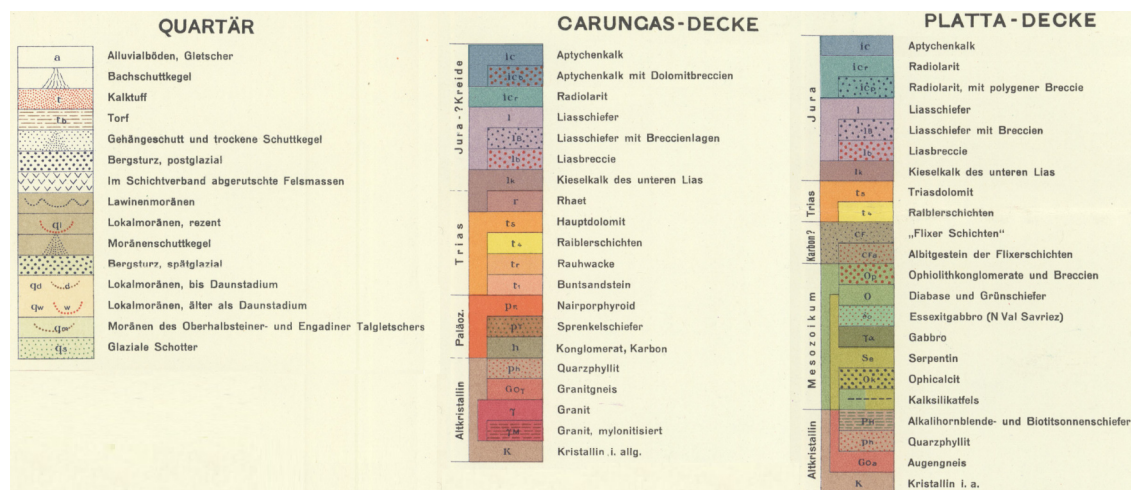


Figure 3.2: Geological map (incl. Quaternary) of Val d'Err, modified after Cornelius [1932]. Tectonic thrusts of first and second order (observed/inferred in red solid/dashed line). Glacier extent as of 2009 (blue line, Fig. 3.1). Legend is slightly modified.



The headwalls above the rockglacier are in the the Tschirpen unit (Err system). The Tschirpen unit is itself subdivided in a sediment-bearing Lower Err unit (mainly radiolarite and limestone) and a crystalline Middle-Err unit (Err granite). Along the secondary thrust, slates, breccias, limestones and dolomites occur in lenses. The rocks have undergone deep burial diagenesis to greenschist metamorphic facies [Manatschal and Niev-ergelt, 1997]. The rockglacier surface is made up of three main rock types, two of which are datable with cosmogenic dating (in order of volumetric importance, Table 3.1): Err granite, derived from the Middle Err unit, and radiolarite and dolomite, derived from the Lower Err unit. The weathering-resistant granite is dominant (towards the toe almost exclusively), followed by radiolarite. The dolomite boulders are few and prone to fragmentation, probably because they are heavily fractured for tectonic reasons. The other lithologies (conglomerates, mudstones/schists, limestones, rauhwacke/cellular dolomite) occur only in lenses or thin seams in the headwall, and are rarely found on the rockglacier surface.

The different lithologies allow a comparison between ^{10}Be and ^{36}Cl ages. More importantly, they can be used as a tracer for the provenance of the deposits: Radiolarites come either from the rock face below *Piz Salteras* or from the NW spur of *Piz Bleis Marscha*, whereas the Err granite comes from the cirque below *Piz Bleis Marscha* (Fig. 3.2, Table 3.1).

Table 3.1: Characteristics and use for cosmogenic surface exposure dating of main lithologies

	Mineralogy	Use for cosmo- genic dating	Provenance and com- ments
Err granite	qtz, fsp (saussuritized), mica	dateable, ^{10}Be	middle Err unit (chemical composition in Böhlert et al. [2011])
radiolarite	microcrystalline silica	not dateable	lower Err unit
dolomite	dol	dateable, ^{36}Cl	lenses along thrust

3.2 Geomorphology and climate

At the Last Glacial Maximum (LGM) 21 ka ago [Ivy-Ochs, 2015; Wirsig et al., 2016], the area was covered up to an altitude of ~ 2800 m a.s.l. by ice flowing northwards from the nearby Engadine ice dome (Inn river catchment) into the Rhine system [Böhlert et al., 2011, Bini et al., 2009]. Only the highest peaks protruded as nunatak above the ice cover. During the *Alpine Lateglacial*, the general disintegration of the large ice domes and retreating glaciers was repeatedly interrupted by short periods of subsequently smaller glacier re-advances (stadials).

The last of these cold phases, the *Younger Dryas* (YD) at the end of the Pleistocene, has left behind the *Egesen stadial* moraines. Lateglacial moraine ridges of the former *Piz Bleis Marscha* cirque glacier are mapped adjacent to the rockglacier (Fig. 3.7) [Frauenfelder et al., 2001, after O. Schlosser (1990)], [Burga, 1987]. Frauenfelder et al. [2001] estimate that in the *Err-Julier region* during the Younger Dryas (YD), mean annual air temperature (MAAT) was 3 to 4°C colder than today, precipitation was reduced by 30-40% (in later YD phases) and the lower permafrost limit (mountain permafrost altitude, MPA) was 500 to 600 m lower than today at ~ 2200 m a.s.l. (Fig. 3.7). The lowering of the equilibrium line altitude (ELA), in contrast, is thought to be of “some 300 m between the

early Younger Dryas and today”. The lower limit of permafrost occurrence was depressed considerably more than glacier equilibrium lines, indicating cold-dry conditions, a abundance of permafrost occurrence and a wide periglacial altitude band [Frauenfelder et al., 2001]. The local glaciers were “mostly surrounded by discontinuous permafrost” (i.e. MPA < ELA, Fig. 3.7) and therefore had a cold to polythermal thermal structure [Frauenfelder et al., 2001; Etzelmüller and Hagen, 2005]. A ^{10}Be age of a boulder on the *Val Mulix* lower Egesen moraine indicates final moraine stabilisation by 10.8 ± 0.9 ka [Böhlert et al., 2011]. The rapid glacier retreat at the end of the Younger Dryas marked the beginning of a rockglacier activity phase that lasted until the early Holocene (exposure dates of a relict rockglacier in *Val Mulix* [Böhlert et al., 2011]).

The Holocene maximum glacier extent was reached during the Little Ice Age around 1850 AD [Kronig et al., 2017; Böhlert et al., 2011]. The Dufour map drawn at this time (Fig. 3.3) shows that the cirque N of *Piz Bleis Marscha*, the root zone of the *Bleis Marscha* rockglacier, was occupied by ice. It is not clear how accurately the glacier outlines were drawn in the Dufour map, but it seems that the glacieret or perennial ice patch remained small and has not advanced beyond the cirque [Frauenfelder et al., 2005]. It had already significantly retreated by 1887 (Siegfried map in Fig. 3.4), and seems to have disappeared between 1912 and 1932 [Cornelius, 1951, p. 25]. In contrast, the *Vadret d’Err* at the southern end of the Val d’Err at that time still reached down to the large LIA end moraine visible today [A. Janett, pers. comm.].

In the upper *Val d’Err*, the ground is expected to be frozen at elevations above 2400 m a.s.l., depending on exposition and ground cover. The permafrost area according to the Alpine permafrost index map (APIM) [Boeckli et al., 2012] is shown in Fig. 3.6, and according to the Potential permafrost distribution map (PPDM) [Gruber et al., 2006] in Fig. 3.5.

Palaeo-permafrost distributions during the LIA and YD in the Err-Julier region are reconstructed by Frauenfelder et al. [2001]. Their results suggest that during the YD permafrost was abundant in unglacierised slopes down to altitudes of (at least) 2200 m a.s.l. (Fig. 3.7). The front of the Egesen *Piz Bleis Marscha* glacier and of the future *Bleis Marscha* rockglacier were within the permafrost zone.

Frauenfelder et al. [2005] describe the *Bleis Marscha* rockglacier as a “stream [that] can be seen as a continuum from active to relict stages with an active zone in the upper part and a densely vegetation-covered possibly relict frontal zone”. Weathering rind measurements and chemical analysis have been performed on the *Bleis Marscha* rockglacier by Laustela et al. [2003]. Frauenfelder et al. [2005] added Schmidt-hammer rebound values (R values, see Fig. 3.8). The results are consistent: increasing weathering rind thickness from the root zone towards the front, decreasing Al_d/Fe_d -ratio (“continuous formation of iron oxihydroxides with time”, iron staining) and decreasing mean R values are indicative of continued exposure to the atmosphere, weathering. Comparison of R values (Fig. 3.9) and weathering rind thicknesses of different rockglaciers, ages obtained from streamline interpolation and morphological constraints suggests an age of the *Bleis Marscha* rockglacier of several ky, the formation possibly in the early Holocene.

In the Err-Julier area, high valleys at altitudes of 1700 m a.s.l. are in the rain shadow of high mountain peaks. This geographical setting is responsible for a generally dry-cold, continental-type climate, low mean annual precipitation (MAP) of $800\text{--}900\text{ mm a}^{-1}$ (1971-1990) [Hydr. Atl. d. Schweiz, Blatt 2.6.], a regional lapse rate of $0.55^\circ\text{C}/100\text{ m}$ and a

Present and past
permafrost distribution

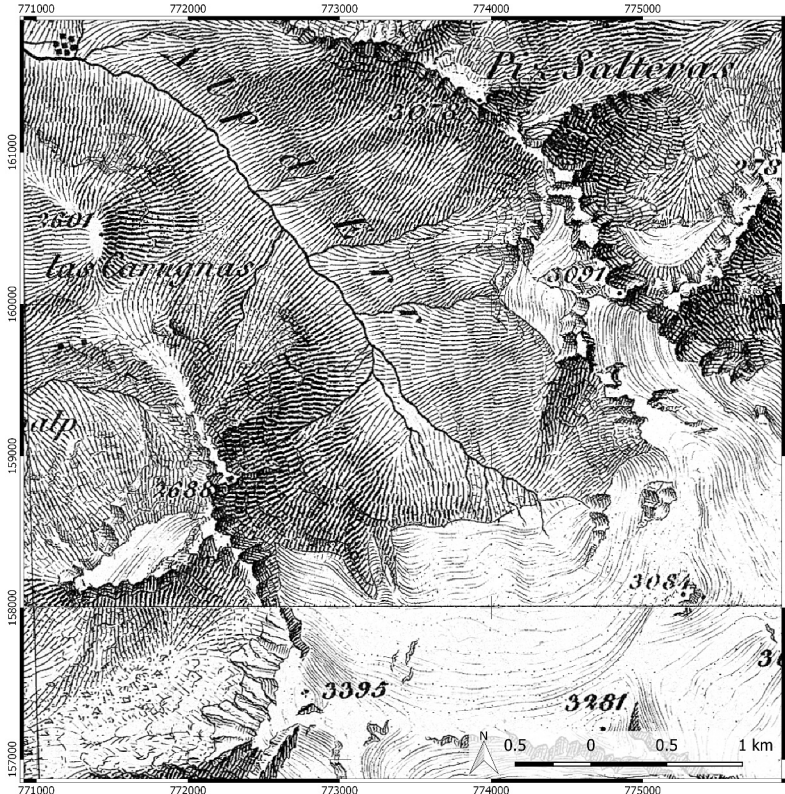
Previous work on *Bleis
Marscha* rockglacier

Meteorological data

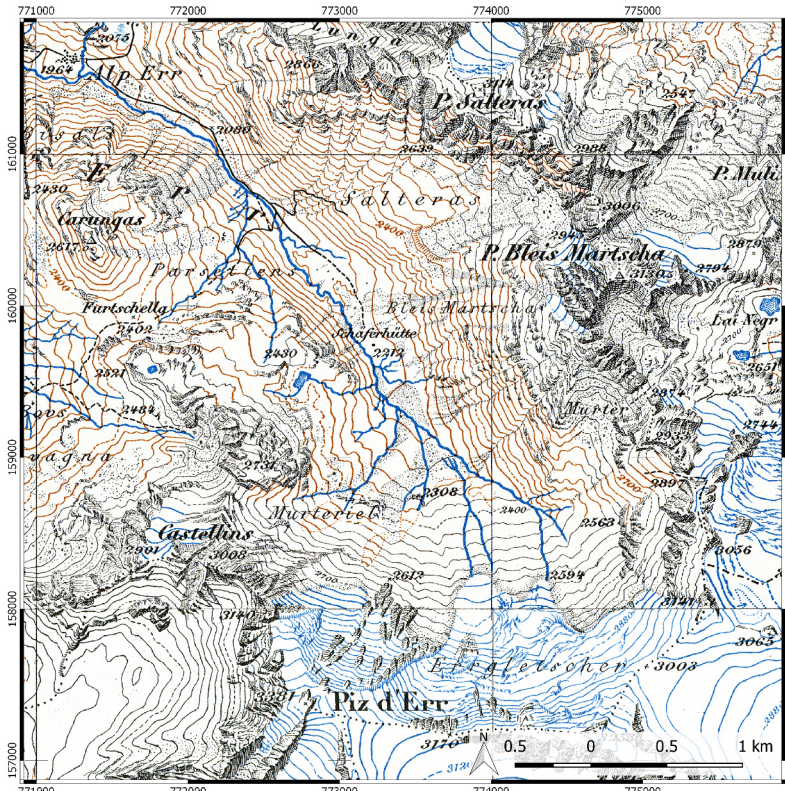
mean annual 0°C-isotherm at c. 2180 m a.s.l. [Frauenfelder et al., 2001].

Interestingly, in Cornelius [1951, p. 25], the *Bleis Marscha* rockglacier is identified as a “1 km-long moraine tongue with many concentric ridges”. The word “permafrost” does not even appear in his report on Quaternary morphology. It is plausible that CORNELIUS, just as many other geologists of that time, were not aware of the fact that permanently frozen ground is a common feature in high Alpine areas [Haeberli et al., 2010; Barsch, 1992].

Historical side note



© 2018 swisstopo (JD100042)



swisstopo (JD100042)

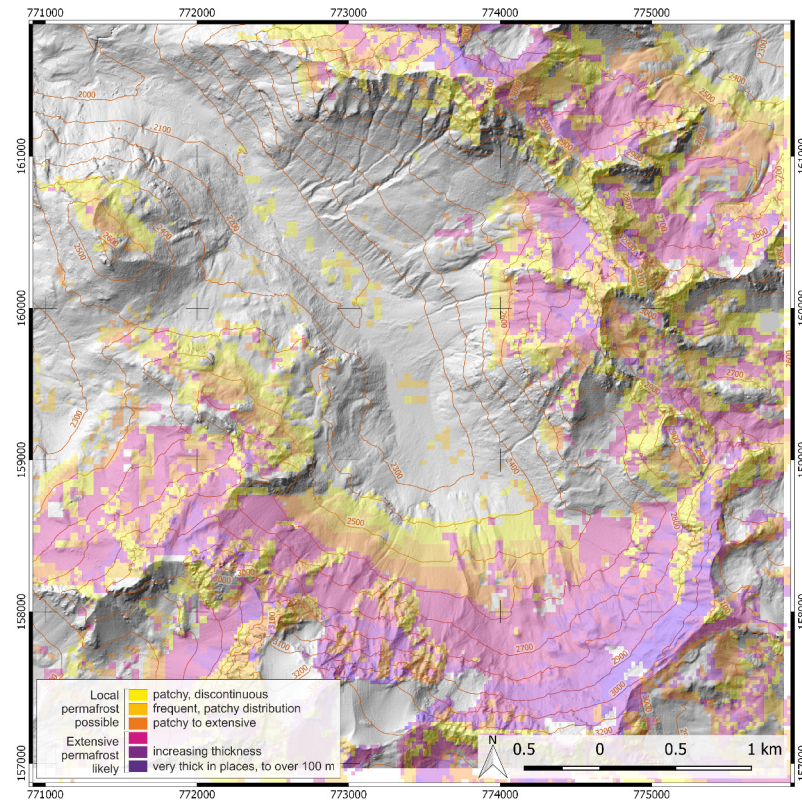


Figure 3.5: Modelled permafrost distribution in Val d'Err according to the potential permafrost distribution map (PPDM) [Gruber et al., 2006].

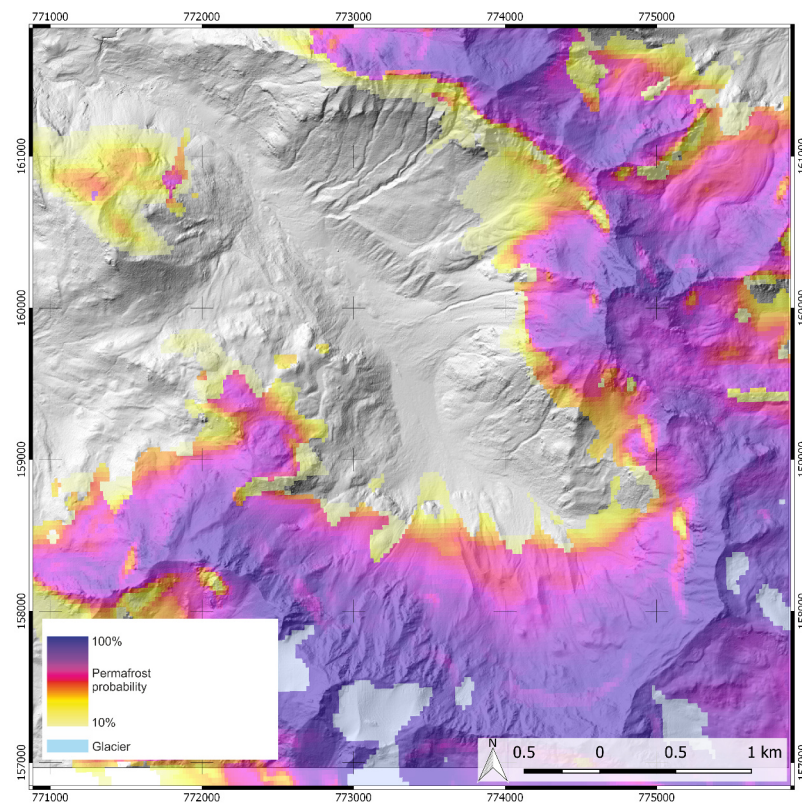


Figure 3.6: Modelled permafrost distribution in Val d'Err according to the Alpine permafrost index map (APIM) [Boeckli et al., 2012].

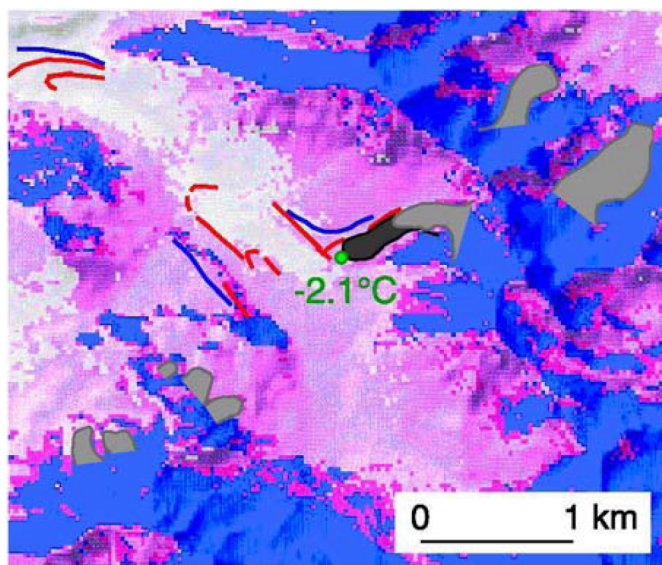


Figure 3.7: Modelled palaeo-permafrost distribution in the upper *Val d'Err*, after Frauenfelder et al. [2001].

Present-day permafrost distribution is depicted in dark blue, permafrost distribution during the Little Ice Age (LIA) in dark pink during the Younger Dryas in light pink. Palaeo-reconstructions for the Older Dryas (Daun) glacier stages are given in dark blue, and the Younger Dryas (Egesen I-III) advance stages are marked with red lines. Today's MAAT at the tongue is estimated to be 2.1°C warmer than during the Younger Dryas.

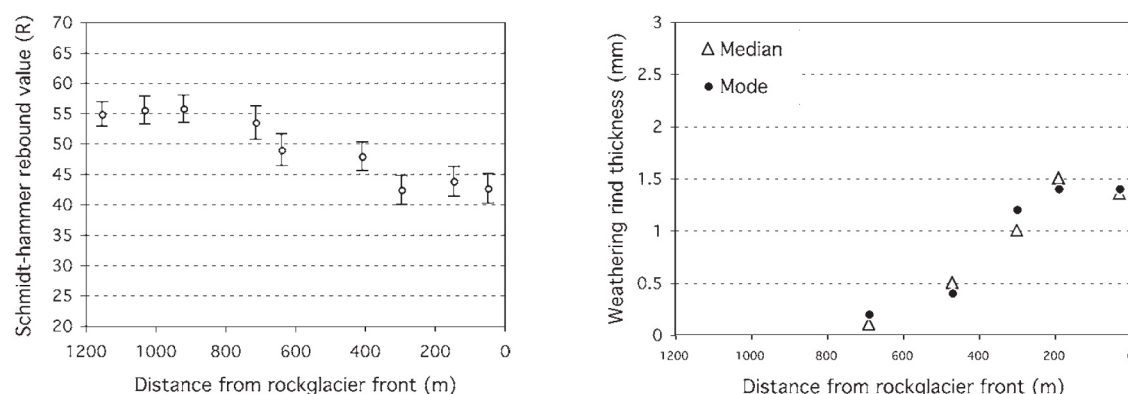


Figure 3.8: Schmidt-hammer rebound value and weathering rind thickness on the *Bleis Marscha* rockglacier [Frauenfelder et al., 2005]. Left panel: Schmidthammer rebound values (R) showing the arithmetic mean on each transect with the corresponding standard error. Right panel: modal and median values of the measured weathering rind thickness transects (modified after Laustela et al. [2003]). Creep direction in both graphs is from left to right.

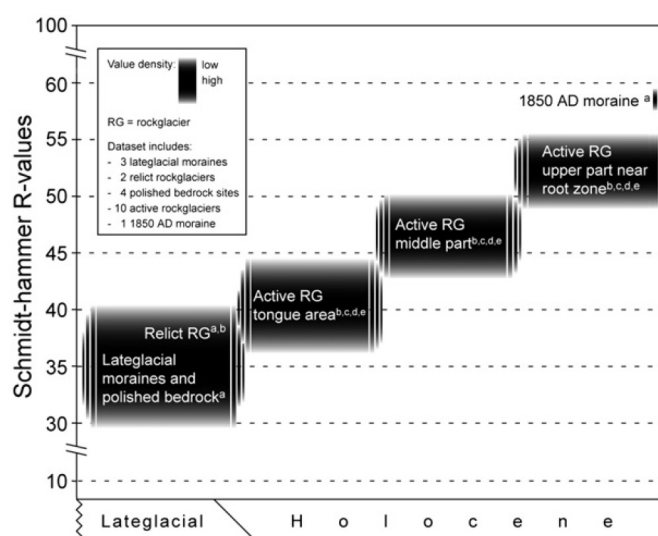



Figure 3.9: Tentative Schmidthammer *R* value calibration curve for the *Julier-Albula* region [Böhlert et al., 2011].

4 Methods

The research questions are addressed with cosmogenic nuclide surface exposure dating and finite-element numerical modelling (FEM), together with field work and analysis of aerial images and a digital elevation model (DEM). Geophysical sounding or drilling and other invasive methods are beyond the scope of this Master's thesis.

4.1 Field work

Main points 
Field work and observations are critical as they are necessary for both the acquisition and interpretation of the exposure ages, as well as for constraining the model parametrisation. A few sampling considerations must be respected for the exposure ages to be meaningful.

For time and weather constraints, extensive field work has been done in summer 2017: On a first scouting excursion on June 16, the suitability of the *Bleis Marscha* rockglacier was verified and contact to the local game keeper was made. The field campaign with sampling took place on August 2–4. Remaining questions were discussed on a follow-up field trip on October 15.

4.1.1 Field observations

Remarks on observations and discussions in the field as well as notes on samples such as location, time, orientation and topographic shielding are stored in the field book. In addition, the sample characteristics are collected digitally using an iPad[®] with GISPro[®] installed. The georeferenced data can be directly exported to ArcGIS or QGIS. The notes are illustrated with sketches and photographs. Panorama images are stitched with the open-source software Hugin.

Field notes, sketches & photographs

4.1.2 Sampling procedure

The boulders to be sampled must be selected carefully (i) to provide a meaningful exposure date as close as possible to the true age of the landform [Ivy-Ochs and Kober, 2008], and (ii) to cover all units of the rockglacier. These points should be considered [Ivy-Ochs and Kober, 2008, S. Ivy-Ochs, pers. comm.]

Sampling considerations

- the boulder should be large (≥ 1.5 m side length), broad and appear stable, such that it has been continuously exposed;
- there should be no signs of fast weathering or spalling so that the original surface is sampled. Patches with high quartz content should be preferred to patches with feldspars or micas;
- boulders in depressions or furrows where the snow remains should not be sampled, as a snow cover attenuates cosmic rays [Böhlert et al., 2011]. A lichen cover poses no problems due to its low density;

- the sample should be taken close to the top of the boulder where the exposure to cosmic rays is greatest, but not right at the tip to avoid edge effects;
- location, elevation, orientation of sampled surface and topographic shielding should be recorded in the field as they enter into elevation and shielding corrections.

For each sample, roughly 500 g of rock should be collected.

4.2 Geomorphological analysis and mapping

Main points
Data derived from a digital elevation model (DEM) serves for morphometric analysis, to constrain the rockglacier model parametrisation and for visualization purposes. The swissALTI3D DEM for 2016 with a grid spacing of 2 m provided by swisstopo is used.

The high-resolution digital elevation model (DEM) “SwissAlti3D” provided by the Swiss Federal Office of Topography swisstopo is used for visualization and topographic analysis. The data was acquired in 2016, and has 2×2 m cell size with an average error in the order $\mathcal{O}(1-3)$ m for areas above 2000 m a.s.l. It captures most of the furrow-and-ridge microrelief. From the DEM raster, data sets such as a hillshade, slope angle or aspect can be derived in Matlab, ArcGIS or QGIS (Fig. 4.1). Most of the topographic analysis will be done either with the Matlab toolbox TopoToolbox 2 [Schwanghart and Kuhn, 2010; Schwanghart and Scherler, 2014] or the open-source software QGIS.

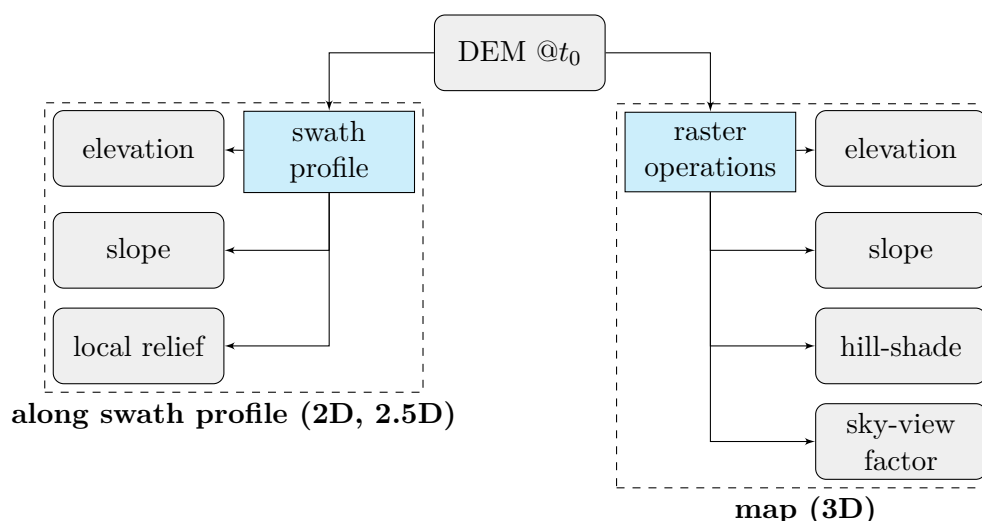


Figure 4.1: DEM processing, derived stuff. Used programs are TopoToolbox in Matlab, QGIS and Relief Visualization Toolbox.

Morphometric parameters such as length, width or area are used to characterize and classify the rockglacier. Since the area of the rockglacier, its source area and the intensity of talus production are connected [Barsch, 1996, p. 29], the weathering rate can be estimated. A swath profile along the rockglacier surface showing the microrelief is used as upper boundary for the two-dimensional numerical model.

Geomorphological mapping is done with the aid of the hillshade and aerial images in ArcGIS or QGIS, taking into account observations made in the field. The map covers the

rockglacier, its source area and immediate surroundings.

The most commonly used relief visualization technique, the single-direction analytical (i.e. computer-based) hill-shading, is based on the direct illumination of the DEM (traditionally from the north west). Even though this is an intuitive way of representing the terrain, slopes facing the fictive light source are over-exposed and slopes facing away are deeply shadowed (under-exposed). Both leads to a loss in perceived relief details [Zakšek et al., 2011], which is particularly unsatisfactory for visualizing the small-scale rockglacier microrelief.

A note on terrain
visualisation

One possible way to overcome the limitations of a single-source directional illumination is to adopt a visualization method which is based on *diffuse illumination*. The relief surface is illuminated by an uniformly bright, isotropic celestial hemisphere. Zakšek et al. [2011] proposed the *sky-view factor* (SVF), the total fraction of visible sky limited by the relief, as a proxy for the diffuse illumination. In a sky-view factor based relief visualization, strongly illuminated ridges appear bright, occluded furrows dark, and topographic details are well presented.

The sky-view factor (SVF) is determined by [Zakšek et al., 2011]

$$SVF := 1 - \frac{\sum_{i=1}^n \sin \gamma_i}{n}, \quad 0 \leq SVF \leq 1, \quad (4.1)$$

where γ_i is the elevation angle from the horizon to the highest obstructed point in the i -th slice, and n is the number of slices used to estimate the sky-view factor at the point of interest (Fig. 4.2). Zakšek et al. [2011] provide a stand-alone executable called “Relief Visualization Toolbox” (RVT) that does the calculations.

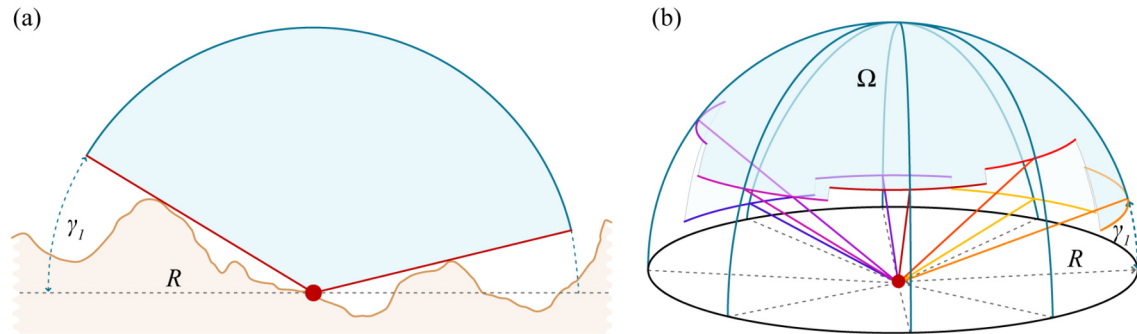



Figure 4.2: Sky-view factor (SVF) is defined by the portion of the visible sky, Ω , above the observation point. The algorithm computes vertical elevation angle of the horizon γ_i in n directions to the specified radius R . Zakšek et al. [2011].

Apart from a purely visualisation purpose, the sky-view factor at the sampling points can in principle be used to calculate the topographic shielding correction for the TCN age calculation Gosse and Phillips [2001].

4.3 Surface exposure dating

Main points	
<p>Cosmogenic nuclides build up at a predictable rate in the mineral lattice (<i>in situ</i>) at or near Earth's surface due to the interaction of a variety of target atoms with secondary cosmic particles. Commonly used nuclides are ^{10}Be produced in quartz and ^{36}Cl produced in carbonates. The number of these cosmogenic nuclides is related to the exposure time. Since the cosmic ray flux and thus the production rate is modulated by the atmosphere and Earth's magnetic field, a physical model is required to convert the number of nuclides to an exposure age. Ideally, the rock surface has undergone single-stage (no pre-exposure or inheritance), continuous (no covering) exposure in the same position (not shifted or toppled) since deposition. The datable age range is between a few hundred years (detection limit) and a few million years (half-life of the nuclide, weathering rate).</p>	

4.3.1 Principles of cosmogenic nuclide exposure dating

Contribution of TCN

Constraining the absolute age of the rockglacier and of its lobes is the key for placing the formation and development of the *Bleis Marscha* rockglacier in the Holocene climate history, elucidates the temporal relationship between the rockglacier (periglacial realm) and the adjacent moraines (glacial realm), dates the period of activity of each unit and allows to quantify long-term average creep rates.

Cosmogenic nuclide build-up

The basis for surface exposure dating with cosmogenic nuclides is that certain nuclides in minerals build up at a predictable rate when exposed to cosmic ray flux, and their concentration is thus a measure of elapsed exposure time at or near the Earth's surface [Ivy-Ochs and Kober, 2008]. These nuclides produced in surface material are referred to as *in-situ* cosmogenic nuclides, in contrast to the *meteoric* ones produced in Earth's atmosphere.

When *primary cosmic radiation* of galactic (and solar) origin mainly consisting of protons, alpha-particles and other small nuclides enter the atmosphere, they interact with the atmospheric molecules and set up a cascade of *secondary particles*, primarily neutrons and muons [Alfimov and Ivy-Ochs, 2009]. Cosmogenic nuclides are produced within minerals by spallation, muon-induced reactions and low-energy (epithermal and thermal) neutron capture [Ivy-Ochs and Kober, 2008; Lal and Peters, 1967]. The *in-situ* concentration build-up C [at g $^{-1}$] in an exposed rock surface is modelled as [Ivy-Ochs and Kober, 2008]

$$C(t) = \frac{P_0}{\lambda + \frac{\rho\varepsilon}{\Lambda}} \left[1 - \exp \left\{ - \left(\lambda + \frac{\rho\varepsilon}{\Lambda} \right) t \right\} \right] + \underbrace{C_{inh} e^{-\lambda t}}_{\text{inheritance term}}, \quad (4.2)$$

where P_0 [at g $^{-1}$ a $^{-1}$] is the local production rate, t [a] the exposure age of the surface, λ [a $^{-1}$] the decay constant, ρ [g cm $^{-3}$] the density of the irradiated rock, ε [cm a $^{-1}$] the erosion rate, Λ [g cm $^{-2}$] the attenuation length and C_{inh} [at g $^{-1}$] the initial, inherited nuclide concentration. Cosmic ray intensity and thus the production rate increases from equator to pole because the particle flux is deflected by the Earth's magnetic field, and increases towards higher altitude because most of the secondary particles are generated in the lower stratosphere. The local production rate P_0 must thus be scaled to site (geomagnetic) latitude, longitude, altitude and topographic shielding. Furthermore, as the cosmic ray flux entering Earth's atmosphere is inversely proportional to the strength of the magnetic field, P_0 varies with time as well. In brief, the *in-situ* production rate is specific to each nuclide

and depends on the secondary particle flux (itself depending on geomagnetic location of the sampling site, the elevation and geomagnetic field strength) and the property of the target mineral (density, composition, availability and thermodynamic state of suitable target nuclei).

Since the production rate within the rock decreases semi-exponentially with depth due to attenuation, the sample thickness must also be corrected for. Exposed rock surfaces with an age not older than three to four half-lives of the measured nuclide can be dated: the concentration then reaches a steady state, called *secular equilibrium*. Weathering shortens the period until saturation is reached, even for the stable nuclides, and can give too young ages. Inheritance, on the other hand, yields too old ages [Ivy-Ochs and Kober, 2008]. “The absolute concentration of a cosmogenic nuclide in surface materials is controlled by the rates of in-situ production, nuclide decay, and removal by surface erosion”.

Commonly utilized are the radionuclides ^{10}Be , ^{14}C , ^{26}Al and ^{36}Cl and the stable noble gases ^3He and ^{21}Ne . Their ubiquity in wide range of minerals (e.g. ^{10}Be in quartz, ^{36}Cl in calcite/dolomite) allow virtually any lithology to be dated for exposure ranging from 10^2 to 10^7 a [Gosse and Phillips, 2001]. The lower age limit is determined by the detection limit, while the upper one by the nuclide half-life and the weathering rate of the rock surface [Ivy-Ochs and Kober, 2008].

Table 4.1: Characteristics of used nuclides for surface exposure dating, after Ivy-Ochs and Kober [2008] and S. Ivy-Ochs [pers. comm.].

Nuclide	Half-life	Target element	Measured ratio	Production rate [at/g a]	Reactions
^{10}Be	1.4 Ma	O	$^{10}\text{Be}/^9\text{Be}$	4	$^{16}\text{O}(\text{n},4\text{p}3\text{n})^{10}\text{Be}$ $^{16}\text{O}(\mu^-,3\text{p}3\text{n})^{10}\text{Be}$
^{36}Cl	301 ka	Ca, K, ^{35}Cl	$^{37}\text{Cl}/^{35}\text{Cl}$, $^{36}\text{Cl}/\text{Cl}$	composition- dependent, ~20 (lime- stone)	$^{39}\text{K}(\text{n},2\text{p}2\text{n})^{36}\text{Cl}$ $^{40}\text{Ca}(\text{n},3\text{p}2\text{n})^{36}\text{Cl}$ $^{39}\text{K}(\mu^-, \text{p}2\text{n})^{36}\text{Cl}$ $^{40}\text{Ca}(\mu^-, 2\text{p}2\text{n})^{36}\text{Cl}$ $^{39}\text{K}(\text{n},\alpha)^{36}\text{Cl}$ $^{35}\text{Cl}(\text{n},\gamma)^{36}\text{Cl}$

4.3.2 Practical aspects of ^{10}Be and ^{36}Cl

^{10}Be mostly comes from ^{16}O nuclide via spallation and negative-muon capture (cf. Table 4.1) and has the highest production rate at the rock surface (Fig. 4.3). It is extracted from a pure quartz mineral separate obtained by selective chemical dissolution of the rock sample in dilute HF (4%) solution. Then, a carrier with a known amount of ^9Be is added, and the mineral separate is completely dissolved in concentrated HF. The Be is separated and purified with ion exchange methods and selective pH precipitation. Finally, the ratio of $^{10}\text{Be}/^9\text{Be}$ is measured with accelerator mass spectrometry (AMS). Quartz is a ubiquitous, resistant mineral that can be reliably cleaned of meteoric ^{10}Be , which clearly outweighs the disadvantages of the low production rate (requires longer exposure periods until detection limit is exceeded) and interferences with ^{10}B [Ivy-Ochs and Kober, 2008].

^{36}Cl in rocks with sufficient natural stable chlorine (carbonates) is produced by several pathways [Alfimov and Ivy-Ochs, 2009]: spallation and muon-related reactions from Ca, but also by ‘low-energy neutron capture on ^{35}Cl ’ (Fig. 4.4). These neutrons are slowed-

^{10}Be sample preparation

^{36}Cl sample preparation

down neutrons derived from spallation and muon-related reactions (secondary particles) and radiogenic neutrons from the decays in the U-Th chain. Unlike in the case of the spallation-dominated vertical production profile of ^{10}Be in quartz, the highest production rate of ^{36}Cl is not at the surface, but roughly at 20 cm depth, depending on the composition and density of the rock (neutron leakage). The ^{36}Cl method is thus somewhat more weathering-tolerant, at the expense of a more complex procedure as the total rock Cl concentration, major element oxides and the concentration of the strong neutron absorbers B, Gd and Sm must be calculated for each sample. The crushed rock samples are leached with a weak HNO_3 solution to remove meteoric or not in-situ produced Cl isotopes. A ^{35}Cl -carrier of known amount is added, and the carbonate samples are dissolved in HNO_3 . To avoid isobaric interference with ^{36}S , sulphur is precipitated with BaSO_4 . The precision and accuracy of the measurements is improved by the implementation of isotope dilution, where both the total rock Cl and ^{36}Cl concentration are determined by measuring the ratios of $^{37}\text{Cl}/^{35}\text{Cl}$ and $^{36}\text{Cl}/\text{Cl}$ [Ivy-Ochs et al., 2004]. To take out subsurface non-cosmogenic neutron capture ^{36}Cl production, the concentrations of U and Th are measured as well. Despite the complicated production reactions that require a long preparation process, the ^{36}Cl method is applicable to almost any rock type (silicates and carbonates), has a low detection limit (low minimum age), and with a half-life of 308 ka suited for dating Holocene and Pleistocene rock surfaces [Davis and Schaeffer, 1955].

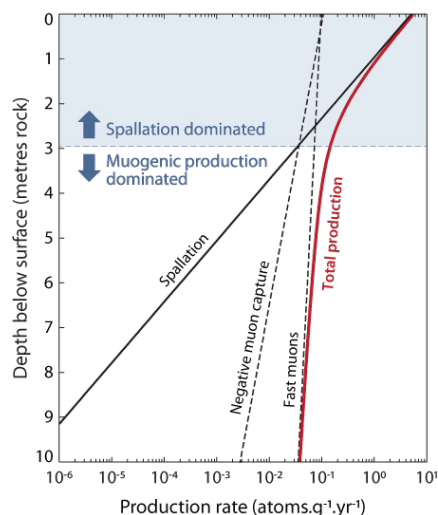


Figure 4.3: Spallation-dominated ^{10}Be production rate profile [von Blanckenburg, 2005], source.

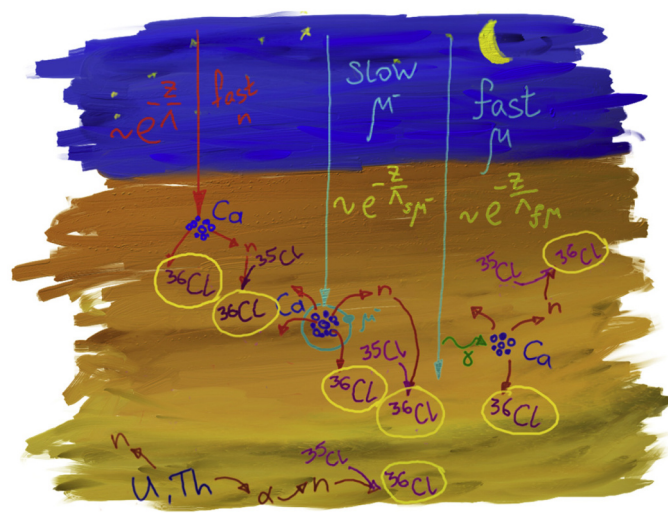


Figure 4.4: ^{36}Cl production mechanisms, after Alfimov and Ivy-Ochs [2009].

Shielding corrections

Shielding by surrounding hillslopes or a dipping rock surface reduces the cosmic ray flux to the sampling site and consequently the local production rate [Ivy-Ochs and Kober, 2008]. *Shielding corrections* are calculated following Dunne et al. [1999], with the online calculators formerly known as the CRONUS-Earth online calculators [Balco et al., 2008].

4.3.3 Laboratory procedure

Sample preparation followed standard procedures described in Ivy Ochs [1996]; Ochs and Ivy-Ochs [1997]; Ivy-Ochs and Kober [2008]; Hippe [2012]. ^{10}Be in the Err granite and ^{36}Cl in the dolomite was measured with the AMS at the Ion Beam Physics group at ETH Zürich. Fig. 4.5 provides an overview of the ^{10}Be and ^{36}Cl processing steps from sampling

to the exposure age calculation.

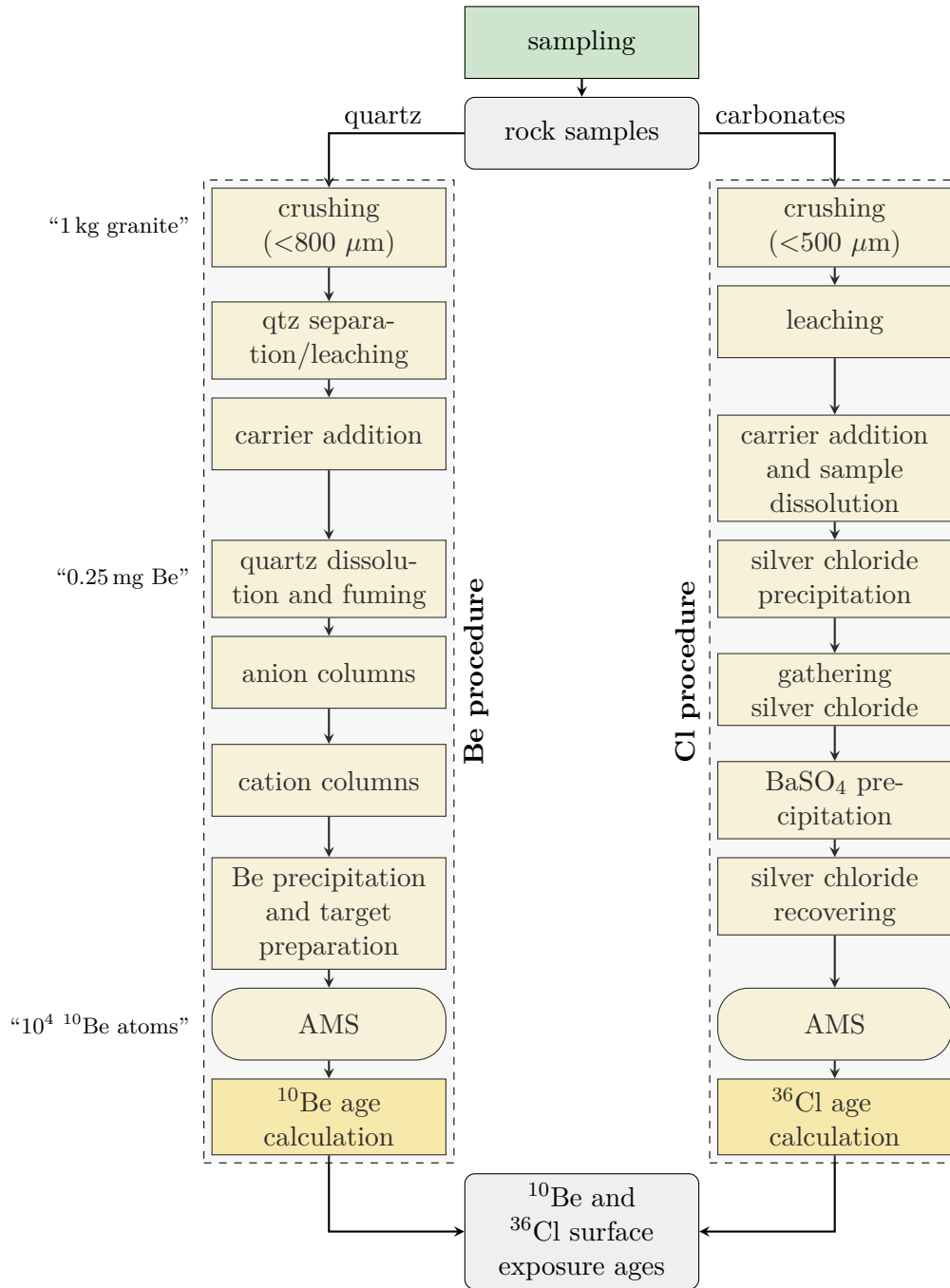


Figure 4.5: Laboratory procedures for the extraction of ^{10}Be (left thread) and ^{36}Cl (right thread).

4.4 Aerial image cross correlation

Main points



The correlation of aerial images is a remote sensing technique to quantify the present, short-term surface translational displacement. A template-based image matching of two orientation images derived from bi-temporal orthophotos with the normalized cross-correlation (NCC) as similarity measure is carried out with the ImGRAFT tool in MATLAB. Calculating orientation images is a pre-processing step that renders the matching robust and illumination invariant. From the velocity field, stream lines and principal strain rate axis are derived that elucidate travel times and deformation mechanisms.

Contribution of IMCOR

To obtain area-wide information on surface kinematics and to assess the activity status of the individual units, feature tracking on repeated georeferenced orthophotos is performed. The obtained two-dimensional flow field is also used to calibrate the surface (horizontal) creep rates in the numerical model.

Repeat optical imagery data

As input serve georeferenced and orthorectified aerial images provided by the Swiss Federal Office of Topography swisstopo (Table. 4.2, accessed via [DownloadService GeoVITe]). The orthophoto mosaic SWISSIMAGE 25 cm is a composition of digital color aerial photographs. Ground resolution for the study area is 0.5 m resampled to 0.25 m. Standard deviation for the precision in position: ± 0.5 m for the ground sample distance of 0.5 m (in hilly terrain ± 3 -5 m) [PDF].

Table 4.2: SWISSIMAGE coverage of the *Val d'Err* (tiles 1236-43, 1236-44).

File name	Acquisition date
swissimage_2003	2003
swissimage_2006	2006
swissimage_2009	2009
swissimage_2012	2012

Process overview

An overview of the processing steps is given in Fig. 4.6.

4.4.1 Principle of NCC, Algorithm

Digital photogrammetric method

We have two discrete images taken at different times, I_0 @ t_0 and I_1 @ $t_1 > t_0$, which are orthorectified and georeferenced. The images I are indexed using pixel-wise image coordinates (x, y) , where x and y are integers. Both images together are referred to as *image pair*. In order to calculate the offset between two features on the image pair, ImGRAFT tracks features between image pairs using the `templatematch` function based on a cross-correlation algorithm [Messerli and Grinsted, 2015; Heid and Käab, 2012], illustrated in Figs. 4.7 and ???. Conceptually, the algorithm searches a distinctive feature in image I_0 at image location \mathbf{x}_0 , the so-called *template* t (e.g. a prominent boulder), within the *search region* W_s on image I_1 . The template location in image I_1 , \mathbf{x}_1 , is defined as the point of maximum correlation between the *template* and the *search region*. The offset in pixel (image coordinates) is transformed to a physical length using the image cell size.

The use of cross-correlation for template matching is motivated by the squared Euclidean distance $d_{f,t}^2$ as a distance measure of the similarity of a reference template $t \subset I_0$ and

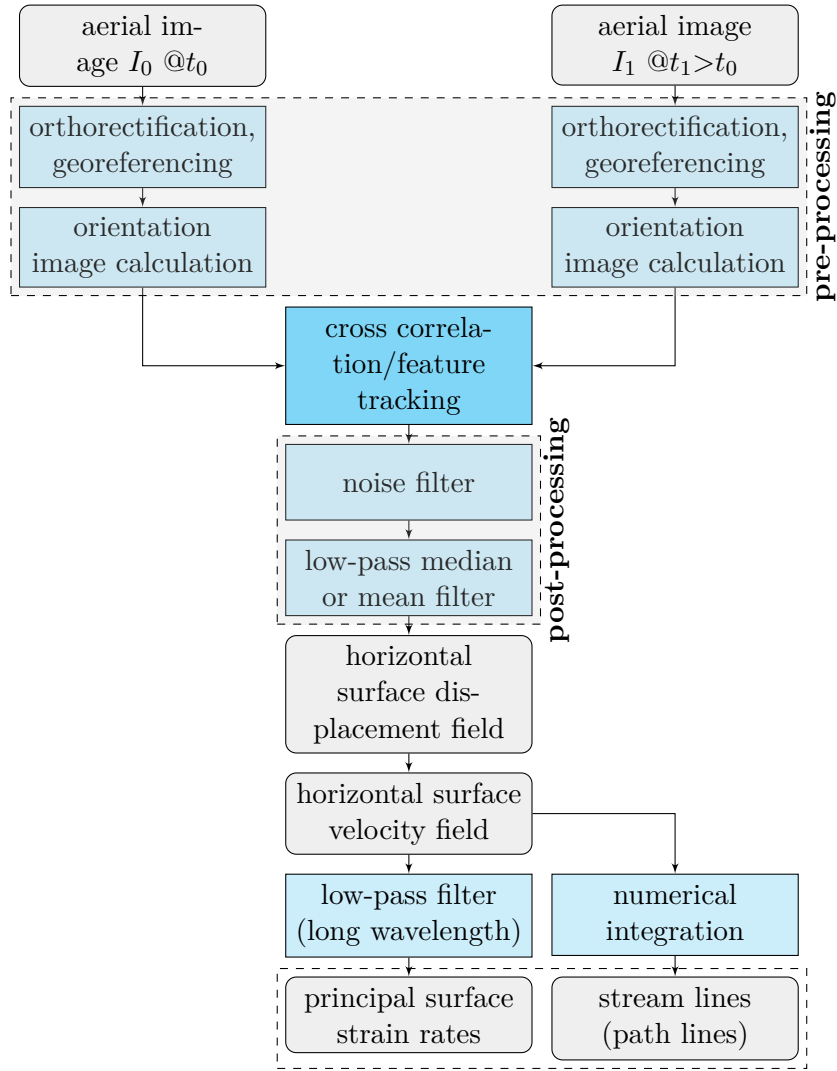


Figure 4.6: Flow chart with the processing steps of bi-temporal (t_0, t_1) aerial image cross correlation. The main steps are pre-processing, correlation, and post-processing. From the velocity field, strain rates and stream lines are derived, requiring additional processing steps.

search template $f \subset I_1$ [Lewis, 1995],

$$d_{f,t}^2(u, v) = \sum_{x,y} [f(u+x, v+y) - t(x, y)]^2 \quad (4.3)$$

In the binomial expansion of $d_{f,t}^2$, the term $\sum t^2$ is constant. If the term $\sum f^2$ is approximately constant, then the remaining mixed term is left as a measure of the similarity between the reference template and the search template. It needs to be normalized by subtracting the average pixel value of the template and local search window area, \bar{t} and $\bar{f}_{u,v}$, respectively. Normalization renders normalized cross correlation (NCC) invariant to template size and image amplitude, thereby accounting for differences in brightness and contrast caused e.g. by changing lighting conditions [Lewis, 1995; Kääb and Vollmer, 2000; Debella-Gilo and Kääb, 2011]. However, normalized cross correlation is still not invariant with respect to imaging scale, (non-rigid) intra-template deformation (strain, rotation) and perspective distortions.

The normalized cross-correlation coefficient γ is in spatial domain defined as (“direct

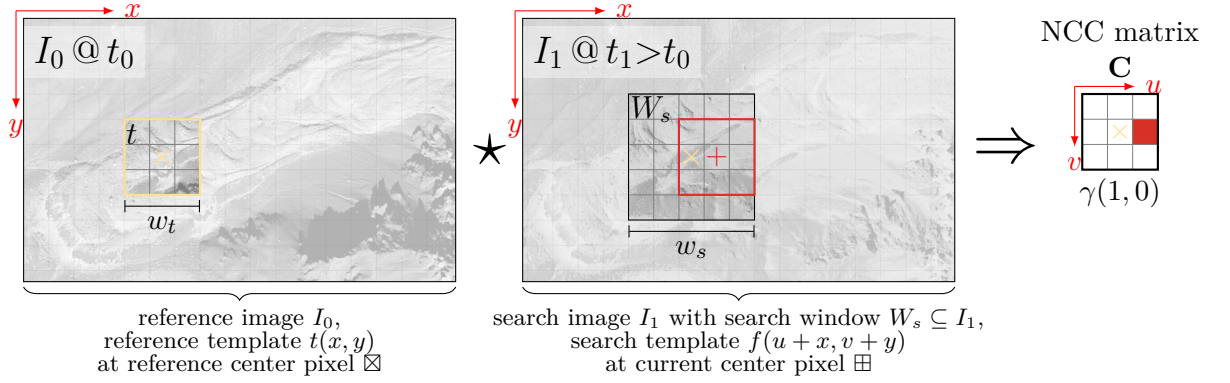


Figure 4.7: Schematic representation of the cross-correlation (denoted by \star , Eq. 4.4) of a 3×3 px reference template t with a 5×5 px search window W_s in area-based image matching (not to scale). After Debella-Gilo and Kääb [2011, 2012]. u and v are integer pixel offsets with respect to the reference center pixel \boxtimes within the search window W_s in x - and y -direction, respectively. Cf. Kääb and Vollmer [2000, Fig. 4]. The pixel size is not to scale.

NCC”) [Lewis, 1995]

$$\gamma(u, v) = \frac{\sum_{x,y} \left[\overbrace{f(u+x, v+y) - \bar{f}_{u,v}}^{f \in W_s \subseteq I_1} \right] \left[\overbrace{t(x,y) - \bar{t}}^{t \in I_0} \right]}{\sqrt{\sum_{x,y} \left[f(u+x, v+y) - \bar{f}_{u,v} \right]^2 \sum_{x,y} \left[t(x,y) - \bar{t} \right]^2}}, \quad -1 \leq \gamma \leq 1. \quad (4.4)$$

The NCC coefficients γ are assembled in the NCC matrix \mathbf{C} . x and y are the image coordinates that are summed over, u and v the pixel offsets with respect to the reference center pixel in x - and y -direction, t the spatial grey-value function of the reference template that gives the grey value at location (x, y) , f the corresponding grey-value function for the shifted search template, \bar{t} is the mean of the intensities in the reference template t , and $\bar{f}_{u,v}$ is the mean of the intensities in the search window under the search template f (*local mean*). For a meaningful normalization, the search window W_s must be larger than the reference template t , and the pixel intensities of the template must not be uniform. The global maximum of the double (two-dimensional) cross-correlation surface γ indicates the location of the best-matching shifted template within the search window, and thus the displacement.

Note on calculation

The numerator of Eq. 4.4, the mixed term from Eq. 4.3, is for large images most often efficiently computed in frequency domain, as cross-correlation in the spatial domain is equivalent to a (computationally advantageous) multiplication in the frequency domain (convolution theorem): $\gamma^{num}(u, v) = \mathcal{F}^{-1}\{\mathcal{F}[(f - \bar{f}_{u,v}) \star (t - \bar{t})]\} = \mathcal{F}^{-1}\{\mathcal{F}[f - \bar{f}_{u,v}] \cdot \mathcal{F}[t - \bar{t}]^*\}$, where \mathcal{F} denotes the Fourier transformation, \star the correlation operation and $*$ complex conjugation (equivalent to time reversal). There is no similarly straightforward and efficient method to compute the denominator.

Template and search window size

The template needs to be large enough to capture distinctive patterns that are recognizable in both images. Its size depends on textural characteristics of the ground surface, the image resolution, and on the temporal baseline (with longer baselines, small-scale morphological features are less likely to be preserved [Monnier and Kinnard, 2017]). The

search window needs to be large enough to contain the maximum expected displacement. This can be estimated by multiplying the time interval between image acquisitions with a typical surface speed [Kääb and Vollmer, 2000; Messerli and Grinsted, 2015]. Decorrelation occurs when the surface texture between the image acquisitions changes too much. It depends on ground resolution, temporal baseline, ground cover/vegetation, and surface processes (typical deformation rates).

Decorrelation

4.4.2 Pre- and postprocessing, filtering

The pre-processing steps are orthorectification, georeferencing and optionally orientation image calculation.

Pre-processing

Orthorectification is the process of removing the effects of lens distortion, image perspective (tilt) and topographic relief (terrain) effects, providing an undistorted, uniformly scaled and planimetrically correct representation of the Earth’s surface. Georeferencing means tying the internal image coordinates to a ground system of geographic coordinates.

orthorectification,
georeferencing

What is termed “orientation correlation” is more precisely a two-dimensional correlation of orientation images (Fig. 4.8). Orientation correlation is a feature-based matching method that shares advantageous properties of area-based methods: it “matches the feature of image intensity gradient orientation for each pixel” and is therefore illumination-invariant [Fitch et al., 2002].

Orientation correlation

The discrete image I represented by a real-valued matrix containing the grey values is transformed to an *orientation image* I^o represented by a complex-valued matrix according to

$$I^o = \text{sgn} \left(\frac{\partial I(x, y)}{\partial x} + i \frac{\partial I(x, y)}{\partial y} \right), \quad (4.5)$$

where sgn is the signum function and i denotes the complex imaginary unit. For non-zero complex numbers z , $\text{sgn}(z)$ returns $z/|z|$, where $|z|$ is the complex modulus of z . The meaning of Eq. 4.5 becomes obvious when rewritten to polar form, $\text{sgn}(z) = e^{i \arg\{z\}}$: It is intimately related to the phase angle via EULER’s formula. Furthermore, the magnitude of a pixel is either one or, in the case of a uniform region of the image with no gradient, zero ($\text{sgn}(0 + 0i) := 0$). Orientation images are thus normalized and have the same unit (radian). Orientation correlation is invariant to the pixel brightness (in contrast to area-based methods).

Matching windows, template t^o and search window f^o , are extracted from the two orientation images I_0^o , I_1^o analogous to the direct NCC method. The orientation correlation matching surface is computed from

$$\gamma := \mathcal{F}^{-1} \{ \mathcal{F}[t^o] \cdot \mathcal{F}[f^o]^* \}. \quad (4.6)$$

This can be efficiently implemented numerically with Fast Fourier Transforms (FFT).

The post-processing steps are noise-filtering to remove erroneous matches and smoothing to attenuate small-scale variations or noise.

Post-processing

The noise and signal levels are estimated with the following parameters: Recall the correlation coefficients γ that form the coefficient matrix \mathbf{C} with elements C_{ij} (Eq. 4.4, 4.6). The global maximum of the NCC surface indicates the most likely terrain displacement. This maximum correlation coefficient C_{max} is defined straightforward as

Noise filtering

$$C_{max} := \max\{\mathbf{C}\}. \quad (4.7)$$

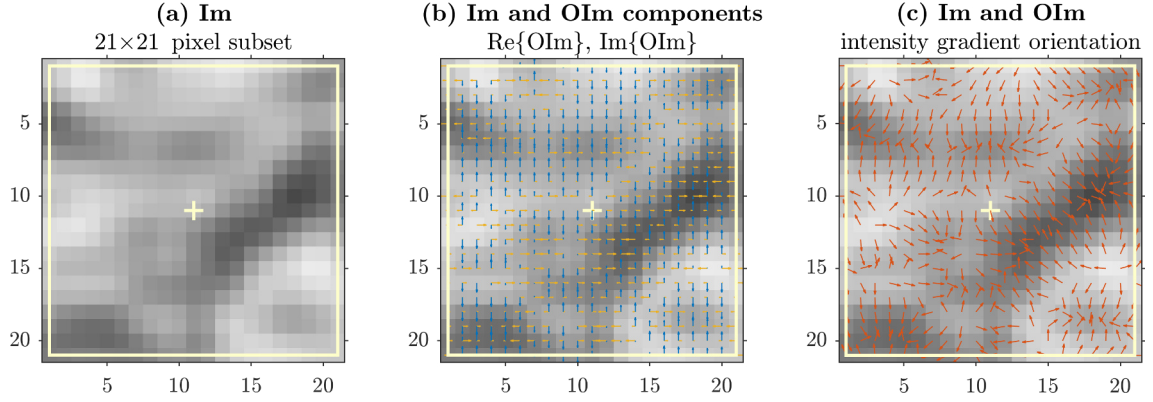


Figure 4.8: Orientation image (c: intensity gradient orientation represented by the red arrows) on top of the image (a: intensities represented by the grey values). Plot b shows how the orientation image is constructed from the intensity differences in x (real part of I^o) and y (imaginary part) direction (yellow and blue arrows, respectively). Note that the orientation vectors have zero value in uniform areas and a length of one in non-uniform areas. This is an advantageous property: Uniform areas do not contribute to the matching and orientation images are inherently normalized. Image coordinates [6919,3002], 21×21 px.

The mean absolute correlation coefficient over the search region (containing N pixels) is an estimate of the noise level [Messerli and Grinsted, 2015]:

$$C_{noise} := \frac{1}{N} \sum_N |C_{ij}|. \quad (4.8)$$

The signal-to-noise ratio SNR is then

$$SNR := \frac{C_{max}}{C_{noise}}. \quad (4.9)$$

It can be thought of as “how tall the correlation peak rises over the noise level”. Pixels with a signal-to-noise ratio SNR lower than a specified threshold SNR_{min} are considered as noise.

Smoothing

To smooth the velocity field, low-pass circular median or mean filter are used. A median filter reduces noise while preserving the edges, at the expense of higher computational costs compared to a mean filter.

The horizontal surface displacement of each pixel is computed separately as the Euclidean distance between the pixels’ positions in the reference and the matching templates. Velocity is then computed as the displacement divided by the temporal baseline of the image pair.

4.4.3 Uncertainty estimate: Significance level for displacements

For the measurement to be reliable the displacements have to exceed the mean pre-processing error arising from orthorectification and co-registration. Furthermore, the precision of NCC is inherently limited to one pixel, and thus depends on the resolution of the image data [Debella-Gilo and Käab, 2011]. The *significance level*, the threshold below which any measured displacement is not distinguishable from immobility, is estimated by matching a reference area where no displacement is expected. Its value is defined either as the mean, median or mode of the velocity data, chosen by inspecting a velocity histogram.

Pixel-level accuracy,
significance level

4.4.4 Flowpaths

A streamline \mathbf{x}_s is a curve that is everywhere tangential to the instantaneous (at time $t = t'$) local surface velocity vector \mathbf{v}_s . In parametric representation with arclength s , it is defined as

$$\frac{d\mathbf{x}_s}{ds} \times \mathbf{v}_s(\mathbf{x}_s, t') = 0 \quad \Leftrightarrow \quad \frac{d\mathbf{x}_s}{ds} = \mathbf{v}_s(\mathbf{x}_s, t'). \quad (4.10)$$

The streamline shows the direction in which a massless particle travels *at any point in time*.

A *pathline* (flow line) \mathbf{x}_p is the trajectory followed by a massless particle over a certain period of time. For a steady flow, streamline and pathline coincide. It is defined by the initial-value problem IVP comprising the ordinary differential equation (ODE) in Eq. 4.11 and seed point Eq. 4.11b:

$$\text{IVP} \begin{cases} \frac{d\mathbf{x}_p}{dt} = \mathbf{v}_s(\mathbf{x}_p), \\ \mathbf{x}_p(t = 0) = \mathbf{x}_0 \end{cases} \quad (4.11a)$$

$$(4.11b)$$

Since the acceleration is negligible for a STOKES flow, the accuracy of the boulder travel path on the rockglacier surface is only limited by the validity of the surface velocity field.

Eq. 4.11 is solved numerically with the classical Runge-Kutta 4th order scheme.

Definitions:
streamline
pathline

Numerical integration

4.4.5 Principal strain rates

The spatial derivatives of the two-dimensional horizontal surface velocity field $\mathbf{v}_s(x, y)$ form the velocity gradient tensor $\nabla \mathbf{v}_s$. This second-order tensor with components $\frac{\partial v_i}{\partial x_j}$ represented in matrix form looks like

$$\nabla \mathbf{v} = \begin{bmatrix} \frac{\partial v_x}{\partial x} & \frac{\partial v_y}{\partial x} \\ \frac{\partial v_x}{\partial y} & \frac{\partial v_y}{\partial y} \end{bmatrix}. \quad (4.12)$$

These are the spatial derivatives of the horizontal velocity components v_x and v_y with respect to the horizontal coordinates x and y .

The surface strain-rate tensor $\dot{\epsilon}_s$ is defined as $\dot{\epsilon}_{ij} := \frac{1}{2} \left(\frac{\partial v_i}{\partial x_j} + \frac{\partial v_j}{\partial x_i} \right)$. In two dimensions with the horizontal coordinates x and y , written out

$$\dot{\epsilon}_s = \begin{bmatrix} \dot{\epsilon}_{xx} & \dot{\epsilon}_{xy} \\ \dot{\epsilon}_{yx} & \dot{\epsilon}_{yy} \end{bmatrix} = \begin{bmatrix} \frac{\partial v_x}{\partial x} & \frac{1}{2} \left(\frac{\partial v_x}{\partial y} + \frac{\partial v_y}{\partial x} \right) \\ \frac{1}{2} \left(\frac{\partial v_y}{\partial x} + \frac{\partial v_x}{\partial y} \right) & \frac{\partial v_y}{\partial y} \end{bmatrix}. \quad (4.13)$$

The off-diagonal entries with the shear strain rate components $\dot{\epsilon}_{xy}$ and $\dot{\epsilon}_{yx}$ are equal because $\dot{\epsilon}_s$ is symmetric.

Analogous to the velocity (represented by a vector) with magnitude and direction, the strain rate (represented by a rank-2 tensor) has scalar invariants and distinguished directions. They are quantities that remain unchanged regardless of the reference system, and are therefore physically meaningful. Useful are the effective strain rate and principal strain rate axis.

The second invariant of the (surface) strain rate tensor $\dot{\epsilon}_s$, called *effective strain rate* and denoted by $\dot{\epsilon}_{II}$, is a measure of the total magnitude of the strain rate (analogous to speed). It has units of s^{-1} (or a^{-1}).

Effective strain rate

$$\dot{\epsilon}_{II}^2 := \frac{1}{2} \dot{\epsilon}_{ij} \dot{\epsilon}_{ij} \quad \Leftrightarrow \quad \dot{\epsilon}_{II}^2 := \frac{1}{2} [\dot{\epsilon}_{xx}^2 + \dot{\epsilon}_{yy}^2] + \dot{\epsilon}_{xy}^2. \quad (4.14)$$

Repeated indices imply the EINSTEIN summation convention. Exploiting the symmetry of the strain rate tensor, the shear strain rate components are gathered.

The (surface) strain rate tensor $\dot{\epsilon}_s$ is independent of the chosen coordinate system, only its representation in matrix form changes according to the chosen reference frame. There is a distinguished coordinate system oriented along the *principal strain rate axes* where the shear strain (off-diagonal) components vanish. The remaining (diagonal) components represent pure extension or contraction and are called *principal strain rates* $\dot{\epsilon}_1, \dot{\epsilon}_2$ (one subscript to differentiate the principal strain values from the normal strain components). This is mathematically equivalent to a diagonalisation of the strain rate tensor: It can be shown that any symmetric second-order tensor has two real eigenvalues, the principal strain rates, and two orthogonal (mutually perpendicular) eigenvectors, the principal strain rate axis.

In the two-dimensional case, the coordinate transformation is a simple rotation and concise formulae for the solutions to this eigenvalue problem exist. The principal angle θ_p gives the direction of $\dot{\epsilon}_1$, Eq. 4.15:

$$\tan(2\theta_p) = \frac{2\dot{\epsilon}_{xy}}{\dot{\epsilon}_{xx} - \dot{\epsilon}_{yy}}. \quad (4.15)$$

The eigenvalues are the solution to the characteristic equation $\det(\dot{\epsilon}_s - \dot{\epsilon}_i \mathbf{I}) = 0$:

$$\dot{\epsilon}_1, \dot{\epsilon}_2 = \frac{\dot{\epsilon}_{xx} + \dot{\epsilon}_{yy}}{2} \pm \sqrt{\left(\frac{\dot{\epsilon}_{xx} - \dot{\epsilon}_{yy}}{2}\right)^2 + \dot{\epsilon}_{xy}^2}. \quad (4.16)$$

In practice, the velocity gradients for the (surface) strain rate tensor $\dot{\epsilon}_s$ are calculated with central finite-difference scheme in the spatial domain. For example, the derivative of v_x at x_0 with respect to x is approximated by

$$\frac{\partial v_x(x_0)}{\partial x} \approx \frac{v_x(x_0 + \Delta x) - v_x(x_0 - \Delta x)}{2\Delta x}. \quad (4.17)$$

Δx is the length scale over which the velocity gradient is evaluated (“spacing”). However, the strain-rate errors $\Delta \dot{\epsilon}_{ij}$ for given velocity errors Δv in the raw data “increase with the inverse of the spatial distance Δh between data points” [Kääb et al., 1997]. For typical velocities and spacings, the strain-rate error is of the same order as the expected strain-rate values. Strain rates from long-wavelength velocity variations yield more accurate and reliable results, but must be extracted from the short-wavelength noise. The spatial averaging of the velocity field is performed in the spatial domain with a low-pass Gaussian filter. Computing finite differences from the smoothed velocity field in spatial domain is an approach equivalent to Wiener filtering in Fourier domain [Kääb et al., 1997].

4.4.6 Kinematic vorticity: hint at deformation mechanism

Any second-order tensor can be decomposed in a symmetric part $\text{sym}\{\nabla \mathbf{v}\} := \dot{\epsilon}$ and an antisymmetric part $\text{skew}\{\nabla \mathbf{v}\} := \boldsymbol{\Omega}$ such that $\nabla \mathbf{v} = \dot{\epsilon} + \boldsymbol{\Omega}$. As this decomposition is independent of the chosen reference frame, the components have a physical meaning: $\dot{\epsilon}$ is the strain-rate tensor related to deformation (Eq. 4.13), and $\boldsymbol{\Omega}$ is the vorticity tensor related to rotation. The vorticity tensor in two dimensions looks like [Schielicke et al., 2016]

$$\boldsymbol{\Omega} = \frac{1}{2} \begin{bmatrix} 0 & \zeta \\ -\zeta & 0 \end{bmatrix}, \quad \zeta = \left(\frac{\partial v_y}{\partial x} - \frac{\partial v_x}{\partial y} \right) \quad (4.18)$$

where the term $\zeta = \hat{\mathbf{k}} \cdot \nabla \times \mathbf{v}$, which is the vertical (third) component of the vorticity vector.

The *kinematic vorticity number* W_k is defined as the ratio of the tensor norms of $\mathbf{\Omega}$ and $\dot{\mathbf{\epsilon}}$ [Truesdell, 1953; Schielicke et al., 2016]:

Definition of W_k

$$W_k := \frac{\|\mathbf{\Omega}\|}{\|\dot{\mathbf{\epsilon}}\|} \quad (4.19)$$

with the invariant Euclidean tensor norms $\|\mathbf{\Omega}\| := \sqrt{\Omega_{ij}\Omega_{ij}}$ and $\|\dot{\mathbf{\epsilon}}\| := \sqrt{\dot{\epsilon}_{ij}\dot{\epsilon}_{ij}}$. (Again, EINSTEIN summation convention is implied, i.e. it is the root of the sum of its components squared).

In two dimensions and for an already solved eigenvalue problem (with eigenvalues $\dot{\epsilon}_1$, $\dot{\epsilon}_2$), then

Calculation of W_k

$$W_k = \frac{\|\mathbf{\Omega}\|}{\|\dot{\mathbf{\epsilon}}\|} = \frac{\sqrt{\zeta^2}}{\sqrt{\dot{\epsilon}_1^2 + \dot{\epsilon}_2^2}}. \quad (4.20)$$

The kinematic vorticity number is interpreted as the the ratio of the (local) rotation rate over (local) strain rate. W_k gives the relative contribution of the end-member cases pure shear and simple shear to the observed surface deformation (Table 4.3).

Interpretation of W_k

Table 4.3: Interpretation of kinematic vorticity number W_k [Schielicke et al., 2016; Fossen, 2010].

$W_k = 0$	pure shear
$0 < W_k < 1$	strain rate prevails over rotation rate (subsimpl shear)
$W_k = 1$	simple shear
$W_k > 1$	rotation rate prevails over strain rate

4.4.7 Slope–velocity relation

The strong topographic control (surface slope) on the creep behaviour as expected based on physical considerations (Eq. 2.5) is investigated with a average slope–surface velocity scatter plot [Frauenfelder et al., 2003; Bodin et al., 2018].

4.5 Numerical modelling

Main points



The thesis involves no drilling or geophysical subsurface investigations, the only information available is limited to the surface. The internal structure and mechanical properties (density and viscosity layering) are investigated with numerical modelling. It is an *inverse problem* where a proposed *a-priori* parametrisation m is refined with the observed surface velocity data until the modelled output d_{pred} matches the observed output d_{obs} within the uncertainty range. The “calculation engine” that produces the predicted data d_{pred} is called the *forward operator* G . Its discretised version \tilde{G} is implemented as a finite-element code.

Contribution of FEM

A series of numerical experiments using a finite-element modelling (FEM) code provides insights in material properties and deformation behaviour of the *Bleis Marscha* rockglacier. The following aspects are investigated:

- Interactions between rockglacier lobes: To what extent is the observed creep rate in the lower lobes owed to pushing by the overriding lobe above?)
- Material properties: How do the velocity differences between the different rockglacier bodies relate to the differences in mechanical properties (mostly effective viscosity)?
- A glimpse into the rockglacier: To what extent is it possible to constrain subsurface structure, for example the thickness?

Sketch of the problem

The problem is structured as follows (Figs. 4.9 and 4.10): We want to investigate parts of a physical system that are not directly accessible and observable, here the internal structure of the *Bleis Marscha* rockglacier. We have collected data, \mathcal{D} , that are relevant to the investigated property or behaviour, here surface velocity data that are an expression of the rockglacier creep. Next, we develop a plausible subsurface structure, \mathcal{M} , based on *a-priori* information, devise a “calculation machine” that predicts data d_{pred} , and compare these modelled data with the observed data d_{obs} . If d_{pred} and d_{obs} do not agree within their uncertainty margins, \mathcal{M} is modified until some chosen measure for the difference between d_{pred} and d_{obs} falls below a chosen threshold. This iterative procedure is nothing else than solving an inverse problem. In a last step, the geophysicist should not fail to discuss the link between “nature” and the model components, which are only an abstract, simplified representation of the real world (appraisal problem).

The “calculation machine” is called *forward operator* G that mathematically describes the deformation of the rockglacier material (Fig. 4.10). For a set of given model parameters m , describing the internal structure, it computes the observable horizontal surface velocity field, d . This is symbolically written as

$$G(m) = d. \quad (4.21)$$

In essence, the forward problem is broken down to a STOKES problem with a linear stress-strain rate relationship (NEWTONIAN fluid).

4.5.1 Physics and rheology

The motion of an incompressible Newtonian fluid is described by the NAVIER-STOKES equations. It establishes a relationship between inertia, divergence of stress and applied

Physical basis for the continuous forward operator G

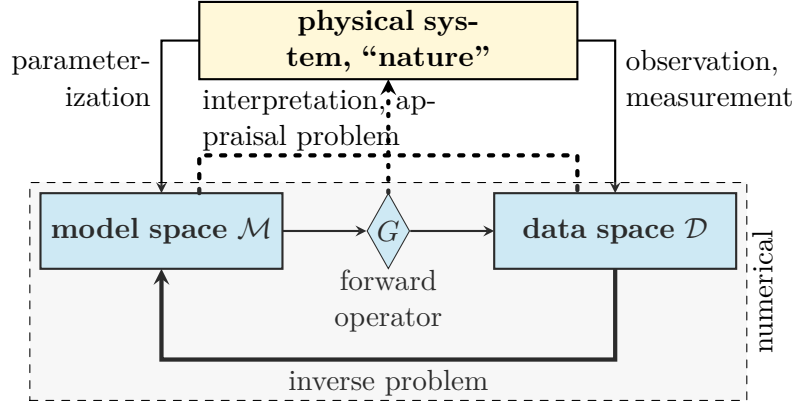


Figure 4.9: Inverse problem structure [redrawn after Felix Bissig, unpub. MSc thesis].

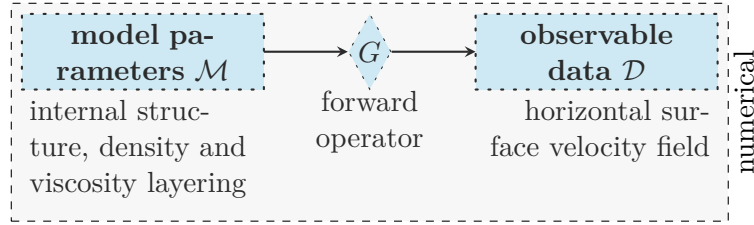


Figure 4.10: Forward problem structure: The model parametrisation \mathcal{M} is an abstract description of the rockglacier in terms of its mechanical properties that are related to the observed data \mathcal{D} via the forward operator G .

external forces for a fluid. The non-linear vector-valued equations for the velocity field \mathbf{v} can be simplified for a fluid flow where the inertial forces are negligibly small compared to the viscous momentum diffusion. For this *order-of-magnitude analysis*, the dimensionless Reynolds number Re defined as the ratio of inertia term to viscous term is calculated by plugging in characteristic down-slope velocity U , typical rockglacier thickness H , length L , density ρ and dynamic viscosity μ (viscosity of pure ice as a conservative estimate) in the corresponding terms of the NAVIER-STOKES equation:

$$Re = \frac{\rho |\mathbf{v} \cdot \nabla \mathbf{v}|}{\mu |\nabla^2 \mathbf{v}|} \stackrel{2D}{=} \frac{\rho v_x dv_x / dx}{\mu d^2 v_x / dz^2} \approx \frac{\rho U^2 / L}{\mu U / H^2} = \frac{\rho U H^2}{\mu L} \quad (4.22)$$

$$\sim \frac{2 \cdot 10^3 \text{ kg/m}^3 \cdot 1.6 \cdot 10^{-8} \text{ m/s} \cdot (30 \text{ m})^2}{2 \cdot 10^{13} \text{ Pa s} \cdot 10^3 \text{ m}} \approx 10^{-18}$$

The inertia term is evaluated along the creep in down-slope direction, while the viscous term, responsible for the vertical velocity profile, is evaluated across the flow in vertical direction. Since $Re \ll 1$, the inertia term is negligible compared to the viscous term and the problem can be considered a *low Reynolds number flow* governed by the STOKES equation [Loewenherz et al., 1989].

Rockglaciers move slowly enough that they can be considered in *static equilibrium* at any time, even while in motion: The sum of all forces is essentially zero. The *force balance* or conservation of linear momentum equations (Eq. 4.23) describe how body forces and boundary stresses are balanced by stress gradients throughout the body. For the *two-dimensional vertical plane-flow model*, the equations (in two different notations) read

[Frehner and Schmalholz, 2006]:

$$\begin{aligned} \frac{\partial \sigma_{xx}}{\partial x} + \frac{\partial \sigma_{xy}}{\partial y} &= 0 \\ \frac{\partial \sigma_{xy}}{\partial x} + \frac{\partial \sigma_{yy}}{\partial y} &= -\rho g \end{aligned} \quad \Leftrightarrow \quad \nabla \cdot \boldsymbol{\sigma} + \rho \mathbf{f} = \mathbf{0}. \quad (4.23)$$

complemented by the conservation of angular momentum that requires

$$\sigma_{ij} = \sigma_{ji} \quad \Leftrightarrow \quad \boldsymbol{\sigma} = \boldsymbol{\sigma}^T. \quad (4.24)$$

The second-order stress tensor $\boldsymbol{\sigma}$ contains normal components σ_{xx} and σ_{yy} and shear components $\sigma_{xy} = \sigma_{yx}$, which are identical due to the symmetry of $\boldsymbol{\sigma}$. The force vector \mathbf{f} contains the gravitational acceleration g , directed vertically downwards. ∇ denotes the nabla operator.

The *conservation of mass* for an incompressible material implies a divergence-free flow field,

$$\frac{\partial v_x}{\partial x} + \frac{\partial v_y}{\partial y} = 0 \quad \Leftrightarrow \quad \nabla \cdot \mathbf{v} = 0, \quad (4.25)$$

where v_x and v_y are the horizontal and vertical components of the vectorial velocity field \mathbf{v} , respectively.

Constitutive relation

The *constitutive equation* establishes the relation between stress and strain rate, i.e. characterises the rheological behaviour of the material. It is specific to the material under certain conditions, and unlike the conservation equations not an universally valid law.

The deformation of an incompressible material is not affected by hydrostatic pressure. The stress-deviator components are obtained by subtracting the magnitude of the hydrostatic pressure (the mean normal stress, σ_m) from each normal-stress component:

$$\sigma'_{ij} := \sigma_{ij} - \frac{1}{3} \sigma_{kk} \delta_{ij} \quad \Leftrightarrow \quad \boldsymbol{\sigma}' := \boldsymbol{\sigma} - \sigma_m \mathbf{I} \quad (4.26)$$

where the EINSTEIN summation convention is implied (e.g. $\sigma_{kk} = \sigma_{xx} + \sigma_{yy}$), δ_{ij} is the Kronecker delta, and \mathbf{I} the identity matrix.

A NEWTONIAN fluid is defined by a linear stress-strain rate relationship with the *dynamic viscosity* μ as the proportionality factor. It is invariant to applied stresses or experienced strain rate. The often strong (exponential) temperature dependence is neglected. NEWTON's law of viscosity relates each components of the deviatoric stress tensor σ'_{ij} to the corresponding component of the strain rate tensor $\dot{\epsilon}_{ij}$

$$\sigma'_{ij} = 2\mu \dot{\epsilon}_{ij} \quad \Leftrightarrow \quad \boldsymbol{\sigma}' = 2\mu \dot{\boldsymbol{\epsilon}}. \quad (4.27)$$

The dynamic viscosity μ is a constant scalar that relates two rank-2 tensors. This implies (i) homogeneity (invariance under translation): the heterogeneous debris-ice mixture is approximated as a continuum with constant (effective) material properties; and (ii) isotropy (invariance under rotation): each strain-rate component is proportional to the corresponding stress-deviator component at any point. In other words, stress and strain rate are collinear (shear stress leads to shearing strain rate, etc.).

Finally, the *kinematic relation* defines the strain rate tensor $\dot{\epsilon}_{ij}$ in terms of velocity gradients as

$$\dot{\epsilon}_{ij} = \frac{1}{2} \left(\frac{\partial v_i}{\partial x_j} + \frac{\partial v_j}{\partial x_i} \right) \quad \Leftrightarrow \quad \dot{\boldsymbol{\epsilon}} = \frac{1}{2} \left(\nabla \mathbf{v} + (\nabla \mathbf{v})^T \right). \quad (4.28)$$

4.5.2 Forward problem: Numerical implementation of FEM algorithm

The set of partial differential equations (PDEs, Eqs. 4.23–4.28) are recast and solved numerically with the finite-element code developed in Frehner et al. [2015].

Discrete forward operator
 \bar{G}

Numerically solving the incompressibility equation (Eq. 4.25) can in practice lead to unphysical results [Pelletier et al., 1989]. By relaxing the incompressibility constraint for now, and allowing the divergence of the velocity field to deviate slightly from zero, the problem is circumvented. Eq. 4.25 is thus rewritten as

$$\frac{\partial p}{\partial t} = -K \left(\frac{\partial v_x}{\partial x} + \frac{\partial v_y}{\partial y} \right) \Leftrightarrow \frac{\partial p}{\partial t} = -K (\nabla \cdot \mathbf{v}), \quad (4.29)$$

where the penalty parameter K is the mathematical pendant of the elastic incompressibility (bulk modulus), and p is pressure. As mass conservation in each element is violated, incompressibility must later be re-introduced. The governing set of equations to be solved numerically for the three unknowns v_x , v_y and p is in the form

$$\mathbf{B}^\top \mathbf{D} \mathbf{B} \mathbf{v} - \nabla p = 0 \quad (4.30a)$$

$$\frac{\partial p}{\partial t} = -K (\nabla \cdot \mathbf{v}), \quad (4.30b)$$

where the matrix \mathbf{B} contains the spatial derivatives and the “rheology matrix” \mathbf{D} expresses the stress-strain rate relationship:

$$\mathbf{B} = \begin{bmatrix} \frac{\partial}{\partial x}(\cdot) & 0 \\ 0 & \frac{\partial}{\partial y}(\cdot) \\ \frac{\partial}{\partial y}(\cdot) & \frac{\partial}{\partial x}(\cdot) \end{bmatrix}, \quad \mathbf{D} = \begin{bmatrix} \frac{4}{3}\mu & -\frac{2}{3}\eta & 0 \\ -\frac{2}{3}\mu & \frac{4}{3}\mu & 0 \\ 0 & 0 & \mu \end{bmatrix}. \quad (4.30c)$$

Temporal derivatives are approximated with finite differences. The velocity field within each element is interpolated from a set of bi-quadratic and continuous shape functions, whereas the pressure shape functions are linear and discontinuous over the element boundary. A 7-node triangular element with 7 integration points is used (Fig. 4.11a). Eqs. 4.30a–4.30b are multiplied with weight functions equal to the the corresponding shape function (*Galerkin method*, Fig. ??) and integrated numerically with the GAUSS-LEGENDRE scheme (Fig. 4.11b), yielding the weighted residuals or *discrete weak form*. They are set to zero, and the continuous velocity and pressure field are discretized. The system of discrete equations is solved simultaneously by standard linear algebra techniques to yield nodal velocities. Incompressibility is enforced with a *penalty approach* where the elastic compression is removed iteratively: The *Uzawa algorithm* yields a quasi-incompressible discrete pressure field, where the divergence of the velocity field is smaller than a chosen threshold value, usually $\mathcal{O}(10^{-10})$.

Discretization

Uzawa algorithm

The triangular mesh is generated with the software “Triangle” [Shewchuk, 1996]. Remeshing is done as soon as any internal angle of any element in the model becomes smaller than 12° .

Mesh generation

4.5.3 Rockglacier parameterisation: Boundary conditions, initial conditions and material parameters

There are two common types of boundary condition that are enforced on a nodal level: DIRICHLET boundary condition where the value at the node is prescribed, or NEUMANN boundary condition, where the first derivative at the node is fixed. It is important to note

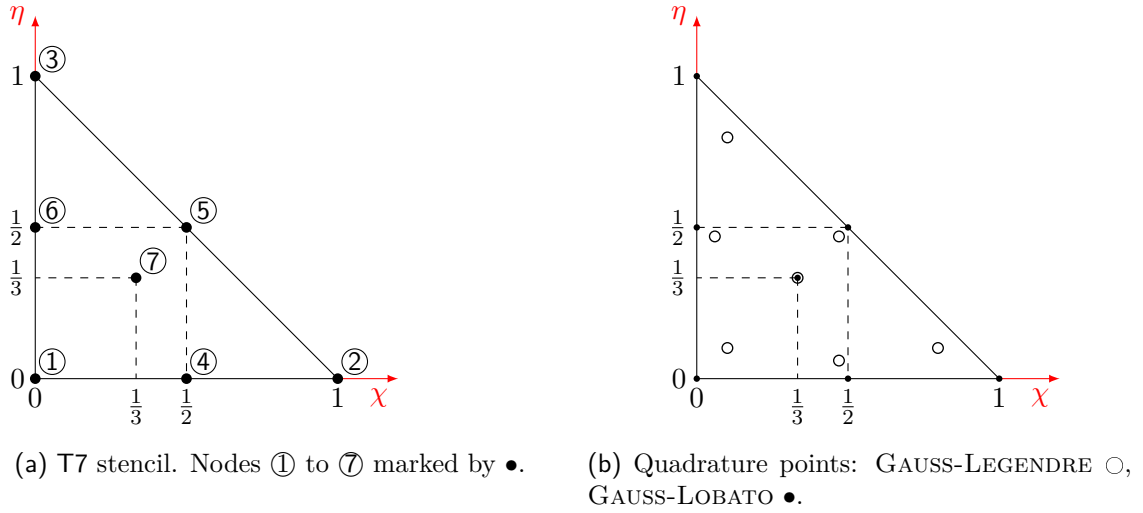


Figure 4.11: Discretisation of space in local χ - η coordinate system. (a) 7-node triangular T7 stencil. (b) numerical integration points

that in the discretization step, integration by parts invoking GREEN'S theorem is done to obtain the weak form. Often, boundary terms arising from the integration by parts are neglected, and NEUMANN boundary conditions are then implicitly assumed.

The **model boundaries** are defined such that the dynamic (deforming) layers of the permafrost body is within the model domain (Table 4.4): The rockglacier is bounded by its surface to the atmosphere and a transition to immobile material at the base. Mechanically, the surface or **top boundary** is a **free surface** and characterised by zero traction and zero boundary-perpendicular normal stress. At the base or **bottom boundary**, the boundary to the immobile layer below (be it bedrock or non-creeping sediments, Figs. 2.11, 2.12), a **no-slip boundary condition** is imposed (Fig. 4.12, Table 4.4).

The complex stratigraphy and internal structure of the rockglacier is translated into a simplified, abstract representation that captures the characteristic mechanical features and properties. This computationally tractable mechanical model is referred to as *parameterisation*, and is passed to the FEM algorithm as *initial conditions*.

A parameterisation of the internal structure draws from the following sources: (i) The surface microrelief is shaped by creep processes and thus an expression of the internal structure, e.g. shear horizons crop out at the base of scarps; (ii) geophysical investigations (seismic or GPR sections) of morphologically similar rockglaciers serve as an analogue; and (iii) physical constraints such as minimum thickness for the creep threshold to be overcome or e.g. empirical scaling laws.

The density of the debris-ice mixture in the rockglacier core is the weighted average of the density of its constituents, debris and ice:

$$\rho_{rgl} = (1 - c_{ice}) \rho_{debris} + c_{ice} \rho_{ice}, \quad (4.31)$$

where c_i is the volume fraction of ice; $c_i = 0.6$ [Müller et al., 2016]. The density is assumed to remain constant in space and time (incompressible, no phase changes between ice and liquid water, constant air fraction). Inserting literature values of 2700 kg m^{-3} for the density of granite, 910 kg m^{-3} for the density of pure ice yields $\rho_{rgl} \sim 1626 \text{ kg m}^{-3}$. The density of the boulder mantle depends on the volume fraction of the voids. With 30 to

40% vol air, $\rho_m \sim 1620\text{--}1890 \text{ kg m}^{-3}$ [Barsch, 1996, p. 101]. The density contrast between boulder mantle and core vanishes for more than 40% vol voids.

The viscosity of a debris-ice mixture is difficult to estimate, particularly for temperatures close to 0°C where liquid water plays an important role [Moore, 2014]. Here, a simple approach will suffice to get an order of magnitude for the initialisation of the model. The viscosity is an output of the model. The viscosity of a suspension is greater than the viscosity of its pure solvent. Roscoe [1952] proposed the following formula based on EINSTEIN’s effective viscosity for a dilute suspension of spheres [Einstein, 1905], cf. [Friedson and Stevenson, 1983].

$$\frac{\mu_{susp}}{\mu_{solv}} := \mu_r = (1 - \phi)^{-2.5}, \quad \phi \lesssim 0.65. \quad (4.32)$$

ϕ is the debris volume fraction, $\phi = 1 - c_i = 0.4$. The dynamic viscosity of pure glacier ice is (very) roughly $\mu_{solv} = 2 \cdot 10^{13} \text{ Pa s}$ [Cuffey and Paterson, 2010, p. 269].

The density and dynamic viscosity values as a function of space are initialised onto the quadrature points via easily implementable Gauss error functions (bottom panel in Fig. 4.12). The values for each element is the average of the values on its integration points, computed in the “element loop” step.

Effective viscosity μ of a debris-ice mixture

Initialisation functions

Table 4.4: Rockglacier interfaces (physical) and boundaries (in model domain). Cf. Fig. 4.12.

Interface	Characteristics	Mechanical behaviour along interface
surface to atmosphere	material contrast	traction free
base over immobile till or bedrock	viscosity contrast	no slip or low-viscosity shear zone
boulder mantle–frozen core	fabric difference	welded/dynamically coupled: no slip [Ikeda et al., 2008]
Boundary	Equivalent interface	Boundary condition
top boundary	surface	free surface
bottom boundary	base	no slip

A possible internal structure of the *Bleis Marscha* rockglacier is drawn in Fig. 4.12. The surface boundary is the well-constrained surface relief along a longitudinal profile, extracted from the DEM as a swath profile with *TopoToolbox* (Section ??). In contrast to the bedrock surface, which might be over-deepened and thus impossible to constrain without geophysical investigations, the base of the dynamic layers of the rockglacier, the shear horizon, can reasonably be drawn: A smoothed DEM of the rockglacier surface, created by interpolating the contour lines within the rock glacier perimeter, serves as a topographic model for the rockglacier base (cf. Scapozza et al. [2014]). However, this is only possible for the lower part where the rockglacier rises above the adjacent terrain. In the cirque, the base is assumed to run parallel to the average surface topography (Figs. in Barsch [1992]; Hausmann et al. [2007]; Monnier et al. [2011, 2014]; Merz et al. [2015]; Buchli et al. [2018]). The intact lobes are further divided into a two-layer structure composed of a clast-supported boulder mantle and a matrix-supported (\sim frozen) core [e.g. Barsch, 1996; Haeberli et al., 2006]. Theoretical considerations [Moore, 2014] and

Initial conditions: structure, density, effective viscosity

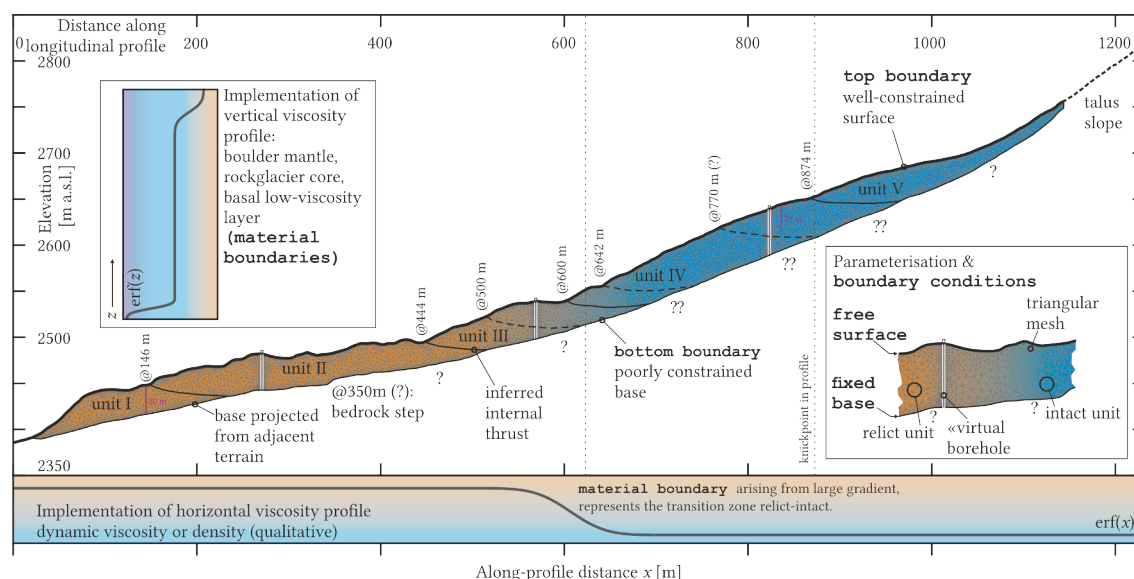


Figure 4.12: Rockglacier parameterisation: From observations to a mechanical model that is simple yet captures the essential features. **Top panel:** Longitudinal section through the rockglacier showing a possible mechanical structure. Based on morphological observations, a relict high-viscosity lower part and an intact low-viscosity upper part is implemented. The vertical layering with boulder mantle and basal shear zone is not drawn. The triangular meshing (fine grey lines) is denser along the “virtual boreholes”. **Bottom panel and top panel inset:** *Initialisation functions* for the material parameters. Density and viscosity variations in along-flow as well as in vertical direction are described with error functions.

observations [Arenson et al., 2002; Springman et al., 2012] agree that the boulder mantle is much less susceptible to creep and can be modelled with a high-viscosity layer passively riding on the viscously deforming core (Fig. 2.11). These interfaces are perfectly welded (Table 4.4). The thrusts are drawn based on recently published GPR-derived longitudinal sections of the multi-lobe *Furggwanhorn* rockglacier [Merz et al., 2015; Buchli et al., 2018]. According to this *thin-skinned model* borrowed from tectonics, thrusts between the different units cut down to the main basal shear horizon. This implies that the thrusts are secondary features: Rockglaciers advance only as long as there is a continuous supply of scree [e.g. Degenhardt, 2009], i.e. they do not creep downslope as a body detached from the talus.

4.5.4 Inverse Problem: Towards plausible subsurface structures

The inverse problem can be formulated as: Find geologically acceptable subsurface structures that satisfy the STOKES flow and reproduce the data within their uncertainty margins.

The problem is solved heuristically inspired by the concepts and notation of probabilistic inverse theory [Tarantola, 2005], however without systematically exploring the parameter space.

The degree of complexity of the problem is massively reduced by assigning the following parameters, termed “fixed parameters”, a given value that is used in all model runs:

- rockglacier surface z_s [m]: the initial surface topography is well-constrained by the available DEM.

- rockglacier base and hence the thickness [m]: In the lower part, where the rockglacier body rises above the adjacent terrain, the base is projected from the surrounding area. This gives a thickness of roughly 40 m, that was simply kept constant based on the mass conservation principle. Towards the talus, the rockglacier becomes gradually thinner.
- thickness of basal shear zone [m]: 3 m thick, from several borehole deformation measurements.
- viscosity contrast between rockglacier core and the low-viscosity basal shear layer: The basal shear zone is assumed to be 10 times less viscous than the rockglacier core (a conservative estimate [Kannan and Rajagopal, 2013]).
- thickness of boulder mantle [m]: 5 m thick, from field observations of the front scarps where the rockglacier stratigraphy is exposed.
- viscosity contrast between rockglacier core and the boulder mantle: The boulder mantle is assumed to be 21 times more viscous with respect to the core. The value is inferred from the dominant wavelength of the furrow-and-ridge microrelief (Section 5.1.3, Frehner et al. [2015]).

The “tuning parameters”, density and viscosity distribution, are fitted to the data.

- viscosity distribution: The dynamic viscosities of different rockglacier parts are defined with respect to the rockglacier core viscosity (“reference viscosity”), which ultimately controls the overall magnitude of deformation. Both along-flow and vertical variations are implemented with the initialisation functions (Fig. 4.12).
- density distribution: Likewise, the (absolute) density distribution is set up with the initialisation functions.

In summary, the outline or “envelope” of the rockglacier with thickness as well as surface and basal slope is given. The fit to the data is essentially achieved by adjusting the viscosity and density distributions. Large gradients in material parameters effectively introduce internal boundaries, although they are not explicitly implemented as such (e.g. high viscosity contrast 3 m below the surface represents the interface between boulder mantle and core). These **material boundaries** are advected with the deforming model boundary they are attached to (e.g. base of boulder mantle follows the top boundary) (Fig. 4.12).

5 Results

5.1 Field work and DEM analysis: Geomorphology

Main points
<p>The <i>Bleis Marscha</i> rockglacier is a 1-km long, multi-unit talus rockglacier with an intact upper part that overrides a relict lower part. It originates in a NNW-facing cirque of <i>Piz Bleis Marscha</i> that until recently accomodated a small cirque glacier. The inner front scarp that separates the rockglacier into the units is at an altitude of ~2500 m a.s.l. Field observations suggest that each unit had its own activity phase (different “generations”). The rockglacier is almost completely surrounded by recent talus or debris flow deposits. It is therefore not possible to establish in the field a relative age relationship between glacial processes related to the <i>Bleis Marscha</i> cirque glacier and the periglacial processes related to the <i>Bleis Marscha</i> rockglacier.</p>

5.1.1 Val d’Err

Glacial & periglacial
landforms

In the *Val d’Err*, glacial and periglacial processes shaped the landscape during the latest Pleistocene and Holocene: In the trough valley, several moraine ridges, moraine ramparts and hummocky terrain witness the past ice cover and at least three glacier re-advances (NOT necessarily linked to three different cold phases): Slightly ascending lateral moraines (up to two individual ridges) run along the trough shoulder on both valley sides at *Parset-tens* (Fig. 5.2) and *Salteras*. They are densely vegetated, smoothed, and only large blocks stick out. Huge moraine ramparts at the valley head (Fig. 5.1) are undoubtedly related to the Little Ice Age re-advance of the *Vadret d’Err*. Rockglaciers, solifluction and ploughing blocks [Schwarz-Zanetti, 1983] are common, which shows that above 2400 m a.s.l., the ground is still extensively frozen (Fig. 3.7). No traces of now relict rockglaciers that developed in the Early Lateglacial (i.e. pre-Younger Dryas [Ivy-Ochs, 2015]) are found. The influence of the lithology on weathering, permafrost occurrence and transport mechanisms can be beautifully observed: All rockglaciers have their root zone in the crystalline, weathering-resistant Err unit that forms coarse debris susceptible to permafrost (Fig. 5.3). In contrast, the weathering-prone rock types like schists, radiolarites and ophiolites disintegrate, form round, smooth hills which are overall more densely vegetated and grassy. No creep features have developed at the talus foots. This hints at more important role of liquid water for mass transport and at the absence of permafrost [Boeckli et al., 2012]. Also larger scale mass wasting processes are particularly intensive in areas of weathering-prone rock types like schists and radiolarites: Post-glacial, slow gravitational ridge-spreading movement (*sackung*) can be observed at the NE flank of *Carungas* [cf. Cornelius, 1951, p. 35]. In locality *Bleis Marscha* (“rotting, steep grass-overgrown slope” [A. Janett, pers. comm.], Frauenfelder et al. [2005]) below the like-named peak, debris flows have cut a deep gully into the talus, and the debris fan extends far onto the glacial till on the valley floor.



Figure 5.1: Piz d'Err, view to SSE. The glacier at the valley head between *Piz d'Err* and *Piz Jenatsch* has retreated from the huge moraine rampart in the last 80 years. In the foreground, the lowermost part of the *Bleis Marscha* rockglacier.



Figure 5.2: Glacial landforms at *Parsettens*: lateral moraines (Egesen?). View from *Salteras* towards SW.

5.1.2 *Bleis Marscha* rockglacier

According to the (field) classification scheme proposed by Barsch [1996], the *Bleis Marscha* rockglacier is a talus rockglacier originating in a north-facing cirque of *Piz Bleis Marscha* with direct connection to the talus slope. The rockglacier is approximately 1200 m long and 210 m wide. It has a subdued to well-developed surface microrelief, and a blocky surface mainly of Err granite boulders. It is a complex, multi-unit tongue-shaped rockglacier of medium size (“polymorphic” *sensu* Frauenfelder and Käab [2000]). Field observations as well as feature tracking preliminary results indicate that the upper units are still active, while the lower ones (below 2500 m a.s.l) are inactive to relict.

A peculiarity of the *Bleis Marscha* rockglacier are the inner front scarps or slopes. Four of them are over-steepened, show signs of recent failure, and expose the fine material beneath the boulder mantle. This indicates that an upper lobe is overriding the lower part of the rockglacier — there must be “differences in activity which allow the development of shearing planes along which the overriding takes place” [Barsch, 1996, p. 162]. The *Bleis Marscha* rockglacier is thus divided in a sequence of five *units* (in the strict sense of

“Taxonomy”

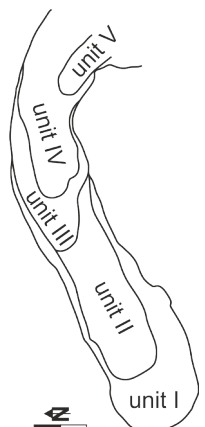




Figure 5.3: Periglacial landforms: Smaller rockglaciers at *Castalegns*. Their root zones are in the crystalline Tschirpen unit. In the ophiolitic units towards *Furschela da Colm* (right), no debris accumulations have formed. Remaining firn field NW of Piz d'Err. View towards SW.

Barsch [1996]).

The *Bleis Marscha* rockglacier emanates from a NNW-facing cirque below *Piz Bleis Marscha* (3127 m a.s.l.). The debris is predominantly supplied by weathering of the granitic headwall of the Middle Err unit. The “small ice patch” mentioned by Frauenfelder et al. [2005] has meanwhile disappeared, and no surface ice is visible in the cirque. The smooth, unstructured talus gradually passes into a clearly delimited, small rockglacier (unit V) at an altitude of 2700 m. In the upper units, the rocks look quite “fresh” and less weathered. The rockglacier turns left to WSW-direction and doubles its width to 150 m as it leaves the cirque. Several lobes are superimposed and the microrelief becomes more accentuated with a set of parallel longitudinal furrow and ridges, whose amplitude rarely exceeds 2 m. An edge is covered by radiolarite rock fall debris from the headwall in the Lower Err unit (Fig. 5.4). The blocky surface mainly consists of granite, followed by radiolarite and dolomite boulders with typical volumes of 0.5–50 m³. A few huge granite blocks >10 m edge length are scattered over the rockglacier. Weathering-prone lithologies such as *rauhwacke* (cellular dolomite), conglomerate, limestone and shales are only rarely found. The dominance of Err granite (> 80 vol%) even increases towards the front. At the scarps, the two-layered stratigraphy of a coarse, clast-supported blocky mantle over a finer, matrix-supported core is exposed (thickness of 3–5 m, Fig. 5.5). The lower units II and I are marked by signs of settling, inactivity and weathering such as vegetated patches (soil formation), lichen cover, iron staining and weathering rinds. A mature furrow-and-ridge microrelief has formed, with crescent-shaped ridges separated by 5 m deep furrows. The rockglacier is bordered by an outer ridge and a stable, vegetated slope except at the lowermost front, where ongoing collapses expose the fine material. The snout, roughly 30 m high, ends just at the edge of the *Salteras* terrace at an elevation of 2380 m a.s.l.

Some lateral ridges at a first glance resemble moraines (and indeed have been mapped as such [Frauenfelder et al., 2001]; “tongue lies within two lateral moraines which are supposed to be from a Younger Dryas glacier advance” in Laustela et al. [2003]; Fig. 5.6). However, they can be “an expression of the cohesive flow” in [Barsch, 1996, p. 218] and are not necessarily a glacial feature, even when the cirque was once glacierised. The outer grassy ridge (Fig. 5.6) that borders the lower rockglacier lobe is simply the margin of the relict unit I. Since the ice content decreases towards the margin, they even have become more prominent due to melting of the ice.

An imaginary hike on the
Bleis Marscha
rockglacier

Problem of
lateral moraines



Figure 5.4: Radiolarite rockfall deposits on the otherwise granite-covered rockglacier. View towards NNE.



Figure 5.5: Oversteepened, unstable front of unit IV, allowing a glimpse into the two-layered stratigraphy. View towards NE (up-slope).



Figure 5.6: Longitudinal ridges on unit I (outer grassy ridge) and unit II (inner bouldery ridge). The outer slope is at the angle of repose (35-40°).

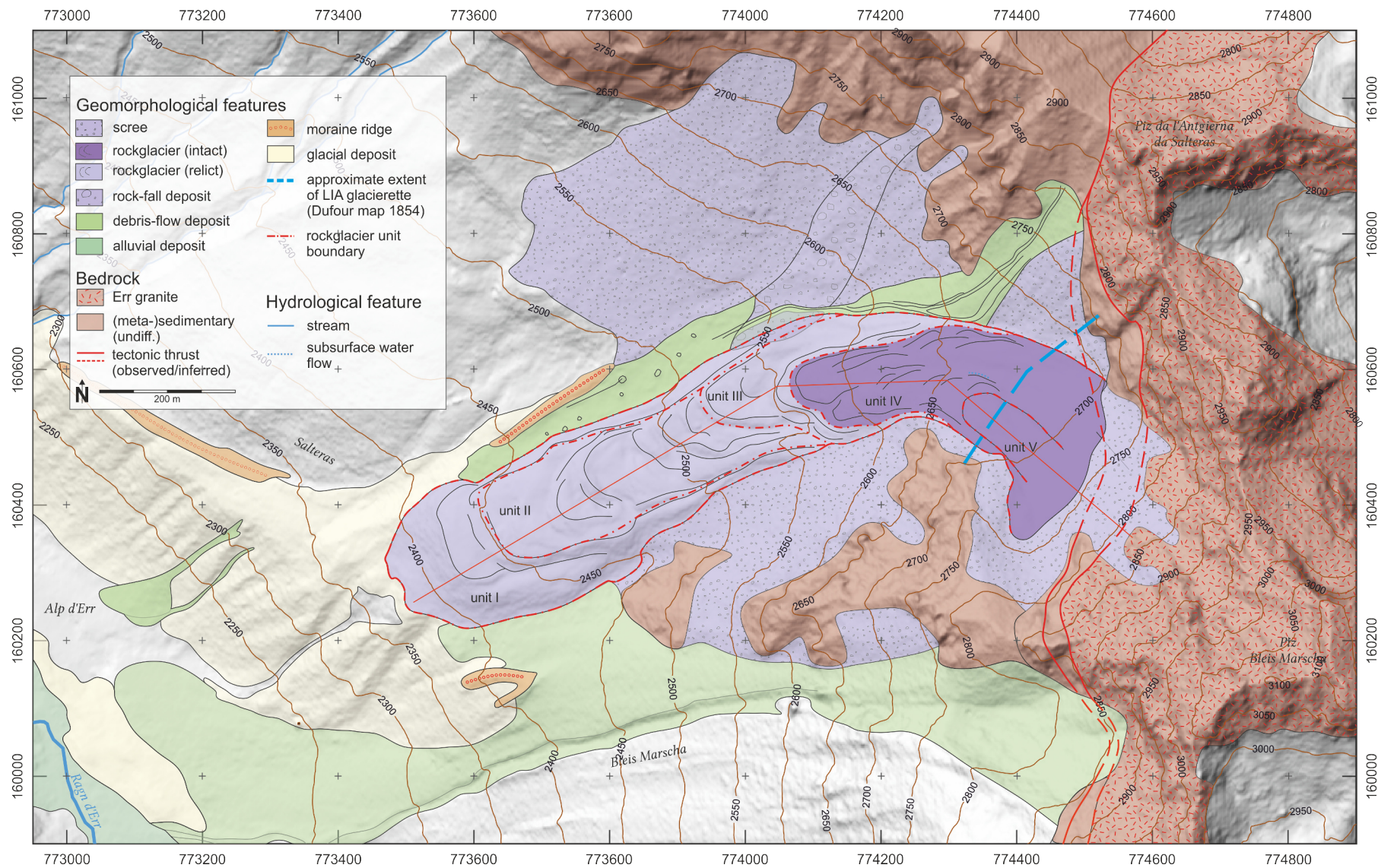


Figure 5.7: Morphological sketch map.

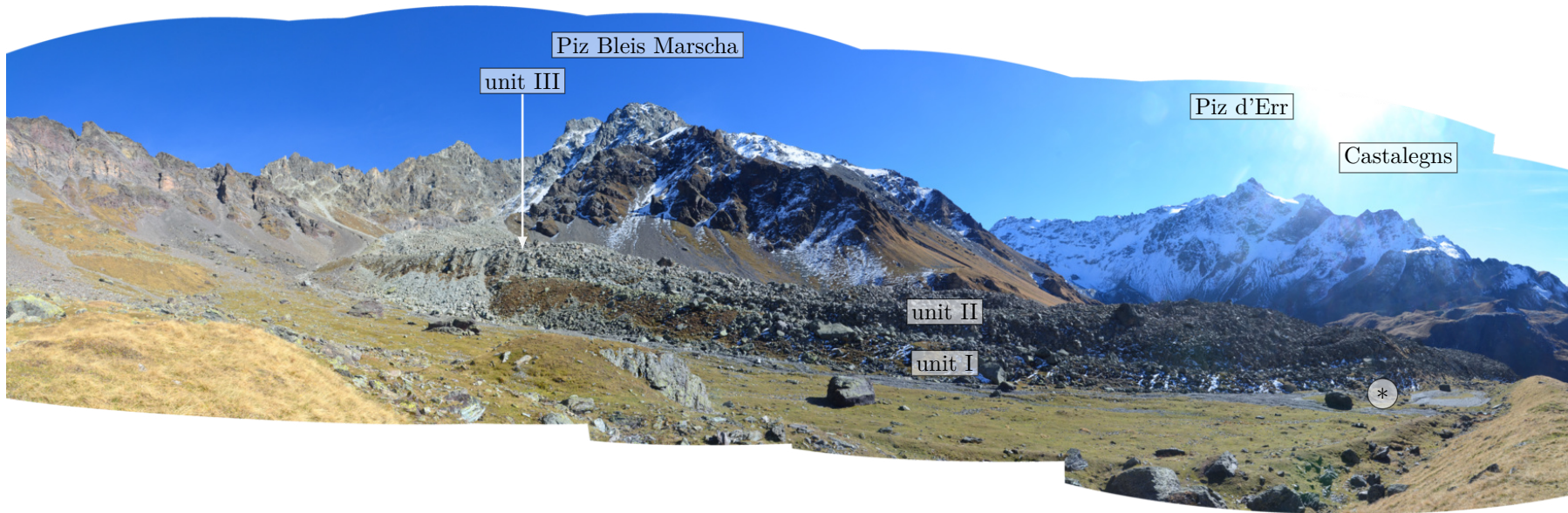


Figure 5.8: Panorama view from the lateral moraine towards SE showing the entire rockglacier, composed of multiple units overriding each other. Units I–III are tagged, the upper units IV–V and the north-facing cirque beneath *Piz Bleis Marscha* are not visible. Note the lateral boulder apron between the rockfall deposits (Figs. 5.9, 5.10) and the frontal thrust of unit III. For scale, the rockglacier stands roughly 30 m above the adjacent terrain. Photo taken Oct 14, 2017. (For comments on the smooth plain between the moraine and the rockglacier, cf. Fig. 5.13. Vantage point marked by *).

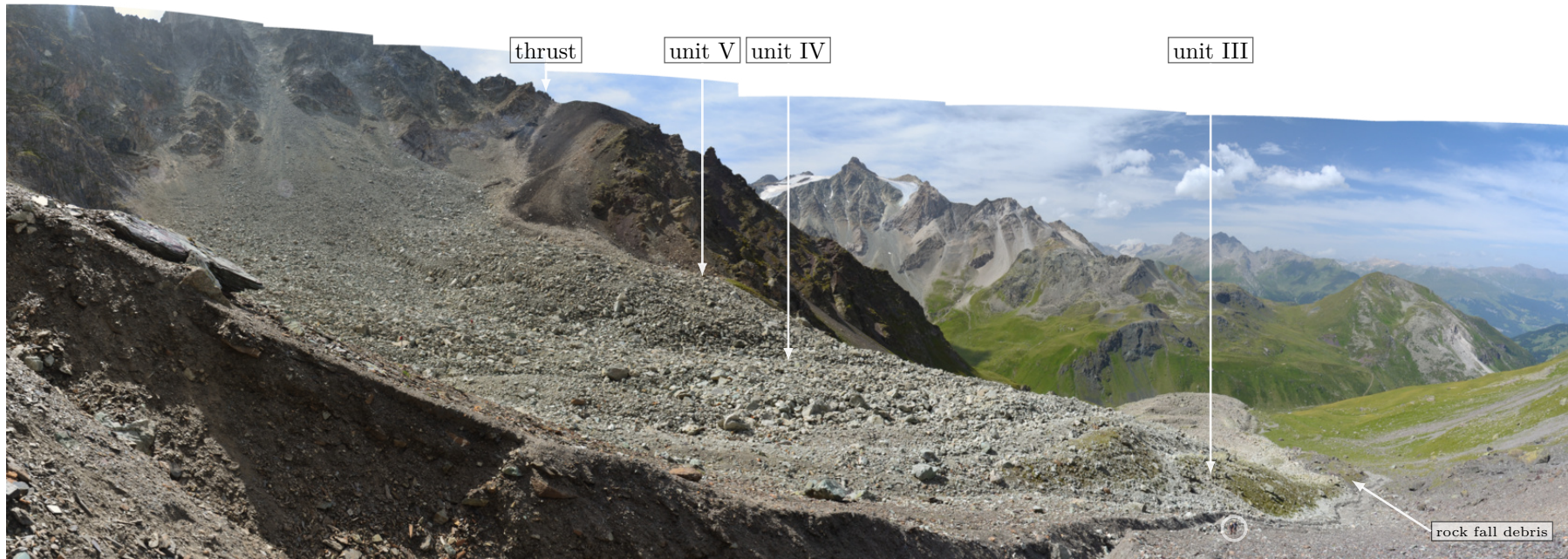


Figure 5.9: View into the cirque and onto the uppermost units IV–V from a nearby debris cone. The thrust between the Lower and Middle Err unit, here separating the sedimentary from the crystalline units of the Err nappe, runs across the cirque towards Piz da l’Antgierna da Salteras. A small ice patch that was still visible in 2005 [Frauenfelder et al., 2005] has disappeared by 2017. The sound of running water on unit V hints at melting subsurface ice. We do not know its source and flowpaths. Despite the very recent glaciation of the cirque, no signs of glacial activity (depositional like moraines or erosional like depressions) are observable: The talus passes into the rockglacier root zone. The debris flow channel runs along the rockglacier, and its levees are deposited on radiolaritic debris derived from slopes below *Piz da l’Antgierna da Salteras*. The rockglacier coarse-debris transport system has a well-defined source in the back of the cirque and is afterwards not connected laterally to the adjacent terrain. No debris from the flanking slopes has been incorporated in the rockglacier (apart from what had been deposited before the rockglacier advanced). The rightmost corner of the rockglacier is covered by dark radiolarite deposits from a rock fall (cf. Fig. 5.10), later eroded and overprinted with light-coloured debris from the debris flows. View is to S. Photo taken Aug 3, 2017. Hiking geologists for scale (white circle), beeline distance across the cirque to the thrust trace is ~500 m.

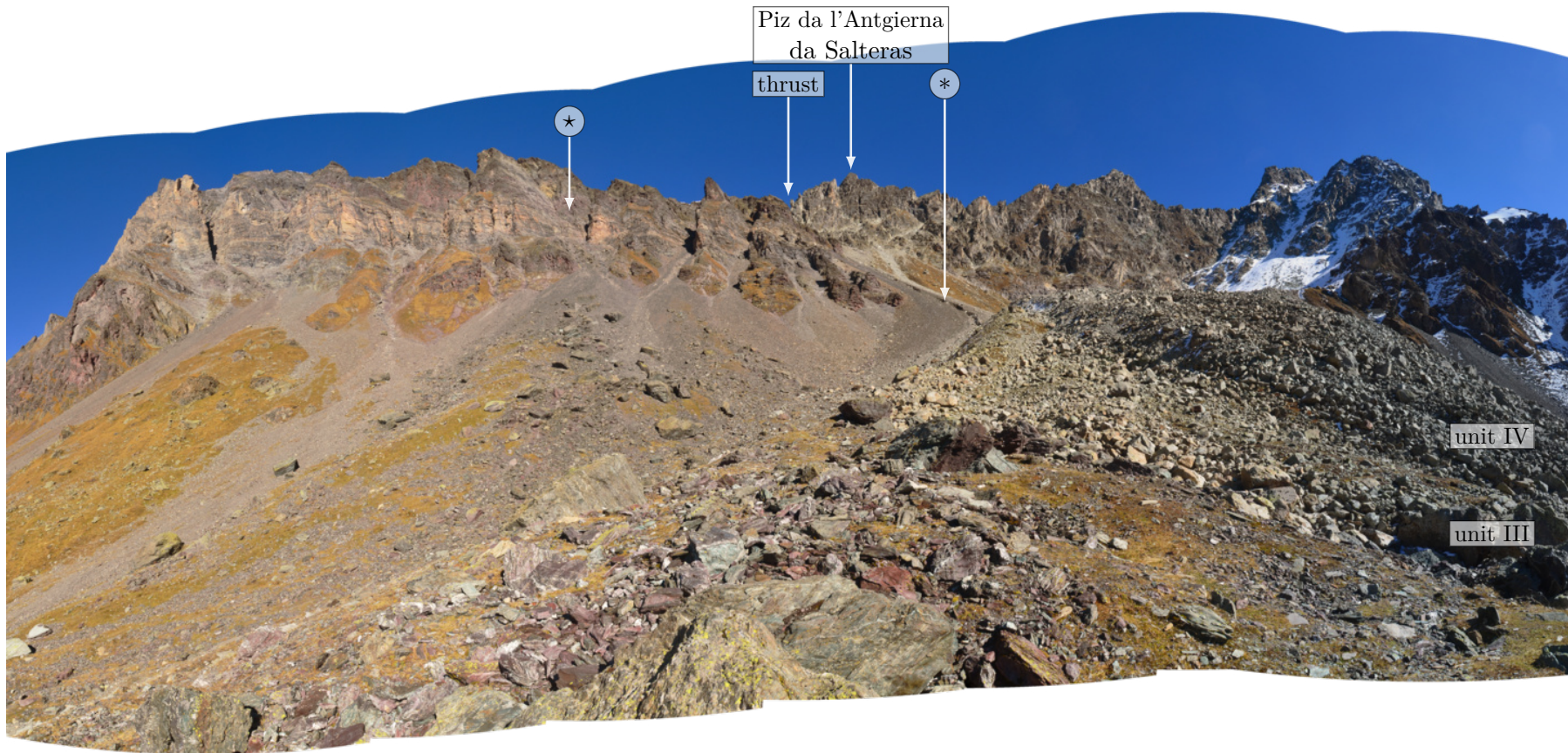


Figure 5.10: Radiolarite debris deposited onto the inactive corner of the rockglacier, most likely from a rockfall (scar between *Piz da l'Antgierna da Salteras* and *Piz Salteras* marked by ☆). The pass to the left of *Piz da l'Antgierna da Salteras* leading over to *Val Tschitta*, has incised at the thrust. A large debris cone with a deeply incised gully originates there. View is to NE. The large radiolarite boulder of the apex of the “radiolarite cone” is ~2m high. Photo taken Oct 14, 2017. The debris cone with vantage point of Fig. 5.9 is marked by ⊛.



Figure 5.11: An active above an inactive front scarp: Steep front of unit IV overriding unit III, exposing the fresh fine material beneath the blocky mantle and showing the inverted stratigraphy that is characteristic for rockglaciers. Coarse debris is still precariously lying on a less coarse substratum, but a boulder apron in front of the lower scarp has not formed (cf. Fig. 5.14) and the forefield is patchily covered by grass. This suggests, despite the unstable-looking configuration, that the substruction unit IV lies on is not advancing, or at least slowly enough to allow soil to develop. This lower thrust is classified as “inactive”. In contrast, the upper thrust that defines the boundary of unit IV is active, i.e. unit IV is advancing. Vantage point near Fig. 5.10, View is to SE-S. The lower scarp is roughly 6–10 m high (cf. Fig. 5.5). Photo taken Aug 4, 2017.

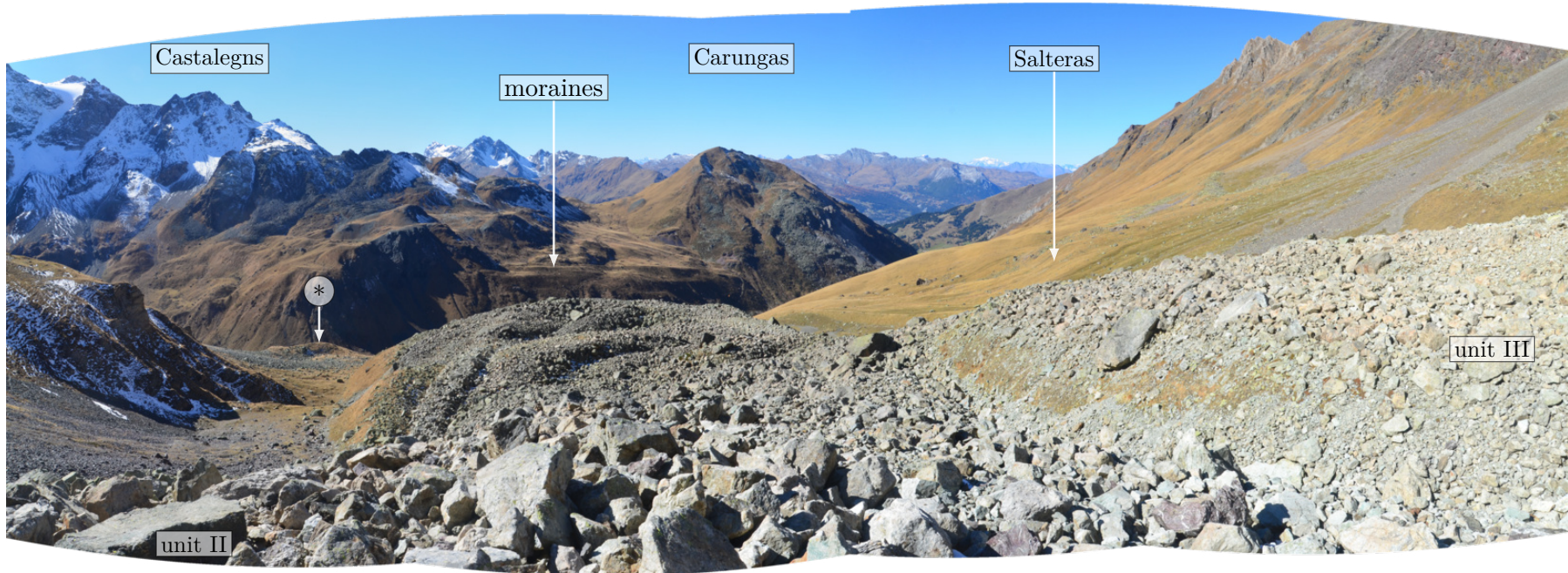


Figure 5.12: Grassy, but still unstable slope of unit III overriding unit II that has a well-developed furrow-and-ridge microrelief. Unit II rests on an older body with weathering-stained, lichen-covered boulders and vegetated slopes where soil formation is advanced, denoted by unit I. Note the rockglaciers and moraine ridges (Daun or Egesen?) on the opposite valley flank, and the deep-seated landslides on *Carungas*. View is to W. The lower scarp is ~8–10 m high. Photo taken Oct 14, 2017. Moraine with vantage point of Fig. 5.15 marked by *.

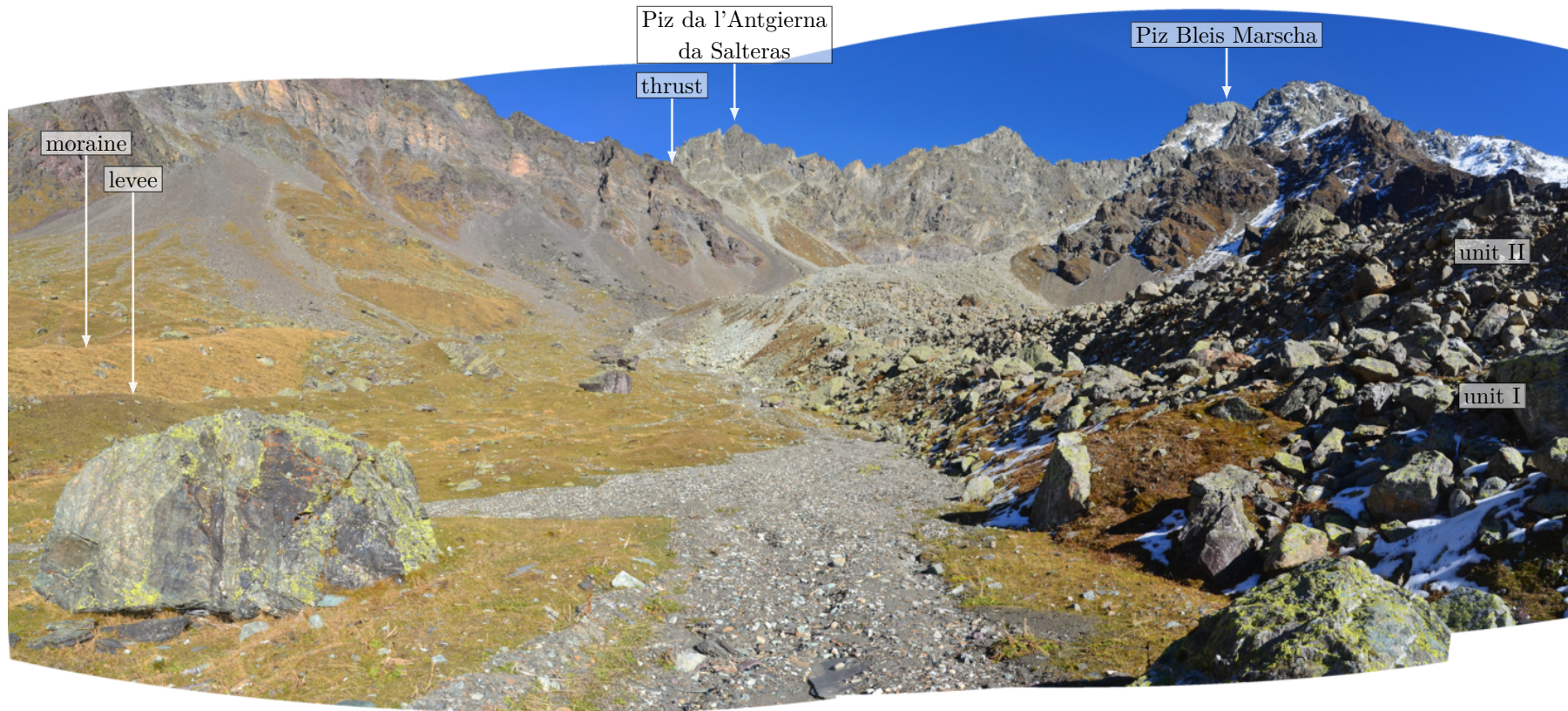


Figure 5.13: The depression between the parallel moraine (left) and rockglacier (right) is filled with down-washed fines (mostly radiolarites, schists and carbonates) and radiolarite rockfall boulders (Fig. 5.10). In autumn, the type of bedrock can be inferred from the the floral composition, manifested in vegetation colour: The moraine ridge mainly built of granite appears light brown, and vegetation on finer material composed of more weathering-prone radiolarite appears darker greenish. This allows to trace back the origin of the sedimentary content of the landforms: The material that makes up the moraine as well as the bouldery mantle of the rockglacier originate from the headwall of the Middle Err unit (right), whereas the talus slopes, debris flow deposits and rockfall boulders are derived from the headwall of the Lower Err unit (left). Note the clear colour contrast at the thrust. The small ridge extending downslope from a large radiolarite block consists of radiolarite, and is thus identified as a right-lateral levee. Its left-lateral counterpart is missing. The terrace on the rockglacier is formed by unit II being recessed by ~5m with respect to the underlying unit I, and is not a moraine. View is to ENE. For scale, the large boulder in the left foreground is 2.5 m high. Photo taken Oct 14, 2017.



Figure 5.14: Image of the front of unit II, standing on unit I near its tongue. The lichen-covered boulders forming an apron and the vegetated seam on thick soil indicates that unit II is not advancing and has become inactive relatively long ago (cf. Fig. 5.11). Nevertheless, parts must have been collapsing towards the south (right), exposing fresh, grey fines. Since there is no coarse debris apron, the mechanism is not toppling from above, but sliding from below: The entire southern part of the large lower lobe (Fig. 5.15) is subsiding southwards. Unit II is recessed with respect to the upper edge of unit I (except for one 70-m long segment where unit II has advanced beyond unit I and subsequently collapsed), and looks like “a rockglacier on a rockglacier”. View is to ENE. The rampart is 5–8 m high. Photo taken Oct 14, 2017.

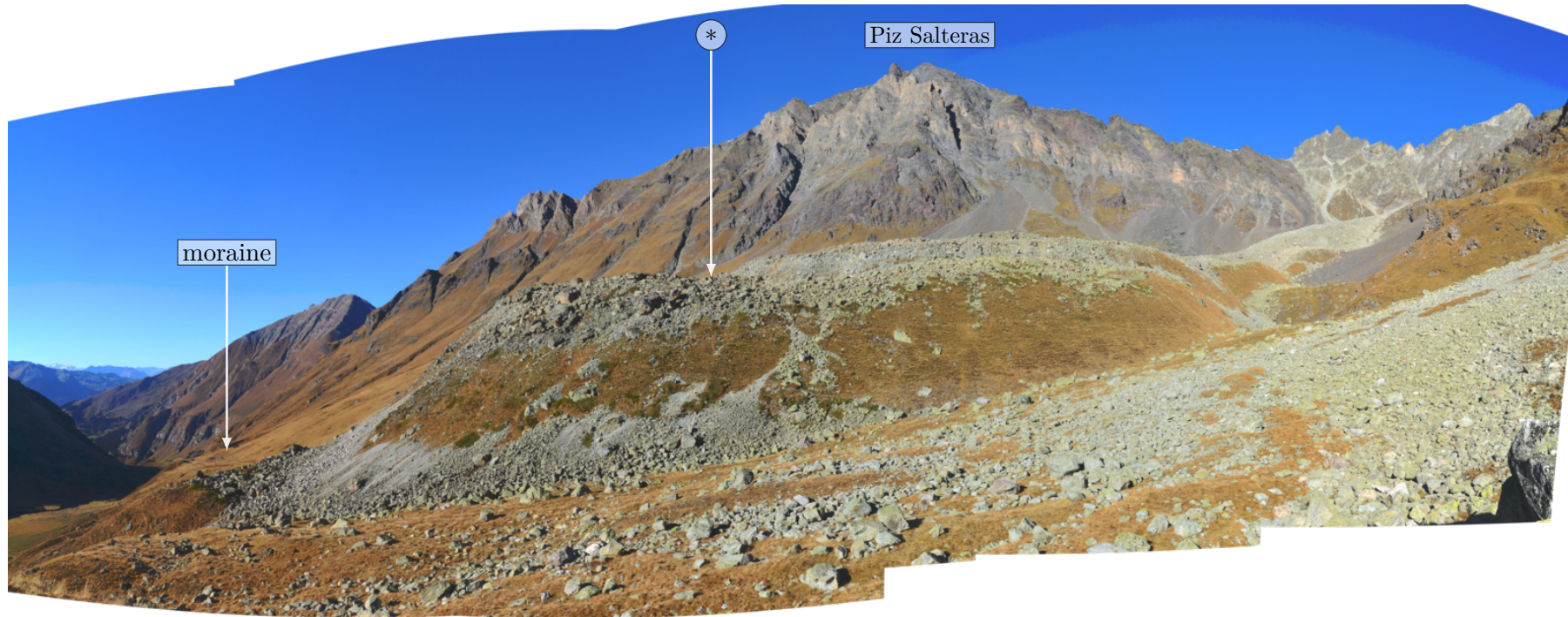


Figure 5.15: Side view on the frontal part of unit I (~30 m high), overlain by unit II on top. The entire southern front is slowly collapsing (moving toward the observer, cf. Fig. 5.14). No bulges at the base of the front are observable. The deformation either is distributed, or the sliding plane is blind and covered by the debris flows. The boulder apron and small debris slides are clear signs of activity. However, since the frontal and lateral slopes of unit I are extensively vegetated and overall appear quite stable, the advance rate must have been small for a long time. The vegetated slopes extend upslope until the body disappears beneath unit IV. In the foreground rubble-covered debris flow fan from *Bleis Marscha*, overlapping the foot of the front slope. Unit I has come to a halt just at the edge of the trough shoulder with the (Egesen) moraine ridge (left-valley side counterparts pictured in Fig. 5.12). However, the moraines and the rockglacier are nowhere in contact, and the relative age cannot be determined in the field. No apparently rockglacier-derived debris is found further downslope. Vantage point is on a short segment of a moraine ridge. View is to NNW. Photo taken Oct 14, 2017. Vantage point of Fig. 5.14 marked by *.



Figure 5.16: Frontal view of the relict lowermost rockglacier front (unit I). Note the fall sorting of the talus apron that mantles the front. Whereas vegetation and shrubs on the distal part of the apron suggests that the main activity phase has ceased long ago, fresh debris slides exposing fine material show that the movement has not ceased altogether. The debris cone and short segment of the moraine ridge with vantage point of previous Fig. 5.15 is on the right. The top of the bouldery, sharp crested moraine is at an elevation of 2415 m.a.s.l. Appearance and position in the landscape link it to the Egesen stadial. View is to ENE. Photo taken July 16, 2017

5.1.3 Digital elevation model analysis

The topography and small-scale micro-topography along the longitudinal transect (its trace in Fig. 5.7) is shown in Fig. 5.17. The micro-topography is computed by subtracting a smoothed DEM from the original DEM. Conceptually, this is a high-pass filter that attenuates the large-scale features from the topography, and the emphasized small-scale features show the rockglacier microrelief. The smoothed, low-pass filtered DEM is obtained by running a circular averaging filter with a diameter of 100 m on the original DEM with the MATLAB® function `filter2`.

The whole *Bleis Marscha* rockglacier (relict units included) has a length of ~1200 m, a width of ~150 m, covers an area of roughly $2.4 \times 10^5 \text{ m}^2$, and has a source area of $\sim 3.1 \times 10^5 \text{ m}^2$. The obtained ratio of rockglacier surface to source area is 1:1.3 [Barsch, 1996, pp. 29, 246]. Assuming a debris column height of 20 m, taking a mean velocity of 30 cm a^{-1} as suggested by the image correlation results, then a typical headwall back-weathering rate is $\sim 3 \text{ mm a}^{-1}$.

The morphologically motivated subdivision of the *Bleis Marscha* rockglacier in a relict lower part and an active upper part is reflected in the longitudinal profile (Fig. 5.17): The lower half (units I–II, below 2500 m a.s.l.) has a mean surface slope of 11° and a pronounced furrow-and-ridge microrelief. The upper units (units III–V) are with 21° roughly twice as steep. The ridges are dominantly longitudinally, not transversally, oriented. A set of prominent ridges is at the northernmost margin of unit IV, at the outer bend of the curve. Different lobes, separated by a break in surface slope, are easily identifiable based on the local minima in the small-scale topography (upward-pointing triangles).

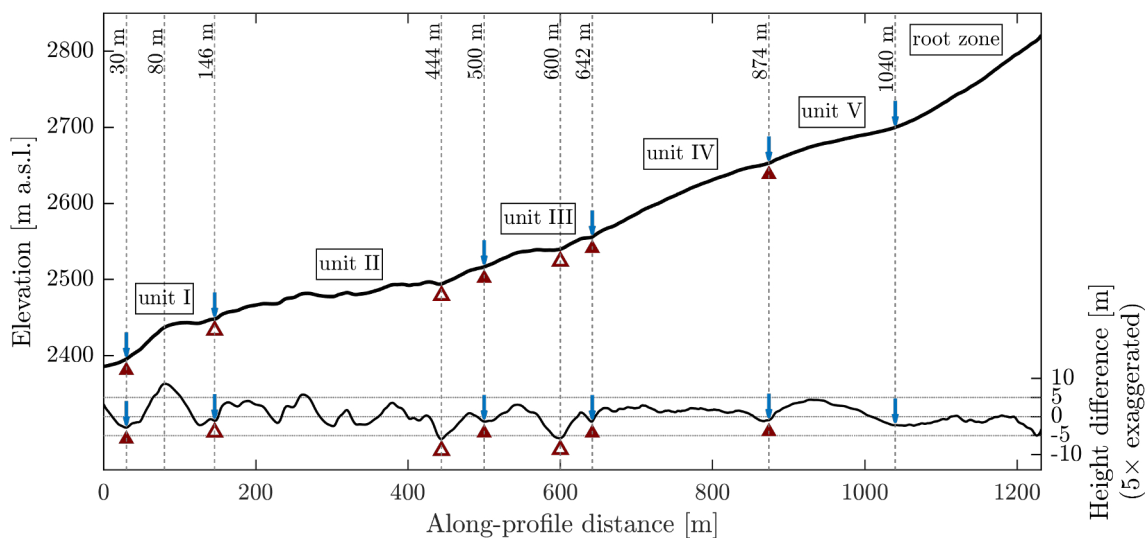


Figure 5.17: Longitudinal transect: Topography and small-scale topography defined as the difference between the surface topography at each point and a running average over 100 m (five times exaggeration). Thrusts: ▲ active, △ inactive.

To investigate the spatial pattern of the micro-relief, it is transformed into the Fourier domain. In the Fourier representation, the characteristic wavelength of the ridges are found as local peaks in the Fourier amplitude spectrum (Fig. 5.18).

Assuming that buckle folding in response to compressive flow of a layered medium was the dominant formation mechanism for the transverse furrow-and-ridge microrelief in

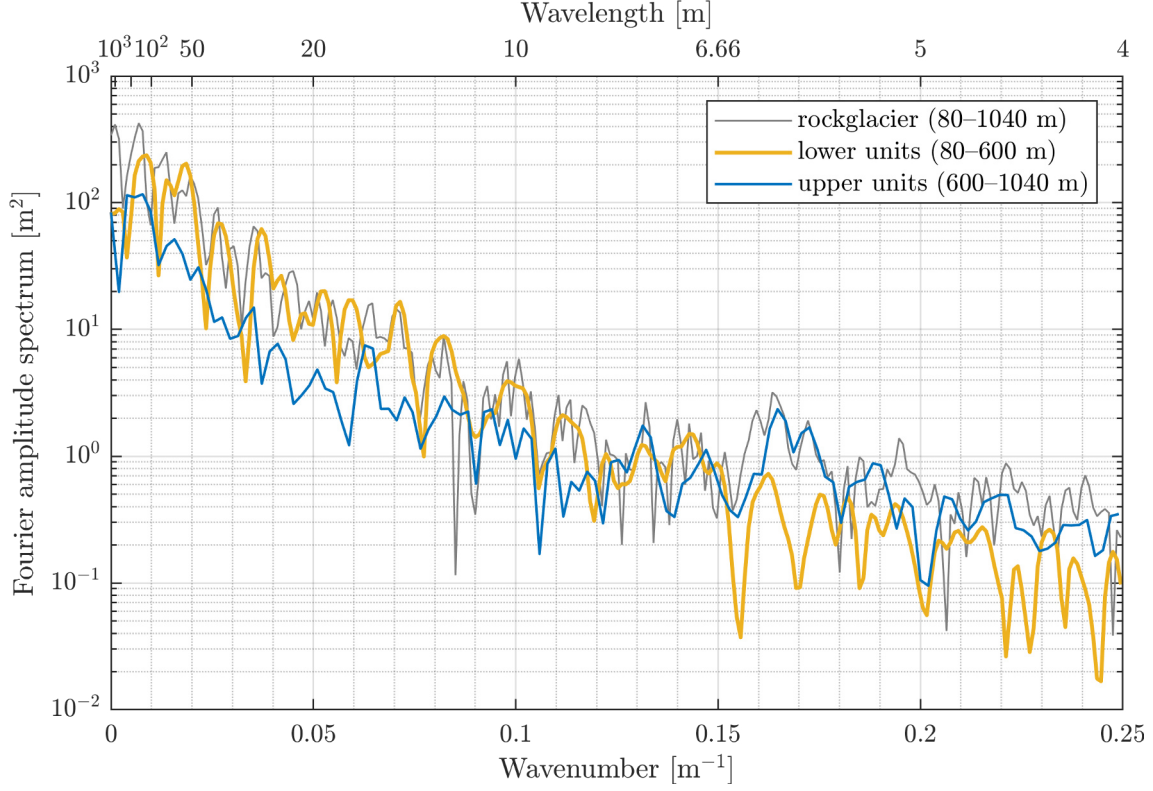


Figure 5.18: Longitudinal transect: Fourier amplitude spectrum of the small-scale topography (Fig. 5.17).

the lower part [Frehner et al., 2015; Kääb and Vollmer, 2000], Biot [1961] proposed an analytical formula for the viscosity contrast R between the rockglacier mantle and core (two-dimensional, equation modified for one-sided support).

$$R := \frac{\mu_{\text{mantle}}}{\mu_{\text{core}}} = \frac{3}{8} \left[\frac{\lambda_d}{\pi h_m} \right]^3 \quad (5.1)$$

The viscosity contrast R is controlled by the dominant wavelength λ_d and rockglacier mantle thickness h_m . Inserting $\lambda_d = 54$ m and $h_m = 5$ m, $R = 15.2$ (agreeing with [Frehner et al., 2015]).

5.2 Exposure dates

Main points
<ul style="list-style-type: none"> • Fifteen boulders, distributed over all morphologically identified lobes, are sampled; 14 granitic boulders for ^{10}Be and 1 dolomite boulder for ^{36}Cl. • The exposure ages increase from rockglacier head towards the front and range from a few hundred years to roughly 9 ka. • The age uncertainty of the lower, older units is as large as the absolute age of the upper, younger units, i.e. in the order of a few hundred years.

Fifteen samples with roughly 500 g material each have been collected on the rockglacier along the longitudinal transect from the (apparently) relict toe to the higher-elevation active areas. Preferred sampling area was the upper, active part (11 of 15 samples). Only one dolomite boulder suitable for sampling has been found. The sedimentary lenses along the thrust fault are fractured, and the dolomites are thus prone to fragmentation. Detailed ^{10}Be sample information is shown in Table 5.1 and Appendix A1, “rock book”.

The ^{10}Be concentration is in the range of $0.7 \cdot 10^4$ to $23.6 \cdot 10^4$ at g^{-1} . The errors at 1σ level are proportional to the ^{10}Be concentration in the range of $0.1 \cdot 10^4$ to $1.2 \cdot 10^4$ at g^{-1} .

Table 5.1: ^{10}Be sample information (sorted by elevation)

Sample name	Latitude [°N]	Longitude [°E]	Elevation [m a.s.l.]	Sample thickness [cm]	Shielding factor ^a [-]	^{10}Be concentration ^b [10^4 at g^{-1}]
Err1	46.5719	9.7036	2 448.7	1.5	0.9739	23.584 ± 1.216
Err2	46.5722	9.7052	2 481.5	1.5	0.9751	18.992 ± 1.004
Err15	46.5726	9.7057	2 485.3	1.0	0.9582	15.257 ± 0.771
Err14	46.5730	9.7070	2 498.3	2.0	0.9484	21.366 ± 0.638
Err13	46.5734	9.7081	2 529.3	2.0	0.9502	14.027 ± 0.659
Err12	46.5737	9.7093	2 551.7	1.5	0.9476	13.234 ± 0.654
Err11	46.5738	9.7102	2 584.9	1.5	0.9450	7.819 ± 0.277
Err10	46.5737	9.7110	2 611.7	1.5	0.9211	3.308 ± 0.425
Err7	46.5741	9.7113	2 623.2	1.5	0.9365	1.854 ± 0.161
Err6	46.5738	9.7121	2 644.1	2.0	0.9406	0.860 ± 0.183
Err9	46.5742	9.7123	2 647.8	1.5	0.9204	2.083 ± 0.213
Err5	46.5735	9.7123	2 648.9	1.5	0.9428	2.940 ± 0.202
Err4	46.5735	9.7128	2 667.5	2.0	0.9392	1.642 ± 0.154
Err3	46.5733	9.7134	2 679.8	1.8	0.9259	0.673 ± 0.115

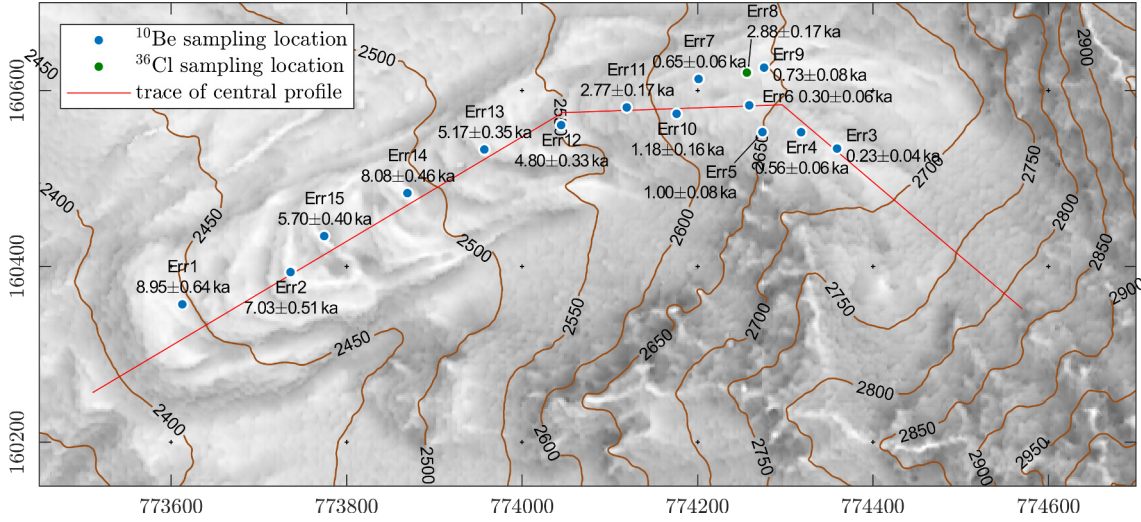
^a Shielding correction factor calculated according to Dunne et al. [1999] includes the shielding due to the dip of the sampled surface and the shielding by the surrounding topography. Shielding by snow cover is not accounted for. ^b AMS measurement errors are at 1σ level and include the AMS analytical uncertainties and the error of the subtracted blank. Measured ratios were calibrated to the 07KNSTD standard.

The ^{10}Be production rate best suited to the Alpine area is the Northeastern North America (NENA) calibration data set of the CRONUS-Earth online calculator [Balco et al., 2009] [S. Ivy-Ochs, pers. comm.]. The TCN exposure ages (with uncertainty) are listed in Table 5.1, shown in map view in Fig. 5.19 and plotted in Figs. 5.20 and 5.21.

The TCN exposure ages and sampling location projected onto the longitudinal profile are plotted in Figs. 5.20 and 5.21. Note the “stratigraphically” directed time axis to

Table 5.2: ^{10}Be and ^{36}Cl exposure ages

Sample name	Nuclide	Exposure age [a]		
		no erosion		
Err1	^{10}Be	8 948	\pm	636
Err2	^{10}Be	7 027	\pm	505
Err15	^{10}Be	5 697	\pm	399
Err14	^{10}Be	8 076	\pm	460
Err13	^{10}Be	5 169	\pm	349
Err12	^{10}Be	4 796	\pm	332
Err11	^{10}Be	2 774	\pm	166
Err10	^{10}Be	1 181	\pm	162
Err7	^{10}Be	646	\pm	64
Err8	^{36}Cl	2 880	\pm	175
Err6	^{10}Be	295	\pm	64
Err9	^{10}Be	727	\pm	82
Err5	^{10}Be	1 001	\pm	84
Err4	^{10}Be	556	\pm	59
Err3	^{10}Be	229	\pm	41

Figure 5.19: Sampling locations and TCN exposure ages on *Bleis Marscha* rockglacier.

emphasize the clear anti-correlation of the exposure ages with elevation. The exposure ages span the last 9 ka, i.e. almost the entire Holocene. A linear regression line is fitted to the samples that lie along the central flow line (Err 3, 4, 5, 7, 9, 10) in the youngest, uppermost part: $t_{exp} = -3.4836 \cdot x + 3685.1$, $R^2 = 0.6175$. The inverse slope gives a mean horizontal surface velocity of $\bar{v}_s \approx 30 \text{ cm a}^{-1}$, and the time-axis intercept (“zero-age crossing”) 1058 m (Fig. 5.21). The ^{36}Cl age is roughly 2 ka older compared to its neighbouring ^{10}Be samples.

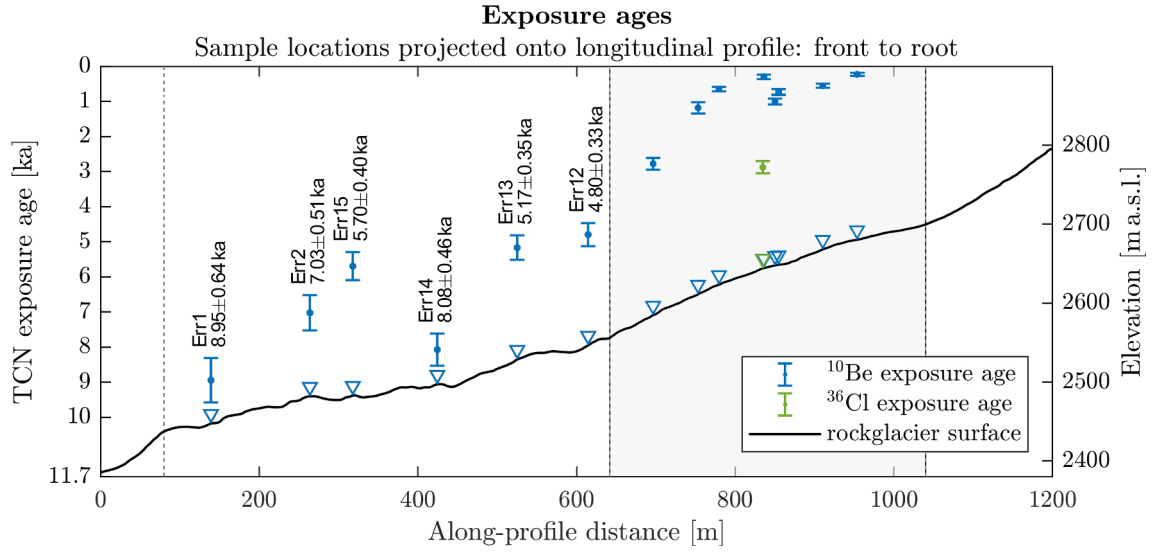


Figure 5.20: TCN exposure ages for the *Bleis Marscha* rockglacier. The grey area is shown in Fig. 5.21. Note the stratigraphically directed time axis to emphasize the correlation with elevation.

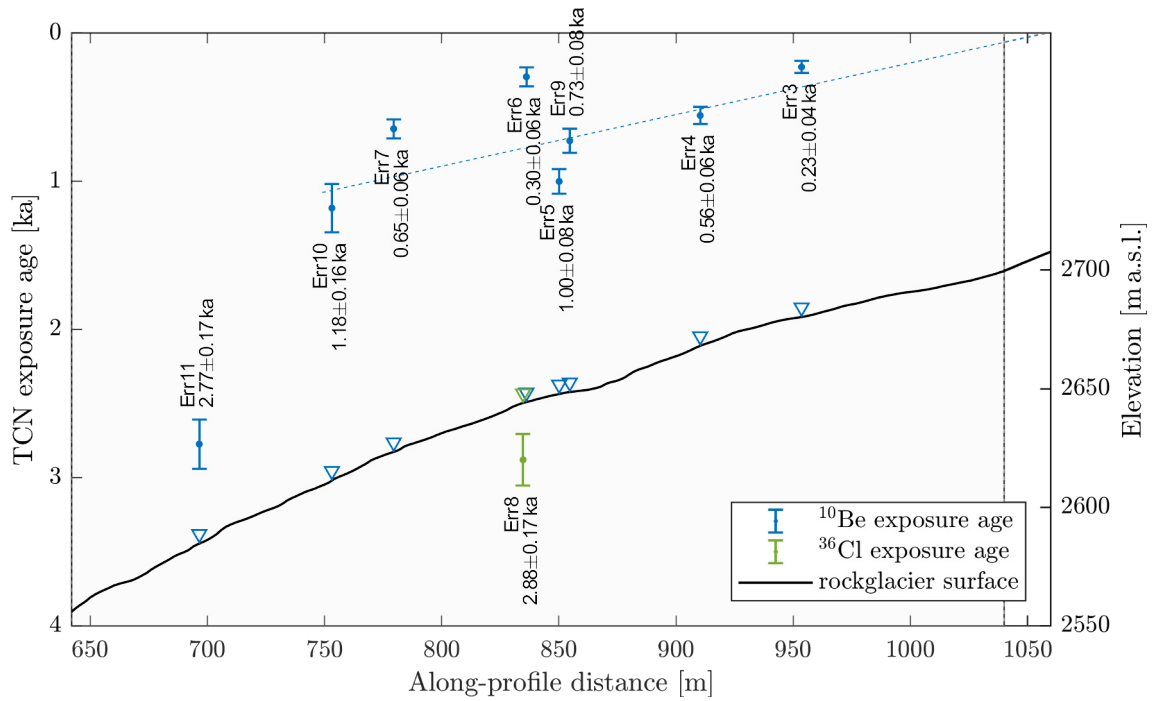



Figure 5.21: TCN exposure ages for the upper part and the linear regression line through samples along the stromstrich (see text).

5.3 Orthophoto matching

Main points	
<ul style="list-style-type: none"> • Two orthophotos from late summer 2003 and 2012 are compared. The long temporal baseline of 9 years averages inter-annual variabilities in rockglacier creep rates. • Measured velocities on the rockglacier are in the order of 20 to 50 cm a^{-1}, clearly higher than the significance level of 5 cm a^{-1} obtained from image matching of a immobile reference area. • Optimal template size is 41×41 pixels or $10.25 \times 10.25 \text{ m}$ on the ground. 	

5.3.1 Algorithm configuration

The relationship between the correlation results and either template size or search window size is investigated with a procedure suggested by Debella-Gilo and Kääb [2012]. Furthermore, the performance of normalized cross correlation (NCC) and orientation correlation (OC) is compared.

The choice of the template size is critical: On the one hand, the template should be large enough so that it has a “unique fingerprint” capturing the texture (maximize the signal-to-noise ratio SNR), thus making false matches unlikely. On the other hand, it should not be too large, as a large template is more prone to shearing and distortion (strain), reduces the density of tracked points (lower resolution of obtained flow field) and it becomes computationally more costly to compute the NCC surface.

Optimal template size

The analysis is illustrated by a representative example for a highly-textured section in the upper part of the *Bleis Marscha* rockglacier as shown in Figs. 5.22–5.28: Fig. 5.22 depicts a subset of the aerial images centred at image coordinates [6919,3002]. Fig. 5.23 shows the same subset of the real part of the orientation image. Panel **a** shows the template (framed in yellow) centered in its surrounding area (panel **b**). Panel **c** shows the best-matching position of the shifted template (red frame) in the search window.

The role of the template size is investigated with Fig. 5.24. For small template widths ($w_t < 30 \text{ px}$), C_{max} is high due to presence of *coincidentally* highly similar patterns in the search window (Fig. 5.24a) (“overfitting”). This peak is hardly discernible from noise (Fig. 5.25a) and located randomly. The matching position and thus the displacement estimates vary strongly with template size (Fig. 5.24c) and are not reliable. With increasing template size, the pattern becomes more unique: the noise level C_{noise} decreases much faster than C_{max} , leading to an increasing signal-to-noise ratio SNR . At some point, the noise is optimally suppressed, C_{max} increases again and reaches a local maximum, close to (but not necessarily co-located with) a local SNR -maximum (45–51 px). At this optimal template size, noise and distortion (strain and shearing) are minimal, and the displacement is reliably accurately matched (Fig. 5.25c). In other words, the minimal template width that grasps the surface texture is 41 px, corresponding to 10.25 m on the ground. Including more pixels in the template adds more noise than information (distortion?) in case of NCC, and its SNR estimate decreases. The SNR estimate for OC, however, keeps increasing in a sawtooth-like manner, where the local peaks correspond to template sizes where they are just large enough to contain a pattern that is well recognised in the search window.

The orientation images work better than the “raw” orthophotos: Comparing Figs. 5.22 and 5.23, the improved contrast is obvious. The template from the orientation correla-

Orientation correlation

tion image is more unique: C_{max} is overall lower (less prone to “overfitting”), SNR is higher because of the relatively lower noise level (Fig. 5.26), and the “true” estimated displacement is reached earlier (Fig. 5.24). Finally, test runs of common normalized cross correlation performed poorly on the rockglacier. Small differences in lighting, illumination direction or cloudiness make the rugged, bouldery rockglacier surface appear differently to the point that only very few patches can reliably be cross-correlated. These decorrelation problems are massively reduced by applying the *orientation correlation* method which is robust and illumination invariant [Fitch et al., 2002].

The search window size must be at least as large as the template size, large enough to accommodate the farthest displacement, but reasonably small to limit the computational cost and to keep the probability of false matches low [Messerli and Grinsted, 2015]. An estimate of the expected direction and maximum magnitude of the displacement, either from other measurements or from a preceding coarse-scale match, can be used as an initial guess to minimise the search area. If both the template and search window are quadratic with side lengths of w_t and w_s , respectively, and if the template center coordinate coincides with the search window center coordinate (initial guess of zero displacement), then the maximum trackable displacement in each horizontal dimension is

$$\Delta h_{max} = \frac{w_s - w_t}{2}, \quad w_s > w_t, \quad (5.2)$$

and the maximum trackable distance thus

$$|\Delta h_{max}| = \frac{w_s - w_t}{\sqrt{2}}. \quad (5.3)$$

Messerli and Grinsted [2015] recommend a search window width of template width added to a (generously dimensioned) maximum expected displacement. An additional argument for a relatively large search window is that it provides a more robust estimate of the noise level (Eq. 4.8). To summarise, the choice of the search window size is much less critical than the template size: As long as the template is large enough to capture a distinctive pattern and the search window large enough to contain the true displacement, the algorithm provides robust, reliable results (Figs. 5.27, 5.28).

After matching of sufficient points with the algorithm configuration according to Table 5.3, the resulting data is filtered. Displacement vectors with low signal-to-noise ratio or incoherent direction or magnitude are filtered out. A noise filter with a very conservative SNR threshold of 5 (Messerli and Grinsted [2015] recommend a value of 2) effectively removed poor-quality displacement vectors, so that an additional directional filter that deletes displacement vectors that deviate strongly from its neighbours was not necessary. For noise-sensitive parameters derived from the velocity field, i.e. the strain rate field and stream line interpolations, additional smoothing (cf. Fig. 4.6) was performed.

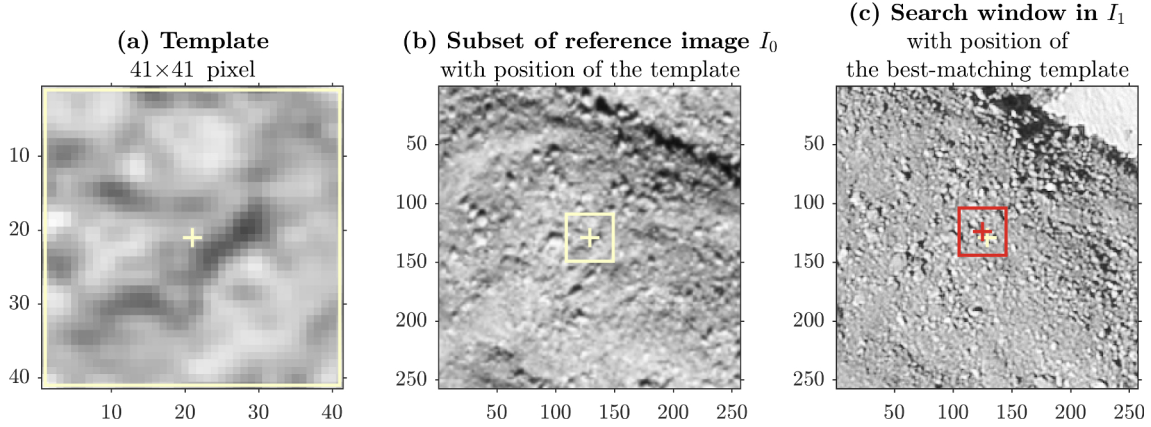


Figure 5.22: Example illustration of conventional NCC: 41×41 px reference template, 257×257 px search window (image coordinates [6919,3002]). See text for explanations.

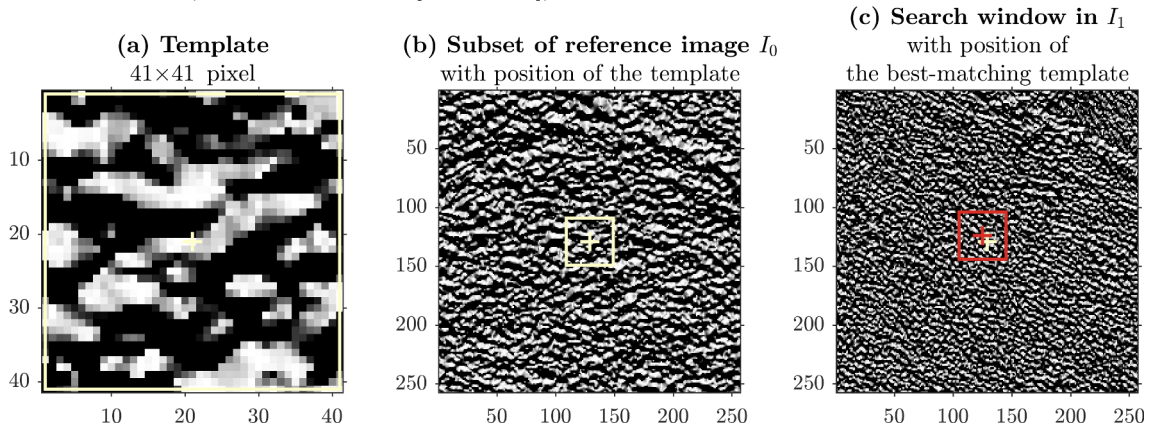


Figure 5.23: Example illustration of OC (real part of orientation image): same configuration as in Fig. 5.22. Note the enhanced optical contrast.

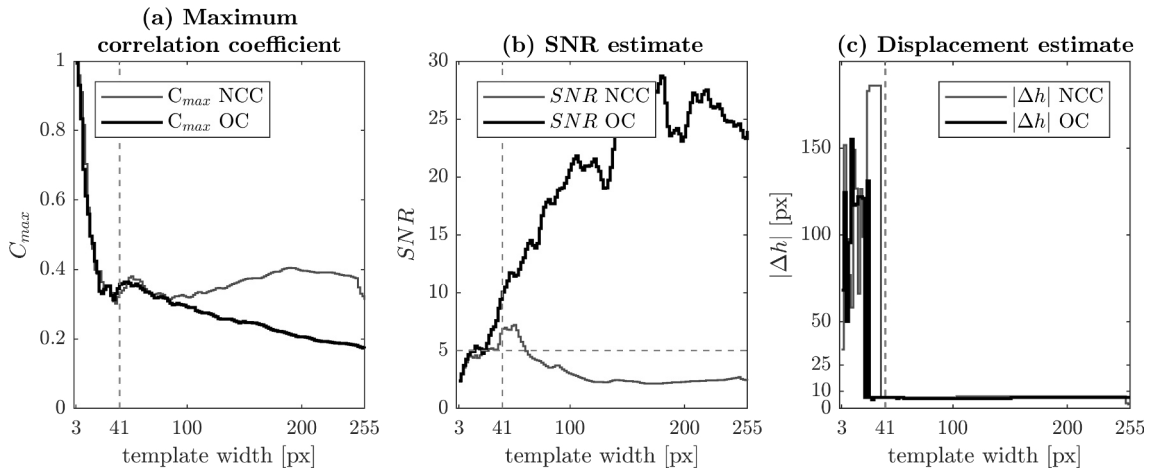


Figure 5.24: Statistical parameters (a: maximum NCC correlation coefficient, b: signal-to-noise ratio) and result of image correlation (c: displacement estimate) as a function of template size for an image subset that contains high signal variance. Common NCC in black, OC in dark grey. Window size is 257×257 pixel. The gray lines show the chosen template size of 41×41 pixel and the SNR threshold of 5, respectively. Idea taken from [Debella-Gilo and Kääb, 2012, Fig. 6]. See text for explanations.

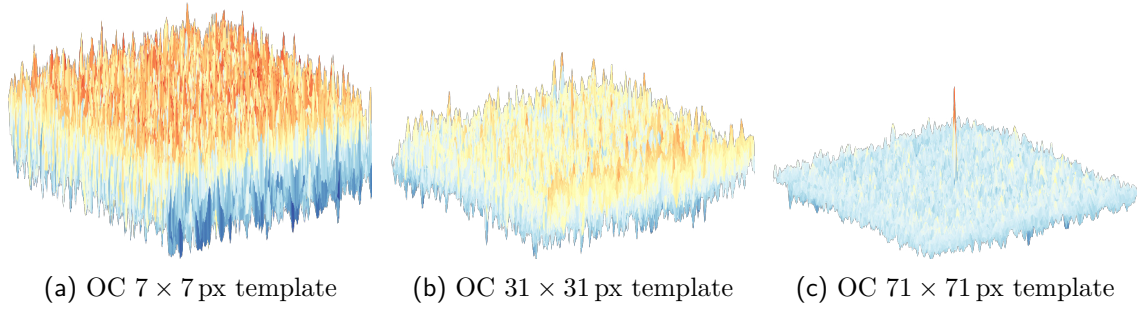


Figure 5.25: Role of template size: NCC coefficient surfaces for different template sizes (real part of orientation image, image coordinates [6919,3002], (cf. Fig. 5.22 and [Kääb and Vollmer, 2000, Fig. 5])). The overall maximum of the NCC surface γ , C_{max} , indicates the most likely terrain displacement.

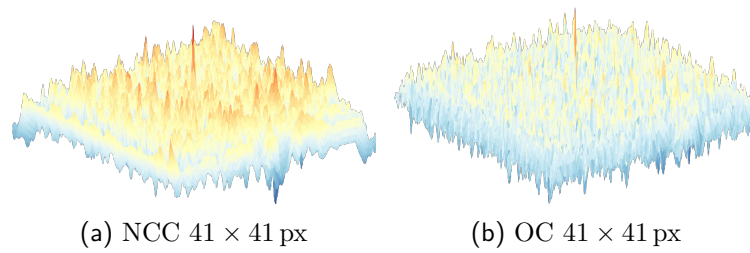


Figure 5.26: Advantage of OC over NCC: NCC coefficient surfaces for (a) NCC (Fig. 5.22), (b) OC (Fig. 5.23) for the configuration in Figs. 5.22–5.24.

Table 5.3: `templatematch` algorithm configurations. Orthophoto pixel length is 0.25 m on the ground. For correlation, The R channel of the RGB image is used.

	Resolution	Time	Template size w_t	Search win- dow size w_s	SNR_{min}
Reference area and rockglacier (incl. surroundings)	2 px, 0.5 m	2003–2012	41×41 px	60×60 px	5

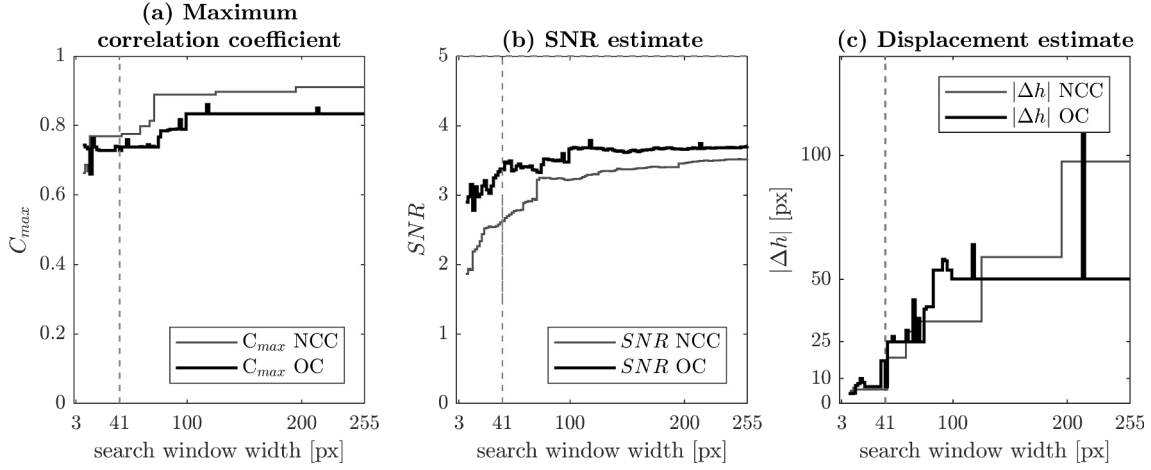


Figure 5.27: Statistical parameters and result of image correlation for a 7×7 pixel template (cf. Fig. 5.24). The displacement estimate is not reliable: the template size is too small. The gray lines in plot **b** show the chosen template size of 41×41 pixel and the SNR threshold of 5, respectively. A too small template is the more prone to false matches the larger the search window is: Both C_{max} and the displacement estimate $|\Delta h|$ increases with increasing window size.

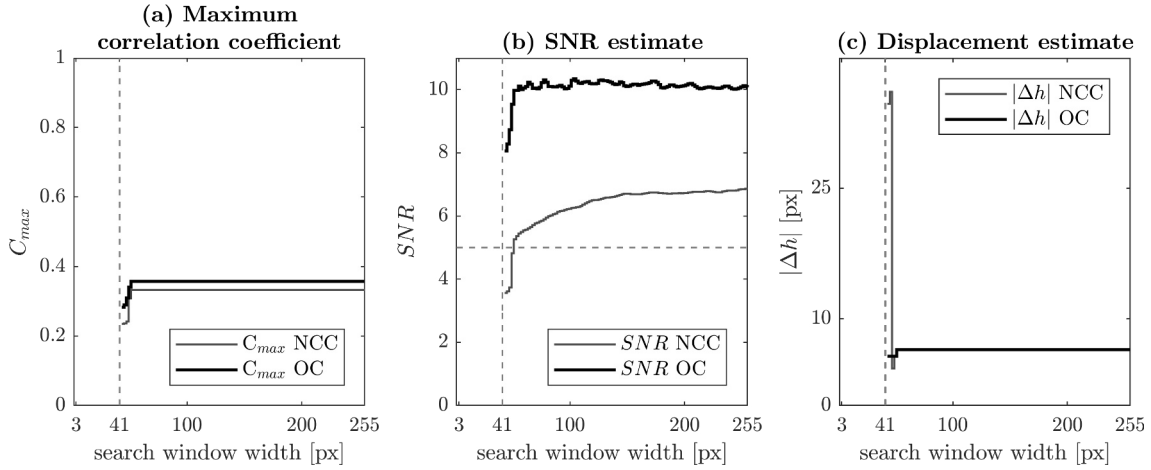


Figure 5.28: Statistical parameters and result of image correlation for a 41×41 pixel template (cf. Fig. 5.24). The displacement estimate $|\Delta h|$ is robust and reliable (~ 6 px). C_{max} remains constant as soon as the pattern is found in the search window, while SNR keeps increasing because the noise level C_{noise} becomes lower. The smallest template size with this behaviour is the ideal template size.

5.3.2 Image Correlation results

Reference area correlation

The noise-filtered horizontal surface velocity field for the reference area (area of 0.17 km^2) in the valley floor, where no displacement is expected, is shown in Fig. 5.29. Velocity data in pixels where the signal-to-noise ratio is below the specified threshold of $SNR_{min} = 5$ are classified as unreliable and deleted, hence the large data gaps. The histogram of the noise-filtered data is plotted in Fig. 5.30. The vertical lines mark the mean, median and mode (the value that appears most often). Median and mode are insensitive to the few large velocity values and differ considerably from the mean for a skewed distribution as is the case here. The median or mode velocity is a robust estimate for the pre-processing errors. The significance level is 5.3 cm a^{-1} , i.e. speeds lower than 5.3 cm a^{-1} are statistically non-significant and respective areas are classified as non-moving.

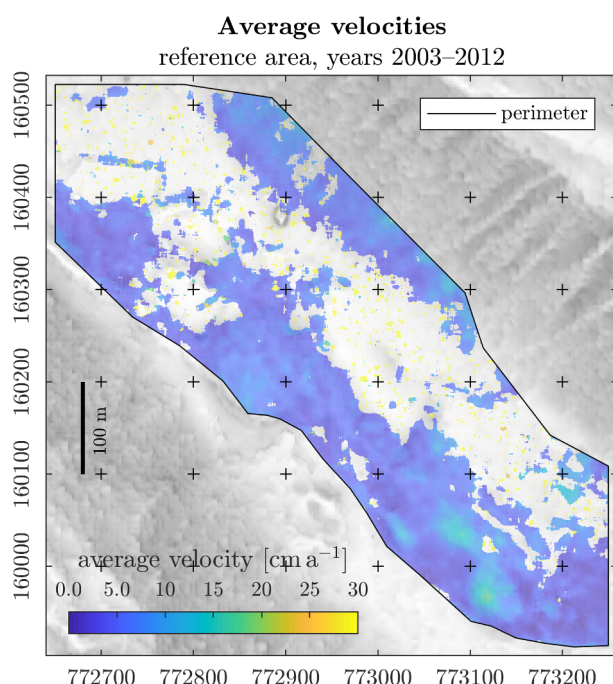


Figure 5.29: Horizontal surface velocities on the stable valley floor (“reference area”).

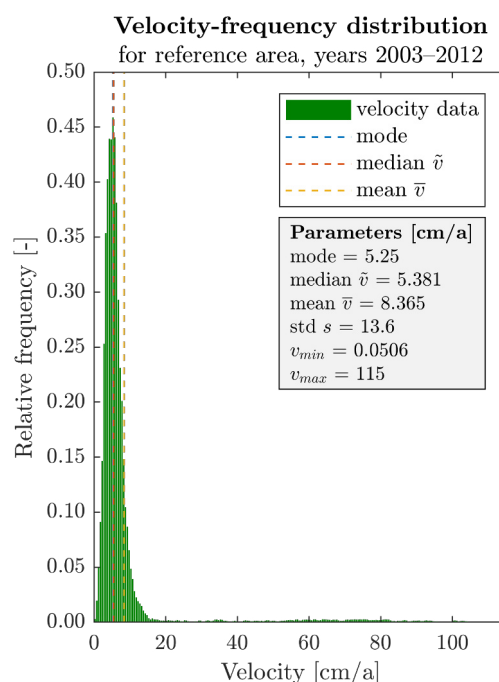


Figure 5.30: Histogram of reference area velocities.

Horizontal surface velocity

The noise-filtered horizontal surface velocity field for the *Bleis Marscha* rockglacier and its immediate surroundings is shown in Fig. 5.31. Typical speeds are 30 cm a^{-1} , with peak speeds up to 60 cm a^{-1} .

The kinematic data suggests the following rockglacier subdivision (front to root, boundaries along isotachs):

- **relict, immobile front**, $v_s < 20 \text{ cm a}^{-1}$ (0–325 m on the longitudinal profile): The lowermost part is characterized by an irregular, “patchy” flow field both in terms of direction and magnitude at an overall low speed.
- **transition zone**, $20 \text{ cm a}^{-1} < v_s < 40 \text{ cm a}^{-1}$ (325–640 m): In this part bounded below by the 20 cm a^{-1} isotach a laterally clearly confined surface velocity field emerges. It is smooth with no sharp gradients except at the lateral margins. The speed gradually increases upslope to 40 cm a^{-1} , and the flow direction follows the large-scale topography.
- **rapid lobes**, $40 \text{ cm a}^{-1} < v_s < 65 \text{ cm a}^{-1}$ (640–874 m): The lower boundary is

marked by a stark speed increase ($\Delta v_s = 10 \text{ cm a}^{-1}$, data gap) and a prominent internal front scarp. Above an altitude of 2600 m. a.s.l, the velocity decreases again. The velocity field remains smooth and aligned with the large-scale surface slope.

- **uppermost lobe**, $10 \text{ cm a}^{-1} < v_s < 35 \text{ cm a}^{-1}$ (874–1040 m): This lobe is individuated based on the slope-velocity relation (Fig. 5.39) with an outline following the morphology. The data becomes more fragmented towards the talus due to decorrelation. The defining character of this lobe is that the surface velocity becomes gradually decoupled towards the talus.

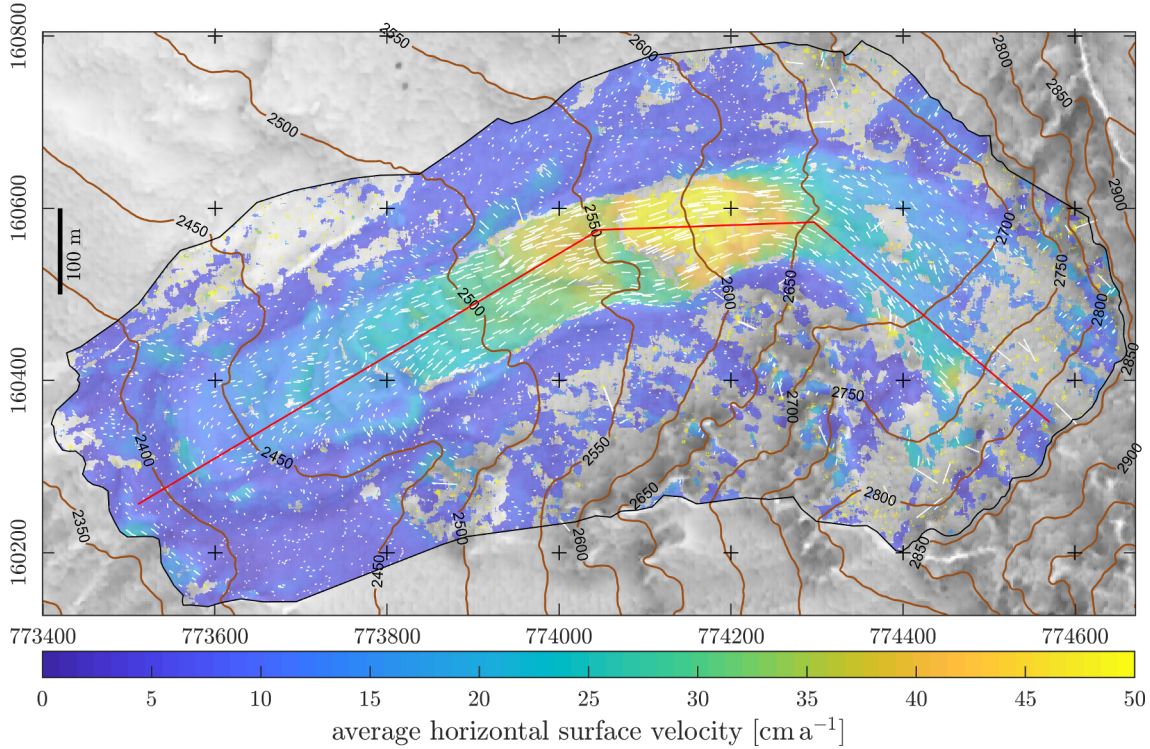


Figure 5.31: Noise-filtered horizontal surface velocity of the *Bleis Marscha* rockglacier, years 2003–2012. Magnitude (color), direction (white arrows). Significance level is 5 cm a^{-1} . Colorbar saturates at 50 cm a^{-1} . No smoothing filter was applied. Data gaps are in the talus, on a snow field and at the margins of lobes.

The strain rates are the spatial velocity gradients, here calculated by means of a central finite-difference scheme with a spacing of 20 m (effective strain rate) and 50 m (principal axes). Additional to the noise filter ($SNR_{min} = 5$), a GAUSSIAN low-pass filter is applied (diameter 10 m).

The effective strain rate (Fig. 5.32) can be interpreted as deformation intensity. Overall, they are in the order of 10^{-2} to 10^{-3} a^{-1} , with pronounced strain concentration at the margins and (internal) front of the creeping bodies. The high effective strain rates around velocity data gaps, however, are artefacts, as these missing values are treated as zero. The typical example is the high-strain rate fringe around the snow field at coordinates 774400/160600.

The principal strain rate axis (Fig. 5.33) show the direction of maximum shortening (red) and maximum stretching (black). Recalling the kinematic-supported rockglacier subdivision from above, the lobes are characterized as follows:

- **relict, immobile front**: Dominant shortening and stretching as well as the ef-

Horizontal surface strain rates

fective strain rate varies according to the small-scale topography, and the principal directions are not aligned with the general WSW–NNO trending *Bleis Marscha* rockglacier.

- **transition zone:** The strain is concentrated at the lateral margins, implying the rockglacier body creeps *en bloc*. At the margins, the principal axes are rotated by roughly 45° with respect to the general creep direction, typical for simple shear.
- **rapid lobes:** Apart from the continuing lateral strain concentration, the deformation is characterized by strong compressive overriding of the lobes in their frontal part and extensive flow behind. The principal axis are aligned with the general creep direction. The shortening is associated with speed decrease (in creep direction) or decelerating creep; stretching/elongation is associated with speed increase or accelerating creep.
- **uppermost lobe:** Towards the talus, the strain rates appear chaotic due to the velocity data gaps.

The kinematic vorticity number W_k (Fig. 5.34) supports the observation that simple shear is dominant at the margins.

Stream lines depict the path and travel time (strictly: the horizontal travel time) for an imaginary particle travelling at the rockglacier surface, assuming that the underlying flow field remains unchanged during the entire travel period. Thanks to the time-reversibility of a STOKES flow, the stream lines can be interpolated down-flow or forward in time (Fig. 5.35) as well as up-flow or backwards in time (Fig. 5.36). The former reveals the surface velocity distribution across the rockglacier: The velocity is highest at the central flow line of the rockglacier and decreases towards the margins. The latter gives theoretical travel time estimates for the sampled boulders.

To attenuate small-scale and thus likely short-lived velocity variations, the velocity field is low-pass filtered, additional to the noise filter with a slightly more severe threshold value of $SNR_{min} = 6$. Velocity data gaps (e.g. the snow patch) are “filled” by interpolation with the tool `inpaint_nans`.

The histogram in Fig. 5.37 shows the relative occurrence frequency of the velocity in the reference area (green, cf. Fig. 5.30) and on the *Bleis Marscha* rockglacier (dark grey). The rockglacier is further subdivided based along the 20 cm a^{-1} isotach in a lower relict part (yellow).

The horizontal surface velocity and slope along the longitudinal profile are shown in Fig. 5.38. The horizontal surface velocity (cf. Fig. 5.31) is plotted in blue: The velocity range across a 20 m stripe perpendicular to the profile (light blue area) and its average (thick blue line). The profile runs roughly along the central flow line (“stromstrich”), so that margin effects (lateral drag) are minimal. The horizontal surface velocity increases from (close to) zero at the front (below significance level) to over 60 cm a^{-1} at the high-velocity lobe, and then decreases again towards the talus. On the talus, the strongly fluctuating velocity is decoupled to the smoothed surface slope, but remains everywhere above the significance level. There are a few velocity data gaps where the image correlation failed: In front of the high-velocity lobe where it overrides the lobe below (non-translational movement, toppling) and on the talus (other factors leading to decorrelation).

In light grey is the unfiltered surface slope on a 20 m stripe along the profile (range and mean). The small-scale slope varies strongly along the profile and the range across

20 m stripe perpendicular to the profile is large, up to 30° . It reflects the small scale topography. The unfiltered slope angle is the angle of steepest descent, regardless of the direction. For example, slopes on the up-valley side of ridges face uphill. The small-scale slope is therefore not driving the creep, this is supported by the data: The velocity (blue) correlates poorly with the small-scale slope.

The orange line shows the slope extracted from the smoothed DEM obtained by Gaussian mean filtering with 100 m diameter, effectively acting as a low-pass filter that attenuates the small-scale topography. The large-scale slope correlates well with the velocity in the central section between 100 and 900 m on the profile. This central section is where the deformation is dominated by viscous creep. At the front and at the talus other deformation mechanisms must be dominant.

The strong topographic control (average surface slope) on the creep behaviour as expected based on physical considerations (Eq. 2.5) is investigated with a slope angle–surface velocity scatter plot in Fig. 5.39. The grey data points are from the entire rockglacier area. They are clustered in a wedge-shaped domain: The relict part (dark grey dots) is characterized by low velocities ($< 20 \text{ cm a}^{-1}$, Fig. 5.37), the few outliers are most probably due to non-translational movement (e.g. sliding, tumbling) and not due to cohesive creep that affects a large area. Higher velocities are reached at higher surface slope angles, in accordance to the shear-stress driven creep. The maximum slope angle slightly decreases with increasing velocity. Possibly, high average slope angles cannot be sustained by the viscous ice-debris mixture over long time periods.

The correlation is clearer when only a 20 m wide stripe along the central profile is considered, unaffected by boundary effects (lateral drag, non-translational movements). Three patterns emerge: (i) the velocity of the lowermost, relict part is low and independent of the slope (yellow dots). (ii) the middle part with the high-velocity lobe (dark blue) and the lobe in front of it (green) have a clear slope-velocity correlation. (iii) The correlation breaks down at the uppermost lobe towards the talus (light blue).

Slope–velocity relation

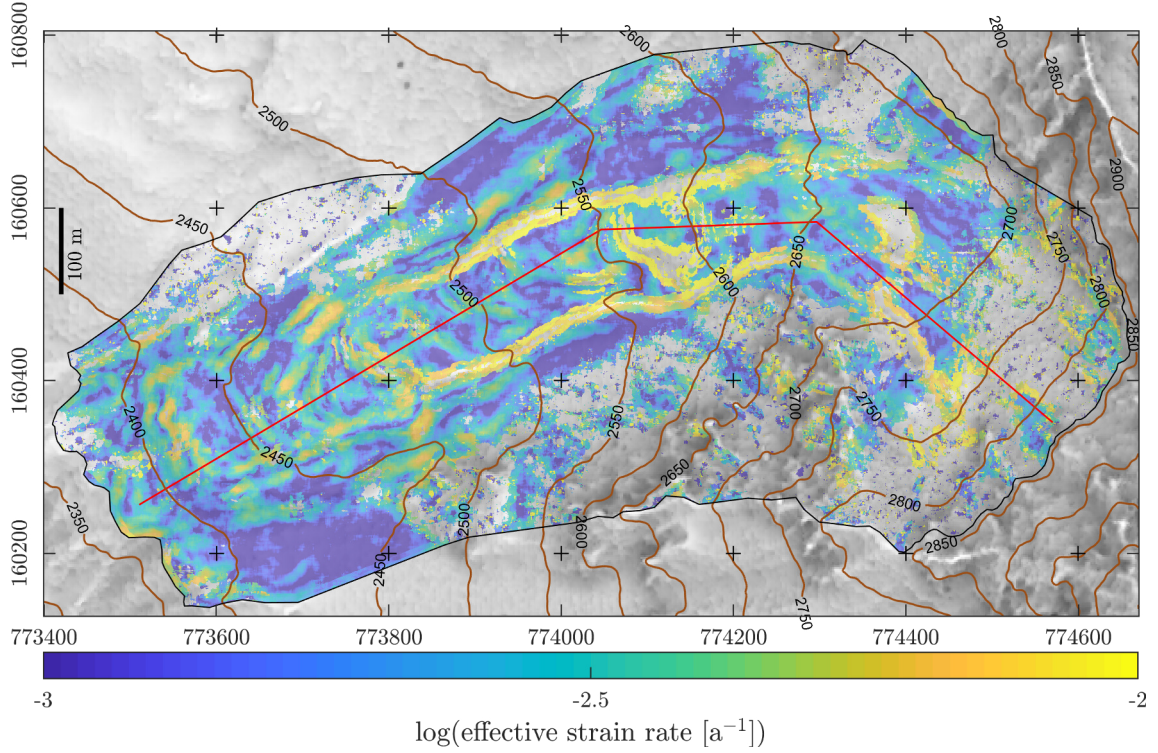


Figure 5.32: Horizontal effective strain rates $\dot{\epsilon}_{II}$ (Eq. 4.14), interpreted as a magnitude of surface strain rate or deformation intensity. It shows the deformation localisation along the margins of the deforming bodies that move *en bloc*. Computed with a 20 m spacing that bridges the data gaps. Nevertheless, the “fringes” around no-data areas are artefacts (e.g. high strain rates around the snow field and in the talus).

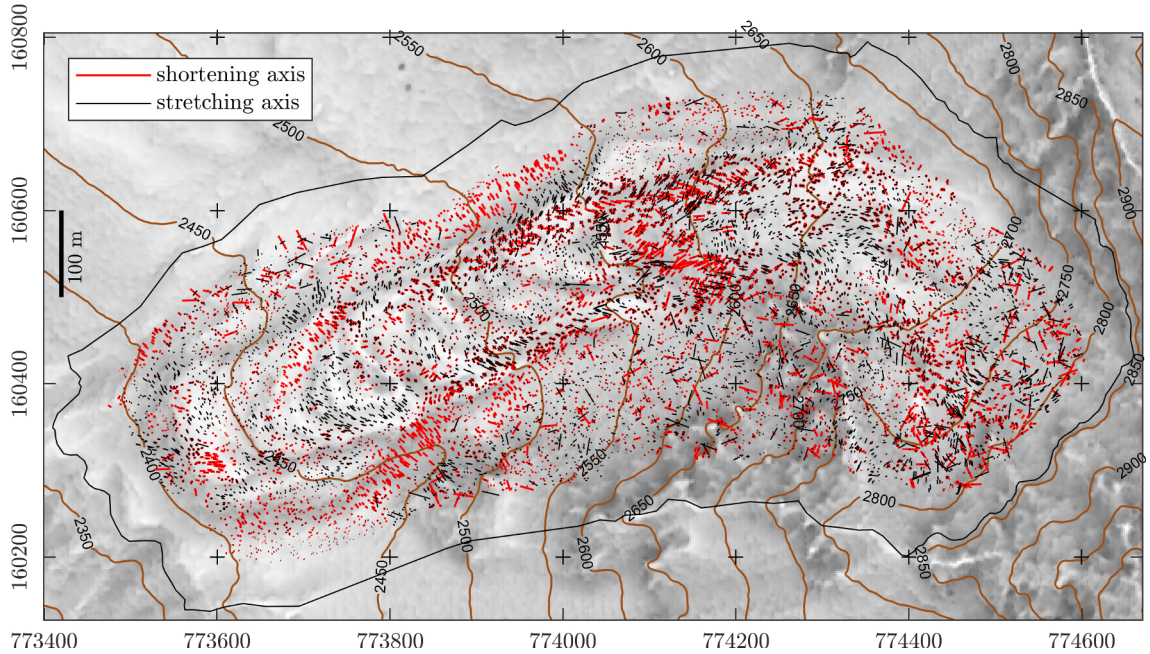


Figure 5.33: Horizontal principal strain rate axis showing the direction of maximum elongation and maximum shortening. The principal axes of strain rate and stress are aligned. Computed with 50 m spacing. Principle axis along the lobe-marginal data gaps are consistent. The random orientation of the axis in the talus suggests that they are artefacts.

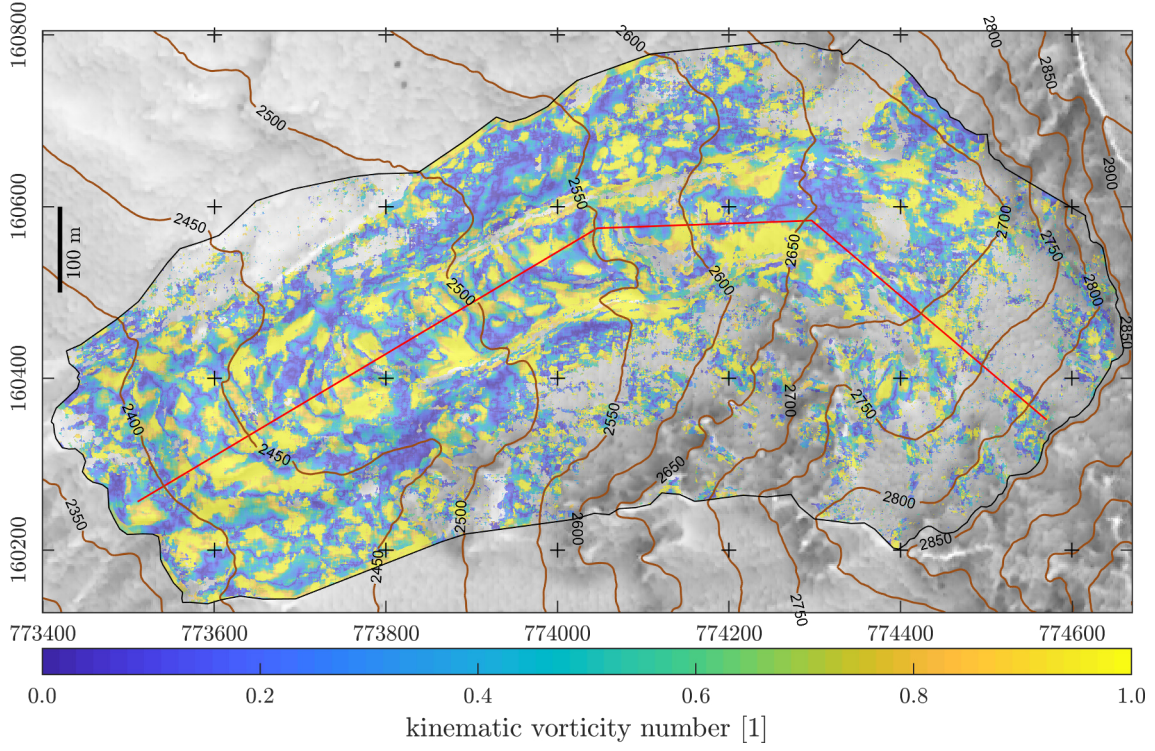


Figure 5.34: Horizontal kinematic vorticity number W_k . Simple shear, $W_k = 1$, prevails at the margins of the deforming bodies, and sub-simple to pure shear, $W_k \leq 1$, in their interior. Computed with 20 m spacing.

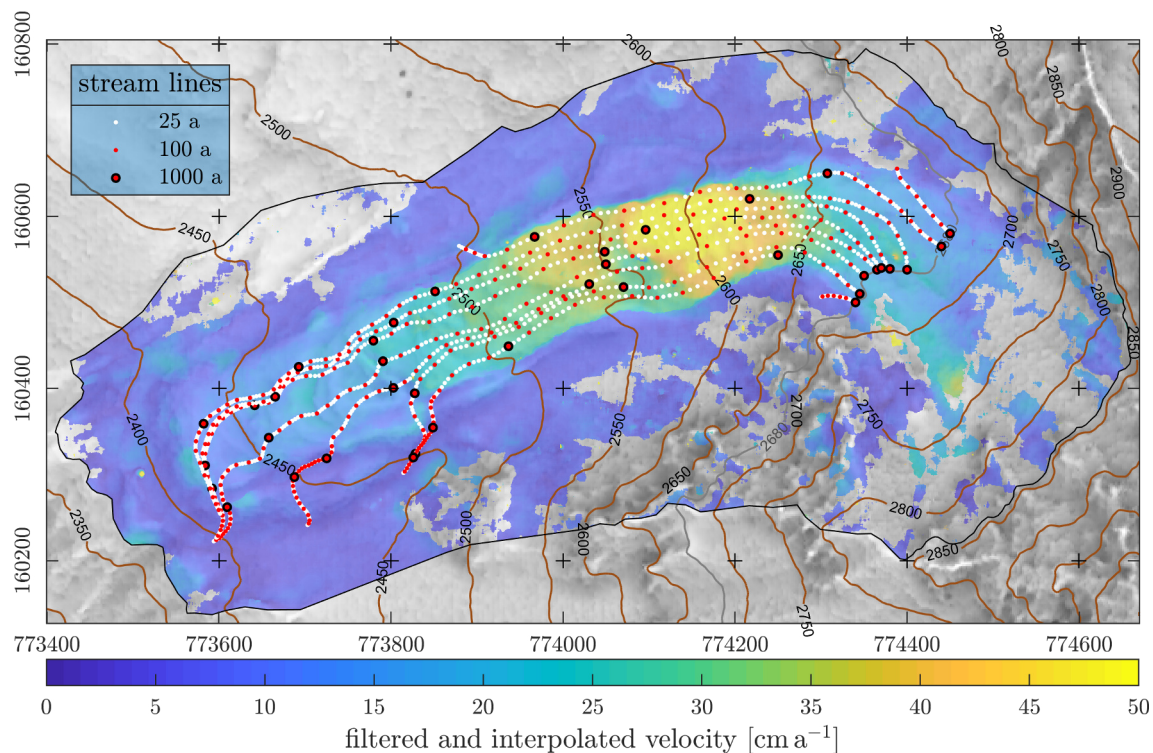


Figure 5.35: Down-flow stream lines for selected points at 2680 m contour line, calculated based on a smoothed and interpolated velocity field. It reveals the viscous flow pattern in map view: speed is highest in the center (along the central flow line or *stromstrich*) and decreases towards the margins (lateral viscous drag). The particle trajectories also show the slow, south-ward directed collapse of the relict front.

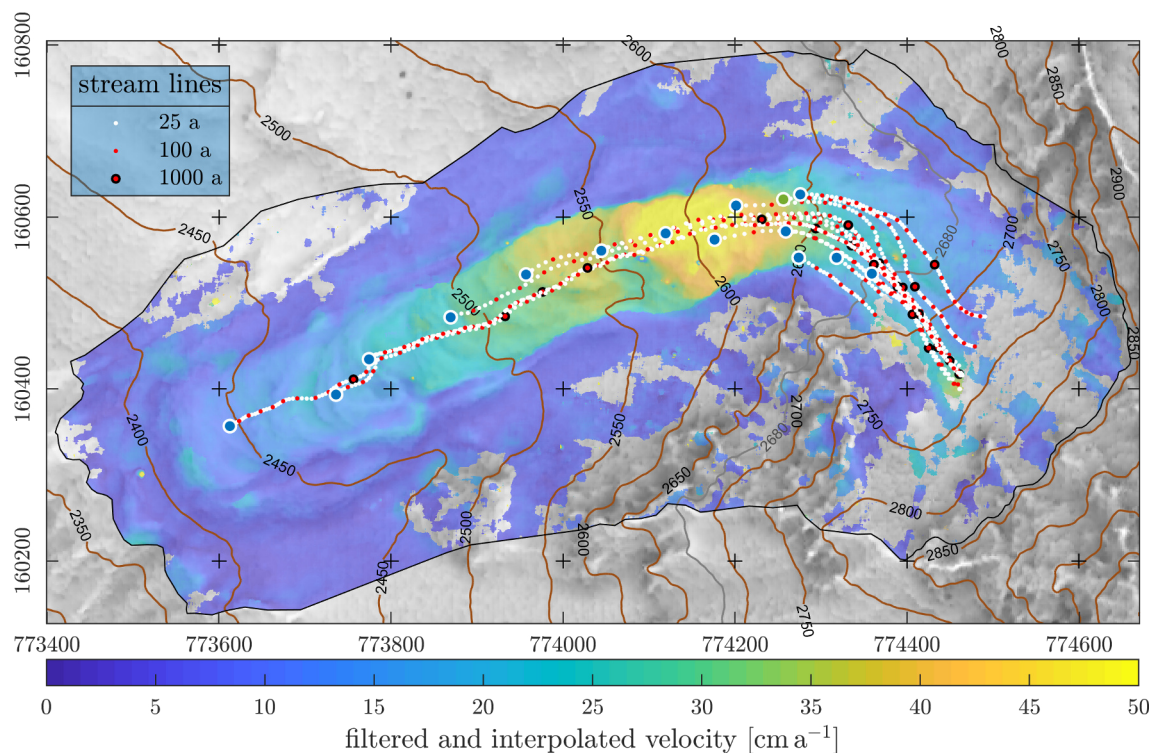


Figure 5.36: Up-flow stream lines from the TCN sampling points give a theoretical trajectory and travel time estimate for the sampled boulders.

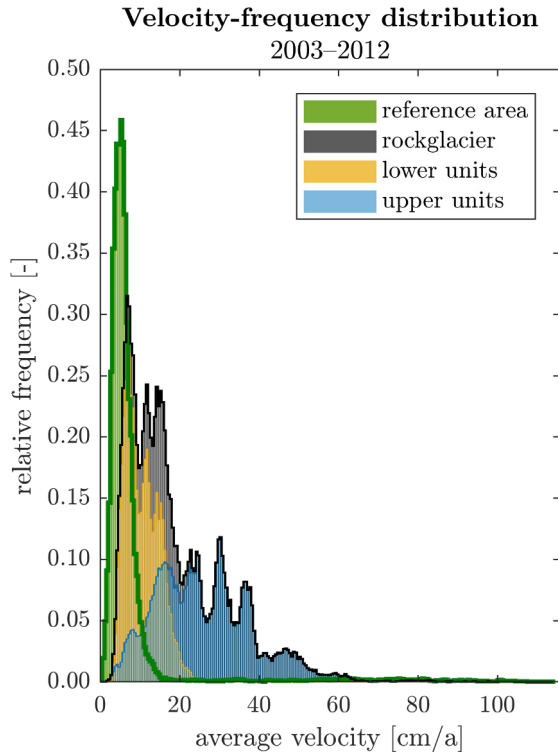


Figure 5.37: Histogram of the horizontal surface velocities for period 2003–2012 for the reference area and different part of the *Bleis Marscha* rockglacier. Cf. Fig. 5.30. The velocity of the lower part hardly exceeds 20 cm a^{-1} .

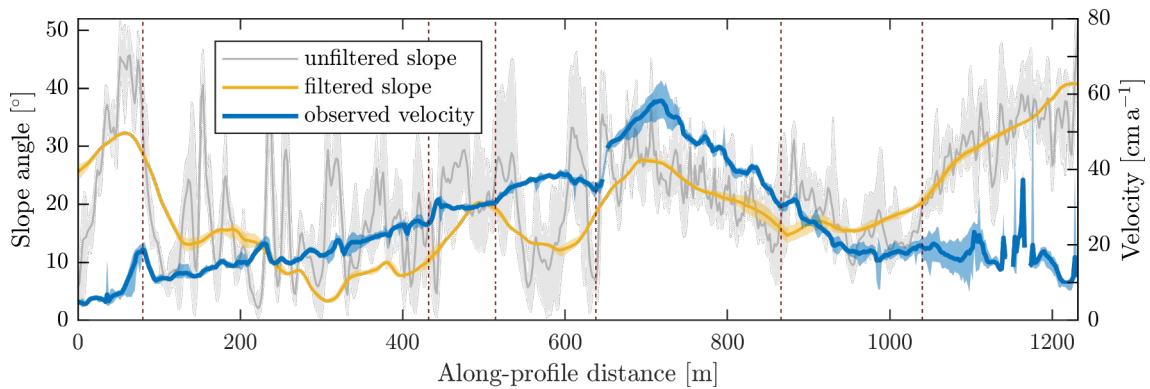
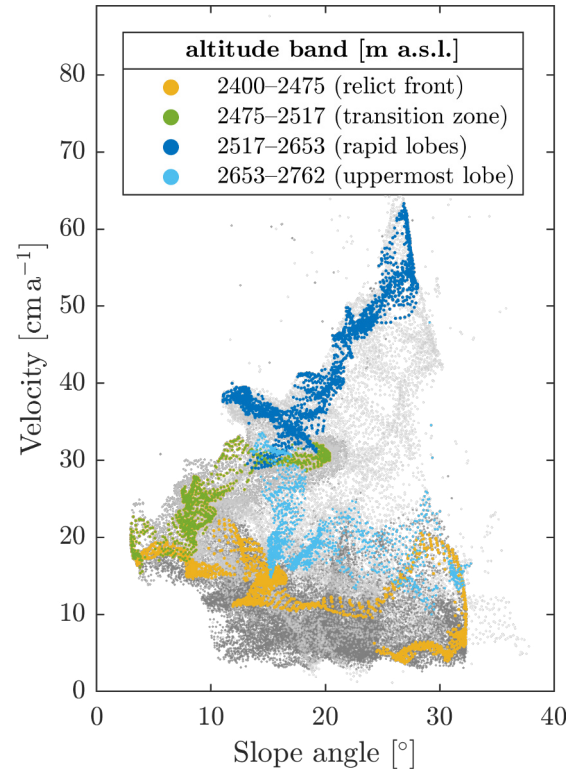



Figure 5.38: Longitudinal transect: slope and horizontal surface velocity (range and mean across a 20 m stripe along the profile). The speed correlates well with the 100m-averaged slope (smoothed), and sharp velocity gradients occur at small-scale slope breaks (dark red dashed vertical lines). Velocity data gap at 646–652 m and on the talus.

Figure 5.39: Scatter plot showing the correlation between the 100-m averaged slope (from smoothed DEM) and the horizontal surface velocity. The grey dots are data points on the entire rockglacier (lower part in light grey, upper active part in dark grey). In colour are the data points on a 20 m stripe along the central profile, where the effect of lateral drag is minimal. They are further subdivided in four altitude bands: The lower 500 m (again divided by the 30 cm a^{-1} isotach; yellow/green), and upper 500–1154 m (blue, and LIA lobe in light blue).



5.4 Numerical modelling

Main points	
<ul style="list-style-type: none"> • The <i>Bleis Marscha</i> rockglacier is parametrised in terms of its mechanical structure using field observations and literature knowledge. • The numerical experiments suggest that effective viscosity controls the deformation rates and patterns, not the density. • There is no unique solution to the inverse problem: Ambiguity between viscosity and thickness 	

The numerical modelling results \mathcal{D} for increasingly complex subsurface configurations \mathcal{M} (Figs. 5.40–5.46). In this section, the material parameters are presented as density and viscosity. The implications of the modelling results on the rockglacier material are treated in the discussion.

In its simplest form as in **FEM 1**, the rockglacier is parameterised as a single layer, representing the rockglacier core. Neither a boulder mantle nor a basal shear layer is implemented (Fig. 5.40). The rationale behind this oversimplification is to obtain a “reference model” to which the following more complex parameterisations are compared to. For a given rockglacier thickness, the material parameters are fitted to the observed surface velocity field. This gives an order of magnitude estimate of the rockglacier core density, $\rho_c \sim 1626 \text{ kg m}^{-3}$, and effective dynamic viscosity, $\mu_c \sim 4.5 \times 10^{14} \text{ Pa s}$. The modelled velocity curve is smoother than the observed one, which is intimately connected to the viscous flow. Furthermore, viscosity variations exert a much stronger influence on the modelled velocity than density variations. For constant material parameters, the *local* thickness and surface slope controls the magnitude of deformation.

In a next step, **FEM 2a**, the surface boulder mantle is added with the following material parameters: $\rho_m \sim 1890 \text{ kg m}^{-3}$, and $\mu_m \sim 8.5 \times 10^{15} \text{ Pa s}$ (Fig. 5.41). The stiff, heavy boulder mantle impedes the deformation, which is suggested by an overall smaller velocity, but also by dampened velocity variations. The boulder mantle seems to play an important role in stress distribution, mainly via its stiffness (high viscosity), not its high density.

The influence of the basal shear layer is investigated with the model **FEM 2b** (Fig. 5.42): A low-viscosity basal shear layer of thickness 3 m and viscosity of $\mu_c \sim 4.5 \times 10^{13} \text{ Pa s}$ is added. An easily deformable layer leads to overall higher velocities. The modelled surface velocity pattern is essentially a scaled copy of the reference model (Fig. 5.40).

In model **FEM 3a**, the morphologically-motivated hypothesis of a relict lower part is tested numerically by implementing a high-viscosity, high-density lower lobe, and the full stratigraphy with boulder mantle, core and basal shear zone in the intact upper lobes (Fig. 5.43). The rockglacier parts below 2500 m a.s.l. are implemented as ice-free debris with the same properties as the boulder mantle, except for the basal low-viscosity layer. It simulates for example the effect of the fine-grained shear zone that retains its properties despite the ice melt-out. While the observed velocities in the intact upper part can be reasonably reproduced, the modelled velocities in the lower part remain clearly too low.

The material parameters in model **FEM 3b** are horizontally freely adjustable. The result reproduces the observed velocity over the entire profile and suggests that the viscosity in the apparently relict lower part is only slightly higher than in the intact part (Fig. 5.44). In contrast, the viscosity in the steep, uppermost part close to the talus increases almost to boulder-mantle value. Apparently, the steep slope and the basal shear zone suffice to

reproduce the low surface velocities, and no additional internal deformation is required.

In a last scenario **FEM 4a**, the hypothesis that the steady velocity increase in the relict part, as well as relatively high velocities in the frontal part of unit III arise from pushing exerted by the rapidly advancing lobe above. In the numerical experiment, the upper lobes are removed while all other material parameters are as in the previous model. The modelled surface velocity drops from 20-40 cm a⁻¹ to 20 cm a⁻¹ (Fig. 5.45), which is the “background level” of the lower relict lobe. The influence zone reaches ~200 m downslope from the front of the pushing lobe, and is the longer, the less viscous the basal shear layer is.

Three vertical interfaces are implemented at profile meter 250, 550 and 800 to visualize vertical profiles of the horizontal deformation along “virtual boreholes” on the different rockglacier lobes (Fig. 5.46). The results for rockglacier parameterisations with the basal shear zone resemble measured borehole deformations. Maximum deformation in the deepest borehole is ~10 m below the surface (boulder mantle is 5 m thick).

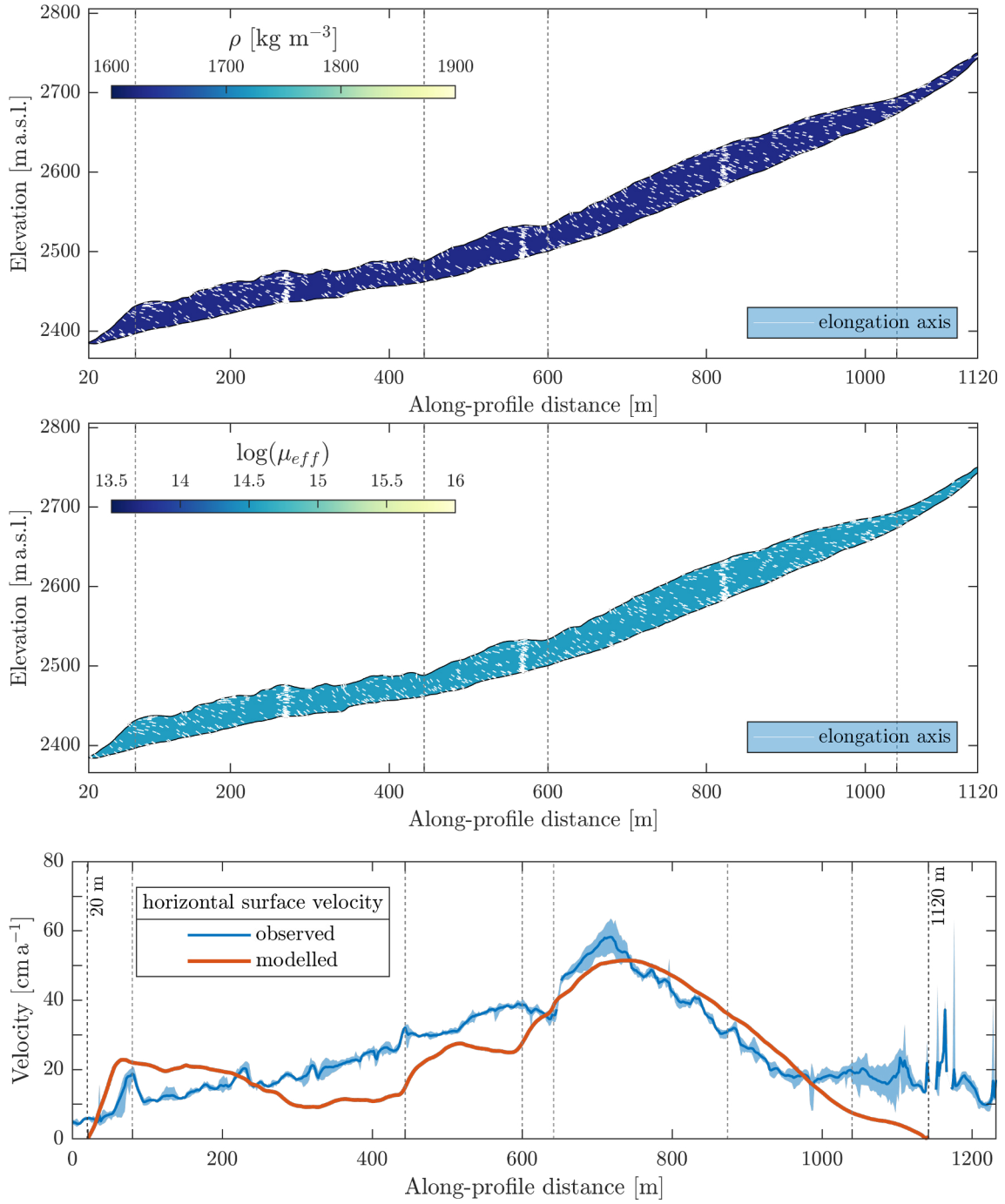


Figure 5.40: FEM 1: “Reference model” with simplest configuration.

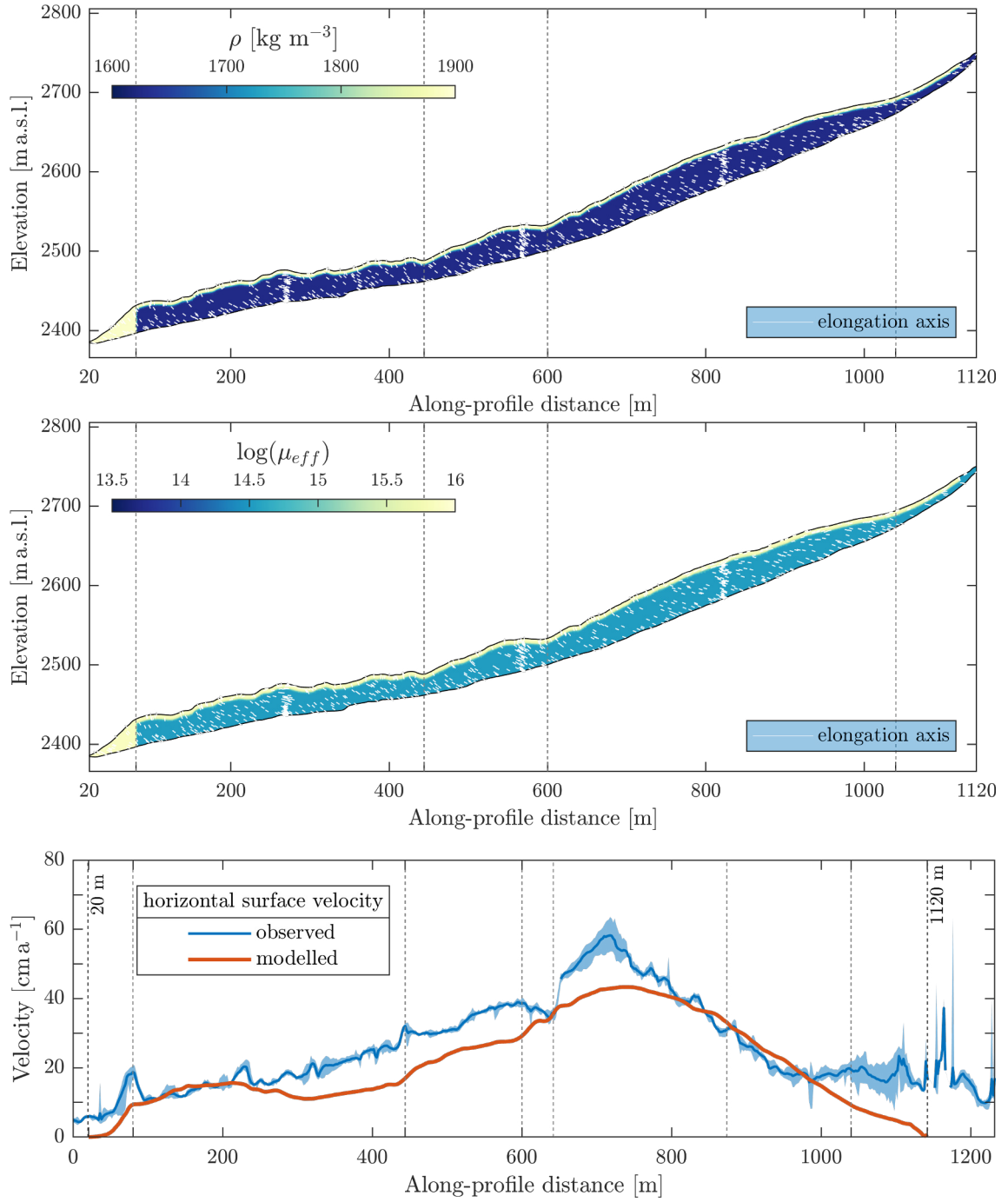


Figure 5.41: FEM 2a: Influence of boulder mantle (no basal shear layer).

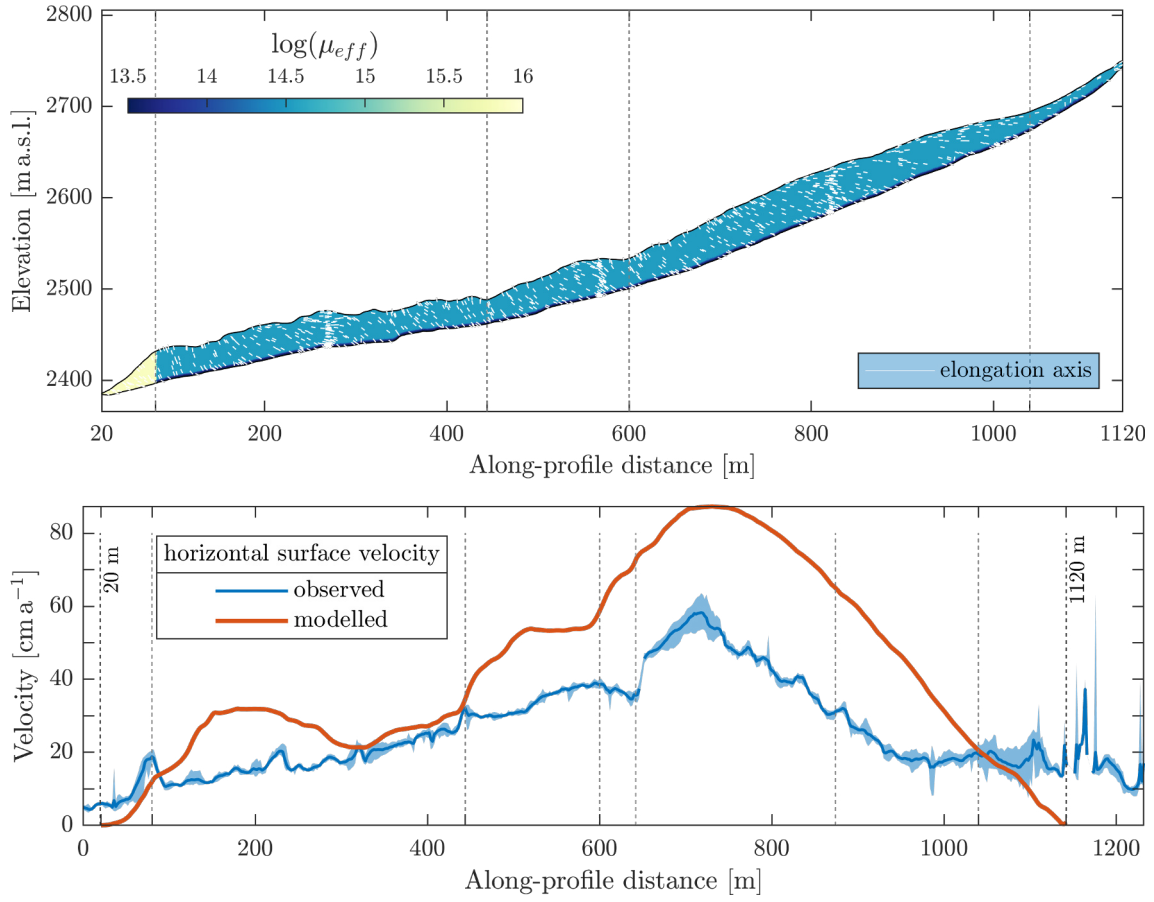


Figure 5.42: FEM 2b: Influence of basal shear layer (no boulder mantle). Density as in reference model FEM 1.

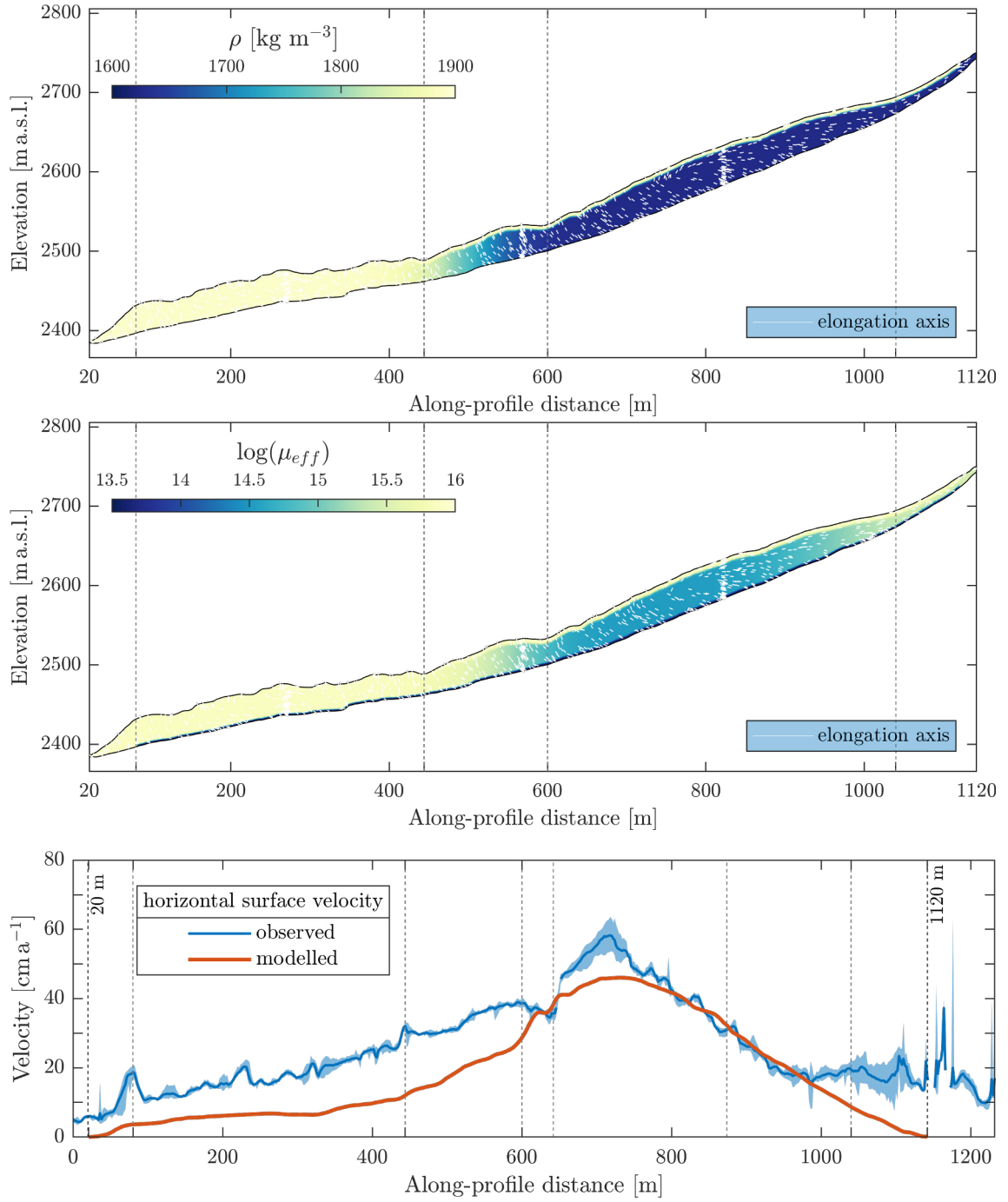


Figure 5.43: FEM 3a: Test of geomorphologically-motivated model.

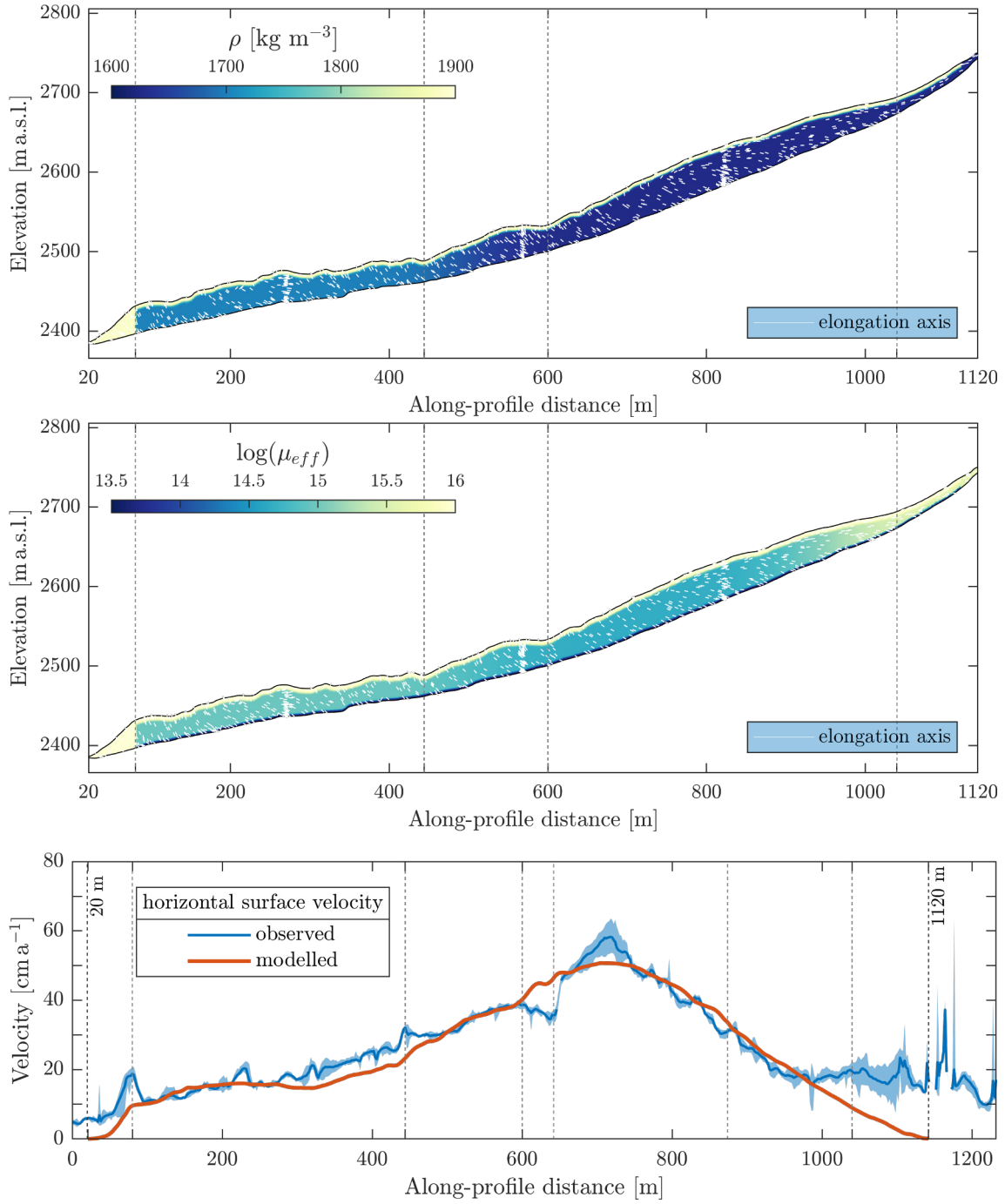


Figure 5.44: FEM 3b: “Best-fit parameterisation”.

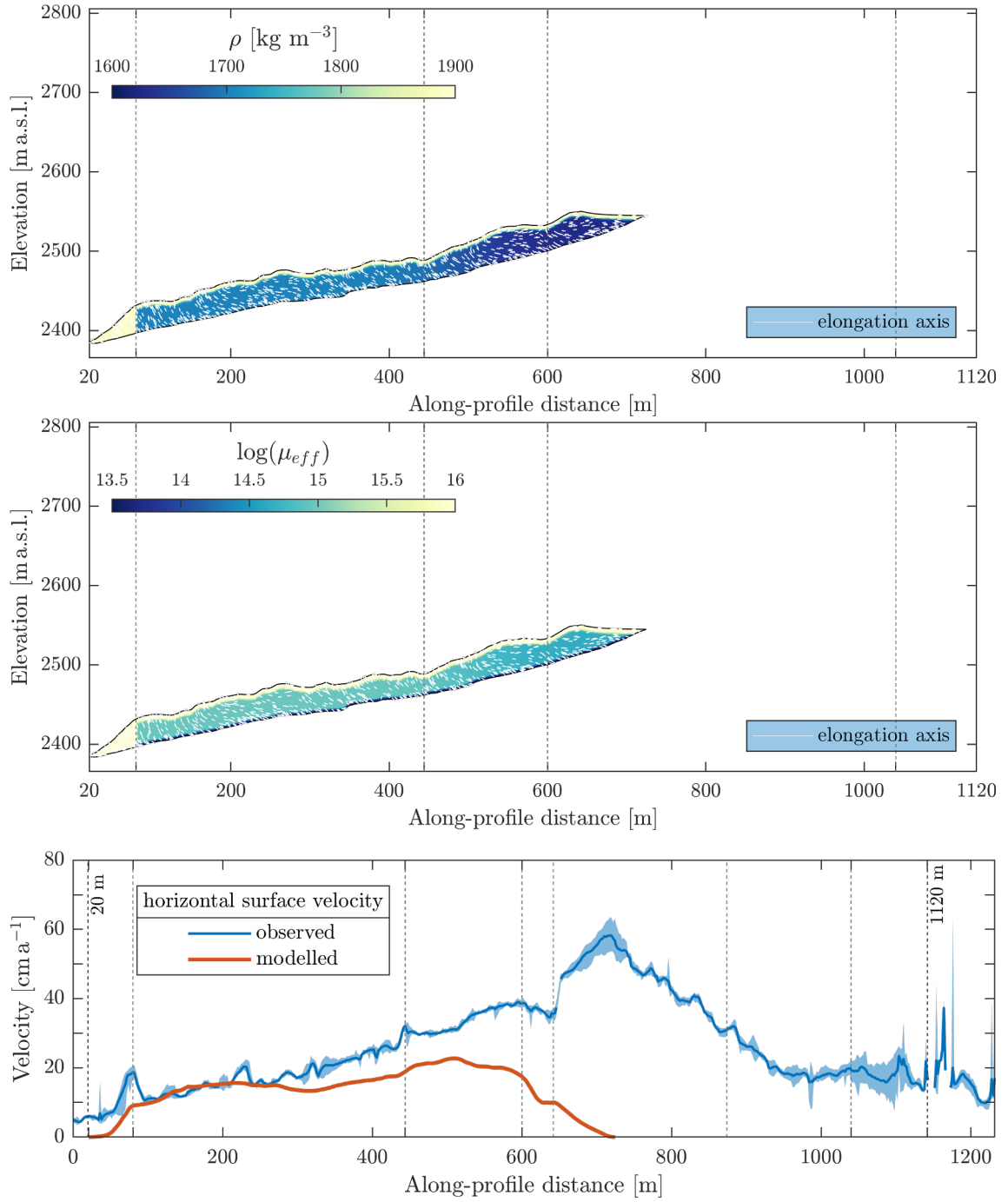


Figure 5.45: FEM 4a: Influence of rapidly advancing lobe on the relict part below. The rockglacier is parameterised without upper lobes, otherwise same configuration as in 3b (Fig. 5.44).

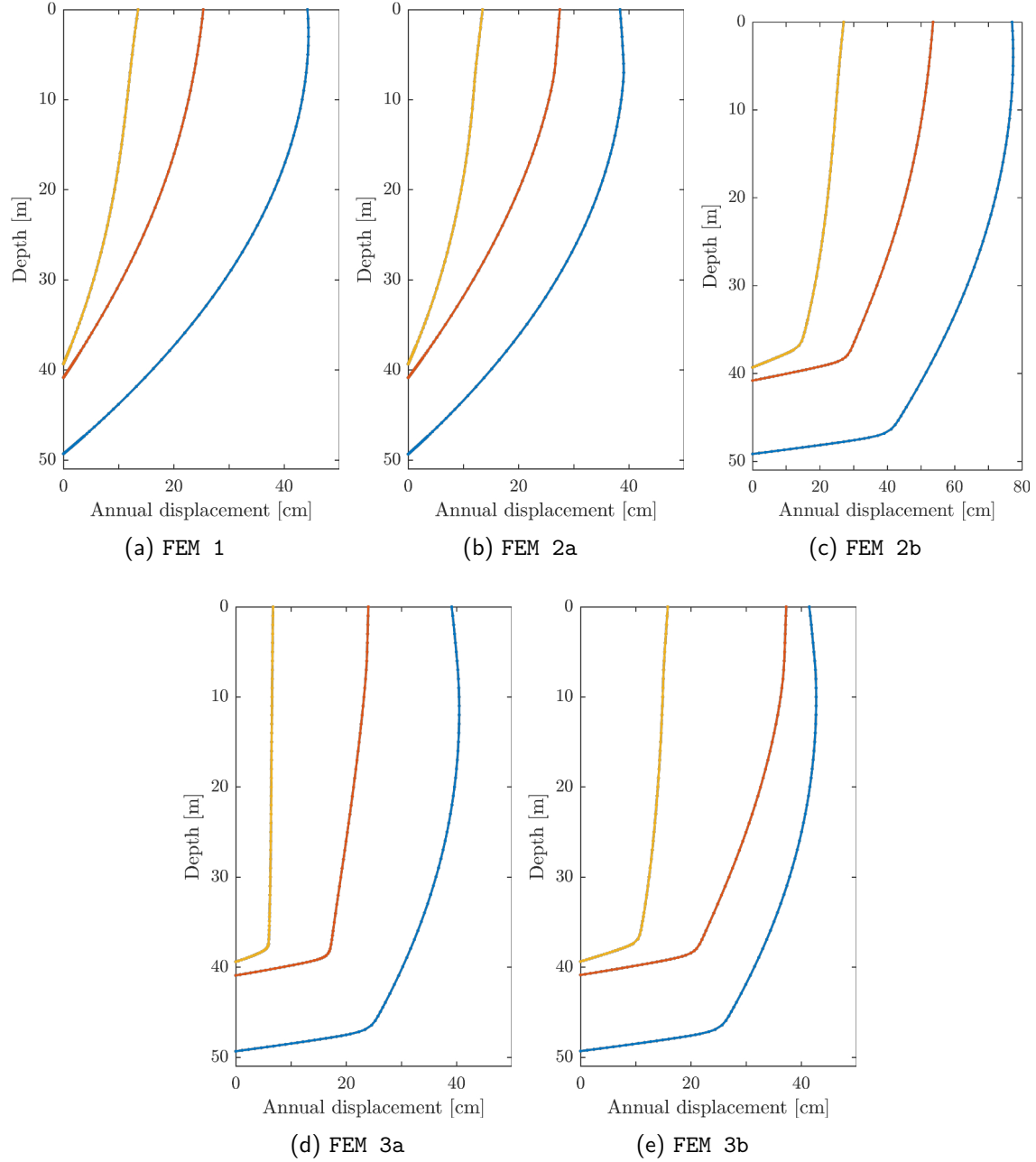



Figure 5.46: Modelled horizontal displacements along “virtual boreholes” in three rockglacier parts: lower borehole (profile meter 250, 39 m deep), middle borehole (m 550, 41 m), upper borehole (800 m, 49 m). The results for rockglacier parameterisations with the full three-part mechanical layering (boulder mantle, core, basal shear layer) resemble measured borehole deformations with strong strain localisation near the base. The NEWTONIAN model with viscosity layering emulates a more complex deformation mechanism as observed in rockglaciers. Maximum horizontal deformation in the deepest borehole is ~ 10 m below the surface within the core (boulder mantle is 5 m thick).

6 Discussion

Main points	
<ul style="list-style-type: none"> • Although the assumption of a linearly viscous stress-strain rate relationship is debatable, the deformation along “virtual boreholes” are similar to observed borehole deformation, thanks to the implementation of vertical viscosity layering. • The deformation mechanism can be described as viscous on a 10 m-scale. The micro-scale deformation might be non-viscous. • The found effective viscosity is an effective material parameter valid for the bulk material on a 10-m scale over at least decadal time periods. None of the constituents have this viscosity. 	

6.1 Limitations

Field work, morphology

A-priori knowledge of the morphology is essential for choosing the sampling locations and interpreting the exposure ages. Field observations are necessary to understand details of the surface structure and material aspects (lithologies, etc.). However, rockglaciers are large and complex landforms which are easier to grasp in its entirety by looking at aerial images or digital elevation models. Field studies and remote sensing approaches are therefore complementary.

The morphology is a snapshot of the accumulated strain history of millennia, where different processes have acted, different structures are superimposed, and others wiped out. A problem specific to rockglaciers is the decision whether, for example, a non-creeping lateral, longitudinal ridge is (i) of dynamic origin (e.g. marginal shearing, cf. lava flows or levees of debris flows) and thus belongs to the current generation of the debris stream, or (ii) are vestiges of an older activity phase, indicating different rockglacier stages, or finally (iii) is a lateral moraine of a former glacier deposited prior to the rockglacier formation [Frauenfelder and Käab, 2000; Barsch, 1996, p. 27,218]. For example, we interpret the vegetated outer ridges on the lower part of the Bleis Marscha rockglacier as part of the rockglacier, not as Egesen moraines [Frauenfelder et al., 2001].

Exposure ages: first-order pattern

To the first order, the exposure ages anticorrelate with altitude and correlate with distance along the longitudinal profile from the talus towards the front (Fig. 6.1). The observed clear age trend spanning the last ~9 ka agrees (i) with the short-term kinematic measurements (moderate surface velocities of 30 cm a^{-1}); (ii) with published Schmidt-hammer exposure studies e.g. by Frauenfelder et al. [2005]; Kellerer-Pirklbauer et al. [2008]; Rode and Kellerer-Pirklbauer [2012]; Scapozza et al. [2014]; Winkler and Lambiel [2018]; and (iii) with our understanding of the periglacial nature and the mechanical behaviour of rockglaciers. This is clear evidence that the rockglacier has not formed in short, discrete events, but slowly by the down-slope creep over activity periods of centuries to millennia. The boulders are passively transported at the rockglacier surface between talus and top of front slope, and the furrows and ridges are preserved.

On the presently active, uppermost lobes, the TCN exposure ages near the stromstrich

(central flow line) allow a linear regression with distance from the rockglacier root, giving a plausible mean velocity of 30 cm a^{-1} and an initial position at 1058 m (“zero age crossing”). This is roughly where the talus passes into the uppermost rockglacier lobe. We conclude that the exposure ages on the active lobe have negligible systematic errors, i.e. practically no overall age shift due to inheritance/pre-exposure (systematically “too old”) or nuclide loss/incomplete exposure (systematically “too young”). This implies that the transit time in the talus is not recorded by the exposure ages, either because it is shorter than the analytical uncertainty and the “lost time” due to snow shielding (not more than decades), or because the boulders were covered in the talus and surfaced only on the rockglacier.

The laminar flow behaviour of a rockglacier implies that no mixing occurs, fluctuations or even exposure age inversions are therefore introduced by surface processes (in the boulder mantle) that affect the nuclide inventory of boulders individually. In fact, the data shows that these fluctuations are of second order. An ideal exposure age requires a single-stage, uninterrupted and undisturbed exposition of the rock face [Ivy-Ochs et al., 2007].

Second-order fluctuations

It is important to note that there is only pre-exposure that leads to “too-old” ages, a process that affects the boulder prior to entering the rockglacier system. In contrast, there are many processes that can lead to incomplete exposure and “too-young” ages [Ivy-Ochs et al., 2007; Heyman et al., 2011] while travelling on the rockglacier surface, for example intermittent boulder instability (self-shielding), rotation or toppling in response to heave, subsidence or collapse, weathering or spalling, and snow shielding.

Incomplete exposure is more likely than prior exposure

The apparent age inversion of the ^{10}Be ages of Err 2 and 15, where Err 15 is 2.4 ka younger than the further up-slope sampled Err 14, cannot reflect internal creep processes, but processes near the surface. We trust the exposure age of the lowermost sample Err 1. Because of the distance to the rockglacier root and proximity to Egesen moraines, we expect an early Holocene age [Frauenfelder et al., 2005]. Two scenarios are possible:

1. The ^{10}Be ages of Err 2 and 15 are “too young” by 2 to 3 ka. This shift cannot be explained by snow shielding, but by boulder rotation or spalling. This part of the rockglacier shows signs of collapse, and the boulders might have rotated during settling.
2. The ^{10}Be age of Err 14 is “too old”, implying inheritance. While we overall do not find inheritance, it can never be excluded for an individual case. But it is not likely.

We therefore think that the first scenario is more plausible.

The shielding effect of the snow cover is the largest single factor of uncertainty [Böhlert et al., 2011], because it is very difficult to estimate the typical snow cover during the entire Holocene. It exerts a multiplicative effect, and is in the order of 10%, leading to uncertainties in the error of decades to centuries. In contrast, the effect of erosion is small (not more than decades) and well known for the quite weathering-resistant Err/Julier granite.

Effect of snow and erosion

Illumination-invariant orientation correlation is a robust image correlation method that yielded reliable displacement results for large parts of the rockglacier, and only sparse post-processing (noise filtering) was necessary. The accuracy is critically determined by the pre-processing steps (orthorectification, co-registration) needed in creating the orthophotos, and should be assessed. The algorithm configuration (template and search window size) must be tested.

Image correlation

The image correlation results yielded rockglacier horizontal surface velocities up to one order of magnitude above significance level of 5 cm a^{-1} . In interpreting the data, it is

important to bear in mind that strictly horizontal translational motion is recorded. First, this means that rotational motion (tumbling, sliding) of boulders cannot be quantified. This poses no issues on the coherently, viscously deforming rockglacier body, but the matching algorithm fails at the margins. Such data gaps outline the advancing and over-riding lobes. On the other hand, it is difficult to estimate the advance rates. Second, the vertical deformation caused by the advection of the rugged surface, or by heave or ice melt-out are not recorded. The lacking data in the third dimension cannot be computed because incompressibility does not hold on a rockglacier surface. The kinematic boundary conditions are not fully resolved, and its assessment must remain incomplete. The long temporal baseline of 9 years means that seasonal variations in surface creep rates are not captured. Since we have no other surface velocity measurements, we cannot construct a time series to assess inter-annual to decennial variations for the *Bleis Marscha* rockglacier.

Numerical modelling

The same computer code as in Frehner et al. [2015] is used, and many of the therein discussed aspects apply analogously in this study.

The model simulates viscous deformation, which describes the deformation of the ice-rich rockglacier core, more specifically the deforming interstitial ice. The effect of the debris on the viscosity depends on the temperature [Moore, 2014] and involves complex processes at the debris-ice interface. With the continuum approximation, material parameters are averaged in space and non-viscous processes neglected. The deformation occurs over time scales longer than the Maxwell time which separates short term elastic behaviour (like a solid) from long term viscous behaviour (like a fluid). The viscosity is therefore a scale-dependent, homogenized, effective material parameter valid for bulk material on large spatial and long time scales. Neither the ice nor the debris has the estimated viscosity. The numerical modelling provides a bulk material property that cannot be estimated in the lab.

Non-viscous deformation processes that occur at the rockglacier front (sliding) cannot be simulated, and because of the fixed base the rockglacier cannot advance. The goal is not to attempt to reconstruct the evolution of the *Bleis Marscha* rockglacier *numerically*, but to perform numerical experiment for which one timestep is enough. It is therefore neither necessary to know the previous deformation history (thanks to the instantaneity property of a Stokes flow), nor to include a temperature-dependent viscosity.

A Newtonian rheology, i.e. a linear stress-strain rate relationship, is assumed, although the localised deformation in the shear zone is more accurately described by a more complex rheology (e.g. a viscous power law or frictional laws). The deformation above the shear zone is well captured by the NEWTONIAN flow law [Frehner et al., 2015]. The vertical deformation profiles in the “virtual boreholes” (Fig. 5.46) are similar to observed deformation measurements (Fig. 2.3). We conclude that the NEWTONIAN model with the vertical viscosity layering (low viscosity basal layer) emulates more complex, non-linear deformation mechanism as observed in rockglaciers (phenomenologically, “by appearance”). While this is beneficial in terms of mathematical tractability and computing speed, it has limited value for improving our understanding of the critical shear layers.

Another critical implication of the NEWTONIAN rheology is incompressibility. Measured three-dimensional rockglacier surface displacement fields show that the horizontal components dominate over the vertical one, and “volume-changing processes do not significantly alter the dynamics” [Frehner et al., 2015]. Additionally, the model is constrained with horizontal measured velocity field.

The two-dimensional model tacitly implies that the rockglacier is infinitely wide. In reality, the non-moving sides exert a lateral drag that slows down the movement (see the stream line Fig. 5.35). Frehner et al. [2015] estimate this of 35%. Since the STOKES problem is linear, this correction can be linearly carried over to viscosity, which need to be slightly corrected. However, it does not affect the viscosity ratios between different rockglacier parts, and does not detract from the modelling findings.

Two issues arise with inverse problems [Snieder and Trampert, 1999; Oldenburg and Li, 2005]: (i) ambiguity or non-uniqueness and (ii) error propagation.

Inverse problem

Non-uniqueness means that theoretically infinitely many models explain the data equally well, even though the forward operator G is unique. It is caused by the finite availability of data that cannot suffice to resolve unambiguously a continuous model space with infinitely many model parameters. Intuitively, it is not possible to infer with arbitrary resolution the two-dimensional subsurface structure with data along a one-dimensional surface profile. More importantly, there is a fundamental ambiguity attached to the physical forward problem formulation: Consider, for example, the surface velocity profile. Higher surface speed can equally well be achieved with either greater thickness, steeper inclination or lower viscosity (or any combination). Errors in the data space are mapped into the model space, the forward problem operator itself could be flawed, and the precision of the numerical evaluation of G is limited. In practice, this means that because the model is fitted to data from 2003-2012, the inferred structure is drawn to a rockglacier state during the measurement period. The long baseline is clearly an advantage, because the effects of a single year (e.g. the warm summer 2003 with exceptionally high creep rates [Delaloye et al., 2010]) are not carried into the model.

The numerical experiments suggest that creep rates and stress distribution are governed by the surface topography (average surface slope), thickness and effective viscosity, and are much less sensitive to density or basal topography. The shape of the base of the creeping permafrost body is therefore difficult to constrain. In detail:

Findings from numerical experiments

- The simplest parameterisation where the rockglacier is treated as a single debris-ice layer shows that the deformation is most sensitive to local thickness and surface slope.
- The boulder mantle acts like a “stiff, rigid blanket” laid over the viscous core: it leads to a more distributed deformation and smoothed velocity variations. The boulder mantle exerts this effect via its high viscosity, not the high density.
- Deformation in the low-viscosity basal shear layer, although only 3 m thick, accounts for 60% of the modelled horizontal surface deformation, in agreement with borehole deformation measurements. This clearly shows that deformation processes in shear layers control the overall deformations to a large degree.
- Interactions between different lobes and units of different age occur via stress transmission of the icy matrix.

An issue common to geophysical problems is what the geophysicist finds out – here the material parameters in terms of density and effective viscosity – is not what the geologist is interested in: Effective viscosity is treated as a proxy for the ice/water content. The interpretation of the estimated model parametrization (appraisal problem) is however difficult: Amount and pathways of liquid water are highly variable and unknown. Unknown, but at least constant over years is the stratigraphy and ice content in the rockglacier. We hypothesize based on the long-baseline argument that we can cautiously interpret the viscosity in terms of ice content: The lower the viscosity, the higher the relative ice-to-debris ratio.

Appraisal problem

6.2 Synthesis

The morphology, TCN exposure ages and the horizontal surface velocity along the longitudinal profile are shown in Fig. 6.1. The morphological and kinematic subdivision of the *Bleis Marscha* rockglacier, later used to address different rockglacier parts in the text, are introduced.

Since both the exposure ages and the surface velocity field are related to surface processes, they can be compared in a meaningful way (Fig. 6.2). There are two main clusters of ages in the travel time–exposure age space separated by the line of equal time estimates (“1:1 line”):

- $t_{exp} < t_{trv}$ (below 1:1 line): The exposure ages are slightly younger than the age from the travel time estimate suggests. This is the “forbidden zone”, because provided the exposure ages are ideal and the velocity field representative, the elapsed time at the surface cannot be shorter than the travel time. In fact, under such ideal conditions, the boulders should move along the 1:1 line. In reality, neither of the two conditions is fulfilled: the exposure is incomplete because the boulders slightly rotate during travel, and the velocity field varies over time. Additional to the uncertainties related to exposure time and travel time comes the unknown transit time in the talus before the block entered the rockglacier system, and the exposure-age underestimation due to the snow cover that increases with altitude. However, the discrepancy between t_{exp} and t_{trv} is small (decades to centuries), and all data points are from the rockglacier lobes where the surface velocity field is passably representative (mean horizontal surface velocity of 30 cm a^{-1} , discussed below). The field immediately below the 1:1 line is characteristic for rockglacier lobes that are presently active, and whose surface is still advected downslope. The exposure ages can with the necessary caution be addressed as (minimal) travel times. It also shows that pre-travel nuclide build-up, inheritance or pre-exposure is very unlikely.
- $t_{exp} > t_{trv}$ (above 1:1 line): The exposure ages considerably exceed the travel time age; the discrepancy is one order of magnitude larger (centuries to millennia). The samples are all located in the lower parts of the *Bleis Marscha* rockglacier that are presently relict. The travel time estimate must not be overinterpreted: In the lower, now relict lobes, today’s surface speed ($10\text{--}20 \text{ cm a}^{-1}$) is not representative but was most likely higher when these lobes were active. In the lower part, the speed is underestimated. Contrarily, in the upper rockglacier part the stream lines pass through active lobes that did not exist at the time the lower lobes were active; the speed might be overestimated in the rapid lobe. The situation is worse on a polymorph/multi-unit rockglacier because of the changing root topography compared to a “simpler” rockglacier consisting of a single debris stream. Despite these uncertainties, the morphologically relict appearance and the relation of rockglacier length (1200 m) and typical surface speed ($\sim 30 \text{ cm a}^{-1}$) clearly indicates that the TCN exposure ages ($< 9 \text{ ka}$) are too old to be addressed as travel time estimates. The field above the 1:1 line is characteristic for rockglacier lobes whose activity phase has ceased: A long time has passed since surface advection came to a halt, and the travel time is hidden in the uncertainty of the exposure age. The exposure ages are rather an inactivity age than travel time estimate.

The dolomite boulder with the ^{36}Cl age (Err 8) lies roughly on the same “travel time contour line” as the granite boulders with ^{10}Be ages of Err 5, 6, 9; but has a 2 ka older exposure age. We consider it a “too old” outlier. The reason for the discrepancy is likely

the different attenuation profile of ^{36}Cl with respect to ^{10}Be : The highest production rate is not immediately below the surface, but at shallow depths [Alfimov and Ivy-Ochs, 2009]. The ^{10}Be age of Err 11 morphologically belongs to the uppermost lobe and is thus expected to plot below the 1:1 line. We hypothesize that the high-velocity lobe (up to $50\text{--}80\text{ cm a}^{-1}$) has sped up only recently, such that the measurements overestimate the velocity along its path, and the travel age is thus underestimated. Maybe the lobe becomes detached from the source area, possibly due to warming, which is commonly observed on many rockglaciers.

“The surface velocity of a creeping mass is the cumulative horizontal deformation over depth and thus, is the maximum horizontal velocity found over the vertical velocity profile. The overall advance rate of the entire creeping body is mainly determined by the average horizontal velocity with depth and mass loss due to ice melt at the front. As a consequence, the actual advance rate can be considerably smaller than the surface velocity and, therefore, surface ages constitute a minimum landform age.” [Frauenfelder et al., 2005]. Surface-exposure ages of rock glacier need to be treated as minimum landform ages [Frauenfelder et al., 2005; Kellerer-Pirklbauer et al., 2008; Scapozza et al., 2014; Winkler and Lambiel, 2018; Haeberli, 1985; Frauenfelder et al., 2008].

Relation exposure
age—landform age

While this theoretical concept is sound, a wide range of values for the ratio between surface velocity above the front and advance rate have been found empirically, reflecting differences mainly in volumetric ice content and vertical velocity profile. Whereas Kääb and Weber [2004] estimated that the total age of the considered rockglaciers is 2 to 5 times higher than the minimum age obtained for the surface, Winkler and Lambiel [2018] judged the lowermost surface age of their studied rockglacier as “as rather representative than only as minimum age for initiation of rock glacier development” based on morphological position of the rockglacier front near the Late Glacial and early-Holocene moraines. Neither the internal composition of the *Bleis Marscha* rockglacier nor its vertical velocity profile near the lowermost front is known, certainly not for the time when it was active. The onset of formation of the first rockglacier generation must thus be interpreted with the available morphological observations and considering the palaeoclimatic history [see Sequence of events].

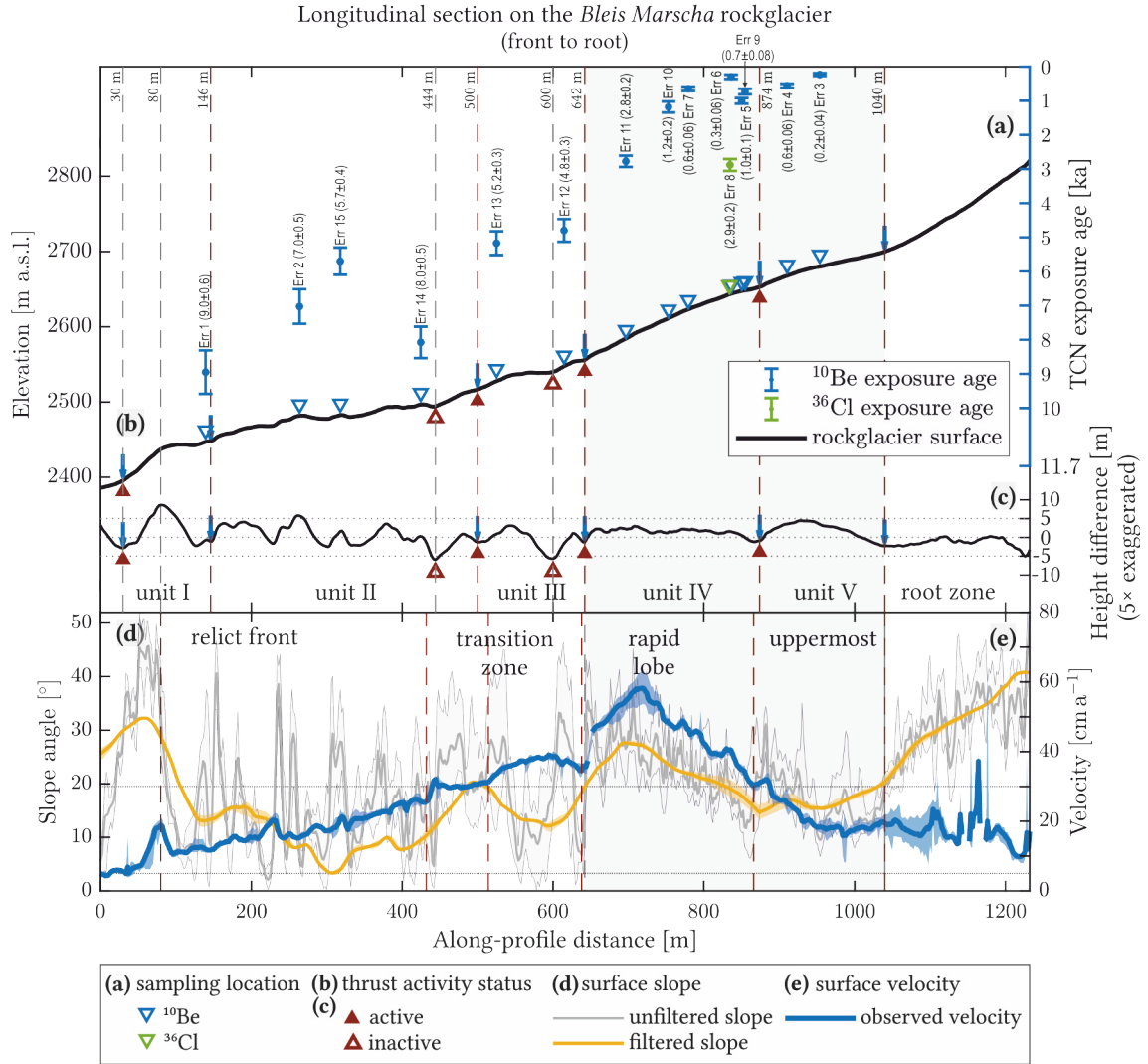
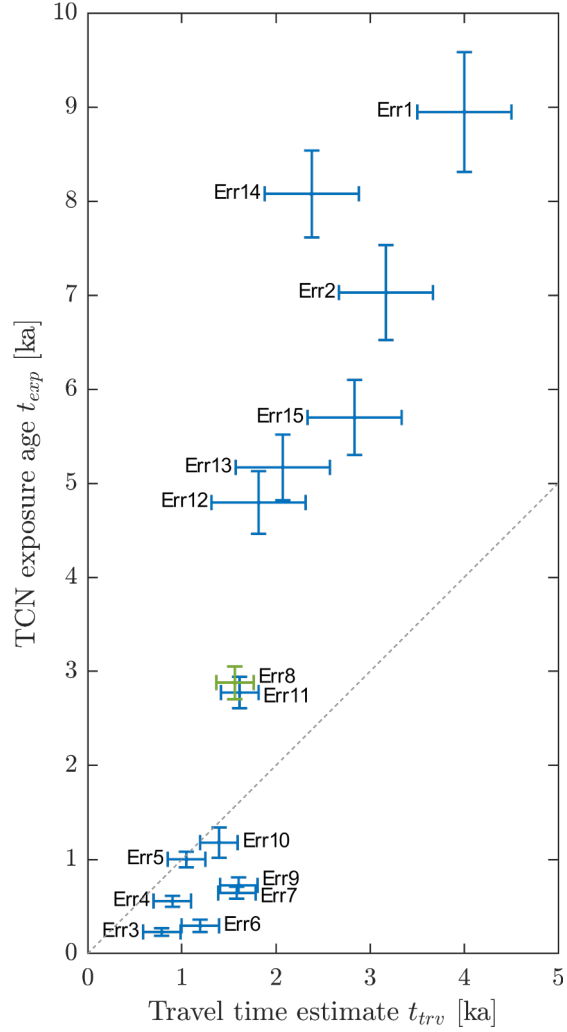


Figure 6.1: Data synthesis: Longitudinal section showing (a) TCN exposure ages, (b) relief, (c) small-scale relief, (d) slope (raw and smoothed) and (d) horizontal surface velocity. The morphological and kinematic subdivision of the *Bleis Marscha* rockglacier are introduced. Compare with the map view in Fig. 6.8.

Top panel: Relief, small-scale relief and TCN exposure ages along the longitudinal profile. The small-scale relief is a high-pass filtered relief and computed by subtracting a smoothed DEM from the original DEM. It emphasizes small-scale features. The sharp breaks in surface slope mark the outcrop of thrust planes of overriding lobes. The morphological subdivision of the rockglacier is based on thrusts. Note that the important break in slope that divides fast from slow moving part as distinguished by the IMCOR data is hardly visible in the profile, because the strike of the scarp is oblique to the profile.

Bottom panel: Slope and horizontal surface velocity along longitudinal profile. Important is the high coincidence between breaks in surface slope (see small-scale relief) and sudden, sharp changes in surface velocity. The kinematic subdivision of the rockglacier is based on these sudden velocity changes. Division in “fast” and “slow-moving” parts by a threshold velocity of 30 cm a^{-1} . Sharp up-slope velocity increase (large gradient) means “differential movement”: the upper lobe advances faster and overrides the lower one. Judging from the morphology at these scarps, the strain seems localised. The “velocity jumps” are therefore linked to thrusts, which are termed “active thrusts”, in contrast to the morphologically identified thrusts across which there is no velocity jump (any more), these are “inactive (relict) thrusts”. The activity status as assessed in the field agrees with the velocity data. Surprisingly, there is no significant velocity gradient across the break in slope at 600 m that looks important in the field; this thrust has become inactive.

Figure 6.2: Travel time estimate t_{trv} (short-term kinematics) versus exposure ages t_{exp} (long-term kinematics). Travel time estimate t_{trv} for each boulder is derived from the image analysis (Fig. 5.36) as the travel time between the current position of each sampled boulder and the reference contour line of 2700 m.a.s.l plus 300 years to reach up to the root zone. Uncertainties of the estimated travel time Δt_{trv} are estimated as 200 a for the intact upper part and 500 a for the lower relict parts. Uncertainties of the exposure ages Δt_{exp} are the analytical uncertainties. The horizontal axis is the along-profile distance (from root to front, Fig. 6.1) transformed to time via the present-day velocities. In a hypothetical ideal case with perfectly representative velocities and ideal exposure ages, the boulders move along the line of equal time estimates (dashed grey line). At activity cessation (instantaneously $v_s \rightarrow 0$), the data points move vertically upwards. This “1:1” line separates the boulder exposure ages on the active lobe (below the 1:1 line, in the “forbidden zone”) from the ages on the relict lobe (above the 1:1 line, long inactivity time). The samples in between, Err 8 and 11, are discussed separately.



Possible sequence of
events

We hypothesize a two-stage evolution of the *Bleis Marscha* rockglacier. During its history from Younger Dryas until today, there were two main activity phases, and each time a new lobe grew: (1) First generation from post-Younger Dryas to earliest Holocene with rejuvenation throughout the mid Holocene; and (2) Second generation from the late Holocene until today. We structure the sequence of events in two acts and six scenes, illustrated in Figs. 6.6, 6.7:

Act 1, Scene 1
latest Lateglacial

At the Younger Dryas (YD) cold spell with mean annual air temperatures (MAAT) of 3–5°C lower than today [Kerschner and Ivy-Ochs, 2008], and glacier equilibrium line altitudes (ELA) depressed by 300 m in the eastern Swiss Alps [Frauenfelder et al., 2001], the *Val d’Err* was heavily glacierised. A set of lateral moraines descends on both trough shoulders (*Parsettens* and *Salteras*, 2300 m a.s.l. Fig. 5.2) and join below *Alp d’Err* at an altitude of 2120 m a.s.l. Judging from their appearance and position in the glacial trough valley, they are tentatively assigned to Egesen I, the furthest glacier advance in the late Lateglacial. Other moraine segments within the Egesen I extent (short ridges that are difficult to connect), and a frontal moraine near the *Alp d’Err* (*Plang dalla Donna Viglia*, 2165 m a.s.l.), are traces of subsequently smaller glacier re-advances during the YD. The orographic left side of the wide valley floor between the Egesen I frontal moraine and the huge *Bleis Marscha* debris fan (2210 m a.s.l.) is irregularly, chaotically blanketed by unsorted debris. We interpret this landform as hummocky moraines, i.e. supraglacial debris emplaced by the irregular melting of an ice patch covered with a thick debris layer.

An upslope-running lateral moraine on *Salteras* along the present *Bleis Marscha* rockglacier is visible up to 2490 m a.s.l. until it disappears beneath large debris flow deposits. A short segment of its left-lateral pendant stands south of the now-relict front of the rockglacier at the trough shoulder, at locality *Bleis Marscha* (2400 m a.s.l.). Both moraines are mainly built of granitic debris from the Middle Err unit that outcrops in the back part of the *Bleis Marscha* cirque. The clearly defined rock source links these moraines to the *Bleis Marscha* cirque glacier, that had its source area in a shadowy, NW-exposed cirque and reached down at least to the terrace edge at *Salteras*. Later mass wasting processes (debris flows) and the advance of the *Bleis Marscha* rockglacier have wiped out many traces, so that it is difficult to link the different short segments, to establish a similarly clear sequence of events as for the valley glacier, and it is not clear whether the glacier joined the main valley glacier. These observations complemented with the known exposure dates of Egesen moraines at *Julier* pass [Ivy-Ochs et al., 1996; Ivy-Ochs, 2015] suggest the following palaeoclimatic implications: At around 12 ka, the climate became drier, the Egesen glaciers “starved” [Kerschner and Ivy-Ochs, 2008; Ivy-Ochs et al., 2009], and the debris influx increased relatively to the snow/ice supply. The *Val d’Err* valley glacier became debris covered, stagnant, and began to decay slowly. The *Bleis Marscha* glacier retreated rapidly. Its former glacier bed is now mostly buried by the *Bleis Marscha* rockglacier, so that unlike for the valley glacier, only few traces are visible today.

Scene 2
post-YD to earliest
Holocene

With vanishing glaciers in dry-cold climate conditions, insulating ice or snow cover became less widespread and the winter cold could penetrate the ground (“antipathetic relationship between glaciers and mountain permafrost” [Harris and Corte, 1992]). Palaeoclimatic reconstructions by Frauenfelder et al. [2001] indicate that the lower limit of discontinuous permafrost was at ~2150 m a.s.l. in west-exposed slopes. The lower permafrost boundary was depressed by 500–600 m compared to today, considerably more than the ELA depression. The greater elevation range between mountain permafrost altitude (MPA) and ELA is a consequence of the cold, continental-type climate that lasted from the late YD

until 10 ka. In addition to these climatically favourable conditions for permafrost and periglacial processes, abundant amounts of frozen debris left behind from the rapidly retreating glaciers: Ideal regional conditions for the growth of rockglaciers. Conditions were particularly “rockglacier-friendly” in the *Bleis Marscha* cirque: The cirque floor above 2700 m a.s.l. lies above the MPA, is surrounded by high headwalls reaching 3100 m a.s.l. (*Piz Bleis Marscha*) of Err granite that weathers to large blocks, in shadow due to NW exposition and rather steep, so that a large glacier cannot accumulate.

In the *Bleis Marscha* cirque above ~2650 m a.s.l. around 11 ka, it is likely that large piles of glacier-derived “frozen rubble” and talus scree (classic paraglacial model [Hinchliffe and Ballantyne, 1999]) became super-saturated with interstitial ice, and a new mechanical behaviour emerged: It began to creep downslope under its own weight, and thus the first generation of the *Bleis Marscha* rockglacier was born.

The rockglacier boulder mantle mainly consists of Err granite, proving that the rockglacier source area always was in the back of the *Bleis Marscha* cirque, the same accumulation area the previous Egesen cirque glacier had had. The rockglacier turned from an initially NW direction as it leaves the cirque to a SW direction, following the topography. We do not know how the bed topography exactly looked like, and whether it was blanketed/veneered by glacial debris (like the valley head of *Val d’Err* by the LIA glaciers). The rockglacier reached down to an elevation of 2400 m asl to the *Salteras* terrace edge. There are no signs that the rockglacier has ever advanced beyond the edge of the trough shoulder. The mean surface slope and presumably also the basal slope drops from 21° to 11° at an altitude of 2500 m a.s.l., causing the lower lobes to decelerate and to buttress against the upper lobes. This way, the break in basal slope induced along-flow compressive stresses and buckle folding of the layered rockglacier (boulder mantle, ice-rich core) [Frehner et al., 2015]. The pronounced furrow-and-ridge microrelief with peculiar, crescent-shaped ridges as observed today witness these palaeo-stress conditions. The lowermost lobes are confined within the Egesen moraines at an elevation of 2400 m a.s.l.: This is morphological evidence against the hypothesis that the rockglacier already grew during an extended stage of contracted glacierisation before the early Younger Dryas with reactivation thereafter. Furthermore, the beautiful, well-preserved microrelief of the lower lobes excludes the scenario of a debris-covered ice-rich core that subsequently melted out. The (strictly periglacial) rockglacier rather advanced onto ice-free terrain during the later phases of the Younger Dryas until the earliest Holocene. With a length of ~1200 m, and a reasonable average advance rate of ~30 cm a⁻¹, the active period must have lasted over 4 ka.

After 10 ka, the climate shifted towards warmer conditions [Schimmelpfennig et al., 2012, 2014; Solomina et al., 2015] and the lower permafrost boundary began to rise above the rockglacier front at 2400 m a.s.l. By the middle Holocene, the lower continuous permafrost boundary was likely at least as high as today, at around 2600 m a.s.l. (present permafrost distribution, Fig. 6.5, and the tree line higher than today [Nicolussi et al., 2005], see Fig. 6.6) close to the topographically constrained talus-rockglacier transition in the back of the cirque. The cold reversals during the mid-Holocene were likely not severe, long and frequent enough [Joerin et al., 2006] to sustain or replenish the interstitial ice in the lower rockglacier parts and its advancement. The interstitial ice melted and rockglacier activity finally faded (climatic inactivity). Practically the entire upper part of the first-generation “rock stream” is now buried beneath the second generation that would evolve later; only along the northern margin the first generation can be traced along the rim for some distance. However, the connection to the root zone is nowhere ex-

Scene 3
earliest to middle
Holocene

posed anymore. We hypothesize that the now-relict rockglacier remained connected to its source, and that climatic, not dynamic inactivity, was responsible for inactivation. Morphological evidence such as grassy, stabilized slopes, iron staining and lichen cover speak in favour that the activity phase ceased long ago. The oldest TCN exposure age, obtained right above the now relict rockglacier front, indicates a stabilisation age of 9.0 ± 0.6 ka. However, intermittent boulder instability due to settling and collapse during inactivation (“effet camembert”) affected the nuclide inventory of each boulder individually. Boulder rotation and tumbling changed the orientation of its faces, i.e. its exposition and local nuclide production rate, and the elapsed time was not continuously “recorded”, making the exposure ages younger to varying degrees (self-shielding). This *apparent rejuvenation* explains the range of exposure ages and the overall underestimation of the true exposure time on the lower rockglacier lobe. Adding some correction time for the rejuvenation and a boulder travel time of 2-3 ka to the stabilisation age of ~ 9 ka, the exposure ages suggest a rockglacier initiation age of ~ 11 -12 ka, towards the end of the Younger Dryas.

In the late Holocene, after 3.3 ka, the climate deteriorated, timberline moved to lower altitudes, and glacier advances became more frequent, longer and more severe compared to the middle Holocene [Ivy-Ochs et al., 2009; Joerin et al., 2006; Le Roy et al., 2015]. The rapidly fluctuating glaciers were forced by climatic instabilities on a centennial timescale, superimposed on a multimillennial-scale cooling trend towards increased glacier extent culminating in the Little Ice Age (LIA) between 1350 and 1850 [Solomina et al., 2016]. This period of rapid climatic oscillations was favourable for frost shattering and debris production.

The *Bleis Marscha* rockglacier nourishment area at an elevation above 2700 m a.s.l. is even now (in a relatively warm climate) above the permafrost limit, and must have been so during extended periods of the late Holocene (Fig. 6.5). The high supply of debris and ice under permafrost conditions released a new wave of down-slope creeping permafrost, and thus the second generation of the *Bleis Marscha* rockglacier was born. The oldest TCN exposure age near the front of the intact upper lobe indicates that its activity phase began (at least!) 2.8 ± 0.2 ka. The first-generation debris stream is presently still active and advancing, reaching down to an altitude of 2550 m a.s.l. and a length of 460 m. It is likely that it buries large parts of the first generation, but makes a somewhat sharper bend as it leaves the cirque and leaves the right-lateral and frontal part of the first generation uncovered. On the second generation, a small lobe with slightly higher velocities is superimposed, whose TCN exposure ages range from 229 ± 41 to 1001 ± 84 a. This “Little Ice Age lobe” occupies only the southern half of the cirque. It might have shrunk in response to shifted debris supply and the location of the LIA glacieret the LIA rockglacier lobe co-existed and most likely interacted with (see below).

During the cold phases, the *Bleis Marscha* cirque was occupied by a cirque glacieret; for the last time by the 1850 LIA glacieret with the extent as roughly indicated by the 1853 Dufour map (Fig. 3.3). The glaciation remained however weak: The ice patch never extended beyond the margins of the cirque. Furthermore, the intact morphology of the uppermost rockglacier lobe and absent signs of glacial activity in the cirque, neither depositional (moraines, tills) nor erosional (spoon-shaped depression, flutes, striations), suggests that the small glacieret was stagnant and/or thin and polythermal (cold-based glacier tongue frozen onto the ground). The late-Holocene cirque glaciers could not destroy the rockglacier; permafrost and the pre-existing rockglacier outlasted beneath the ice patch [Frauenfelder et al., 2005, 2001]. This morphologically-motivated finding of a continued rockglacier activity is supported by exposure dating and feature-tracking results: The lin-

early increasing TCN exposure age progression with distance to the rockglacier root during the last 1.2 ka, as well as the high correlation between exposure time and estimated travel time suggest a (on average!) steady, uninterrupted creep.

This means that there has been a continuously creeping rockglacier rooted in a cirque that was interruptedly glacierised, in accordance with the severe climatic oscillations typical for the late Holocene. The altitude of the constantly shifting ELA with respect to the cirque floor determined the delicate balance between debris input and snow/firn accumulation (Fig. 6.3 [Zasadni, 2007]): In “glacier mode” with the ELA at or below the cirque bottom, snow input is proportionally high compared to debris input, and ice glaciers prevail. In “rockglacier mode” with the ELA above the cirque floor in the steep headwall, debris input prevails over snow accumulation, and rockglaciers form. The continuously growing rockglacier coexisted with a fluctuating cirque glacier since a few thousand years. The observed retreat and disappearance of the LIA cirque glacieret since 1850 and the consequent change in debris supply chain since 1850 is just the last one of a long series since a few thousand years: In accordance with the climatic oscillations, the dominant coarse debris transport process in the rear part of the Bleis Marscha cirque alternated between a “conveyor-belt like” englacial and supraglacial transport during cold phases and permafrost creep during ice-free warm phases. Conceptually, the rockglacier oscillated between debris rockglacier and talus rockglacier (Fig. 6.4).

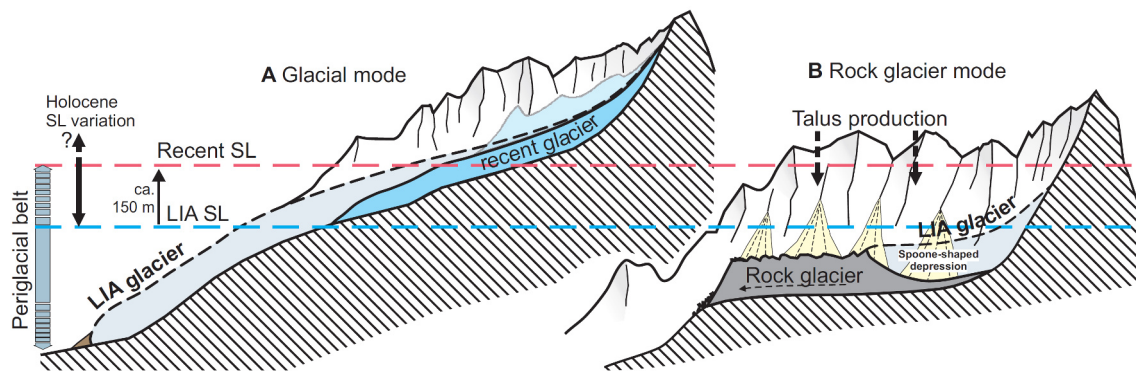
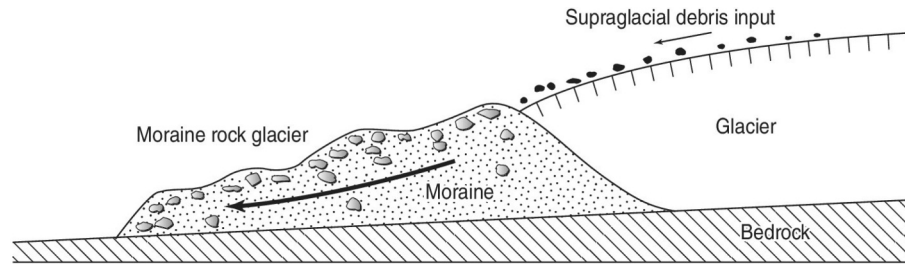


Figure 6.3: Schematic relation between cirque bottom and snow line and its consequences in glacial/rockglacier formation [Zasadni, 2007].

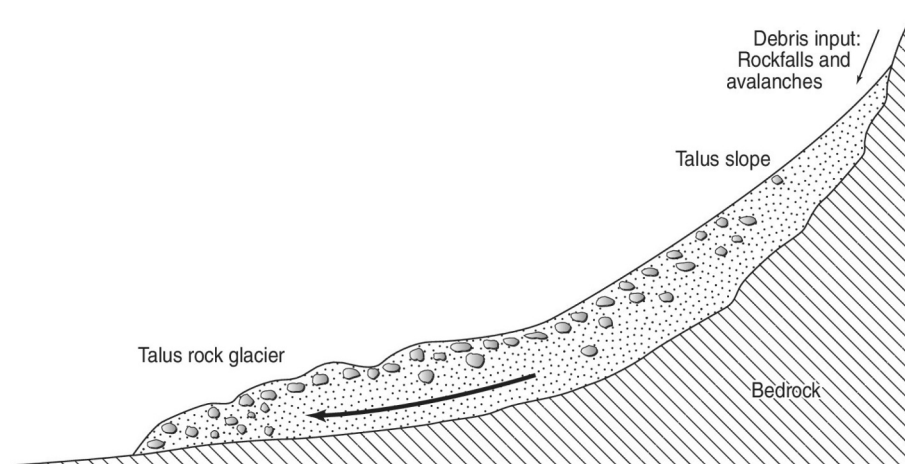
A glacial mode: glaciers originate where topographic conditions allow for accumulating snow above the snow line. B rock glacier mode: rock glaciers form where most of the cirque bottom is substantially below the snow line and sufficient debris load from head walls is available.

SL: snow line, LIA SL: snow line during the Little Ice Age maximum.

A linear regression through the TCN exposure ages on the youngest, uppermost LIA lobe yields a long-term averaged horizontal surface velocity of 30 cm a^{-1} over the last 1200 a. This is surprisingly consistent with the short-term horizontal surface velocity as obtained from image correlation of orthophotos from the period 2003 to 2012. The agreement of short and long-term average surface velocities may be due to the 9-year baseline between the orthophotos that make the results robust against seasonal and to some degree inter-annual creep rate variations (discussed below). The moderate surface velocities imply an estimated debris transport rate of 150 m (rockglacier width) $\times 30 \text{ m}$ (thickness) $\times 0.6$ (volume fraction of debris) $\times 0.3 \text{ m a}^{-1}$ (typical velocity) spread over an area of $3 \cdot 10^5 \text{ m}^2$, equivalent to a headwall back-weathering rate of $\sim 2.7 \text{ mm a}^{-1}$. The limited LIA (and thus late Holocene) glacieret size and the continuous age progression on the uppermost lobe indicating slow creep (30 cm a^{-1}) are strong arguments in favour of a periglacial rockglacier origin. The *Bleis Marscha* rockglacier is clearly not a “glacigenic



(a) Morainic rockglaciers (or debris rockglaciers *sensu* Barsch [1988]) form below glaciers. During phases of glacier advances, the glacier advances onto the upper end of the rockglacier and feeds glacial debris (till, moraine) that is incorporated into the rockglacier. Apart from the need of sufficient debris supply, the moraine must be frozen (area of at least discontinuous permafrost). The rockglacier deforms under its own weight and is not pushed by the glacier (unlike a push moraine).



(b) Talus rockglaciers form below talus slopes; they are built up by frozen talus. The ground ice is derived from snow meltwater as well as from avalanches.

Figure 6.4: Genetic classification of rockglaciers: Debris/moraine and talus rockglaciers. After Ballantyne [2018], cf. Barsch [1988].

(ice-cored) rock glacier” that has transformed from a LIA “ice” glacier.

Two TCN exposure ages (Err 12, 13) on unit III, although separated by a presently inactive internal front scarp (Fig. 5.11), are indistinguishable within their uncertainties and have a mid-Holocene age of 5.0 ± 0.3 ka. The simplest explanation is supported by observations and numerical modelling results (Fig. 5.45): Unit III belongs to the early-Holocene first generation, the front scarp is a secondary feature thrust by the later advance and push exerted by the second generation, and the “too-young” ages are caused by intermittent boulder instability and passive deformation by pushing of the rapidly advancing, thick lobe above (unit IV, rapid lobe) as soon as it reached there. The lateral boulder apron (Fig. 5.8) between the rockfall deposits and the frontal thrust of unit III is a clear sign of ongoing deformation that is much stronger than on the rest of the kinematically-defined transition zone (unit III and upper part of unit II). This explains the high surface velocities of 20 to 40 cm a^{-1} on a morphologically relict lobe. To test this hypothesis, the upper intact lobes are removed in a numerical experiment to assess the deformation rates of the lower relict part if it stood alone. Without the pushing upper lobe, the horizontal surface velocity on the lower part does not exceed 20 cm a^{-1} , and the influence of the pushing lobe reaches 150-200 m downstream from the thrust. The implied stress transmission over

such large distances and such high velocities require the presence of ground ice (discussed below).

In the upper, intact lobes, the moderate to high surface velocities are controlled by the topography on a 100-m scale. Aerial images back to 1959 show that the surface morphology has not substantially changed in the last few decades. There are no signs of rapid permafrost degradation such as opening of scars or crevasse-like cracks, or independently-moving lobes that soon become detached from the main body. The moderate surface speeds ($<50 \text{ cm a}^{-1}$) are almost one magnitude lower than in the recently observed collapsing rockglaciers [Delaloye et al., 2010; Roer et al., 2008]. Furthermore, the measured short-term 2003-2012 average surface creep rate on the uppermost lobe seems representative for the last thousand years, despite the climatic oscillations during the LIA that must have affected the rockglacier and the current warming. This might have the following reasons:

- The present creep rate captures the lobe lifetime-averaged creep rates quasi by coincidence (intermediate value theorem, implying that creep rates must have been much higher at some point in the past). This seems unlikely because very high creep rates are associated with permafrost degradation of which no traces are observable on the LIA lobe;
- Climatic oscillations were shorter than the rockglacier response time, so that the creep rate has not adapted to changing conditions in ice and debris supply. This hypothesis is contradicting to current observations of accelerating rockglacier that adapt quickly (within months to years) to warming; or
- Permafrost conditions have been relatively stable in the high-altitude ($>2700 \text{ m a.s.l.}$), shadowed cirque during the LIA; this is plausible given the fact that the shadowed cirque floor is in the permafrost belt even today (Fig. 6.5).

The high correlation between the present velocity field (in terms of speed, creep direction, strain rates, stream lines, isochrones) and the present 100-m scale topography of the upper lobes indicates that the permafrost body is in equilibrium and “has not undergone drastic dynamic changes in the past” [Kääb et al., 2003]. In other words, the active part of the Bleis Marscha rockglacier is in a “healthy” state to date. It is not surprising that all permafrost models classify the *Bleis Marscha* cirque floor as perennially frozen.

The coherent, uniform, and smooth horizontal surface velocity field is a characteristic, even fundamental feature of active rockglaciers. Topographic gradient, velocity and principal strain rate axis are aligned on a 100-m scale. The creep direction (and to some degree the magnitude) is governed by the average surface slope. Along the central flow line, the flow is either extensive (accelerating creep close to root) or compressive (decelerating creep close to buttressing front). This is the expression of a both spatially and temporally continuous deformation [Kääb and Vollmer, 2000; Kääb et al., 2003]. Unlike in the talus where the debris moves independently, the rockglacier material deforms as a whole, requiring a stress-transferring material component: The ice is responsible for the stress transmission (in space and time) and accommodates the deformation. Sharp spatial velocity gradients are observed along the margin of the clearly delineated permafrost body, either frontal overriding or lateral shearing. Conversely, oversteepened, active scarps mapped in the field always coincide with velocity jumps in the surface velocity data. Since non-translational surface movement occur there, these motions cannot be quantified with feature tracking. It is particularly difficult to estimate the rockglacier advance rate this way.

The surface deformation pattern on the *Bleis Marscha* rockglacier changes below an altitude of 2500 m a.s.l. The relict, collapsing lower lobes are characterised by an irregular surface velocity field that is strongly coupled to the small-scale topography, and affected by collapsing ridges (“effet camembert”). The presently observed microrelief is an expression of the palaeo-stress conditions that are different from today’s stress field estimated from the strain rate field: buckle folding in response to compressive flow of a layered medium was the dominant formation mechanism for the transverse furrow-and-ridge microrelief [Frehner et al., 2015]. The strain-rate data does not suggest along-flow compression, and the now relict part must have “undergone drastic dynamic changes in the past” [Kääb et al., 2003]. To conclude: The morphology memorises the cumulative deformation history over the lifetime of the rockglacier and is largely preserved after inactivation.

Observed surface velocities of up to 35 cm a^{-1} on the upper part of the apparently relict lobe (transition zone in Fig. 6.8) could only be numerically reproduced assuming a viscosity only slightly higher than for the intact part. In other words, the modelling results imply a considerable fraction of ice and water that weakens the material. The subsurface ice currently below the altitudinal limit of the discontinuous permafrost zone either has been preserved throughout the Holocene (convective cooling thanks to the boulder mantle, Balch ventilation [Delaloye and Lambiel, 2005, e.g.], or has reformed more recently by refreezing of ground or rain water. Today, the relict lobe might be frozen as the boulder mantle is susceptible for permafrost conditions (Kenner et al. [2017], Fig. 6.5).

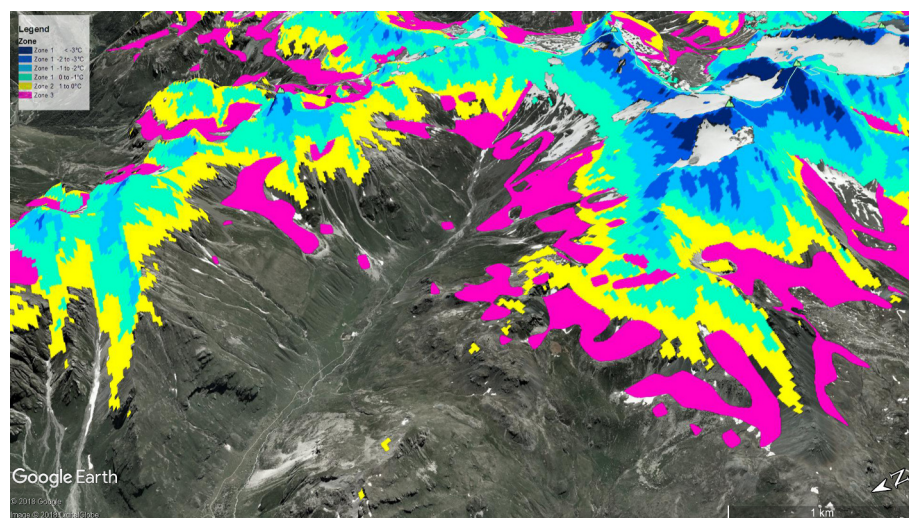


Figure 6.5: Modelled permafrost distribution in *Val d'Err* according to the permafrost and ground ice map (PGIM) [Kenner et al., 2017]. Visualization © 2018 Google.

Rockfall deposits of dark radiolaritic material on the northernmost “bulge” of the rockglacier can be distinguished from the Err granites the boulder mantle is mainly consists of. It is lying on unit III (first generation) that must have already been inactive at the time of fall: The impact caused no deformation; the material is just banked up against the rockglacier lateral scarp. The outline of the deposition can be seen on aerial image as a dark patch, it leads directly to the failure scar. This means the debris was subsequently not transported downslope. The rockfall must have occurred since the middle Holocene.

Synchronous variations — and acceleration — of many rockglaciers in the Swiss Alps over

the two last decades indicates a common dependence on external climatic factors (summer air temperature, seasonal snow cover development) [Roer et al., 2005; Delaloye et al., 2010; Kellerer-Pirklbauer and Kaufmann, 2012]: The surface creep rate seems to respond within months to changing MAGST (used as a proxy for the temperature of the upper permafrost layers), timing of snow cover and meltwater availability. Decennial, interannual, and to some degree seasonal creep rate changes appear to be linked to permafrost temperature variations. The viscosity is highly sensitive to permafrost temperature when close to 0°C [Kääb et al., 2007]. Cases of destabilising rockglaciers are reported by Roer et al. [2008]. Horizontal surface velocities up to 4 m a⁻¹ are reached, usually close to the front where most of the morphological changes occur. To conclude, Alpine rockglaciers show a rather synchronous behaviour and are responding sensitively to the recent temperature increase. The response is first a thermally-governed (moderate) acceleration, then, if the temperature keeps rising, permafrost degradation and destabilisation where meltwater plays an important role, and finally ice melt-out, collapse and deactivation [Kääb et al., 2007].

Are the high surface velocities on the rapid lobe a sign of beginning destabilization and permafrost degradation in response to recent warming (external climate forcing, ultimately leading to dynamic inactivation) or just induced by the steep slope and large thickness (internal processes, in equilibrium)? Since the most rapidly moving part is several hundred meters away from the source headwall and talus and the rockglacier has a constant width, the material (debris and ice) discharge increases with distance to the source (assuming a constant thickness). It is unlikely that ice accumulation “on the way” can fully account for the increasing mass discharge, and there seems to be a negative mass balance. However, this is only true for the current surface velocity field: Since the currently active LIA only occupies half of the cirque width, discharge must have been higher in the past. However, peak creep rates of ~80 cm a⁻¹ are still moderate compared to literature values of destabilising rockglacier tongues (<4 m a⁻¹). In conclusion, the destabilisation hypothesis can be discarded for the moment, but it is worthwhile to observe the lobe in the coming years.

Hazards directly related to destabilisation of the Bleis Marscha rockglacier are not to be expected since the ice-debris mass is overall stable and bounded (“dammed”) by the outer ridges. The southern part of the relict front is slowly subsiding, but a catastrophic collapse is unlikely. Horizontal displacement rates are small, and no bulges at the base of the front are observable. The deformation either is distributed, or the sliding plane is blind. Small debris slides may, however, release the fine material in the rockglacier interior, that is then transported towards the active Bleis Marscha debris fan. This potential continuation of the debris transport chain from the trough shoulder to the valley floor could enhance debris flow activity, particularly if the ground ice in the relict core is exposed and melts. Since the Val d’Err is not inhabited, only Alpine pasture is potentially affected, and the risks are small.

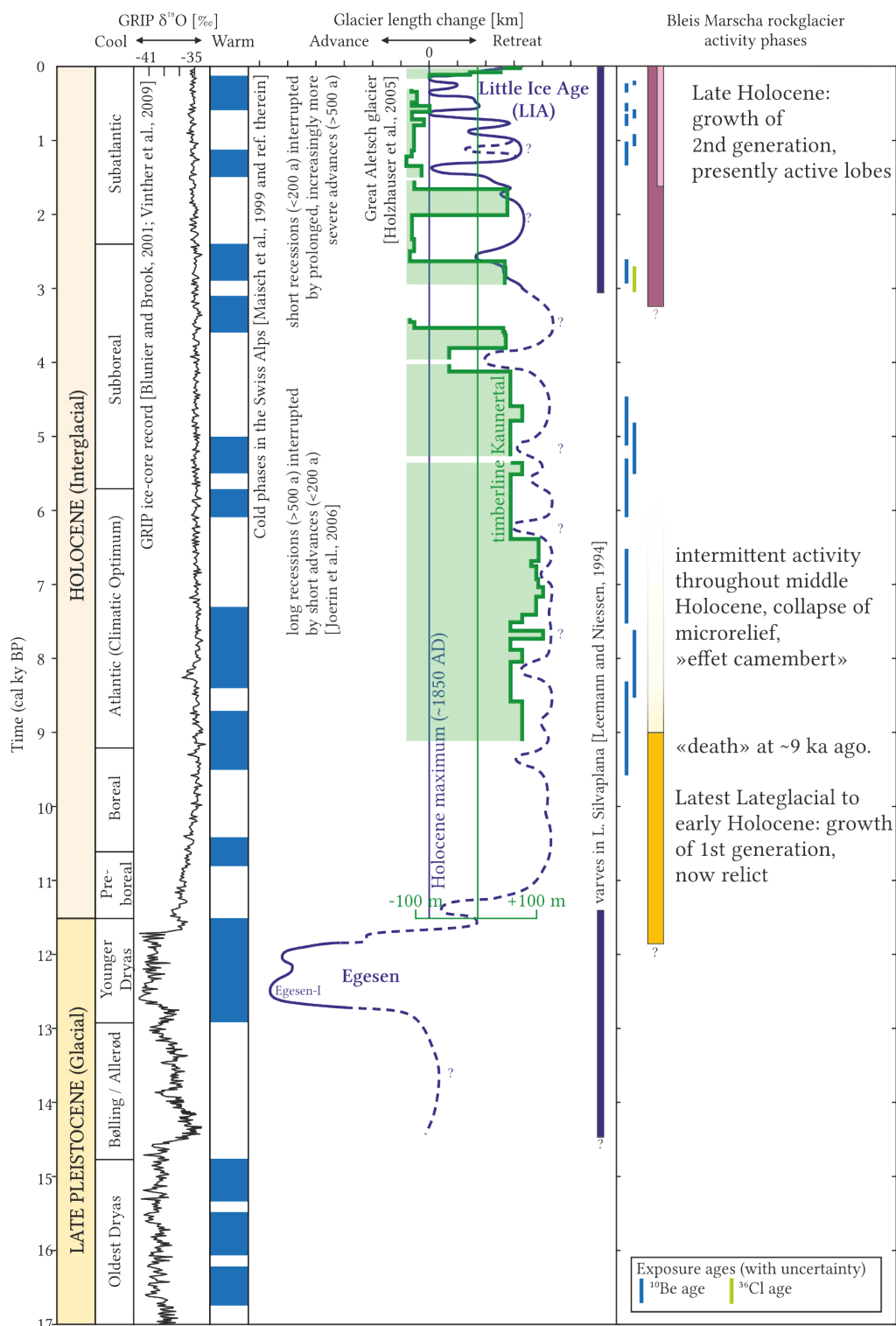
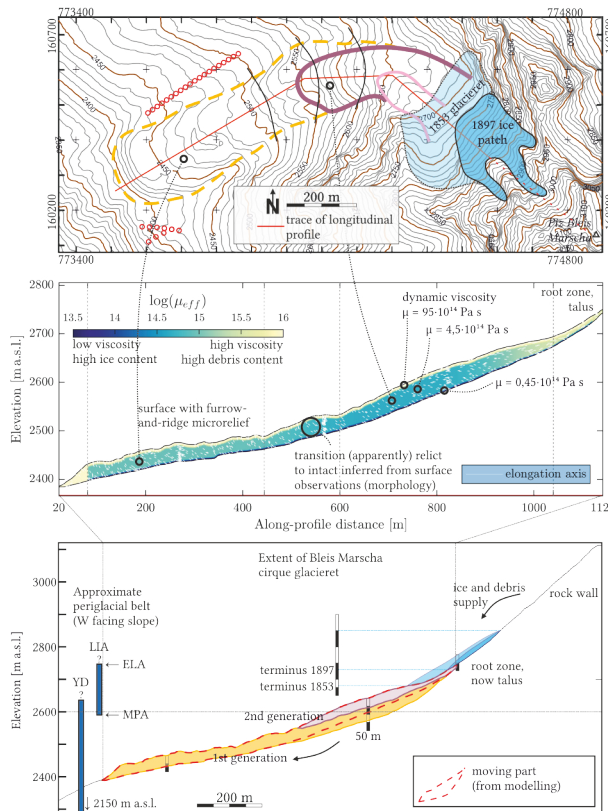


Figure 6.6: Synopsis of glacier variations and general climate evolution during the Younger Dryas and the Holocene in the Alps. Modified and complemented after Grämiger et al. [2017].

Map sketches illustrating a reconstructed sequence of events in the evolution of the Bleis Marscha rockglacier during the Holocene



(a) Sketch map of present rockglacier

Morphologically motivated subdivision of the *Bleis Marscha* rockglacier in a lower relict and an upper intact (active) part. Approximate glacieret extent from Dufour and Siegfried map. The **second generation** of the *Bleis Marscha* rockglacier grew during the late Holocene and is still active.

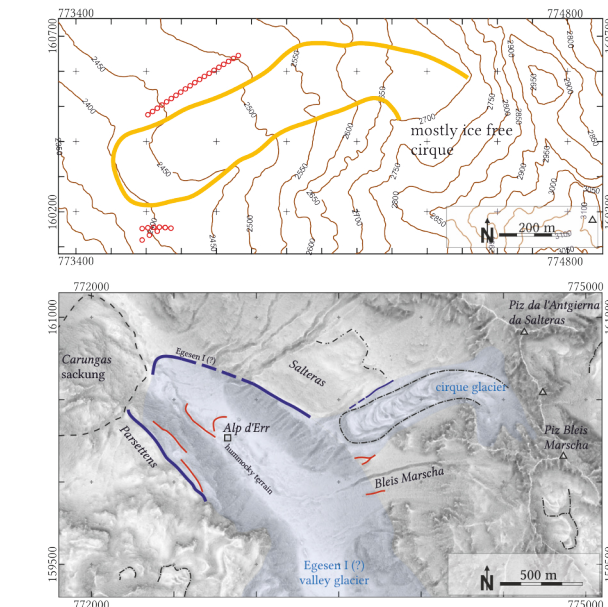
(b) Mechanical layering inferred from numerical modelling

Stratigraphy in terms of effective viscosity, numerical model along longitudinal profile (trace shown in (a)). The viscosity is interpreted as a proxy for ice/water content.

(c) Topography and climate interaction

The altitude of the ELA with respect to the cirque floor controls the delicate balance between debris and ice supply, and whether a rockglacier or a glacier forms. During the cold phases of the late Holocene, the cirque was intermittently occupied by a small glacieret, for the last time at LIA-max ~1850 until ~1930.

The periglacial belt is bounded by the lower boundary of discontinuous permafrost (MPA) [Frauenfelder et al., 2001] and the glacier equilibrium line altitude (ELA). Due to high elevation and north/west-ward exposition of the *Bleis Marscha* cirque, permafrost conditions have likely lasted uninterruptedly during the late Holocene, allowing continuous growth of the rockglacier.



(d) Sketch map of reconstructed mid-Holocene rockglacier

The **first generation** of the *Bleis Marscha* rockglacier likely grew during a «rockglacier-friendly» period after Egesen I glacier retreat and the earliest Holocene. It became inactive around 9 ka ago, and began to collapse. Drawn on present topography

oooo Egesen (?) moraine

(e) Sketch map of reconstructed late Holocene (Egesen I) glacier extents

Main glacial and periglacial morphological features, topographic names. The Egesen I (?) moraines (blue) descend on both trough shoulders (Salteras and Parsetten) and close at 2120 m a.s.l. They likely mark the maximum Younger Dryas (YD) glacier extent. Several short segments (red) were deposited during subsequently smaller advances during the YD.

— moraine (observed, inferred)
— rockglacier
— nivation ridge
— sackung

Abbreviations
ELA equilibrium line altitude, MPA mountain permafrost altitude
LIA Little Ice Age, YD Younger Dryas

Dominik AMSCHWAND, Sep 3, 2018

Figure 6.7: Illustrated sequence of events.

Combining exposure dating, finite-element modelling, and feature tracking to decipher rockglacier evolution: A case study from the Bleis Marscha rockglacier (Val d'Err, Grisons)

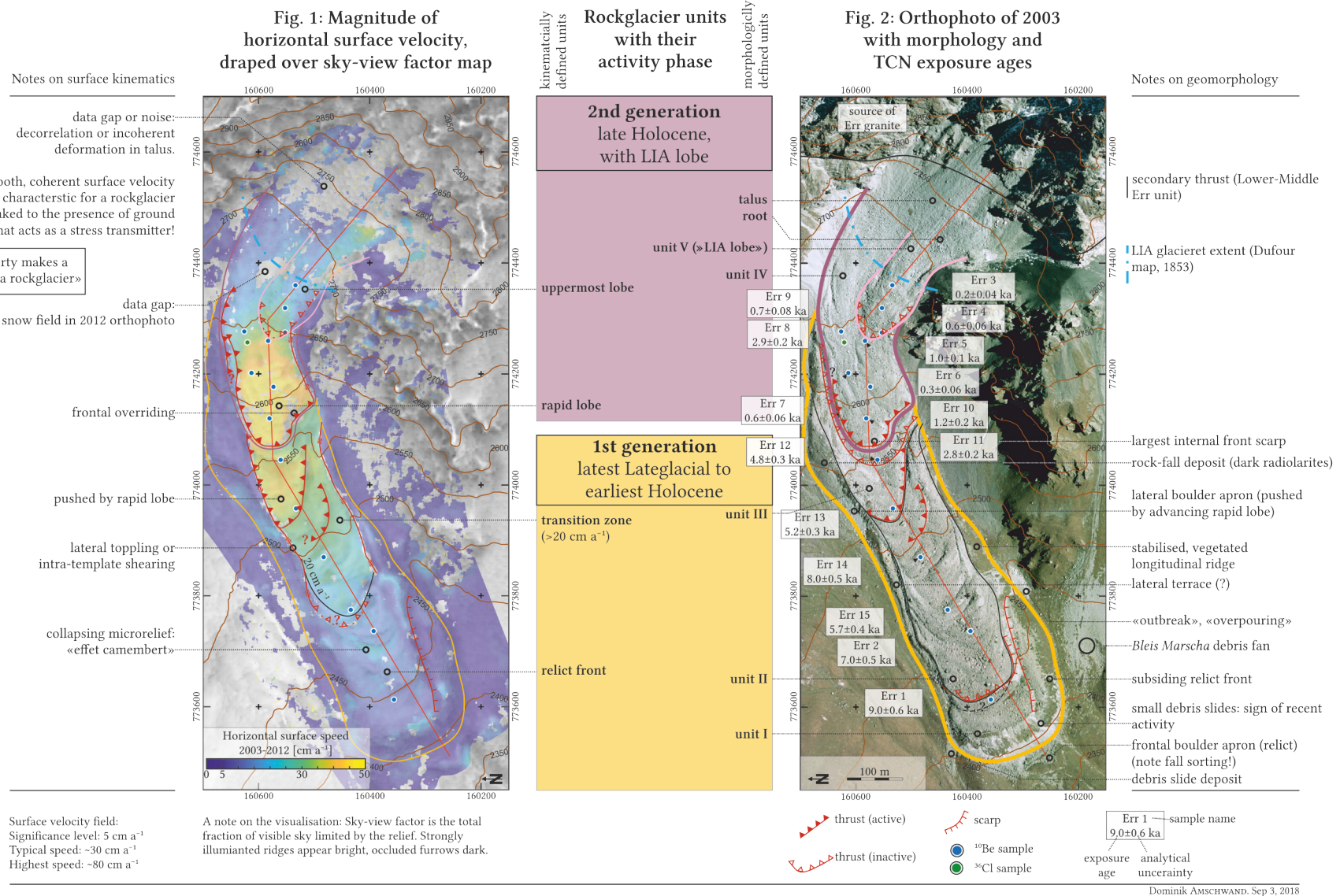
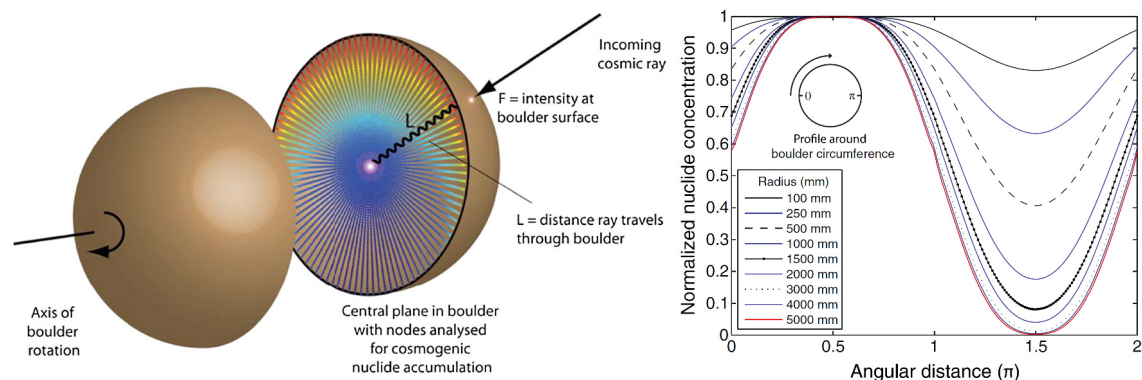


Figure 6.8: Data synthesis (2).

6.3 Outlook

Mackey and Lamb [2013] proposed a method to estimate past boulder stability by measuring the surface TCN concentration distribution. Key idea is that the more a boulder has been rotating in the past, the more the self-shielding is averaged out and the more radially symmetric the nuclide concentration in the boulder becomes (Fig. 6.9). Measuring the nuclide concentration of 10 (!) samples evenly distributed in the plane perpendicular to the preferred axis of rotation is required to capture the true statistics of surface concentration to within 5%. Provided the initial boulder diameter and the erosion rate is known, the minimum exposure time can be derived independently of past rotation. Since this approach relies heavily on statistics, it requires involved lab work.



(a) Irradiated boulder that is stable: The maximum nuclide concentration is on the upper boulder surface. (b) Transects of nuclide concentrations around the margin of boulders of different sizes.

Figure 6.9: Boulder mobility estimate according to Mackey and Lamb [2013].

(a) Sketch of a boulder with preferred rotation axis (horizontal). In practice, suitable boulders are elliptically shaped (prolate spheroids). (b) Transects of nuclide concentrations around the margin of boulders of different sizes. Constant irradiation from the upper hemisphere (maximum at $\pi/2$) leads to asymmetric nuclide concentration in the boulder. They are reduced for smaller boulders (rays penetrate through boulder) or more frequent rotation. The exact boulder dimensions depends among others in its density (here: $\Lambda = 208 \text{ g cm}^{-2}$).

Unresolved questions mainly stem from the limited surface observations:

How do the upper first generation lobes buried beneath the second generation look like, and how do the lobes interact (welded, weak zone, doubling of stratigraphy)? How does an advancing rockglacier lobe interact with debris beneath, be it a basal till blanket or an older rockglacier?

Some parts of the morphology are difficult to decipher: The non-creeping lateral parts with stable outer ridges on the otherwise active part and the lateral terraces along the lower part is not exposure dated. The different lichen cover suggests that there are two bodies of different age overlaid. In case of doubt, we proceeded by Occam's razor and have not postulated more generations that the TCN data minimally suggests. – Were there two distinctly separate activity phases already before the late Holocene?

How important was glacial erosion in the *Bleis Marscha* cirque, and to what extent did it contribute to the rockglacier debris? What are the debris fluxes since the latest Lateglacial?

The numerical modelling results imply that the relict part still contains substantial amount of ground ice, and the permafrost model by Kenner agrees that the ground is

Stratigraphy of superimposed lobes

Morphology

Erosion, debris provenance

Preservation or reformation of the ice in the relict part

frozen. How large is the ice content in reality? What is the origin and the age of the ice in the apparently relict part? Is it preserved early-Holocene ice mainly coming from the root zone, or recently formed in-situ by trickling rain and meltwater during cold periods in Late Holocene, or even more recently during the LIA?

7 Conclusion

We have investigated the *Bleis Marscha* rockglacier (*Val d'Err*, Grisons) with terrestrial cosmogenic nuclide exposure dating, aerial image correlation and finite-element numerical modelling attempting to reconstruct the formation of the rockglacier. These three different techniques provide data that covers a wide time span over the entire Holocene. Surface exposure dating with cosmogenic ^{10}Be and ^{36}Cl places a long-term framework (ka scale) on rockglacier movement periods. It is applied on an active rockglacier for the first time, and the implications for the interpretation of TCN exposure ages are of interest for periglacial geomorphologists as well as mountain permafrost and palaeoclimatology researchers. Furthermore, the present-day dynamics are numerically modelled using a two-dimensional finite-element approach to gain insights into the mechanical and material properties. The model is constrained with short-term horizontal surface velocities obtained from feature-tracking analysis of multitemporal orthorectified aerial images (2003-2012).

Aim, motivation, methods

The *Bleis Marscha* rockglacier is a polymorphic rockglacier with an active upper part that overrides a lower part. It has a length of 1200 m and a width of 150-210 m. Its debris-supplying headwalls are mainly composed of Err granite, besides limestone, radiolarite and schists. The creeping debris stream is separated by internal front scarps into different units, each with its own activity phase. While the upper lobes are presently active, lichen-covered boulders, vegetated, stabilized slopes, and signs of settling suggest that the parts below ~2500 m a.s.l. are relict today. The morphology-based subdivision coincides with the subdivision in terms of horizontal surface kinematics. Morphological evidence and the TCN exposure ages indicate that the rockglacier began to form in the later phases of the Younger Dryas. This first activity phase lasted into the earliest Holocene until ~9 ka, when the first generation became climatically inactive. Settling and collapse occurred during the warm middle Holocene and continues today. During the late-Holocene climate deteriorations, a second generation began to evolve ~3 ka from the intermittently glacierised *Piz Bleis Marscha* cirque and is now overriding the relict first generation. The last remnants of the LIA cirque glacieret, more a small perennial ice patch, disappeared between 2005 and 2017. The talus grades directly into rockglacier root, and signs of glacial activity in the cirque are weak. It shows that the small, stagnant and/or cold-based cirque glacieret could not destroy the rockglacier, and that during the cold phases of the late Holocene glacial and periglacial processes and landforms co-existed in the *Bleis Marscha* cirque. The overall timescales of centuries to millennia show that process rates have been modest, and that the debris was supplied by continuous weathering. The *Bleis Marscha* rockglacier is a truly periglacial landform. Whether the talus debris is derived from episodic high magnitude, low-frequency rockfalls or more steadily from high-frequency, low-magnitude events cannot be decided from surface observations.

Morphology and history

On the presently active lobes with an age younger than ~1.5 ka, the 8 ^{10}Be exposure ages scale reasonably well with distance from the root zone and can therefore be addressed as (minimal) surface travel times of the boulders. The oldest age, found above the internal front scarp, is consequently the minimum time of onset of the current activity phase. There are no signs for pre-exposure or any other systematic shifts. The fluctuations

Exposure ages

do not greatly exceed the analytical uncertainties that are in the order of decades; the exposure ages pattern is not heavily disturbed. The boulders are advected more or less passively with the boulder mantle.

On the lower relict lobes with 6 TCN exposure ages in the range of 5.0 to 9.0 ka, the fluctuations are in the order of centuries and exceed the analytical uncertainties. These fluctuations are introduced by surface processes (in the boulder mantle) that affect the nuclide inventory of boulders individually. Intermittent boulder instability due to settling and collapse during the long time periods since inactivation caused the exposure of the rock faces to deviate from ideal conditions (single-stage, uninterrupted and undisturbed). This apparent rejuvenation explains both the tendentially “too-young” ages and the large spread. The oldest age (ideally, but not necessarily found above the relict front) is interpreted as the (rough) inactivity age. The first generation of the Bleis Marscha rockglacier ceased its activity around 9.0 ± 0.6 ka.

A complication common to both active and relict TCN ages is the relationship between surface age and landform age: While it is generally agreed that surface ages are minimum ages, the “missing time” is difficult to estimate, and not possible without independent information on e.g. morphostratigraphical relations to adjacent glacial landforms. The ratio between along-slope surface velocity and advance rate mainly depends on the vertical variation of horizontal velocity and the melt-out of excess ice. These internal parameters are impossible to reconstruct for relict rockglacier lobes. The single largest source of uncertainty that leads to scattering of TCN ages is geologic uncertainty, and careful field observations are needed to interpret the exposure age pattern. A complication specific to rockglaciers are stagnant marginal lobes which could either be relict parts of a previous rockglacier generation or be of dynamic origin and belong to the current activity phase.

Image correlation

An illumination-invariant method for correlating the orthophotos yielded reliable displacements on the rugged rockglacier surface. Important features of the present (2003-2012) horizontal surface velocity field such as large velocity gradients and data gaps due to non-translational motion coincides with morphological features such as active thrusts (overriding lobes) and advancing front scarps. The image correlation results support the morphologically motivated subdivision of the *Bleis Marscha* rockglacier in an active upper part and a relict, collapsing lower part. On the upper, intact lobes, the high correlation between the present velocity field and the present 100-m scale topography indicates that the permafrost body is in equilibrium with its environment (moderate surface speeds $< 50 \text{ cm a}^{-1}$; creep direction, strain rates, stream lines are aligned; isochrones have a similar crescent-shaped form as the ridges). The intact part of the rockglacier is in a “healthy” state today. The lower, relict part is characterised by an irregular surface velocity field strongly coupled to the collapsing small-scale topography (“effet camembert”). Part of the relict front is slowly subsiding southwards. The microrelief with transversal, crescent-shaped furrow and ridges was formed by buckle folding in response to along-flow compressive creep of a layered medium, a stress state that can no longer be inferred from the present strain-rate field. The relict part must have undergone drastic dynamic changes in the past. The morphology memorises the cumulative deformation history over the lifetime of the rockglacier and is largely preserved after inactivation. The coherent surface velocity field is an expression of stress transmission (in space and time) and clearly indicates that the strain is accommodated by viscous deformation of the ground ice.

Numerical modelling

A series of six numerical experiments were carried out with a two-dimensional finite-element model along a longitudinal section of the rockglacier. An incompressible, linearly-

viscous Stokes flow is solved numerically. With forward approaches, the influence of the mechanical rockglacier stratigraphy (boulder mantle, core, low-viscosity basal shear layer) on the surface velocity distribution is assessed: (i) the boulder mantle plays an important role of stress distribution via its stiffness; (ii) deformation processes in shear layers largely control the overall deformations, in agreement with observations; and (iii) pushing of the rapidly advancing lobe explains partly the relatively high surface speed on the upper transition zone. With an inverse approach, material parameters in terms of dynamic viscosity and density are inferred with the image correlation data. The parameters were estimated for viscous deformation and are time- and space-averaged mechanical properties valid for the bulk material (termed effective parameters). Surface velocities of up to 35 cm a^{-1} on the uppermost part of the apparently relict part could only be numerically reproduced assuming stress transmission from the advancing active lobe immediately above and a considerable fraction of ice and/or water that weakens the material. The subsurface ice either has been preserved throughout the Holocene or has reformed more recently. The mechanical layering with a low-viscosity basal shear zone produces a vertical deformation profile that looks similar to measured borehole deformation measurements. A likely more complex, non-linear rheological behaviour in shear layers can be emulated (reproduced phenomenologically, “by appearance”) with a NEWTONIAN model with the viscosity layering. This is advantageous in terms of mathematical tractability and computing speed.

Clyde Wahrhaftig and Alan Cox (1959): “It is difficult to escape the conclusion that the motion of these rock glaciers is the motion of frozen rubble”.

8 Acknowledgements

I thank my main supervisor PD Dr. Susan IVY-OCHS for suggesting me the project, for the freedom in choosing the rockglacier, for the guidance in the field, supervision in the lab, and the long geomorphological discussions in the office. Her knowledge of the Alpine Lateglacial and experience in interpreting exposure ages were indispensable for writing the “sequence of events” as a closed, coherent, and well-founded history. I am glad that PD. Dr. Marcel FREHNER has accepted to be my co-supervisor and continued to offer his advice on the numerical modelling part, even after having left ETH in the end of February. He has provided the ready-to-use numerical code and answers to my questions on the physics and numerics whenever his office door stood open. I am indebted to my co-supervisor Olivia KRONIG, who patiently showed and supervised all required steps in the lab. She kept the HF process running even over Christmas, and took care of the chlorine sample. Thanks to her, life-threatening acid solutions in teflon beakers were turned into meaningful numbers. In case Olivia was absent, Ewelina BROS and Dr. Kristina HIPPE helped me whenever necessary.

I am very fortunate that my project has met benevolent interest of Armando JANETT, the local gamekeeper who provided me the necessary permissions and driving permit, and his wife Anina JANETT-SONDER who translated the abstract to *Surmiran*, the local dialect of the Romansh language. Carole MÜLLER and Peter KAISER warmly opened their home for tired and hungry field workers (the barbecue grill was particularly appreciated). Without their approval and logistical support, it would not have been possible to carry out the 4-day field campaign in a protected area. A special thank goes to my highly motivated, cheerful and experienced field team with PD Dr. Susan Ivy-Ochs, PD. Dr. Marcel Frehner, Olivia Kronig, Ueli STEINEMANN and Dr. Reto GRISCHOTT. No matter how mercilessly the August sun burned onto the barren boulder stream, we kept taking samples, kept discussing the microrelief, and speculating on the history of the largest rockglacier in the *Val d’Err*. Thanks also to my peer, office neighbour and engineering geologist Jonas VON WARTBURG, who accompanied me on a follow-up field trip on the rockglacier. He pointed out rockfall deposits that I overlooked during the field work, focusing on periglacial features — “You see only what you look for”.

Finally, I’d like to thank for the financial support granted by the Swiss Society for Quaternary Research (CH-QUAT), covering all my expenses for the field work, and the Alumni-Fonds des Geologischen Instituts (ETH Zürich) for a travel cost contribution to the 5th European Conference on Permafrost (Chamonix-Mont Blanc, France).

This Master’s thesis concludes my 5-year studies of Earth Sciences. I’d like to express my gratitude to the people that accompanied me during my time at ETH: To my peers Felix Bissig (“essentially any problem can be treated as an inverse problem”), Aurélia Meister, Lukas Müller, Noah Jäggi...

To my family and parents Lisbeth and Albert, who always supported me and allowed me to concentrate fully on the studies. I had the opportunity to freely follow my interests and to take more lectures and field courses than minimally required, lectures given by excellent teachers. This was a unique privilege.

Above all, to Stefanie.



Honoré Daumier, 1858. [source]

9 References

Articles and books

- Alfimov, V. and Ivy-Ochs, S. (2009). How well do we understand production of ^{36}Cl in limestone and dolomite? *Quaternary Geochronology*, 4(6):462 – 474. Advances in Cosmogenic Isotope Research from CRONUS-EU.
- Arenson, L., Almási, N., and Springman, S. (2003). Shearing response of ice-rich rock glacier material. In *Permafrost*, pages 39 – 44. Balkema. 8th International Conference on Permafrost; Conference Location: Zürich Switzerland; Conference Date: July 21-25, 2003; .
- Arenson, L., Hoelzle, M., and Springman, S. (2002). Borehole deformation measurements and internal structure of some rock glaciers in Switzerland. *Permafrost and Periglacial Processes*, 13(2):117–135.
- Arenson, L., M. Springman, S., and Sego, D. (2006). The rheology of frozen soils. *Appl. Rheol.*, 17(1):12147–1–12147–14.
- Arenson, L. U., Hauck, C., Hilbich, C., Seward, L., Yamamoto, Y., and Springman, S. M. (2010). Sub-surface heterogeneities in the Murtèl. Corvatsch rock glacier, Switzerland. In *Proceedings of the joint 63rd Canadian Geotechnical Conference and the 6th Canadian Permafrost Conference*, pages 1494 – 1500. Canadian Geotechnical Society. the 6th Canadian Permafrost Conference; Conference Location: Calgary, Canada; Conference Date: September 12-16, 2010; .
- Arenson, L. U. and Springman, S. M. (2005a). Mathematical descriptions for the behaviour of ice-rich frozen soils at temperatures close to 0°C . *Canadian Geotechnical Journal*, 42(2):431–442.
- Arenson, L. U. and Springman, S. M. (2005b). Triaxial constant stress and constant strain rate tests on ice-rich permafrost samples. *Canadian Geotechnical Journal*, 42(2):412–430.
- Associate Committee on Geotechnical Research (ACGR) (1988). Glossary of permafrost and related ground-ice terms. Technical memorandum 142, National Research Council of Canada.
- Azizi, F. and Whalley, W. (1995). Finite element analysis of the creep of debris containing thin ice bodies. In *Proceedings of the Fifth (1995) International Offshore and Polar Engineering Conference, The Hague, The Netherlands, June 11–16, 1995*, volume 2, pages 336–341. International Society of Offshore and Polar Engineers, International Society of Offshore and Polar Engineers.
- Badino, F., Ravazzi, C., Vallè, F., Pini, R., Aceti, A., Brunetti, M., Champvillair, E., Maggi, V., Maspero, F., Perego, R., and Orombelli, G. (2018). 8800 years of high-altitude vegetation and climate history at the Rutor Glacier forefield, Italian Alps. Evidence of middle Holocene timberline rise and glacier contraction. *Quaternary Science Reviews*, 185:41 – 68.
- Balco, G., Briner, J., Finkel, R. C., Rayburn, J. A., Ridge, J. C., and Schaefer, J. M. (2009). Regional beryllium-10 production rate calibration for late-glacial northeastern North America. *Quaternary Geochronology*, 4(2):93 – 107.
- Balco, G., Stone, J. O., Lifton, N. A., and Dunai, T. J. (2008). A complete and easily accessible means of calculating surface exposure ages or erosion rates from ^{10}Be and ^{26}Al measurements. *Quaternary Geochronology*, 3(3):174–195. Prospects for the New Frontiers of earth and Environmental Sciences.
- Ballantyne, C. K. (2018). *Periglacial Geomorphology*. Wiley-Blackwell, 1 edition.
- Ballantyne, C. K., Schnabel, C., and Xu, S. (2009). Exposure dating and reinterpretation of coarse debris accumulations (‘rock glaciers’) in the Cairngorm Mountains, Scotland. *Journal of Quaternary Science*, 24(1):19–31.
- Barrows, T. T., Stone, J. O., and Fifield, L. (2004). Exposure ages for Pleistocene periglacial deposits in Australia. *Quaternary Science Reviews*, 23(5):697 – 708.
- Barsch, D. (1988). Rockglaciers. In Clark, M. J., editor, *Advances in periglacial geomorphology*, chapter 4, pages 69–90. Wiley, Chichester.
- Barsch, D. (1992). Permafrost creep and rockglaciers. *Permafrost and Periglacial Processes*, 3(3):175–188.
- Barsch, D. (1996). *Rockglaciers. Indicators for the Present and Former Geoecology in High Mountain Environments*, volume 16 of *Springer Series in Physical Environment*. Springer, Berlin, Heidelberg.
- Berthling, I. (2011). Beyond confusion: rock glaciers as cryo-conditioned landforms. *Geomorphology*, 131(3):98–106.
- Biot, M. A. (1961). Theory of folding of stratified viscoelastic media and its implications in tectonics and orogenesis. *GSA Bulletin*, 72(11):1595.

- Bodin, X., Thibert, E., Sanchez, O., Rabatel, A., and Jaillet, S. (2018). Multi-annual kinematics of an active rock glacier quantified from very high-resolution dms: An application-case in the French Alps. *Remote Sensing*, 10(4):547.
- Boeckli, L., Brenning, A., Gruber, S., and Noetzli, J. (2012). Permafrost distribution in the European Alps: calculation and evaluation of an index map and summary statistics. *The Cryosphere*, 6(4):807–820.
- Böhlert, R., Egli, M., Maisch, M., Brandová, D., Ivy-Ochs, S., Kubik, P. W., and Haeberli, W. (2011). Application of a combination of dating techniques to reconstruct the Lateglacial and early Holocene landscape history of the Albula region (eastern Switzerland). *Geomorphology*, 127(1):1–13.
- Buchli, T., Kos, A., Limpach, P., Merz, K., Zhou, X., and Springman, S. M. (2018). Kinematic investigations on the Furggwanhorn rock glacier, Switzerland. *Permafrost and Periglacial Processes*, pages n/a–n/a. PPP-16-0033.R3.
- Burga, C. (1987). Das alpine Spät- und Postglazial in Graubünden aufgrund geomorphologischer und pollenanalytischer Untersuchungen. *Vierteljahresschrift der Naturforschenden Gesellschaft in Zürich*, 132(1):26–44.
- Burn, C. (2013). Permafrost and periglacial features | permafrost. In Elias, S. A. and Mock, C. J., editors, *Encyclopedia of Quaternary Science (Second Edition)*, pages 464 – 471. Elsevier, Amsterdam, second edition edition.
- Capps, S. R. (1910). Rock glaciers in Alaska. *The Journal of Geology*, 18(4):359–375.
- Chaix, A. (1943). Les coulées de blocs du Parc national suisse. nouvelles mesures et comparaison avec les «rock stream» de la Sierra Nevada de Californie. *Le Globe (Organe de la Société de Géographie de Genève)*, 82(1):121–128.
- Chuang, F. C. and Greeley, R. (2000). Large mass movements on Callisto. *Journal of Geophysical Research: Planets*, 105(E8):20227–20244.
- Cicoira, A., Vieli, A., and Faillettaz, J. (2018). Investigating the influence of temperature and liquid water on variations in rockglacier flow. In Edited by Philip Deline, X. B. and Ravel, L., editors, *Proceedings of the 5th European Conference on Permafrost*. EDYTEM - Environnements, Dynamiques et Territoires de la Montagne. The 5th European Permafrost Conference; Conference Location: Chamonix-Mont Blanc, France; Conference Date: June 23–July 1, 2018; .
- Clark, P. U., Dyke, A. S., Shakun, J. D., Carlson, A. E., Clark, J., Wohlfarth, B., Mitrovica, J. X., Hostetler, S. W., and McCabe, A. M. (2009). The Last Glacial Maximum. *Science*, 325(5941):710–714.
- Cornelius, H. P. (1935). *Geologie der Err-Julier-Gruppe (Erläuterungen zur Spezialkarte Nr. 115). 1. Teil: Das Baumaterial (Stratigraphie und Petrographie, excl. Quartär)*. Beiträge zur Geologischen Karte der Schweiz, Nr. 70.1.
- Cornelius, H. P. (1950). *Geologie der Err-Julier-Gruppe (Erläuterungen zur Spezialkarte Nr. 115). 2. Teil: Der Gebirgsbau*. Beiträge zur Geologischen Karte der Schweiz, Nr. 70.2.
- Cornelius, H. P. (1951). *Geologie der Err-Julier-Gruppe (Erläuterungen zur Spezialkarte Nr. 115). 3. Teil: Quartär und Oberflächengestaltung. Hydrologie. Anhang: Nutzbare Mineralien und Gesteine*. Beiträge zur Geologischen Karte der Schweiz, Nr. 70.3.
- Cossart, E., Fort, M., Bourles, D., Carcaillet, J., Perrier, R., Siame, L., and Braucher, R. (2010). Climatic significance of glacier retreat and rockglaciers re-assessed in the light of cosmogenic dating and weathering rind thickness in Clarée valley (Briançonnais, French Alps). *CATENA*, 80(3):204 – 219.
- Coulomb, C. A. (1776). Essai sur une application des règles de maximis et minimis à quelques problèmes de statique relatifs à l’architecture. *Acad. Roy. des Sciences. Memoires de math. et physique par divers savants*, 7:343–382. Mémoire de mécanique appliquée.
- Cross, W. and Howe, E. (1905). Geography and general geology of the quadrangle in Silverton folio. *U.S. Geol. Surv. Folio*, (120):1–25.
- Cuffey, K. and Paterson, W. (2010). *The Physics of Glaciers*. Elsevier Science, 4 edition.
- Davis, R. and Schaeffer, O. A. (1955). Chlorine-36 in nature. *Annals of the New York Academy of Sciences*, 62(5):107–121.
- Debella-Gilo, M. and Käab, A. (2011). Sub-pixel precision image matching for measuring surface displacements on mass movements using normalized cross-correlation. *Remote Sensing of Environment*, 115(1):130–142.
- Debella-Gilo, M. and Käab, A. (2012). Locally adaptive template sizes for matching repeat images of Earth surface mass movements. *ISPRS Journal of Photogrammetry and Remote Sensing*, 69:10 – 28.
- Dede, V., İhsan Çiçek, Sarıkaya, M. A., Çiner, A., and Uncu, L. (2017). First cosmogenic geochronology from the Lesser Caucasus: Late Pleistocene glaciation and rock glacier development in the Karçal Valley, NE Turkey. *Quaternary Science Reviews*, 164:54–67.
- Degenhardt, J. J. (2009). Development of tongue-shaped and multilobate rock glaciers in alpine environments—interpretations from ground penetrating radar surveys. *Geomorphology*, 109(3):94–107.
- Delaloye, R., Barboux, C., Bodin, X., Brenning, A., Hartl, L., Hu, Y., Ikeda, A., Kaufmann, V., Kellerer-Pirklbauer, A., Lambiel, C., Liu, L., Marcer, M., Rick, B., Scotti, R., Takadema, H., Trombottio Liaudat,

- D., Vivero, S., and Winterberger, M. (2018). Rock glacier inventories and kinematics: a new IPA Action Group. In Edited by Philip Deline, X. B. and Ravel, L., editors, *Proceedings of the 5th European Conference on Permafrost*. EDYTEM - Environnements, Dynamiques et Territoires de la Montagne. The 5th European Permafrost Conference; Conference Location: Chamonix-Mont Blanc, France; Conference Date: June 23–July 1, 2018; .
- Delaloye, R. and Lambiel, C. (2005). Evidence of winter ascending air circulation throughout talus slopes and rock glaciers situated in the lower belt of alpine discontinuous permafrost (swiss alps). *Norsk Geografisk Tidsskrift - Norwegian Journal of Geography*, 59(2):194–203.
- Delaloye, R., Lambiel, C., and Gärtner-Roer, I. (2010). Overview of rock glacier kinematics research in the Swiss Alps. *Geographica Helvetica*, 65(2):135–145.
- Domaradzki, J. (1951). *Blockströme im Kanton Graubünden*. Sonderdruck aus: Ergebnisse der wissenschaftlichen Untersuchungen des schweizerischen Nationalparks, Band 3 (Neue Folge), Nr. 24, 1951. Liestal: Lüdlin.
- Dunne, J., Elmore, D., and Muzikar, P. (1999). Scaling factors for the rates of production of cosmogenic nuclides for geometric shielding and attenuation at depth on sloped surfaces. *Geomorphology*, 27(1):3–11.
- Ehlers, J. and Gibbard, P. L. (2007). The extent and chronology of Cenozoic Global Glaciation. *Quaternary International*, 164-165:6 – 20. From the Swiss Alps to the Crimean Mountains - Alpine Quaternary stratigraphy in a European context.
- Einstein, A. (1905). *Eine neue Bestimmung der Moleküldimensionen*. PhD thesis, ETH Zurich. Dissertation Univ. Zürich, 1905. – Ref.: A. Kleiner; Korref.: H. Burkhardt.
- Etzelmüller, B. and Frauenfelder, R. (2009). Factors controlling the distribution of mountain permafrost in the northern hemisphere and their influence on sediment transfer. *Arctic, Antarctic, and Alpine Research*, 41(1):48–58.
- Etzelmüller, B. and Hagen, J. O. (2005). Glacier-permafrost interaction in Arctic and alpine mountain environments with examples from southern Norway and Svalbard. *Geological Society, London, Special Publications*, 242(1):11–27.
- Evin, M. (1987). Lithology and fracturing control of rock glaciers in southwestern Alps of France and Italy. In *Rock glaciers*, pages 83–106.
- Fitch, A. J., Kadyrov, A., Christmas, W. J., and Kittler, J. (2002). Orientation correlation. In *British Machine Vision Conference*, pages 133–142.
- Fossen, H. (2010). *Structural Geology*. Cambridge University Press.
- Frauenfelder, R., Haeberli, W., and Hoelzle, M. (2003). Rockglacier occurrence and related terrain parameters in a study area of the Eastern Swiss Alps. In *Proceedings of the Eighth International Conference on Permafrost*, volume 1, pages 253–258. Balkema Publishers: Lisse.
- Frauenfelder, R., Haeberli, W., Hoelzle, M., and Maisch, M. (2001). Using relict rockglaciers in GIS-based modelling to reconstruct Younger Dryas permafrost distribution patterns in the Err-Julier area, Swiss Alps. *Norsk Geografisk Tidsskrift - Norwegian Journal of Geography*, 55(4):195–202.
- Frauenfelder, R. and Kääb, A. (2000). Towards a palaeoclimatic model of rock-glacier formation in the Swiss Alps. *Annals of Glaciology*, 31(1):281–286.
- Frauenfelder, R., Laustela, M., and Kääb, A. (2005). Relative age dating of Alpine rockglacier surfaces. *Zeitschrift für Geomorphologie, NF*, 49(2):145–166.
- Frauenfelder, R., Schneider, B., and Kääb, A. (2008). Using dynamic modelling to simulate the distribution of rockglaciers. *Geomorphology*, 93(1):130–143. Challenges in Geomorphological Methods and Techniques.
- Frehner, M., Ling, A. H. M., and Gärtner-Roer, I. (2015). Furrow-and-ridge morphology on rockglaciers explained by gravity-driven buckle folding: A case study from the Murtèl rockglacier (Switzerland). *Permafrost and Periglacial Processes*, 26(1):57–66.
- Frehner, M. and Schmalholz, S. M. (2006). Numerical simulations of parasitic folding in multilayers. *Journal of Structural Geology*, 28(9):1647–1657.
- French, H. M. (2017). *The periglacial environment*. John Wiley & Sons, 4 edition.
- Friedson, A. and Stevenson, D. (1983). Viscosity of rock-ice mixtures and applications to the evolution of icy satellites. *Icarus*, 56(1):1–14.
- Fuchs, M. C., Böhlert, R., Krbetschek, M., Preusser, F., and Egli, M. (2013). Exploring the potential of luminescence methods for dating Alpine rock glaciers. *Quaternary Geochronology*, 18(Supplement C):17–33.
- Giardino, J. R., Shroder, J. F., and Vitek, J. D., editors (1987). *Rock glaciers*. Boston, London, Wellington, Sydney: Allen & Unwin.
- Glen, J. W. (1952). Experiments on the deformation of ice. *Journal of Glaciology*, 2(12):111–114.
- Gosse, J. C. and Phillips, F. M. (2001). Terrestrial in situ cosmogenic nuclides: theory and application. *Quaternary Science Reviews*, 20(14):1475–1560.
- Grämiger, L. M., Moore, J. R., Gisclig, V. S., Ivy-Ochs, S., and Loew, S. (2017). Beyond debuttress-

- ing: Mechanics of paraglacial rock slope damage during repeat glacial cycles. *Journal of Geophysical Research: Earth Surface*, 122(4):1004–1036.
- Gärtner-Roer, I. (2012). Sediment transfer rates of two active rockglaciers in the Swiss Alps. *Geomorphology*, 167–168:45–50. Sedimentary fluxes and budgets in natural and anthropogenically modified landscapes – Effects of climate change and land-use change on geomorphic processes.
- Gruber, S., Haeberli, W., Krummenacher, B., Keller, F., Mani, P., Hunziker, G., Hölzle, M., Vonder Mühll, D., Zimmermann, M., Keusen, H.-R., Götz, A., and Raetzo, H. (2006). Erläuterungen zur Hinweiskarte der potentiellen Permafrostverbreitung in der Schweiz 1:50'000. *Bundesamt für Umwelt (BAFU)*, Bern.
- Haeberli, W. (1985). *Creep of mountain permafrost: internal structure and flow of alpine rock glaciers*, volume 77. Mitteilungen der Versuchsanstalt für Wasserbau, Hydrologie und Glaziologie an der ETH Zürich.
- Haeberli, W. (1996). On the morphodynamics of ice/debris-transport systems in cold mountain areas. *Norsk Geografisk Tidsskrift - Norwegian Journal of Geography*, 50(1):3–9.
- Haeberli, W. (2000). Modern research perspectives relating to permafrost creep and rock glaciers: A discussion. *Permafrost and Periglacial Processes*, 11(4):290–293.
- Haeberli, W., Brandova, D., Burga, C., Egli, M., Frauenfelder, R., Kääb, A., Maisch, M., Mauz, B., and Dikau, R. (2003). Methods for absolute and relative age dating of rock-glacier surfaces in Alpine permafrost. In *Proceedings of the 8th International Conference on Permafrost*, volume 1, pages 343–348.
- Haeberli, W., Hallet, B., Arenson, L., Elconin, R., Humlum, O., Kääb, A., Kaufmann, V., Ladanyi, B., Matsuoka, N., Springman, S., and Vonder Mühll, D. (2006). Permafrost creep and rock glacier dynamics. *Permafrost and Periglacial Processes*, 17(3):189–214.
- Haeberli, W., Hoelzle, M., Kääb, A., Keller, F., Vonder Mühll, D., and Wagner, S. (1998). Ten years after drilling through the permafrost of the active rock glacier Murtèl, Eastern Swiss Alps: answered questions and new perspectives. In *Proceedings of the Seventh International Conference on Permafrost*, pages 403–410. Université Laval.
- Haeberli, W., Kääb, A., Wagner, S., Mühll, D. V., Geissler, P., Haas, J. N., Glatzel-Mattheier, H., and Wagenbach, D. (1999). Pollen analysis and ^{14}C age of moss remains in a permafrost core recovered from the active rock glacier Murtèl-Corvatsch, Swiss Alps: geomorphological and glaciological implications. *Journal of Glaciology*, 45(149):1–8.
- Haeberli, W., King, L., and Flotron, A. (1979). Surface movement and lichen-cover studies at the active rock glacier near the Grubengletscher, Wallis, Swiss Alps. *Arctic and Alpine Research*, 11(4):421–441.
- Haeberli, W., Noetzli, J., Arenson, L., Delaloye, R., Gärtner-Roer, I., Gruber, S., Isaksen, K., Kneisel, C., Krautblatter, M., and Phillips, M. (2010). Mountain permafrost: development and challenges of a young research field. *Journal of Glaciology*, 56(200):1043–1058.
- Haeberli, W., Schaub, Y., and Huggel, C. (2017). Increasing risks related to landslides from degrading permafrost into new lakes in de-glaciating mountain ranges. *Geomorphology*, 293:405–417. Permafrost and periglacial research from coasts to mountains.
- Harris, C., Arenson, L. U., Christiansen, H. H., Etzelmüller, B., Frauenfelder, R., Gruber, S., Haeberli, W., Hauck, C., Hölzle, M., Humlum, O., Isaksen, K., Kääb, A., Kern-Lütschg, M. A., Lehning, M., Matsuoka, N., Murton, J. B., Nötzli, J., Phillips, M., Ross, N., Seppälä, M., Springman, S. M., and Mühll, D. V. (2009). Permafrost and climate in Europe: Monitoring and modelling thermal, geomorphological and geotechnical responses. *Earth-Science Reviews*, 92(3):117 – 171.
- Harris, C. and Murton, J. B. (2005). Interactions between glaciers and permafrost: an introduction. *Geological Society, London, Special Publications*, 242(1):1–9.
- Harris, S. A. and Corte, A. E. (1992). Interactions and relations between mountain permafrost, glaciers, snow and water. *Permafrost and Periglacial Processes*, 3(2):103–110.
- Haug, T., Kääb, A., and Skvarca, P. (2010). Monitoring ice shelf velocities from repeat modis and landsat data – a method study on the larsen c ice shelf, antarctic peninsula, and 10 other ice shelves around antarctica. *The Cryosphere*, 4(2):161–178.
- Hausmann, H., Krainer, K., Brückl, E., and Mostler, W. (2007). Internal structure and ice content of Reichenkar rock glacier (Stubai Alps, Austria) assessed by geophysical investigations. *Permafrost and Periglacial Processes*, 18(4):351–367.
- Hedding, D. (2011). Pronival rampart and protalus rampart: a review of terminology. *Journal of Glaciology*, 57(206):1179–1180.
- Hedding, D. W. (2016). Pronival ramparts: A review. *Progress in Physical Geography: Earth and Environment*, 40(6):835–855.
- Heid, T. and Kääb, A. (2012). Evaluation of existing image matching methods for deriving glacier surface displacements globally from optical satellite imagery. *Remote Sensing of Environment*, 118:339–355.
- Heyman, J., Stroeven, A. P., Harbor, J. M., and Caffee, M. W. (2011). Too young or too old: Evaluating cosmogenic exposure dating based on an analysis of compiled boulder exposure ages. *Earth and Planetary Science Letters*, 302(1):71 – 80.

- Hinchliffe, S. and Ballantyne, C. K. (1999). Talus accumulation and rockwall retreat, Trotternish, Isle of Skye, Scotland. *Scottish Geographical Journal*, 115(1):53–70.
- Hippe, K. (2012). *Combining cosmogenic ^{10}Be and in situ ^{14}C in Earth surface sciences: A new ^{14}C extraction system and two case studies on sediment transfer and surface exposure dating*. PhD thesis, ETH Zurich. Diss., Eidgenössische Technische Hochschule ETH Zürich, Nr. 20198, 2012.
- Hippolyte, J.-C., Bourlès, D., Braucher, R., Carcaillet, J., Léanni, L., Arnold, M., and Aumaitre, G. (2009). Cosmogenic ^{10}Be dating of a sackung and its faulted rock glaciers, in the Alps of Savoy (France). *Geomorphology*, 108(3):312–320.
- Hippolyte, J.-C., Bourlès, D., Léanni, L., Braucher, R., Chauvet, F., and Lebatard, A. E. (2012). ^{10}Be ages reveal >12ka of gravitational movement in a major sackung of the Western Alps (France). *Geomorphology*, 171–172:139–153.
- Hoelzle, M., Wagner, S., Kääb, A., and Vonder Mühll, D. (1998). Surface movement and internal deformation of ice-rock mixtures within rock glaciers at Pontresina-Schafberg, Upper Engadin, Switzerland. In *Proceedings of the Seventh International Conference on Permafrost*, volume 2327. Université Laval.
- Humlum, O. (1998). The climatic significance of rock glaciers. *Permafrost and Periglacial Processes*, 9(4):375–395.
- Humlum, O. (2000). The geomorphic significance of rock glaciers: estimates of rock glacier debris volumes and headwall recession rates in West Greenland. *Geomorphology*, 35(1):41 – 67.
- Ikeda, A. and Matsuoka, N. (2006). Pebbly versus bouldery rock glaciers: Morphology, structure and processes. *Geomorphology*, 73(3):279 – 296.
- Ikeda, A., Matsuoka, N., and Kääb, A. (2008). Fast deformation of perennially frozen debris in a warm rock glacier in the Swiss Alps: an effect of liquid water. *Journal of Geophysical Research: Earth Surface*, 113(F01021).
- Ivy-Ochs, S. (2015). Glacier variations in the European Alps at the end of the last glaciation. *Cuadernos de Investigación Geográfica*, 41(2):295–315.
- Ivy-Ochs, S., Kerschner, H., Maisch, M., Christl, M., Kubik, P. W., and Schlüchter, C. (2009). Latest Pleistocene and Holocene glacier variations in the European Alps. *Quaternary Science Reviews*, 28(21):2137–2149. Holocene and Latest Pleistocene Alpine Glacier Fluctuations: A Global Perspective.
- Ivy-Ochs, S., Kerschner, H., Reuther, A., Maisch, M., Sailer, R., Schaefer, J., Kubik, P. W., Synal, H.-A., and Schlüchter, C. (2006). The timing of glacier advances in the northern European Alps based on surface exposure dating with cosmogenic ^{10}Be , ^{26}Al , ^{36}Cl , and ^{21}Ne . *Special Papers Geological Society of America*, 415:43.
- Ivy-Ochs, S., Kerschner, H., Reuther, A., Preusser, F., Heine, K., Maisch, M., Kubik, P. W., and Schlüchter, C. (2008). Chronology of the last glacial cycle in the European Alps. *Journal of Quaternary Science*, 23(6-7):559–573.
- Ivy-Ochs, S., Kerschner, H., and Schlüchter, C. (2007). Cosmogenic nuclides and the dating of Lateglacial and early Holocene glacier variations: The Alpine perspective. *Quaternary International*, 164–165(Supplement C):53–63. From the Swiss Alps to the Crimean Mountains - Alpine Quaternary stratigraphy in a European context.
- Ivy-Ochs, S. and Kober, F. (2008). Surface exposure dating with cosmogenic nuclides. *Quaternary Science Journal*, 57(1-2):179–209. .
- Ivy-Ochs, S., Schäfer, J., Kubik, P. W., Synal, H.-A., and Schlüchter, C. (2004). Timing of deglaciation on the northern Alpine foreland (Switzerland). *Eclogae Geologicae Helvetiae*, 97(1):47–55.
- Ivy-Ochs, S., Schlüchter, C., Kubik, P. W., Synal, H.-A., Beer, J., and Kerschner, H. (1996). The exposure age of an Egesen moraine at Julier Pass, Switzerland, measured with the cosmogenic radionuclides ^{10}Be , ^{26}Al and ^{36}Cl . *Eclogae Geologicae Helvetiae*, 89(3):1049–1063.
- Ivy Ochs, S. D. (1996). *The dating of rock surfaces using in situ produced ^{10}Be , ^{26}Al and ^{36}Cl , with examples from Antarctica and the Swiss Alps*. PhD thesis, ETH Zurich. Rückentitel: Rock surface dating with ^{10}Be , ^{26}Al and ^{36}Cl . Diss. Naturwiss. ETH Zürich, Nr. 11763, 1996. Ref.: Christian Schlüchter ; Korref.: Peter W. Kubik ; Korref.: Jürg Beer.
- Janke, J. and Frauenfelder, R. (2007). The relationship between rock glacier and contributing area parameters in the Front Range of Colorado. *Journal of Quaternary Science*, 23(2):153–163.
- Janke, J., Regmi, N., Giardino, J., and Vitek, J. (2013). 8.17 rock glaciers. In Shroder, J. F., editor, *Treatise on Geomorphology*, pages 238–273. Academic Press, San Diego.
- Jansen, F. and Hergarten, S. (2006). Rock glacier dynamics: Stick-slip motion coupled to hydrology. *Geophysical Research Letters*, 33(10):L10502, 1–4. L10502.
- Joerin, U. E., Stocker, T. F., and Schlüchter, C. (2006). Multicentury glacier fluctuations in the Swiss Alps during the Holocene. *The Holocene*, 16(5):697–704.
- Johnson Jr., J. P. and Nickling, W. G. (1979). Englacial temperature and deformation of a rock glacier in the Kluane Range, Yukon Territory, Canada. *Canadian Journal of Earth Sciences*, 16(12):2275–2283.
- Kääb, A. (2005). *Remote sensing of mountain glaciers and permafrost creep*. Schriftenreihe Physische

- Geographie ; 48 ; Glaziologie und Geomorphodynamik. Zürich: Geographisches Institut der Universität Zürich. Überarb. Habil.-Schr. Univ. Zürich, 2004.
- Kannan, K. and Rajagopal, K. (2013). A model for the flow of rock glaciers. *International Journal of Non-Linear Mechanics*, 48(Supplement C):59–64.
- Kääb, A. (2013). Permafrost and periglacial features | rock glaciers and protalus forms. In Elias, S. A. and Mock, C. J., editors, *Encyclopedia of Quaternary Science (Second Edition)*, pages 535–541. Elsevier, Amsterdam, second edition edition.
- Kääb, A., Frauenfelder, R., and Roer, I. (2007). On the response of rockglacier creep to surface temperature increase. *Global and Planetary Change*, 56(1):172 – 187. Climate Change Impacts on Mountain Glaciers and Permafrost.
- Kääb, A., Haeberli, W., and Gudmundsson, G. H. (1997). Analysing the creep of mountain permafrost using high precision aerial photogrammetry: 25 years of monitoring Gruben rock glacier, Swiss Alps. *Permafrost and Periglacial Processes*, 8(4):409–426.
- Kääb, A., Kaufmann, V., Ladstädter, R., and Eiken, T. (2003). Rock glacier dynamics: implications from high-resolution measurements of surface velocity fields. In Phillips, S. . A., editor, *Proceedings of the 8th International Conference on Permafrost*, pages 501–506. Balkema: Zurich, Swets & Zeitlinger, Lisse.
- Kääb, A. and Reichmuth, T. (2005). Advance mechanisms of rock glaciers. *Permafrost and Periglacial Processes*, 16(2):187–193.
- Kääb, A. and Vollmer, M. (2000). Surface geometry, thickness changes and flow fields on creeping mountain permafrost: Automatic extraction by digital image analysis. *Permafrost and Periglacial Processes*, 11(4):315–326.
- Kääb, A. and Weber, M. (2004). Development of transverse ridges on rock glaciers: field measurements and laboratory experiments. *Permafrost and Periglacial Processes*, 15(4):379–391.
- Kellerer-Pirklbauer, A. and Kaufmann, V. (2012). About the relationship between rock glacier velocity and climate parameters in central Austria. *Austrian Journal of Earth Science*, 105(2):94–112.
- Kellerer-Pirklbauer, A., Lieb, G. K., and Kleinfierchner, H. (2012). A new rock glacier inventory of the Eastern European Alps. *Austrian Journal of Earth Sciences*, 105(2):78–93.
- Kellerer-Pirklbauer, A., Wangenstein, B., Farbrót, H., and Etzelmüller, B. (2008). Relative surface age-dating of rock glacier systems near Hólar in Hjalatalur, northern Iceland. *Journal of Quaternary Science*, 23(2):137–151.
- Kenner, R., Phillips, M., Hauck, C., Hilbich, C., Mulsow, C., Bühler, Y., Stoffel, A., and Buchroithner, M. (2017). New insights on permafrost genesis and conservation in talus slopes based on observations at Flüelapass, Eastern Switzerland. *Geomorphology*, 290:101 – 113.
- Kerschner, H. and Ivy-Ochs, S. (2008). Palaeoclimate from glaciers: Examples from the Eastern Alps during the Alpine Lateglacial and early Holocene. *Global and Planetary Change*, 60(1):58 – 71. Historical and Holocene glacier – climate variations.
- Krainer, K., Ausserer, P., Bressan, D., Lang, K., Mair, V., Mussner, L., Nickus, U., Schmidt, V., Schiestl, E., Tessadri, R., Thies, H., and Tonidandel, D. (2017). Aufbau und Dynamik ausgewählter Blockgletscher in Nord- und Südtirol. *Geo.Alp*, 12/2015:75–134.
- Krainer, K., Bressan, D., Dietre, B., Haas, J. N., Hajdas, I., Lang, K., Mair, V., Nickus, U., Reidl, D., Thies, H., and Tonidandel, D. (2015). A 10,300-year-old permafrost core from the active rock glacier Lazaun, southern Ötztal Alps (South Tyrol, northern Italy). *Quaternary Research*, 83(2):324–335.
- Kronig, O., Ivy-Ochs, S., Hajdas, I., Christl, M., Wirsig, C., and Schlüchter, C. (2017). Holocene evolution of the Triftje- and the Oberseeegletscher (Swiss Alps) constrained with ¹⁰Be exposure and radiocarbon dating. *Swiss Journal of Geosciences*.
- Lal, D. and Peters, B. (1967). *Cosmic Ray Produced Radioactivity on the Earth*, pages 551–612. Springer Berlin Heidelberg, Berlin, Heidelberg.
- Laustela, M., Egli, M., Frauenfelder, R., Kääb, A., Maisch, M., and Haeberli, W. (2003). Weathering rind measurements and relative age dating of rockglacier surfaces in crystalline regions of the Eastern Swiss Alps. In *Proceedings of the 8th International Conference on Permafrost*, pages 627–632. Balkema: Zurich.
- Le Roy, M., Nicolussi, K., Deline, P., Astrade, L., Edouard, J.-L., Miramont, C., and Arnaud, F. (2015). Calendar-dated glacier variations in the western European Alps during the Neoglacial: the Mer de Glace record, Mont Blanc massif. *Quaternary Science Reviews*, 108:1 – 22.
- Lewis, J. P. (1995). Fast normalized cross-correlation. In *Vision interface*, volume 10, pages 120–123.
- Leyssinger Vieli, G. and Gudmundsson, G. H. (2003). Evolution of Rock Glaciers and Alpine Glaciers: A Model–Model Approach. In Phillips, M., Springman, S., and Arenson, L. U., editors, *Proceedings of the 8th International Permafrost Conference, Zurich 2003*, pages 673–677. Swets & Zeitlinger.
- Lisiecki, L. E. and Raymo, M. E. (2005). A Pliocene-Pleistocene stack of 57 globally distributed benthic $\delta^{18}\text{O}$ records. *Paleoceanography*, 20(1).
- Loewenherz, D. S., Lawrence, C. J., and Weaver, R. L. (1989). On the development of transverse ridges

- on rock glaciers. *Journal of Glaciology*, 35(121):383–391.
- Luethi, R., Phillips, M., and Lehning, M. (2016). Estimating non-conductive heat flow leading to intra-permafrost talik formation at the Ritigraben rock glacier (western swiss alps). *Permafrost and Periglacial Processes*, 28(1):183–194.
- Mackey, B. H. and Lamb, M. P. (2013). Deciphering boulder mobility and erosion from cosmogenic nuclide exposure dating. *Journal of Geophysical Research: Earth Surface*, 118(1):184–197.
- Manatschal, G. and Nievergelt, P. (1997). A continent-ocean transition recorded in the Err and Platta nappes (Eastern Switzerland). *Eclogae Geologicae Helvetiae*, 90(1):3–28.
- Marrero, S. M., Phillips, F. M., Borchers, B., Lifton, N., Aumer, R., and Balco, G. (2016). Cosmogenic nuclide systematics and the CRONUScal program. *Quaternary Geochronology*, 31:160–187.
- Masini, E. and Manatschal, G. (2014). The Err detachment in SE Switzerland: a witness of how continents break apart. *International Journal of Earth Sciences*, 103(1):121–122.
- Masini, E., Manatschal, G., Mohn, G., and Unternehr, P. (2012). Anatomy and tectono-sedimentary evolution of a rift-related detachment system: The example of the Err detachment (central Alps, SE Switzerland). *GSA Bulletin*, 124(9-10):1535–1551.
- Matsuoka, N. and Ikeda, A. (2001). Geological control on the distribution and characteristics of talus-derived rock glaciers. *Annual Report of the Institute of Geoscience*, 27:11. Document Type: Journal Article.
- Merz, K., Green, A. G., Buchli, T., Springman, S. M., and Maurer, H. (2015). A new 3-D thin-skinned rock glacier model based on helicopter GPR results from the Swiss Alps. *Geophysical Research Letters*, 42(11):4464–4472. 2015GL063951.
- Messerli, A. and Grinsted, A. (2015). Image georectification and feature tracking toolbox: ImGRAFT. *Geoscientific Instrumentation, Methods and Data Systems*, 4(1):23–34.
- Monnier, S., Camerlynck, C., Rejiba, F., Kinnard, C., Feuillet, T., and Dhemaied, A. (2011). Structure and genesis of the Thabor rock glacier (Northern French Alps) determined from morphological and ground-penetrating radar surveys. *Geomorphology*, 134(3):269–279.
- Monnier, S. and Kinnard, C. (2016). Interrogating the time and processes of development of the Las Liebres rock glacier, central Chilean Andes, using a numerical flow model. *Earth Surface Processes and Landforms*, 41(13):1884–1893. ESP-15-0413.R1.
- Monnier, S. and Kinnard, C. (2017). Pluri-decadal (1955–2014) evolution of glacier–rock glacier transitional landforms in the central Andes of Chile (30–33°S). *Earth Surface Dynamics*, 5(3):493–509.
- Monnier, S., Kinnard, C., Surazakov, A., and Bossy, W. (2014). Geomorphology, internal structure, and successive development of a glacier foreland in the semiarid Chilean Andes (Cerro Tapado, upper Elqui Valley, 30°08' s., 69°55' w.). *Geomorphology*, 207(Supplement C):126–140.
- Moore, P. L. (2014). Deformation of debris-ice mixtures. *Reviews of Geophysics*, 52(3):435–467. 2014RG000453.
- Müller, J., Vieli, A., and Gärtner-Roer, I. (2016). Rock glaciers on the run – understanding rock glacier landform evolution and recent changes from numerical flow modeling. *The Cryosphere*, 10(6):2865–2886.
- Müller, J., Vieli, A., and Gärtner-Roer, I. (2016). Rock glaciers on the run – understanding rock glacier landform evolution and recent changes from numerical flow modeling. *The Cryosphere*, 10(6):2865–2886.
- Nickling, W. and Bennett, L. (1984). The shear strength characteristics of frozen coarse granular debris. *Journal of Glaciology*, 30(106):348–357.
- Nicolussi, K., Kaufmann, M., Patzelt, G., Plicht van der, J., and Thurner, A. (2005). Holocene tree-line variability in the Kauner Valley, Central Eastern Alps, indicated by dendrochronological analysis of living trees and subfossil logs. *Vegetation History and Archaeobotany*, 14(3):221–234.
- Nye, J. F. (1952a). A comparison between the theoretical and the measured long profile of the Unteraar Glacier. *Journal of Glaciology*, 2(12):103–107.
- Nye, J. F. (1952b). The mechanics of glacier flow. *Journal of Glaciology*, 2(12):82–93.
- Nye, J. F. (1957). The distribution of stress and velocity in glaciers and ice-sheets. *Proceedings of the Royal Society of London A: Mathematical, Physical and Engineering Sciences*, 239(1216):113–133.
- Ochs, M. and Ivy-Ochs, S. (1997). The chemical behavior of Be, Al, Fe, Ca and Mg during AMS target preparation from terrestrial silicates modeled with chemical speciation calculations. *Nuclear Instruments and Methods in Physics Research Section B: Beam Interactions with Materials and Atoms*, 123(1):235–240. Accelerator Mass Spectrometry.
- Oldenburg, D. W. and Li, Y. (2005). Inversion for applied geophysics: A tutorial. In Butler, D. K., editor, *Near-Surface Geophysics*, volume 13 of *SEG Investigations in Geophysics*, chapter 5, pages 89–150. Society of Exploration Geophysicists (SEG).
- Olyphant, G. A. (1983). Computer simulation of rock-glacier development under viscous and pseudoplastic flow. *GSA Bulletin*, 94(4):499.
- Palacios, D., García-Ruiz, J. M., Andrés, N., Schimmelpfennig, I., Campos, N., and Léanni, L. (2017). Deglaciation in the central Pyrenees during the Pleistocene–Holocene transition: Timing and geomor-

- phological significance. *Quaternary Science Reviews*, 162:111–127.
- Pelletier, D., Fortin, A., and Camarero, R. (1989). Are FEM solutions of incompressible flows really incompressible? (or how simple flows can cause headaches!). *International Journal for Numerical Methods in Fluids*, 9(1):99–112.
- Pfiffner, O. A. (2014). *Geology of the Alps. Revised and updated translation of Geologie der Alpen, Second Edition*. Wiley Blackwell.
- Pruessner, L., Phillips, M., Farinotti, D., Hoelzle, M., and Lehning, M. (2018). Near-surface ventilation as a key for modeling the thermal regime of coarse blocky rock glaciers. *Permafrost and Periglacial Processes*, 29(3):152–163.
- Reitner, J. M., Ivy-Ochs, S., Drescher-Schneider, R., Hajdas, I., and Linner, M. (2016). Reconsidering the current stratigraphy of the Alpine Lateglacial: Implications of the sedimentary and morphological record of the Lienz area (Tyrol/Austria). *E&G Quaternary Science Journal*, 65(2):113–144.
- Rode, M. and Kellerer-Pirklbauer, A. (2012). Schmidt-hammer exposure-age dating (shd) of rock glaciers in the Schöderkogel-Eisenhut area, Schladminger Tauern Range, Austria. *The Holocene*, 22(7):761–771.
- Roer, I., Haeberli, W., Avian, M., Kaufmann, V., Delaloye, R., Lambiel, C., and Kääb, A. (2008). Observations and considerations on destabilizing active rock glaciers in the European Alps. In *Ninth International Conference on Permafrost*, volume 2, pages 1505–1510. Institute of Northern Engineering, University of Alaska Fairbanks Fairbanks, Alaska.
- Roer, I., Kääb, A., and Dikau, R. (2005). Rockglacier acceleration in the Turtmann valley (swiss alps): Probable controls. *Norsk Geografisk Tidsskrift - Norwegian Journal of Geography*, 59(2):157–163.
- Roscoe, R. (1952). The viscosity of suspensions of rigid spheres. *British Journal of Applied Physics*, 3(8):267.
- Scapozza, C. (2015). Investigation on protalus ramparts in the Swiss Alps. *Geographica Helvetica*, 70(2):135–139.
- Scapozza, C., Lambiel, C., Bozzini, C., Mari, S., and Conedera, M. (2014). Assessing the rock glacier kinematics on three different timescales: a case study from the southern Swiss Alps. *Earth Surface Processes and Landforms*, 39(15):2056–2069. ESP-13-0183.R3.
- Scapozza, C., Lambiel, C., Reynard, E., Fallot, J.-M., Antognini, M., and Schoeneich, P. (2010). Radiocarbon dating of fossil wood remains buried by the Piancabella rock glacier, Blenio Valley (Ticino, southern Swiss Alps): Implications for rock glacier, treeline and climate history. *Permafrost and Periglacial Processes*, 21(1):90–96.
- Scherler, M., Schneider, S., Hoelzle, M., and Hauck, C. (2014). A two-sided approach to estimate heat transfer processes within the active layer of the Murtèl-Corvatsch rock glacier. *Earth Surface Dynamics*, 2(1):141–154.
- Schlicke, L., Névir, P., and Ulbrich, U. (2016). Kinematic vorticity number – a tool for estimating vortex sizes and circulations. *Tellus A: Dynamic Meteorology and Oceanography*, 68(1):29464.
- Schimmelpfennig, I., Schaefer, J., Akçar, N., Ivy-Ochs, S., Finkel, R., and Schlüchter, C. (2012). Holocene glacier culminations in the Western Alps and their hemispheric relevance. *Geology*, 40(10):891.
- Schimmelpfennig, I., Schaefer, J. M., Akçar, N., Koffman, T., Ivy-Ochs, S., Schwartz, R., Finkel, R. C., Zimmerman, S., and Schlüchter, C. (2014). A chronology of Holocene and Little Ice Age glacier culminations of the Steingletscher, Central Alps, Switzerland, based on high-sensitivity beryllium-10 moraine dating. *Earth and Planetary Science Letters*, 393:220 – 230.
- Schwanghart, W. and Kuhn, N. J. (2010). Topotoolbox: A set of Matlab functions for topographic analysis. *Environmental Modelling & Software*, 25(6):770–781.
- Schwanghart, W. and Scherler, D. (2014). Short communication: TopoToolbox 2 – MATLAB-based software for topographic analysis and modeling in Earth surface sciences. *Earth Surface Dynamics*, 2(1):1–7.
- Schwarz-Zanetti, W. (1983). Wanderblöcke im Gebiet der Bergünnerstöcke (Kt. Graubünden/Schweiz). *Geographica Helvetica*, 38(3):103–111.
- Shewchuk, J. R. (1996). Triangle: Engineering a 2D Quality Mesh Generator and Delaunay Triangulator. In Lin, M. C. and Manocha, D., editors, *Applied Computational Geometry: Towards Geometric Engineering*, volume 1148 of *Lecture Notes in Computer Science*, pages 203–222. Springer-Verlag. From the First ACM Workshop on Applied Computational Geometry.
- Snieder, R. and Trampert, J. (1999). Inverse problems in geophysics. In Wirgin, A., editor, *Wavefield Inversion*, pages 119–190. Vienna. Springer Vienna.
- Solomina, O. N., Bradley, R. S., Hodgson, D. A., Ivy-Ochs, S., Jomelli, V., Mackintosh, A. N., Nesje, A., Owen, L. A., Wanner, H., Wiles, G. C., and Young, N. E. (2015). Holocene glacier fluctuations. *Quaternary Science Reviews*, 111:9–34.
- Solomina, O. N., Bradley, R. S., Jomelli, V., Geirsdottir, A., Kaufman, D. S., Koch, J., McKay, N. P., Masiokas, M., Miller, G., Nesje, A., Nicolussi, K., Owen, L. A., Putnam, A. E., Wanner, H., Wiles, G., and Yang, B. (2016). Glacier fluctuations during the past 2000 years. *Quaternary Science Reviews*,

- 149:61–90.
- Sorg, A., Kääb, A., Roesch, A., Bigler, C., and Stoffel, M. (2015). Contrasting responses of Central Asian rock glaciers to global warming. *Scientific reports*, 5:8228.
- Springman, S. M., Arenson, L. U., Yamamoto, Y., Maurer, H., Kos, A., Buchli, T., and Derungs, G. (2012). Multidisciplinary investigations on three rock glaciers in the Swiss Alps: legacies and future perspectives. *Geografiska Annaler: Series A, Physical Geography*, 94(2):215–243.
- Steffen, W., Rockström, J., Richardson, K., Lenton, T. M., Folke, C., Liverman, D., Summerhayes, C. P., Barnosky, A. D., Cornell, S. E., Crucifix, M., Donges, J. F., Fetzer, I., Lade, S. J., Scheffer, M., Winkelmann, R., and Schellnhuber, H. J. (2018). Trajectories of the Earth system in the Anthropocene. *Proceedings of the National Academy of Sciences*.
- Studer, J. (1896). *Schweizer Ortsnamen. Ein historisch-etymologischer Versuch*. Zürich: F. Schulthess.
- Tarantola, A. (2005). *Inverse problem theory and methods for model parameter estimation*, volume 89. Society for Industrial and Applied Mathematics (siam), Philadelphia.
- Truesdell, C. (1953). Two measures of vorticity. *Journal of Rational Mechanics and Analysis*, 2:173–217.
- Vitek, J. D. and Giardino, J. R. (1987a). Rock glacier bibliography. In Giardino, J. R., Shroder, J. F. J., and Vitek, J. D., editors, *Rock glaciers*, Rock glaciers, chapter 18, pages 305–344. Allen & Unwin. Document Type: Monograph.
- Vitek, J. D. and Giardino, J. R. (1987b). Rock glaciers: A review of the knowledge base. In Giardino, J. R., Shroder, J. F. J., and Vitek, J. D., editors, *Rock glaciers*, Rock Glaciers, chapter 1, pages 1–26. Allen & Unwin. Document Type: Monograph.
- von Blanckenburg, F. (2005). The control mechanisms of erosion and weathering at basin scale from cosmogenic nuclides in river sediment. *Earth and Planetary Science Letters*, 237(3):462 – 479.
- Wagner, S. (1992). Creep of Alpine permafrost, investigated on the Murtèl rock glacier. *Permafrost and Periglacial Processes*, 3(2):157–162.
- Wahrhaftig, C. and Cox, A. (1959). Rock glaciers in the Alaska Range. *Geological Society of America Bulletin*, 70(4):383–436.
- Whalley, W. B. (2009). On the interpretation of discrete debris accumulations associated with glaciers with special reference to the British Isles. *Geological Society, London, Special Publications*, 320(1):85–102.
- Whalley, W. B. and Azizi, F. (2003). Rock glaciers and protalus landforms: Analogous forms and ice sources on Earth and Mars. *Journal of Geophysical Research: Planets*, 108(E4):13–1–13–7. 8032.
- Wicky, J. and Hauck, C. (2017). Numerical modelling of convective heat transport by air flow in permafrost talus slopes. *The Cryosphere*, 11(3):1311–1325.
- Winkler, S. (2009). First attempt to combine terrestrial cosmogenic nuclide (^{10}Be) and schmidt hammer relative-age dating: Strauchon Glacier, Southern Alps, New Zealand. *Central European Journal of Geosciences*, 1(3):274–290.
- Winkler, S. and Lambiel, C. (2018). Age constraints of rock glaciers in the Southern Alps/New Zealand – Exploring their palaeoclimatic potential. *The Holocene*, 28(5):778–790.
- Wirsig, C., Zasadni, J., Christl, M., Akçar, N., and Ivy-Ochs, S. (2016). Dating the onset of LGM ice surface lowering in the High Alps. *Quaternary Science Reviews*, 143:37 – 50.
- Wirz, V., Gruber, S., Purves, R. S., Beutel, J., Gärtner-Roer, I., Gubler, S., and Vieli, A. (2016). Short-term velocity variations at three rock glaciers and their relationship with meteorological conditions. *Earth Surface Dynamics*, 4(1):103–123.
- Zachos, J., Pagani, M., Sloan, L., Thomas, E., and Billups, K. (2001). Trends, rhythms, and aberrations in global climate 65 Ma to present. *Science*, 292(5517):686–693.
- Zakšek, K., Oštir, K., and Kokalj, Ž. (2011). Sky-view factor as a relief visualization technique. *Remote Sensing*, 3(2):398–415.
- Zasadni, J. (2007). The Little Ice Age in the Alps: Its record in glacial deposits and rock glacier formation. *Studia Geomorphologica Carpatho-Balcanica*, 41:117–137.

Maps

- Bini, A., Schlüchter, Christian, Burkhalter, Reto Michael, Urech, Martin, & Schweiz. Landesgeologie. (2009). Die Schweiz während des letzteiszeitlichen Maximums (LGM) = La Suisse durant le dernier maximum glaciaire = La Svizzera durante l'ultimo massimo glaciale = Switzerland during the Last Glacial Maximum. Wabern: Bundesamt für Landestopografie.
- Cornelius, H.P. (1932). *Geologische Karte der Err-Julier-Gruppe 1:25 000*, 2 Blätter. Beitr. Geol. Karte Schweiz, Spezialkarte Nr. 115 A (Westblatt)
- Bundesamt für Umwelt, 2005: Hinweiskarte der potentiellen Permafrostverbreitung in der Schweiz
- Topographische Karte der Schweiz (Dufourkarte). Blatt XV (1853) and Blatt XX (1854) (© swisstopo)

Topographischer Atlas der Schweiz (Siegfriedkarte). Blatt 426 (1887), Blatt 517 (1877) (© swisstopo)

Landeskarte 1:25000, 2009 (© swisstopo)

Schwarb, M., Daly, C., Frei, C., Schär, C. (2000). Mittlere jährliche Niederschlagshöhe im europäischen Alpenraum 1971-1990. Hydrologischer Atlas der Schweiz, Blatt 2.6

Web pages

last accessed September 2018

<https://map.geo.admin.ch/>

“The online calculators formerly known as the CRONUS-Earth online calculators” <http://hess.ess.washington.edu/math/> [Balco et al., 2008]

“CRONUS geometric-shielding calculator” <http://cronus.cosmogenicnuclides.rocks/2.0/> [Marrero et al., 2016].

Computer programs

QGIS Development Team (2018). *QGIS Geographic Information System*. Open Source Geospatial Foundation. URL <https://www.qgis.org/> QGIS-Desktop

“Imagemagick” <https://www.imagemagick.org/>

“Hugin” <http://hugin.sourceforge.net/>

“ImGRAFT” <http://imgraft.glaciology.net/>

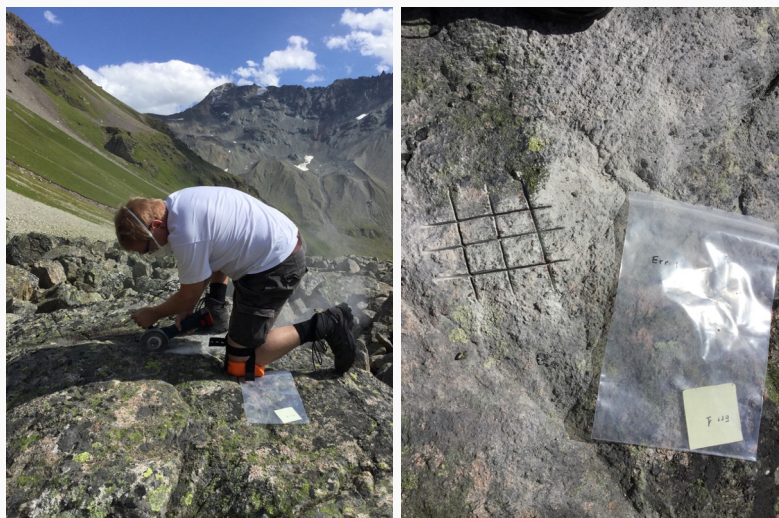
“Triangle” <https://www.cs.cmu.edu/~quake/triangle.html>

Appendix

A1 Rock book

Photos of the sampled boulders with their coordinates, elevation, orientation of the sampled surface, lithology, shielding factor, sample thickness and date/time.

Rock Book



sample name	Err 1
CH03 [E/N, m]	773613/160358
WGS84 [lat/lon]	9°42'13"/46°34'19"
elevation [m a.s.l.]	2457
direction/dip	200/05 (?)
lithology	Err granite
shielding factor	0.9739
thickness [cm]	1.5 (2.0)
date, time	Aug 2, 16:27
comments	approx. boulder size 6×3×5 m



sample name	Err 2
CH03 [E/N, m]	773734/160393
WGS84 [lat/lon]	9°42'18"/46°34'20"
elevation [m a.s.l.]	2493
direction/dip	000/00
lithology	Err granite
shielding factor	0.9751
thickness [cm]	1.5
date, time	Aug 2, 17:29
comments	approx. boulder size 5×2×3 m. Tip of boulder.



sample name	Err 3
CH03 [E/N, m]	774365/160529
WGS84 [lat/lon]	9°42'48"/46°34'23"
elevation [m a.s.l.]	2682
direction/dip	150/10 (?)
lithology	Err granite
shielding factor	0.9259
thickness [cm]	1.8 (1.5)
date, time	Aug 3, 11:50
comments	approx. boulder size 2×4×3 m. Uppermost sample.



sample name	Err 4
CH03 [E/N, m]	774320/160547
WGS84 [lat/lon]	9°42'46"/46°34'24"
elevation [m a.s.l.]	2678 (2670!)
direction/dip	032/10 (038/10)
lithology	Err granite
shielding factor	0.9392
thickness [cm]	2.0
date, time	Aug 3, 12:23
comments	approx. boulder size 3×1.5×2.5 m.



sample name	Err 5
CH03 [E/N, m]	774281/160562
WGS84 [lat/lon]	9°42'44"/46°34'25"
elevation [m a.s.l.]	2661
direction/dip	
lithology	Err granite
shielding factor	0.9428
thickness [cm]	1.5 (2.0)
date, time	Aug 3, 13:13
comments	approx. boulder size 3×3×4 m



sample name	Err 6
CH03 [E/N, m]	774295/160579
WGS84 [lat/lon]	9°42'45"/46°34'25"
elevation [m a.s.l.]	2650 (2643)
direction/dip	217/15
lithology	Err granite
shielding factor	0.9406
thickness [cm]	2.0 (1.5)
date, time	Aug 3, 13:58
comments	approx. boulder size 6×3×3 (5×3×2.5) m



sample name	Err 7
CH03 [E/N, m]	774199/160612
WGS84 [lat/lon]	9°42'40"/46°34'26"
elevation [m a.s.l.]	2635 (2629)
direction/dip	033/20
lithology	Err granite
shielding factor	0.9365
thickness [cm]	1.5 (1.0)
date, time	Aug 3
comments	approx. boulder size 3×3×2 (2×2×2) m, higher than wide



sample name	Err 8
CH03 [E/N, m]	774254/160635
WGS84 [lat/lon]	9°42'43"/46°34'27"
elevation [m a.s.l.]	2658 (2624)
direction/dip	208/03
lithology	dolomite
shielding factor	0.9372
thickness [cm]	2.0
date, time	Aug 3, 15:49
comments	approx. boulder size 1×0.7×1.5 m



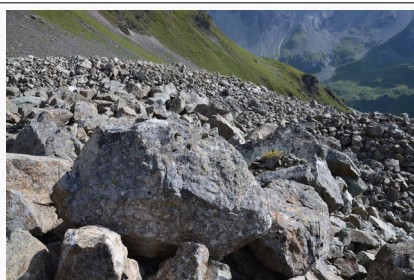
sample name	Err 9
CH03 [E/N, m]	774278/160626
WGS84 [lat/lon]	9°42'44"/46°34'27"
elevation [m a.s.l.]	2665
direction/dip	160/15
lithology	Err granite
shielding factor	0.9204
thickness [cm]	1.5 (1.0)
date, time	Aug 3, 15:42
comments	approx. boulder size 1×2×2 m



sample name	Err 10
CH03 [E/N, m]	774181/160577 (774177/160565)
WGS84 [lat/lon]	9°42'40"/46°34'25"
elevation [m a.s.l.]	2626 (2636)
direction/dip	313/29
lithology	Err granite
shielding factor	0.9211
thickness [cm]	1.5 (1.0)
date, time	Aug 3, 16:22
comments	approx. boulder size 1×1×2 m



sample name	Err 11
CH03 [E/N, m]	774121/160580 (774116/160580)
WGS84 [lat/lon]	9°42'37"/46°34'25"
elevation [m a.s.l.]	2608 (2602)
direction/dip	302/11
lithology	Err granite
shielding factor	0.945
thickness [cm]	1.5
date, time	Aug 3, 17:05
comments	approx. boulder size 5×3×5 (5×3×3) m



sample name	Err 12
CH03 [E/N, m]	774048/160565
WGS84 [lat/lon]	9°42'33"/46°34'25"
elevation [m a.s.l.]	2575
direction/dip	
lithology	Err granite
shielding factor	0.9476
thickness [cm]	1.5
date, time	Aug 3, 17:31
comments	approx. boulder size 1×1×2 m



sample name	Err 13
CH03 [E/N, m]	773926/160532
WGS84 [lat/lon]	9°42'28"/46°34'24"
elevation [m a.s.l.]	2547 (2536)
direction/dip	044/20
lithology	Err granite
shielding factor	0.9502
thickness [cm]	2.0
date, time	Aug 4, 10:40
comments	none



sample name	Err 14
CH03 [E/N, m]	773871/160482
WGS84 [lat/lon]	9°42'25"/46°34'22"
elevation [m a.s.l.]	2517 (2501)
direction/dip	056/27
lithology	Err granite
shielding factor	0.9484
thickness [cm]	2.0
date, time	Aug 4, 11:16
comments	approx. boulder size 4×6×5 m



sample name	Err 15
CH03 [E/N, m]	773769/160429
WGS84 [lat/lon]	9°42'20"/46°34'21"
elevation [m a.s.l.]	2494
direction/dip	019/14
lithology	Err granite
shielding factor	0.9582
thickness [cm]	1.0
date, time	Aug 4, 11:49
comments	none

A2 Conference submissions

- Abstract and poster to 5th European Conference on Permafrost (EUCOP), Chamonix-Mont Blanc (France), June 23–July 1, 2018 (accepted)
- Abstract to the Swiss Geoscience Meeting (SGM), Bern, Nov 30–Dec 1, 2018 (submitted)

Active, inactive, relict: Tracking the evolution of the Bleis Marscha rockglacier (Val d'Err, Grisons) with cosmogenic nuclide dating and finite-element modelling

Dominik Amschwand¹

Susan Ivy-Ochs²

Marcel Frehner¹

Olivia Kronig²

Marcus Christl²

¹Geological Institute, ETH Zürich, adominik@student.ethz.ch

²Laboratory of Ion Beam Physics, ETH Zürich

Abstract

This work aims at reconstructing the evolution of the *Bleis Marscha* rockglacier in the Val d'Err, Grisons (Switzerland). It is a one-kilometre long, multi-unit talus rockglacier with an active upper part, a relict snout, and a furrow-and-ridge microrelief. The timing of formation of each unit is investigated with surface exposure dating with ¹⁰Be and ³⁶Cl. Insights into mechanical properties and internal structure is gained with numerical finite-element modelling. The model is constrained with the horizontal surface velocity field obtained from feature-tracking of multitemporal orthorectified aerial images. The illumination-invariant orientation correlation method overcomes most of the difficulties posed by different lighting on a rugged rockglacier surface, and is a simple, yet powerful tool to capture the horizontal surface kinematics. The overarching aim is to place the development of the *Bleis Marscha* rockglacier within the Holocene climate history and to constrain the timing of glacial and periglacial processes and the relevant mechanical parameters that shaped the formerly glaciated Piz Bleis Marscha cirque.

Keywords: rockglacier; image correlation; feature tracking; numerical modelling; inverse problem

Introduction

The *Bleis Marscha* rockglacier is a talus rockglacier originating in a cirque of Piz Bleis Marscha in the Val d'Err, Grisons, Switzerland. It is more than one kilometre long, exhibits a furrow-and-ridge microrelief in the lower parts and is divided by steep front scarps into several units. Field observations such as lichen coverage and iron staining as well as results from multitemporal aerial image correlation suggests that the lower units below 2500 m a.s.l. are inactive to relict. Several previous studies have obtained exposure or luminescence dates on moraines and rockglaciers in nearby valleys, and the Holocene climate history is well established for the area (Ivy-Ochs *et al.*, 1996; Fuchs *et al.*, 2013).

Aim and methods

In the presented work, the different units of the *Bleis Marscha* rockglacier are exposure-dated with ¹⁰Be and ³⁶Cl, as an aid to reconstructing the development of the rockglacier. Furthermore, the present-day dynamics is

modelled with a numerical two-dimensional finite-element approach to gain insights into mechanical and material properties. The deformation above the shear zone is well captured by a linearly viscous (Newtonian) flow law (Frehner *et al.*, 2015). The model is constrained with horizontal surface velocities obtained from a feature-tracking analysis of multitemporal orthorectified aerial images with the Matlab tool “ImGRAFT” (Messerli & Grinsted, 2015).

Preliminary results

Slight differences in lighting, illumination direction or cloudiness suffice to make the rugged, bouldery surface of the rockglacier appear differently on aerial image such that a common normalized cross-correlation approach may perform poorly. The cross-correlation of orientation images is illumination invariant (Fitch *et al.*, 2002) and yields a connected displacement field all over the rockglacier. The correlation inherently fails near steep slopes, involving rotational movement of boulders, and on snow patches.

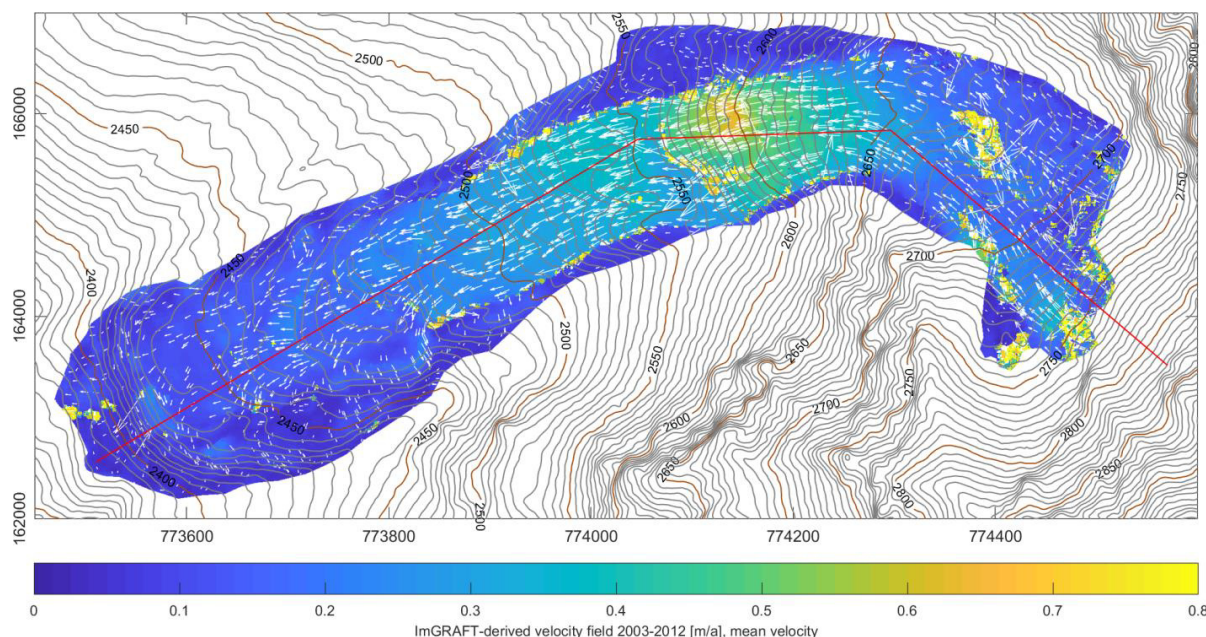


Figure 1. Horizontal surface velocity on the *Bleis Marscha* rockglacier as obtained from a feature-tracking analysis of orthorectified aerial images from 2003 and 2012. Magnitude shown by colours, direction by white arrows. The colorbar is fixed at 0.8 m/a. Higher velocities are most likely artifacts such as rotational movement of blocks at scarps or correlation problems. The red line traces the section along which the 2D numerical model is defined. Coordinates in CH1903 grid, unit in meter. Aerial images © swisstopo.

References

- Preliminary results support the subdivision of the rockglacier into units of varying degree of activity based on field observation: the upper unit is characterized by a unidirectional downslope directed creep, with increasing velocity towards the front of the upper lobe (up to 0.8 m/a, Fig. 1). The over-steepened, failure-prone front scarp shows that this unit is overriding the lower, inactive to relict units of the rockglacier, which exhibit a more “patchy” flow field of slightly varying directions and smaller velocities (<0.4 m/a). This data is used to constrain the numerical model, reproducing the deformation on a longitudinal section along the central flowline of the rockglacier (red line in Fig. 1). The model parameters that will be tested are rockglacier thickness, effective viscosity, viscosity contrast to the low-viscosity basal shear zone and thickness of a rigid blocky mantle. In a series of numerical experiments, the influence of different parameter configurations on the modelled horizontal surface velocity is tested, and plausible configurations that reproduce the observed velocities within their error margins represent solutions to this inverse problem.
- We will present a detailed analysis of the horizontal surface flow field, its relationship to the microrelief, rockglacier activity status and changes throughout the recent years.
- Barsch, D., 1996. *Rockglaciers. Indicators for the Present and Former Geoecology in High Mountain Environments*. Springer, Berlin, Heidelberg, 331 pp.
- Fitch, A. J.; Kadyrov, A.; Christmas, W. J. & Kittler, J., 2002. Orientation correlation. *Proceedings of the 13th British Machine Vision Conference*, Cardiff, England, 2-5 September:133-142.
- Fuchs, M. C.; Böhlert, R.; Krbetschek, M.; Preusser, F. & Egli, M., 2013. Exploring the potential of luminescence methods for dating Alpine rock glaciers. *Quaternary Geochronology* 18:17-33.
- Frehner, M.; Ling, A. H. M. & Gärtner-Roer, I., 2015. Furrow-and-ridge morphology on rockglaciers explained by gravity-driven buckle folding: A case study from the Murtèl rockglacier (Switzerland). *Permafrost and Periglacial Processes* 26:57-66.
- Ivy-Ochs, S.; Schlüchter, C.; Kubik, P. W.; Synal, H.-A.; Beer, J. & Kerschner, H., 1996. The exposure age of an Egesen moraine at Julier Pass, Switzerland measured with the cosmogenic radionuclides ^{10}Be , ^{26}Al and ^{36}Cl . *Eclogae Geologicae Helveticae, Schweizerische Geologische Gesellschaft* 89:1049-106.
- Messerli, A. & Grinsted, A., 2015. Image georectification and feature tracking toolbox: ImGRAFT. *Geoscientific Instrumentation, Methods and Data Systems* 4:23-34.

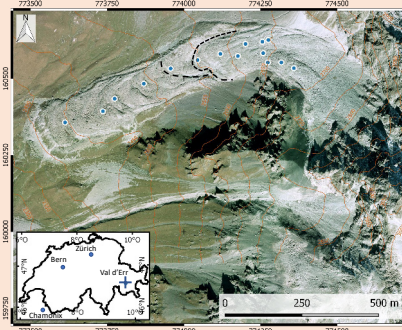
Active, inactive, relict: Tracking the evolution of the *Bleis Marscha* rockglacier (Val d'Err, Grisons) with cosmogenic nuclide dating and finite-element modelling

Dominik Amschwand^{1*}, Susan Ivy-Ochs², Marcel Frehner¹, Olivia Kronig², Marcus Christl²

[1] Introduction and goals

We attempt to reconstruct the formation of the *Bleis Marscha* rockglacier in the Val d'Err, Grisons (Switzerland) [Fig. 1]. It is a one kilometer long, *multi-unit talus rockglacier* [1] with an active upper part that overrides a lower part. Lichen-covered boulders, vegetated, stabilized slopes and signs of settling suggest that the parts below ~2500 m a.s.l. are relict. Inner front scarps separate the rockglacier into different units, each with their own activity phase.

The aim is to place the evolution of the *Bleis Marscha* rockglacier within the Holocene climate history and to constrain the timing of glacial and periglacial processes that shaped the formerly glaciated *Bleis Marscha* cirque.



← Fig. 1 | Aerial image showing the *Bleis Marscha* rockglacier in the Val d'Err, Grisons, and its location within Switzerland (inset). This is the 2003 orthophoto used for image cross correlation. Inner front scarps of advancing upper lobes are outlined by dashed lines. Sampling locations are marked by circles.

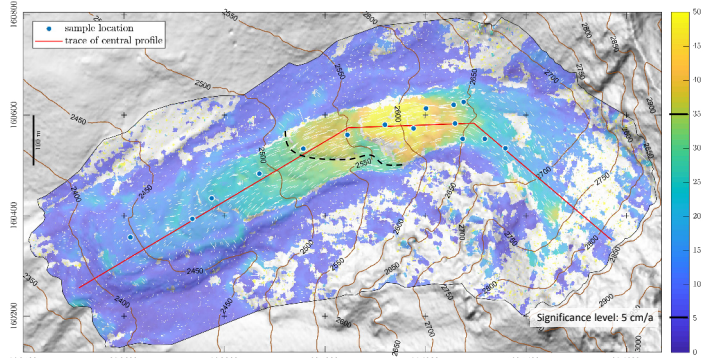
[2] Research idea and methods

- We constrain the present horizontal surface velocity field with feature-tracking of bi-temporal orthorectified aerial images (IMCOR).
- We investigate the mechanical properties and internal structure with numerical finite-element modelling (inverse problem, FEM).
- Surface exposure dating with cosmogenic ¹⁰Be and ³⁶Cl allows us now to place a temporal framework (ka scale) on rock-glacier movement periods (TCN).

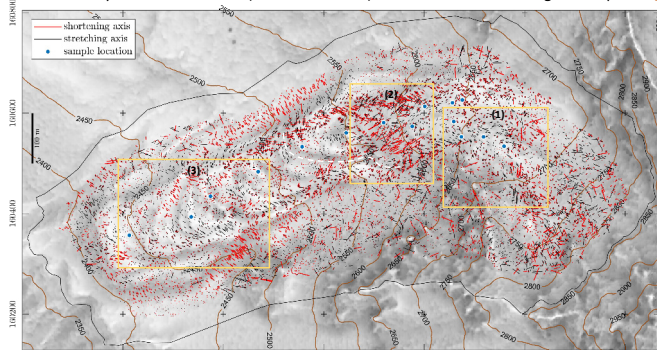
This approach combines information from different spatial and temporal scales.

[3] Aerial image correlation (IMCOR)

- Image matching of two orthophotos provides the present, short-term horizontal surface velocity [Fig. 2], whose spatial derivative is the strain rate tensor [Fig. 3][2, 6].
- Template-based image matching of two orientation images derived from orthophotos with normalized cross-correlation (NCC) as similarity measure, computed with IMGrAT [7] in Matlab (41 px ± 10.25 m template width). An orientation image represents the orientation of the intensity gradient, and is thus more robust against illumination changes [3].



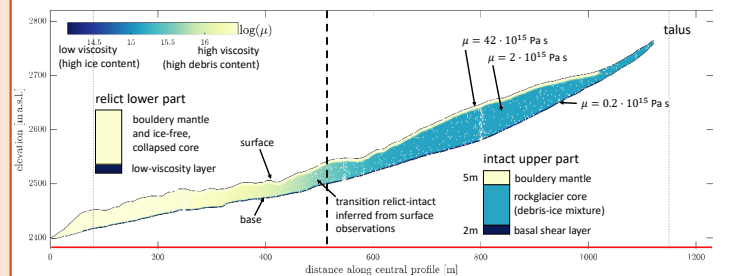
↑ Fig. 2 | Image correlation result: Horizontal surface velocity field 2003-2012 mapped onto the hillshade map. The transition relict-intact as suggested by the velocity field (threshold velocity of 35 cm/a) follows the boundary between two lobes (black dashed line). Red line: trace of the longitudinal profile [Figs. 4, 5].



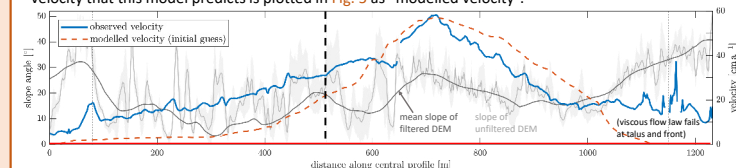
↑ Fig. 3 | Orientation of principal strain rates (velocity gradients) hinting at deformation mechanism: (1) extensive flow on intact upper part, (2) compressive overriding, (3) extensive collapse of ridges on relict lower part. Strain rates are computed with central finite-difference scheme, spacing of 50 m. Background map: sky view factor map. Strongly illuminated ridges appear bright, occluded furrows dark [8].

[4] Finite-element numerical modelling (FEM)

- We simulate the viscous deformation of the rockglacier with a computer model: An initial guess of the internal structure [Fig. 4] predicts a modelled velocity that is compared to the observed one [Fig. 5]. The subsurface structure is then adapted until the modelled and observed velocities match (*inverse problem*).
- The relation between hidden subsurface rockglacier structure and observable surface velocity is described by an incompressible (linearly-viscous) Stokes flow, solved numerically with a two-dimensional finite-element numerical model [4]. The internal structure is parameterized with thickness, density layering and viscosity layering [Fig. 4].



↑ Fig. 4 | Initial guess of the internal structure (parameterization): vertical section of the rockglacier along the profile showing a possible effective dynamic viscosity structure and mechanical layering. The surface is extracted from the DEM, the base inferred from the surrounding topography. The surface velocity that this model predicts is plotted in Fig. 5 as "modelled velocity".



↑ Fig. 5 | Preliminary modelling result: Observed and modelled horizontal surface velocity on the longitudinal profile. The observed velocity on the intact upper part correlates well with the surface slope extracted from the filtered DEM (100 m circular averaging filter, dark grey line). Unfiltered slope is averaged across a 20 m wide stripe along the profile (light grey).

[5] Exposure dating (TCN)

- We sampled fifteen boulders along a longitudinal transect of the rockglacier from the (apparently) relict toe to the higher elevation active areas [Figs. 1, 2].
- Fourteen samples are granitic boulders dated with ¹⁰Be; one dolomite boulder with ³⁶Cl.
- The cosmogenic nuclide data allow us to examine periods of activity as well as to understand nuclide inventories possibly acquired during lobe and thus boulder movement.
- Age results will be compared to image analysis-based velocity determinations [Figs. 2, 5].

[6] Main findings

- Illumination-invariant orientation correlation is a powerful tool to capture the present horizontal surface kinematics of the rugged rockglacier surface; background level is about 5 cm/a [Fig. 2].
- The upper, active part moves at a velocity up to 50 cm/a. The most rapidly moving part is several hundred meters from the talus and source headwall.
- The lower, relict rockglacier part shows clear morphological signs of inactivity, yet it is moving at speeds of up to 35 cm/a. The deformation mechanism is not known.

- Strain-rate tensors derived from illumination-invariant orientation correlation allow quantitative identification of regions dominated by extensive flow (the upper part) and compressive overriding [Fig. 3].
- Both image analysis and numerical modelling suggest that the degree of coupling between slope and velocity characterises the rockglacier activity status [Figs. 3, 5]: The active part has a uniform flow field, where the topographic gradient, velocity and principal strain rate axis are aligned on a 100-m scale. On the collapsing relict part, the strain rates are sensitive to the small-scale topography and do not align with the velocity (so-called "effet camembert").

References and data sources

- DEM: swissALTI3D 2016 (resolution 2 m). Aerial image: swisstopo 2003 (resolution 0.25 m)
- [1] Barsch, D., 1996. Rockglaciers: Indicators for the Present and Former Geoclimatology in High Mountain Environments. Springer, Berlin, Heidelberg, 331 pp.
- [2] Bodin, X., Thibert, E., Sanchez, O., Rabatel, A. & Jallet, S., 2018. Multi-annual kinematics of an active rock glacier quantified from very high-resolution DEMs: An application case in the French Alps. *Remote Sensing* 10:547-560.
- [3] Fitch, A. J., Kalyoncu, A., Christmas, W. J. & Kitter, J., 2002. Orientation correlation. *Proceedings of the 13th British Machine Vision Conference*, Cardiff, England, 2-5 September: 133-142.
- [4] Frehner, M., Ling, A. H. M. & Gärtner-Robel, I., 2015. Furrow-and-ridge morphology on rockglaciers explained by gravity-driven buckle folding: A case study from the Murten rockglacier (Switzerland). *Permafrost and Periglacial Processes* 26:57-66.
- [5] Ivy-Ochs, S., Schlüchter, C., Kubik, P. W., Snyal, H.-A., Beer, J. & Kerschner, H., 1996. The exposure age of an Egesen moraine at Jüli Pass, Switzerland measured with the cosmogenic radionuclides ¹⁰Be, ²⁶Al and ³⁶Cl. *Eclogae Geologicae Helveticae* 89:1049-1063.
- [6] Kääb, A., Gudmundsson, G. H. & Hoelzle, M., 1998. Surface deformation of creeping mountain permafrost. Photogrammetric investigations on rock glacier Murten, Swiss Alps. *Proceedings of the 7th International Conference on Permafrost* 57:531-537.
- [7] Messerli, A. & Grinold, A., 2015. Image georectification and feature tracking toolbox: IMGrAT. *Geoscientific Instrumentation, Methods and Data Systems* 4:23-34.
- [8] Zankl, K., Oble, K. & Kobel, R., 2011. Sky view factor as a relief visualization technique. *Remote Sensing*, 2(3), 398-415.

Combining exposure dating, finite-element modelling, and feature tracking to decipher rockglacier evolution: A case study from the *Bleis Marscha* rockglacier (Val d'Err, Grisons)

Dominik Amschwand*, Susan Ivy-Ochs**, Marcel Frehner*, Olivia Kronig**, Marcus Christl**

*Geological Institute, ETH Zürich, Sonneggstrasse 5, 8092 Zürich
(adominik@student.ethz.ch)

**Laboratory of Ion Beam Physics, ETH Zürich, Otto-Stern-Weg 5, 8093 Zürich

We attempt to reconstruct the formation of the *Bleis Marscha* rockglacier in the Val d'Err, Grisons (Switzerland). It is a one kilometer long, multi-unit talus rockglacier (Barsch 1996) with an active upper part that overrides a lower part. Lichen-covered boulders, vegetated, stabilized slopes, and signs of settling suggest that the parts below ~2500 m a.s.l. are relict. Internal front scarps separate the rockglacier into different units, each with its own activity phase. Morphological evidence suggests that the rockglacier started forming in the earliest Holocene.

Surface exposure dating with cosmogenic ^{10}Be and ^{36}Cl places a temporal framework (ka scale) on rockglacier movement periods (Ivy-Ochs et al. 2009). Furthermore, the present-day dynamics are numerically modelled using a two-dimensional finite-element approach to gain insights into the mechanical and material properties. Deformation above the shear zone is well captured by a linear viscous flow law (Frehner et al. 2015). The model is constrained with

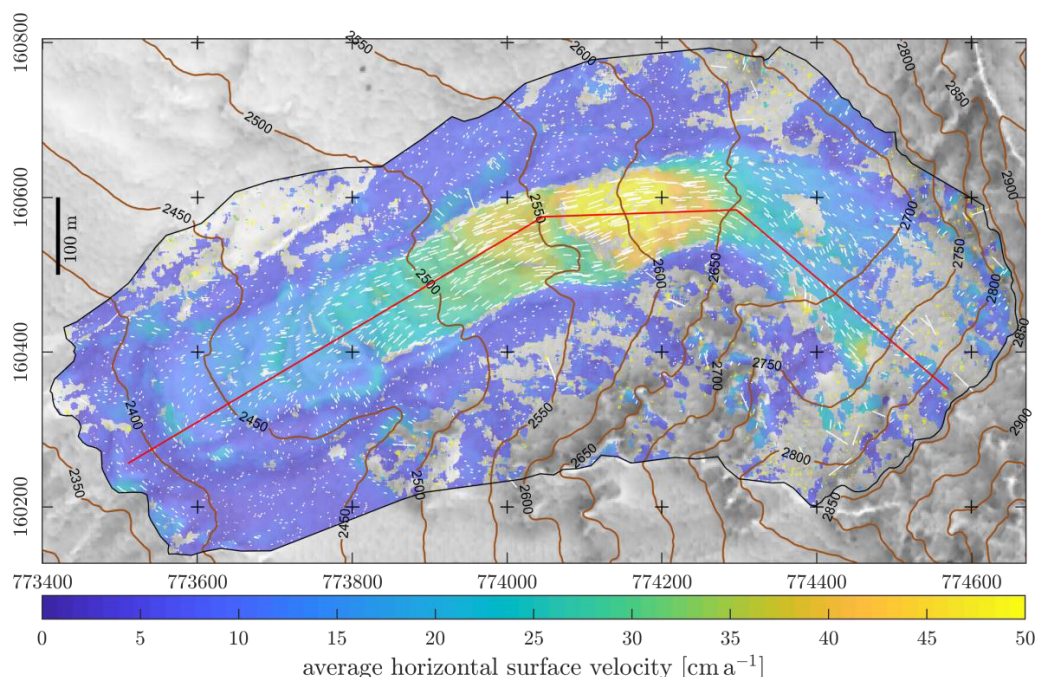


Figure 1. Noise-filtered horizontal surface velocity field 2003-2012 as obtained from feature-tracking analysis of orthorectified aerial images, draped over a sky-view map. Magnitude shown by colours, direction by white arrows. Significance level is 5 cm/a.

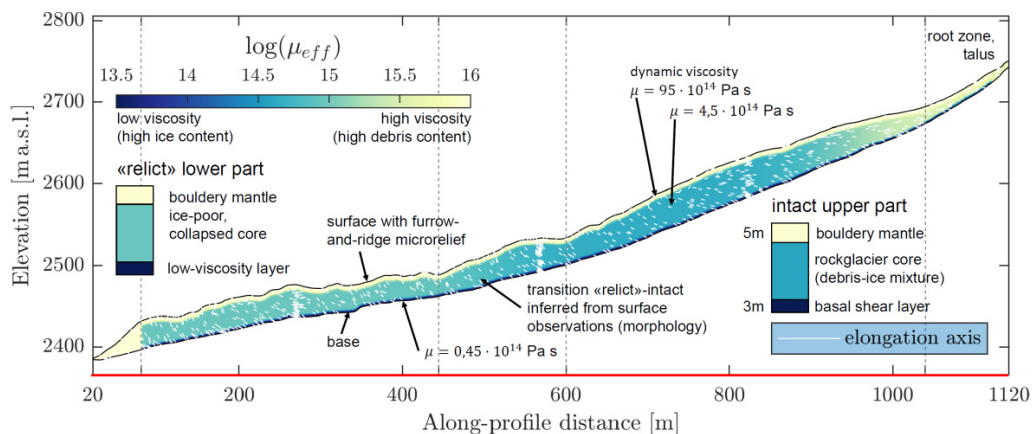


Figure 2. Inferred viscosity structure along a longitudinal section (trace in Fig. 1). Viscosity is interpreted as a proxy for ice and liquid water content.

horizontal surface velocities obtained from feature-tracking analysis of multitemporal orthorectified aerial images (Messerli & Grinsted 2015).

An illumination-invariant method for correlating the orthophotos (Fitch 2002) yielded reliable displacements on the rugged rockglacier surface. The image correlation results (Fig. 1) support the subdivision of the *Bleis Marscha* rockglacier in an active upper part, characterised by moderate to high surface velocities controlled by the topography on a 100-m scale, and a relict, collapsing lower part, characterised by an irregular surface velocity field strongly coupled to the small-scale topography ("effet camembert"). However, surface velocities of up to 30 cm/a on the apparently relict part could only be numerically reproduced assuming a considerable fraction of ice and/or water that weakens the material (Fig. 2). The subsurface ice either has been preserved throughout the Holocene or has reformed more recently.

REFERENCES

- Barsch, D. 1996: Rockglaciers. Indicators for the Present and Former Geocology in High Mountain Environments. Springer, Berlin, Heidelberg.
- Fitch, A. J., Kadyrov, A., Christmas, W. J. & Kittler, J. 2002: Orientation correlation. Proceedings of the 13th British Machine Vision Conference, Cardiff, England, 2-5 September, 133-142.
- Frehner, M., Ling, A. H. M. & Gärtner-Roer, I. 2015: Furrow-and-ridge morphology on rockglaciers explained by gravity-driven buckle folding: A case study from the Murtèl rockglacier (Switzerland). *Permafrost and Periglacial Processes* 26, 57-66.
- Ivy-Ochs, S., Kerschner, H., Maisch, M., Christl, M., Kubik, P. W. & Schlüchter, C. 2009: Latest Pleistocene and Holocene glacier variations in the European Alps. *Quaternary Science Reviews* 28, 2137-2149.
- Messerli, A. & Grinsted, A. 2015. Image georectification and feature tracking toolbox: ImGRAFT. *Geoscientific Instrumentation, Methods and Data Systems* 4, 23-34.



Eidgenössische Technische Hochschule Zürich
Swiss Federal Institute of Technology Zurich

Declaration of originality

The signed declaration of originality is a component of every semester paper, Bachelor's thesis, Master's thesis and any other degree paper undertaken during the course of studies, including the respective electronic versions.

Lecturers may also require a declaration of originality for other written papers compiled for their courses.

I hereby confirm that I am the sole author of the written work here enclosed and that I have compiled it in my own words. Parts excepted are corrections of form and content by the supervisor.

Title of work (in block letters):

MSc Thesis

Active, inactive, relict: Tracking the evolution of the Bleis Martscha
rockglacier (Val d'Er, Grisons) with cosmogenic nuclide dating and finite-
element modelling

Authored by (in block letters):

For papers written by groups the names of all authors are required.

Name(s):

AMSCHWAND

First name(s):

Dominik

With my signature I confirm that

- I have committed none of the forms of plagiarism described in the 'Citation etiquette' information sheet.
- I have documented all methods, data and processes truthfully.
- I have not manipulated any data.
- I have mentioned all persons who were significant facilitators of the work.

I am aware that the work may be screened electronically for plagiarism.

Place, date

Zürich, 14. Sep 2018

Signature(s)

For papers written by groups the names of all authors are required. Their signatures collectively guarantee the entire content of the written paper.

Landforms of viscous flow



Left: *Bleis Marscha* rockglacier, *Val d'Err*. Photo by Armando Janett. **Right:** 1906 lava flow on Kanaga Volcano, Aleutian Islands. Photo by Michelle Combs, Alaska Volcano Observatory / U.S. Geological Survey [source].